

Electrical control of excitons in a gated two-dimensional semiconductor

Inauguraldissertation

zur
Erlangung der Würde eines Doktors der Philosophie
vorgelegt der
Philosophisch-Naturwissenschaftlichen Fakultät
der Universität Basel

von

Nadine Martine Leisgang

Basel, 2022

The original document is saved on the University of Basel document server
<http://edoc.unibas.ch>



This work is licensed under a Creative Commons Attribution-NonCommercial-NoDerivatives 4.0
International License.

The complete text may be reviewed here:

<http://creativecommons.org/licenses/by-nc-nd/4.0/>

Genehmigt von der Philosophisch-Naturwissenschaftlichen Fakultät auf Antrag von

Prof. Dr. Richard J. Warburton

Prof. Dr. Ilaria Zardo

Prof. Dr. Ursula Wurstbauer

Basel, den 21. September 2021

Prof. Dr. Marcel Mayor
Dekan

Abstract

The emergence of two-dimensional (2D) materials, such as graphene and transition metal dichalcogenides (TMDs), and the ability to build artificial van der Waals heterostructures (vdWHs) by stacking different combinations of materials, has opened a new route for engineering quantum systems. 2D TMDs support bound electron-hole pairs, or excitons, that have particularly large binding energies, such that excitons dominate their optical properties, even at room temperature. The ability to electrically tune their properties via external electric gates is essential for various interesting opto-electronic applications.

A crucial feature of semiconductor nanostructures is the quantum confined Stark effect (QCSE), the change in optical energy on applying an electric field perpendicular to the layers. Using a gated vdWH, we demonstrated that in monolayer MoS₂ optical absorption is strong, but the transition energy is not tunable as the neutral exciton has essentially no permanent out-of-plane electric dipole and is only slightly polarizable. The electrical control of excitons via the QCSE requires larger polarizabilities or a non-zero dipole moment as observed in heterobilayers where the bound electrons and holes reside in different layers. However, the coupling to light in these systems is considerably reduced. To combine best of both worlds, a polarizable yet strong optical dipole, we integrated homobilayer MoS₂ in a dual-gate device structure. In its natural bilayer form, we discovered interlayer excitons which exhibit both a high oscillator strength and highly tunable energies in an applied electric field. Owing to their very large dipole moments, we were able to bring these interlayer excitons energetically close to resonance with the excitons confined to the single layers, and study exciton-exciton interactions in these systems.

Equipping MoS₂ with gates allows electrons to be injected, creating a 2D electron gas. By probing the electronic ground state at various electron densities, we presented experimental evidence for a spontaneous spin-polarization in monolayer MoS₂. Significantly, the extremely small Bohr radius of an electron in this material suggests that Coulomb effects play an important role at experimental relevant electron densities.

The ability to control the properties of thin semiconductors by electrical means makes these systems a versatile platform for rich exciton physics and unique opto-electronic applications.

Contents

| | |
|--|-----------|
| Abstract | i |
| Acronyms | ix |
| Acknowledgements | xi |
| 1 Introduction | 1 |
| 2 Excitons in two-dimensional transition metal dichalcogenides | 5 |
| 2.1 Crystal structure | 6 |
| 2.2 Basic bandstructure | 6 |
| 2.3 Excitonic particles | 9 |
| 2.3.1 Coulomb-bound electron-hole pairs | 9 |
| 2.3.2 Intralayer and interlayer excitons | 10 |
| 2.3.3 Neutral and charged excitons | 11 |
| 2.4 Optical selection rules and valley Zeeman effect | 12 |
| 3 Building high-quality opto-electronic devices with two-dimensional semiconductors | 15 |
| 3.1 From 3D to 2D: preparation and identification | 16 |
| 3.1.1 Exfoliation of 2D crystals | 16 |
| 3.1.2 Layer identification and characterization | 18 |
| 3.2 Assembling van der Waals heterostructures | 20 |
| 3.3 Strategies for optimizing the sample quality in opto-electronic devices . . | 25 |
| 3.3.1 Sample encapsulation | 25 |
| 3.3.2 Device structure | 27 |

| | | |
|----------|---|-----------|
| 4 | Experimental methods: optical spectroscopy of two-dimensional semiconductors | 31 |
| 4.1 | Concepts: light-matter interactions | 31 |
| 4.1.1 | Linear optical spectroscopy | 32 |
| 4.1.2 | Second harmonic generation | 37 |
| 4.2 | Microscope design for optical measurements | 40 |
| 4.2.1 | Photoluminescence and reflectivity measurements | 42 |
| 4.2.2 | Optical second harmonic generation measurements | 43 |
| 5 | Optical second harmonic generation in indium selenide | 47 |
| 5.1 | Summary | 47 |
| 5.2 | Introduction to SHG in 2D materials | 48 |
| 5.3 | SHG response of single- and few-layer InSe flakes | 49 |
| 5.4 | Polarization-resolved SHG of single-layer InSe | 50 |
| 5.5 | Second-order nonlinear sheet susceptibility | 52 |
| 5.5.1 | Relationship between generated second harmonics and nonlinear sheet susceptibility | 52 |
| 5.5.2 | Experimental estimate of the nonlinear sheet susceptibility | 55 |
| 5.6 | Conclusion and outlook | 55 |
| 5.6.1 | Nonlinear response of single- and few-layer InSe | 55 |
| 5.6.2 | Accessing the crystal structure and orientation in TMDs | 56 |
| 6 | Quantum confined Stark effect in a MoS₂ monolayer van der Waals heterostructure | 59 |
| 6.1 | Summary | 59 |
| 6.2 | Introduction | 60 |
| 6.2.1 | Concept of the quantum confined Stark effect in monolayer MoS ₂ | 60 |
| 6.2.2 | A high-quality MoS ₂ monolayer van der Waals heterostructure | 61 |
| 6.3 | Energy tuning of excitons in monolayer MoS ₂ | 62 |
| 6.3.1 | Charge control in a gated monolayer MoS ₂ heterostructure | 63 |
| 6.3.2 | Polarizability of neutral and charged excitons | 64 |
| 6.4 | Conclusion and outlook | 67 |
| 6.4.1 | Quantum confined Stark effect in monolayer MoS ₂ | 67 |
| 6.4.2 | Electrical control of interlayer excitons in MoSe ₂ /WSe ₂ heterobilayers | 67 |

| | | |
|----------|---|------------|
| 7 | Giant Stark splitting of an exciton in bilayer MoS₂ | 71 |
| 7.1 | Summary | 71 |
| 7.2 | Introduction | 72 |
| 7.3 | Experimental methods | 73 |
| 7.4 | Stark effect tuning of interlayer excitons in bilayer MoS ₂ | 73 |
| 7.5 | Zeeman splitting of interlayer excitons | 76 |
| 7.6 | Tuning interlayer and intralayer excitons into resonance | 79 |
| 7.6.1 | IE-A interaction | 79 |
| 7.6.2 | IE-B interaction | 80 |
| 7.6.3 | DFT GW+BSE modelling of excitons in MoS ₂ bilayers | 83 |
| 7.7 | Interlayer excitons in MoS ₂ trilayers | 86 |
| 7.8 | Conclusion and outlook | 88 |
| 8 | Spin-polarized electrons in monolayer MoS₂ | 89 |
| 8.1 | Summary | 89 |
| 8.2 | Introduction | 90 |
| 8.3 | Experimental methods | 90 |
| 8.4 | Optical absorption in gated monolayer MoS ₂ | 91 |
| 8.4.1 | Exciton-polaron theory | 91 |
| 8.4.2 | Stable spin-polarization in a magnetic field | 93 |
| 8.5 | Photoluminescence in gated monolayer MoS ₂ | 94 |
| 8.5.1 | Exciton valley depolarization in monolayer MoS ₂ | 97 |
| 8.5.2 | Trion states in monolayer MoS ₂ | 98 |
| 8.5.3 | Evidence of full spin-polarization in a magnetic field | 100 |
| 8.6 | Conclusion and outlook | 103 |
| 9 | Conclusion and outlook | 105 |
| | Appendices | 109 |
| A | Supplementary information to Chapter 3: “Building high-quality opto-electronic devices with two-dimensional semi-conductors” | 111 |
| A.1 | Building blocks for van der Waals heterostructures | 111 |
| A.1.1 | Two-dimensional crystals | 111 |
| A.1.2 | Exfoliation material | 112 |
| A.1.3 | Substrates | 112 |

| | | |
|----------|--|------------|
| A.2 | Assembly of van der Waals heterostructures | 113 |
| A.2.1 | Polymer stamp | 113 |
| A.2.2 | Heterostructure assembly techniques | 114 |
| A.2.3 | Spin-coating 2D materials for pick-up | 117 |
| A.3 | Nanofabrication processes | 118 |
| A.3.1 | Base structure fabrication: pre-patterning substrates | 118 |
| A.3.2 | Electron-beam lithography for contacts and etching | 120 |
| A.3.3 | Reactive ion etching | 120 |
| A.3.4 | Metallization of contacts | 121 |
| A.3.5 | Device connection | 121 |
| B | Details of samples and opto-electronic devices | 125 |
| B.1 | Encapsulated indium selenide sample | 125 |
| B.2 | Monolayer MoS ₂ vdWH device for measuring the QCSE | 126 |
| B.3 | Gated MoSe ₂ /WSe ₂ heterobilayer devices | 127 |
| B.4 | Homobilayer MoS ₂ devices | 127 |
| B.5 | Gated monolayer MoS ₂ devices | 129 |
| C | Supplementary information to Chapter 4: | |
| | “Experimental methods: optical spectroscopy of two-dimensional semiconductors” | 131 |
| C.1 | Components of the optical set-ups | 131 |
| D | Supplementary information to Chapter 5: | |
| | “Optical second harmonic generation in indium selenide” | 133 |
| D.1 | Electric field simulations | 133 |
| E | Supplementary information to Chapter 7: | |
| | “Giant Stark splitting of an exciton in bilayer MoS₂” | 135 |
| E.1 | Data acquisition details | 135 |
| E.2 | Beyond DFT calculations | 136 |
| E.2.1 | Computational details | 136 |
| E.2.2 | Bandstructure modifications due to the electric field | 137 |
| E.2.3 | Decomposition of the exciton oscillator strength with respect to single-particle transitions | 138 |

| | |
|--|------------|
| F Supplementary information to Chapter 8: | |
| “Spin-polarized electrons in monolayer MoS₂” | 141 |
| F.1 Optical absorption in gated monolayer MoS ₂ | 141 |
| F.1.1 Theory of the trion absorption in a 2DEG | 141 |
| F.2 Photoluminescence in gated monolayer MoS ₂ | 144 |
| F.2.1 Trion states in monolayer MoS ₂ | 144 |
| F.2.2 Valley polarization | 148 |
| F.2.3 Data reproducibility | 149 |
| References | 152 |
| Curriculum vitae | 179 |
| List of publications | 181 |

Citations to previously published work

Some parts of this thesis have appeared previously in published articles.

Nadine Leisgang, Jonas G. Roch, Guillaume Froehlicher, Matthew Hamer, Daniel Terry, Roman Gorbachev, and Richard J. Warburton,
“Optical second harmonic generation in encapsulated single-layer InSe”, AIP Advances **8**, 105120 (2018).

Jonas G. Roch, Nadine Leisgang, Guillaume Froehlicher, Kenji Watanabe, Takashi Taniguchi, Peter Makk, Christian Schönenberger, and Richard J. Warburton,
“Quantum confined Stark effect in a MoS₂ monolayer van der Waals heterostructure”, Nano Letters **18**, 1070–107 (2018).

Nadine Leisgang^{*}, Shivangi Shree^{*}, Ioannis Paradisanos^{*}, Lukas Sponfeldner^{*}, Cedric Robert, Delphine Lagarde, Andrea Balocchi, Kenji Watanabe, Takashi Taniguchi, Xavier Marie, Richard J. Warburton, Iann C. Gerber, and Bernhard Urbaszek,
“Giant Stark splitting of an exciton in bilayer MoS₂”, Nature Nanotechnology **15**, 901–907 (2020).

^{*}These authors contributed equally.

Jonas G. Roch, Guillaume Froehlicher, Nadine Leisgang, Peter Makk, Kenji Watanabe, Takashi Taniguchi, and R. J. Warburton,
“Spin-polarized electrons in monolayer MoS₂”, Nature Nanotechnology **14**, 432-436 (2019).

Acronyms

| | | | |
|------------------------|---|-------------------------|--|
| $\lambda/2$ | Half-wave plate | MoS₂ | Molybdenum disulfide |
| $\lambda/4$ | Quarter-wave plate | MoSe₂ | Molybdenum diselenide |
| 2D | Two-dimensional | ML | Monolayer |
| 3D | Three-dimensional | N₂ | Nitrogen |
| 2DEG | Two-dimensional electron gas | NA | Numerical aperture |
| AFM | Atomic force microscopy | O₂ | Diatomic oxygen |
| Ar | Argon | PC | Polycarbonate |
| Au | Gold | PBS | Polarizing beam-splitter |
| BEC | Bose-Einstein condensate | PDMS | Polydimethylsiloxane |
| BL | Bilayer | PL | Photoluminescence |
| BS | Beam-splitter | PMMA | Polymethyl methacrylat |
| BZ | Brillouin zone | QCSE | Quantum confined Stark effect |
| CB | Conduction band | rpm | Rounds per minute |
| CCD | Charge coupled device | RIE | Reactive ion etching |
| CHF₃ | Trifluoromethane | RT | Room temperature |
| Cr | Chromium | scm | Standard cubic centimeters per minute |
| CVD | Chemical vapor deposition | SEM | Scanning electron microscopy |
| DI | Deionized | SHG | Second harmonic generation |
| DFT | Density functional theory | Si | Silicon |
| E-beam | Electron-beam | SiO₂ | Silicon dioxide |
| EBL | Electron-beam lithography | SF₆ | Sulfur hexafluoride |
| FLG | Few-layer graphene | SM | Single-mode |
| FWHM | Full-width-at-half-maximum | SO(I) | Spin-orbit (interaction) |
| GW | One-particle Green's function G, dynamically screened Coulomb in- teraction W | Ti | Titanium |
| He | Helium | Ti:Sa | Titanium-sapphire |
| HeNe | Helium-neon | TL | Trilayer |
| hBN | Hexagonal boron nitride | TFSI | Bis(trifluoromethane)sulfonimide |
| InSe | Indium selenide | TMAH | Tetramethylammonium hydroxide |
| IPA | Isopropyl alcohol | TMD | Transition metal dichalcogenide |
| LC | Liquid crystal | VB | Valence band |
| LED | Light-emitting diode | vdWH | Van der Waals heterostructure |
| Lin. Pol. | Linear polarizer | WS₂ | Tungsten disulfide |
| LP | Long-pass | WSe₂ | Tungsten diselenide |
| M | Metal atom | X | Chalcogen atom |

To my parents.

Acknowledgements

“Non quia difficilia sunt non audemus, sed quia non audemus difficilia sunt.”

— Seneca, *“Epistulae morales ad Lucilium”* (XVII/XVIII, CIV, 26)

During my time in Basel, I had the privilege to meet many talented and motivating people who influenced and shaped my journey. Joining different research groups and being involved in many exciting projects in and outside of Basel broadened my expertise in various research areas and laid the foundation for many successful research activities, as well as great friendships.

First and foremost, I would like to thank my advisor, Richard, for his constant support and encouragement, and for giving me the opportunity to work on this interesting and challenging project. He gave me the freedom to explore different research directions during my PhD in order to find my own way in the large and exciting field of 2D materials. He helped me to become more independent and to approach new and challenging projects with self-confidence. I would also like to thank my committee members, Ursula Wurstbauer and Ilaria Zardo, for their interest in my work. In particular, I would like to express my gratitude to Ilaria for always having an open door and valuable advice, as well as to Christian Schönenberger and Martino Poggio for their constant support.

I shared my time in the lab with many brilliant experimentalists and benefitted a lot from their experience and knowledge: Nadia Antoniadis, Marta De Luca, Sigurd Flågan, Guillaume Froehlicher, Lukas Gubser, Clevin Handschin, David Indolese, Jan-Philipp Jahn, Tomek Jakubczyk, Alisa Javadi, Matthias Löbl, Hinrich Mattiat, Mathieu Munsch, Daniel Najer, Paritosh Karnatak, Ioannis Paradisanos Ben Petrak, Jonas Roch, Lukas Schneider, Shivangi Shree, Immo Söllner, Lukas Sponfeldner and Simon Zihlmann.

Even though I never had the privilege to work with Mathieu in the lab, it was him who introduced me to 2D materials and their great potential for opto-electronics. He pushed me from the beginning with his critical and challenging questions and greatly influenced my approach towards science.

Jonas taught me everything in the lab I needed to know about confocal microscopy, photoluminescence and absorption spectroscopy. Besides that, we spent hours in front of the optical microscope finding monolayer flakes and eventually building our first heterostructures. I still remember this special moment when the last step of our fabrication process turned out to be successful and we completed our first device together – with a little celebration in the cleanroom. Thank you Jonas for all these fond memories.

Our great success in the cleanroom – and in the lab – would have never been possible without the help from the Schönenberger group, especially Clevin, Simon, David and Paritosh who shared their fabrication experience with us. Particularly, when the devices became more and more complicated (twist-angle control, multiple gate electrodes, ...), their knowledge and advice was incredibly valuable. Thank you for your support, motivation and encouragement during all the hours, weeks and months in the cleanroom and, more importantly, for making it such a fun place to be. Eventually, Guillaume joined our team as a postdoc and provided a lot of new ideas and impetus. Guillaume has been the nicest and most encouraging colleague I could have ever wished to work with. He has always been willing to explain and re-explain any of the details in our experiments and theories with incredible patience and care. I am particularly grateful for his motivation and encouragement to design and build an optical SHG set-up. Jonas, Guillaume and me spent hours and evenings together in the lab until finally getting our first SH counts on the spectrometer. When Guillaume subsequently misaligned the whole set-up on purpose, I didn't understand at first – until I realigned the set-up all by myself and even improved it. Thank you Guillaume – I am absolutely grateful for having had such an amazing teacher. Shortly after Guillaume left our group, Lukas (Sponfeldner) joined our small team and brought new skills and approaches.

With time, our devices became more and more complicated, as did the physics behind them. I am very lucky to have met Dima. His broad understanding of physics, interest in complex theories and excitement for our experiments have been very inspiring. His curiosity and ideas opened entirely different perspectives – thank you for sharing all your knowledge with me in such an understandable and joyful way.

The third year of my PhD has been the most intense, exciting and rewarding one. It is the result of an exceptional collaboration with Bernhard Urbaszek and his research team in Toulouse including Shivangi Shree, Ioannis Paradisanos and Iann Gerber. During this

time, Bernhard became a mentor for me, scientifically and personally. His constant support, energy and enthusiasm, as well as his clear way to communicate complex ideas, sparked a new excitement and motivation for my research. In Shivangi, I found a supportive colleague in the lab and a wonderful friend. I always enjoy our hour-long Skype calls about science and life.

For the last year or so, I had the opportunity to join the Poggio lab for a very ambitious project, combining optical and magnetic experiments on gated monolayer MoS₂. Even though, Hinrich, Lukas (Schneider) and I encountered one hurdle after the other, everyone worked with joy and a smile. I am very fortunate to have experienced such a great team spirit. Their patience and consistent work ethic had a huge contribution to our progress together. Especially, Hinrich's cheerful and open attitude have made this time incredible enjoyable, during which I have found a true friend.

During my time as a PhD student, I was supported by the fantastic staff and mechanical and electrical workshop of the Physics Department, especially, Germaine Weaver-Malzach, Barbara Kammermann, Astrid Kalt, Jennifer Kern, Bernd Heimann, Beat Glatz, Sascha Martin, Patrick Stöcklin, Dominik Sifrig, Sascha Linder and Michael Steinacher.

I am particularly thankful for everyone who crossed my path outside the lab. In my office, Natasha Tomm and Viktoria Yurgens have been constant friends, who always seem to understand me and know how to cheer me. To the Nano-Photonics group as a whole and the many people elsewhere in the Physics Department, who have always been good friends to talk to: Mara Batzer, Floris Braakman, Lorenzo Ceccarelli, Andrea Corazza, Martin Endres, Marcel Erbe, Simon Geyer, Yannik Fontana, Jodok Happacher, Natascha Hedrich, Mark Hogg, Christian Jünger, Timo Kaldewey, Andreas Kuhlmann, Nam Nguyen, Simon Philipp, Daniel Riedel, Giulio Romagnoli, Clemens Spinnler, Lujun Wang and Liang Zhai. I have very fond memories of all the summer BBQs, hiking and skiing trips, Christmas dinners, and coffee breaks on the roof.

And to all the people outside of physics, who have touched my life in the last few years, especially Tanja Amport, Cornelia Blättchen, Miguel Carballido, Fabio Cimei, Daniel Haas, Fränzi Maurer, Vincent Maurer, Angelina Nachtrab, Melissa and Frederic Osterwalder, Dieter Raps, Joseph Saner, Luana Saner, Olivier Stehlin, Alexandra Toscanelli, Fabienne Stalder, Patrick Winkler, and the entire FC Breitenbach soccer team. Many thanks for making me see things from a fresh and different angle.

Finally, I would like thank Brendan, who has been there all along to celebrate the successes and to cheer me up during the frustrations, who taught me patience and per-

Acknowledgements

severance and never stopped believing in me – and, who will always have a special place in my heart. And last but not least, my parents, Pia and Georg and my two brothers, Marc and Yannick, without whom I would not be who I am, and who gave me the confidence to meet this challenge.

Thank you.

1

Introduction

“What could we do with layered structures with just the right layers? What would the properties of materials be if we could really arrange the atoms the way we want them?”

— Richard P. Feynman,

“There’s Plenty of Room at the Bottom” (1959)

The pursuit of scalable quantum technologies has led to an ever increasing demand for better control of quantum properties of materials. For example, control over individual particles, such as electrons and holes, and their degrees of freedom is a long-standing goal in the field. Quasi-two-dimensional (2D) materials in layered artificial structures, or heterostructures, such as semiconductor quantum wells, have been widely used for quantum opto-electronic applications, as their properties can be conveniently engineered. In these systems, particles can be constrained to one quantum state perpendicular to the structure, while moving freely along the other directions.

Building on these concepts, the regime of atomically thin, truly 2D sheets of material promises a novel alternative for quantum technologies. The possibility to isolate a single layer of graphite, called graphene, and hundreds of other graphene-like 2D atomic layers, generates a completely new material platform – with properties ranging from metal to superconductor, and insulator to semiconductor. Among these materials, the class of semiconducting transition metal dichalcogenides (TMDs), such as MoS₂, has emerged as a promising quantum system that operates in the optical domain, offering new functionality relative to the established III–V semiconductors. A key feature is that, unlike GaAs, there are no dangling bonds. As a result, single TMD layers are well-isolated

and perform well optically and electronically. Being stable on their own, these materials can be combined with many other building blocks, such as insulating hexagonal boron nitride (hBN) and graphene, while retaining their 2D nature. This flexibility in device design provides a perfect platform to manipulate the properties of materials on an atomic scale, as already proposed in 1959 by Richard P. Feynman in his famous lecture “*There’s Plenty of Room at the Bottom*”. More than seventy years later, we come one step closer to answering his question using the new class of 2D materials, a material system that is robust enough to be controlled on the atomic scale.

In this thesis, the material properties of different atomically thin layers stacked in so-called van der Waals heterostructures (vdWHs) are combined to create new ultrathin opto-electronic devices. We focus on the class of semiconducting TMDs, as monolayers strongly interact with light. Generally, when light is absorbed in a semiconductor, an electron is promoted to an excited state, leaving behind a hole. In 2D TMDs, the low-dimensionality leads to a strong Coulomb interaction between the particles, binding them to form excitons which are stable even at room temperature. The ability to tune the excitonic properties electrically is essential for opto-electronic applications based on light emission, detection, modulation and manipulation, and paves the way towards engineered quantum structures.

This thesis outlines efforts over the past four years to control electrically excitons in 2D semiconducting TMDs.

Chapter 2 provides a brief introduction into the concept of excitons, Coulomb-bound electron-hole pairs, in these confined systems. The crystal symmetry and basic band-structure of monolayer TMDs are discussed, as well as the resulting spin-valley properties and optical selection rules.

In **Chapter 3**, a dry-transfer technique for assembling 2D materials is introduced, which allows complicated opto-electronic devices to be fabricated with extremely high quality. Upon encapsulation, hBN/MoS₂/hBN devices with ultras-small linewidths (~ 1.8 meV) are realized, resulting in well-resolved neutral and charged exciton transitions in monolayer MoS₂. Combining the narrow linewidth with field-effect devices allows full control of the excitons through charge and field modulation via external gates.

Optical spectroscopy is a powerful, local and non-invasive probe. Within this the-

sis, photoluminescence (PL), absorption and optical second harmonic generation (SHG) are used to access key information of the semiconducting vdWH devices, such as light-matter interactions, spin-valley properties and crystal orientation. **Chapter 4** provides an overview of the the different experimental techniques and the corresponding set-ups.

Creating vdW stacks of individual layers opens up the possibility of realizing materials with new properties that are not held by any of the constituents alone. This requires control over the angle of each single layer as the stack is built. In other words, the crystal structure of each layer needs to be precisely aligned with respect to the crystal structure of the others. **Chapter 5** reports the observation of optical second harmonic generation (SHG) in single layer indium selenide (InSe). We show that the SHG is sensitive to the axis of the crystal, even when the material is encapsulated, and that it serves as a powerful tool for creating high-quality vdWHs where precise control of the twist angle between single layers is required.

Excitons, Coulomb-bound electron-hole pairs, dominate the optical response in monolayer MoS₂. A crucial property of semiconductor nanostructures is the quantum confined Stark effect (QCSE) – the change in exciton energy as a function of electric field. On the one hand, it characterizes the sensitivity of the exciton energy to charge noise. On the other hand, the QCSE allows excitons to be localized and then routed around a semiconductor device. In **Chapter 6** we show that the intensity and the energy of the emission associated with excitons can be varied with an external gate. By changing the electric field without changing the electron density in the device, a clear signature of the QCSE is presented in a MoS₂ vdWH. We quantitatively determine the polarizability of both the neutral and the charged exciton, demonstrating that the excitons in a single MoS₂ layer are only slightly polarizable. As an alternative, we present interlayer excitons in a type-II MoSe₂/WSe₂ vdWH, where the bound electrons and holes reside in different layers. These excitons exhibit a permanent dipole moment, and can therefore be electrically controlled via the QCSE.

In **Chapter 7** the large oscillator strength of excitons in TMD monolayers is combined with the high tunability of interlayer excitons in external electric fields. For this, homobilayer MoS₂ is integrated in a dual-gate device structure to apply a static out-of-plane electric field, while keeping the carrier concentration constant. We identify two hybridized interlayer transitions with large opposite electric dipoles, and show that MoS₂, in its natural bilayer form, is a rich system for probing exciton-exciton interactions: the

interlayer excitons interact with both A and B excitons, which are confined to the single layers.

In **Chapter 8**, the strong light-matter interactions in monolayer MoS₂ are electrically tuned by changing the electron density in the vdWH. Monolayer MoS₂ is a natural host for a two-dimensional electron gas (2DEG). We use optical spectroscopy as a local spin- and valley-sensitive tool to probe the electronic ground state of the 2DEG at various electron densities. Identifying the formation of different trion states, experimental evidence is presented for a spontaneous spin-polarization in gated monolayer MoS₂.

We conclude our work in **Chapter 9** and present perspectives and future directions.

2

Excitons in two-dimensional transition metal dichalcogenides

The isolation of a single sheet of graphite, called graphene [5, 6], and of other graphene-like 2D materials [3, 7], through mechanical exfoliation has generated intense research interest in so-called van der Waals heterostructures (vdWHs). These materials can be metallic, semiconducting, or insulating, and can possess a whole variety of optical and electronic properties. Of particular interest are atomically thin transition metal dichalcogenides (TMDs), such as MoS_2 , which are semiconductors with a direct bandgap optical transition in the monolayer limit [3, 7]. In contrast to conventional III–V semiconductor systems, such as GaAs, the bandgap is located at the two inequivalent band edges of the first Brillouin zone (BZ), the $+K$ and $-K$ valleys. Absorption of a photon promotes an electron from the valence band (VB) to the conduction band (CB). In 2D TMDs, the optical transitions at $+K$ and $-K$ can be individually addressed using σ^+ and σ^- circularly polarized light [2, 8–11]. The resulting electron and hole can form a bound

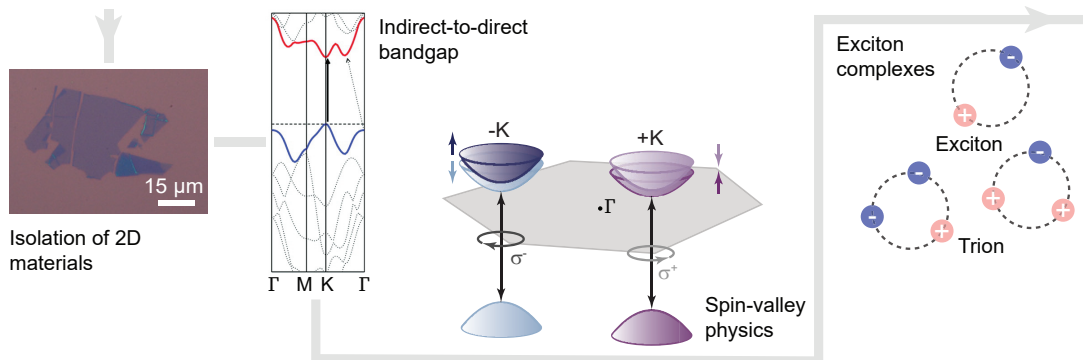


Figure 2.1. **Introduction to two-dimensional (2D) semiconducting transition metal dichalcogenides (TMDs).** From the isolation of a 2D TMD layer to the formation of strongly bound exciton complexes [1] with unique spin and valley properties [2]. Figures are adapted from Refs. [3, 4].

state, called exciton. In 2D TMDs, the electron-hole pairs have particularly large binding energies, hundreds of meV [12, 13], such that two-particle neutral excitons, as well as three-particle charged excitons (trions), are stable even at room temperature [1, 12, 13].

Fig. 2.1 illustrates the described evolution from the exfoliation of a single TMD layer to the observation of strongly bound excitons with interesting spin-valley physics. In the following, 2D TMDs and their general properties will be introduced, including their crystal structure and bandstructure, strong excitonic effects and unique optical spin and valley selection rules.

2.1 Crystal structure

The focus is on semiconducting TMDs with generalized formula MX_2 , where M (= Mo, W) represents the metal atom and X (= S, Se) the chalcogen atom (Fig. 2.2). Each single layer consists of one plane of metal atoms between two planes of chalcogen atoms in a trigonal prismatic arrangement. Fig. 2.2a and Fig. 2.2c depict the trigonal prismatic unit cell of this X-M-X structure, with one metal atom in the center being connected to six chalcogen atoms via strong covalent bonds. It becomes apparent that single layers exhibit an out-of-plane mirror symmetry, but lack an in-plane inversion center. The top view of the single TMD layer (Fig. 2.2a) reveals its hexagonal symmetry, similar to graphene but with alternating M and X atoms at the corners. This results in a hexagonal BZ, with high symmetry points Γ in its center ($\mathbf{k} = 0$) and $+K$ and $-K$ points at the corners ($\mathbf{k} \neq 0$) (Fig. 2.2b). \mathbf{k} corresponds to the wavevector in momentum space. These points, $+K$ and $-K$, are inequivalent, as they cannot be related to each other by the two elementary reciprocal lattice vectors \mathbf{b}_1 and \mathbf{b}_2 [14]. In the bulk crystal, the individual layers are attached to one another through weak van der Waals interactions with a distance of $d = 0.65$ nm between the layers. Figs. 2.2c,d depict the configuration for the bilayer system in the natural 2H-phase*. Here, neighboring layers are rotated by 180° with respect to each other, that is, the metal atoms (M) of layer 1 sit right on top of the chalcogen atoms (X) of layer 2, and vice versa.

2.2 Basic bandstructure

In their bulk form, TMDs are indirect bandgap semiconductors with the transition between the VB maximum at the Γ point and the CB minimum at the midpoint along

*As thin TMD flakes exfoliated from natural bulk crystals mostly occur in the centrosymmetric 2H-phase, we will refer to 2H-stacking when discussing TMD bilayers and multilayers (unless otherwise stated).

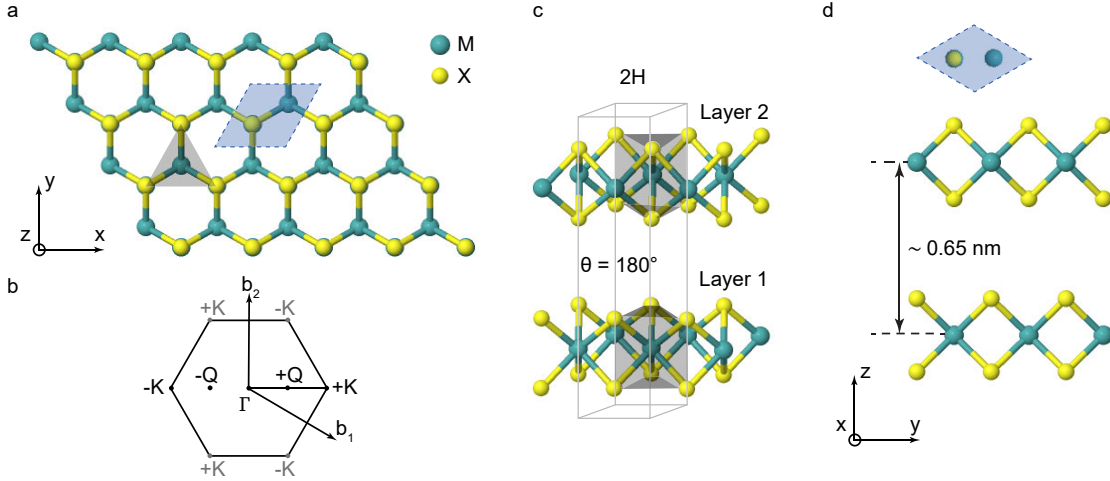


Figure 2.2. **Crystal structure of transition metal dichalcogenides (TMDs).** **a**, Top view of a single TMD layer. Chalcogen atoms (X) are shown in yellow, while metal atoms (M) are shown in green. The shaded (blue) rhomboid represents the two-dimensional (2D) unit cell. **b**, First Brillouin zone (BZ) of a single-layer TMD. \mathbf{b}_1 and \mathbf{b}_2 are the reciprocal lattice vectors. The center of the first BZ Γ , and the $+K$ and $-K$ points located at the edges are labelled. **c**, Bilayer structure with natural 2H-stacking. The two layers are rotated by 180° with respect to each other so that the $+K$ points in layer 1 are aligned with the $-K$ points of layer 2. **d**, Side view of the 2H-stacked bilayer crystal structure. The individual layers are separated by an interlayer distance $d = 0.65$ nm.

Γ - K (Q point) (Fig. 2.2b) [22, 23]. When reduced to a single layer, the bandgap becomes direct with the corresponding band extrema located at the inequivalent $+K$ and $-K$ points [3, 7]. Due to the broken inversion symmetry, interband transitions at these two points have valley-contrasting optical selection rules (see Fig. 2.3a and Section 2.4) [24]. The resulting valley degree of freedom τ is in stark contrast to GaAs, where the bandgap lies in the middle of the BZ. Strong spin-orbit interaction (SOI) originating from the d -orbitals of the metal atoms*, further lifts the spin-degeneracy in both the CB and VB in the two valleys [16]. This spin-splitting is large in the VB, while it is small in the CB [13, 15–17, 19, 21]. Large SO splitting in the VB gives rise to the well-separated A and B spin-allowed interband transitions between the spin-split CBs and VBs (Fig. 2.3b). Additionally, time reversal symmetry dictates the splitting to have opposite sign at the $+K$ and $-K$ valleys. Together with the valley degree of freedom, this gives rise to an effective coupling between spin and valley which is often referred to as spin-valley locking [25].

Fig. 2.3b depicts the single-particle bandstructure of monolayer MoS_2 at the $+K$ and

*CB and VB states at the $\pm K$ points are composed of transition metal atom $d_{x^2-y^2} \pm id_{xy}$ states (VB) and d_{z^2} states (CB) slightly mixed with chalcogen $p_x \mp ip_y$ states [14, 15].

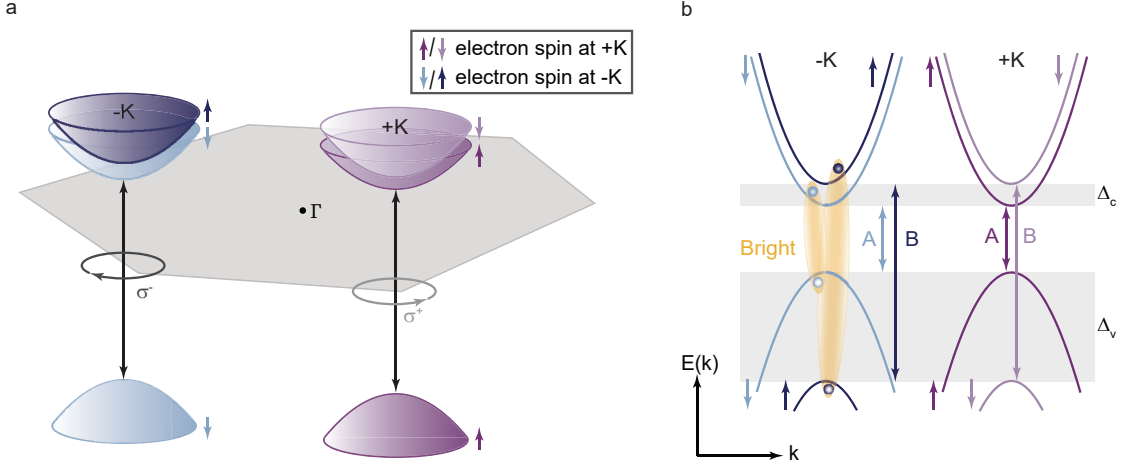


Figure 2.3. **Bandstructure and valley-dependent optical selection rules in monolayer MoS₂.** **a**, Valley-dependent optical selection rules for interband transitions. σ^+ (black) circularly polarized light couples to the $+K$ valley and σ^- (grey) circularly polarized light couples to the $-K$ valley. **b**, Schematic bandstructure at the edges of the Brillouin zone (BZ). The colors (light/dark purple, light/dark blue) correspond to the electron spin states (spin \downarrow / spin \uparrow) at the $+K$ and $-K$ point. For monolayer MoS₂, the spin-orbit splitting is large in the valence band, $\Delta_v \approx 150$ meV [13, 15–18], while it is very small in the conduction band, $\Delta_c \approx -3$ meV [2, 19–21]. This gives rise to spin-allowed, bright A and B excitons with opposite spins in the two valleys, as indicated by the colored vertical arrows.

$-K$ point*. It can be accurately described by an effective Hamiltonian [21]

$$H_{\text{eff}} = H_0 + H_{\text{SO}} = \frac{\hbar^2 q^2}{2m_{c,v}^{\text{eff}}} + \Delta_{c,v} s_z \tau, \quad (2.1)$$

where q is the wave vector measured from the $+K$ or $-K$ point, respectively. The effective electron or hole mass $m_{c,v}^{\text{eff}}$ for a given spin s_z (z -projection) and valley $\tau = \pm 1$ ($\pm K$) quantum number describes the curvature of the electronic bands. The term H_{SO} accounts for the effect of the strong spin-orbit (SO) interaction, which couples s_z of the

*The sign of the CB splitting is reversed for W-based TMDs.

| Bandgap (E_g) | CB splitting (Δ_c) | VB splitting (Δ_v) | Effective electron mass (m_c^{eff}) | Effective hole mass (m_v^{eff}) |
|----------------------|--------------------------------|--------------------------------|---|---|
| 1.59 – 2.97 eV | –3 meV | 148 meV | $0.44 m_0$ | $0.54 m_0$ |

Table 2.1. **Bandstructure parameters for MoS₂ at the K point.** All values are taken from Ref. [15].

electron or hole to τ , thus lifting the spin-degeneracy of both valleys. $\Delta_{c,v}$ labels the SO splitting in the CB and VB, respectively. Table 2.1 summarizes the values of the important parameters for MoS₂.

2.3 Excitonic particles

2.3.1 Coulomb-bound electron-hole pairs

In a semiconductor, the absorption of a photon by an interband transition with an energy above the bandgap lifts the electron from the VB into the CB, leaving behind a hole in the VB. These electrons and holes attract each other through Coulomb interaction to form bound electron-hole pairs, called excitons [1, 12, 13, 25]. In 2D TMDs, the interaction between the electrons and holes is particularly strong due to several effects [25]. First, the low dimensionality leads to a small separation of the electrons and holes, which are strongly confined to the monolayer plane. Second, electrons and holes in the two valleys $+K$ and $-K$ have relatively large effective masses $m_{c,v}^{\text{eff}} \approx 0.44 m_0$ [21], where m_0 corresponds to the free electron mass. Third, the 2D layers are generally embedded within a dielectric material with a comparably small permittivity ϵ_{eff} , and therefore the screening of the Coulomb interactions is weak [26, 27]. This leads to large exciton binding energies, hundreds of meV [12, 13], and bandgap renormalization effects.

In general, the exciton properties can appropriately be described in the Wannier-Mott picture, with the ground ($n = 1$) and excited ($n > 1$) states* in analogy to the physics of the hydrogen atom assuming an unscreened Coulomb potential $1/r$ [28]. Fig. 2.4 illustrates the optical absorption in an ideal undoped 2D semiconductor. Excitons appear as strong resonances at an energy $E_X^{(n)}$ below the renormalized quasi-particle bandgap $E_{\text{gap}} (n = \infty)$

$$E_X^{(n)} = E_{\text{gap}} - E_b^{(n)}. \quad (2.2)$$

$E_b^{(n)}$ is the binding energy of the n^{th} excitonic state in 2D [12]

$$E_b^{(n)} = \text{Ry} \frac{\mu_{\text{eff}}}{m_0 \epsilon_{\text{eff}}^2} \cdot \frac{1}{(n - \frac{1}{2})^2} \quad (2.3)$$

where $\text{Ry} = 13.6 \text{ eV}$ is the Rydberg energy and $\mu_{\text{eff}} = \frac{m_c^{\text{eff}} m_v^{\text{eff}}}{m_c^{\text{eff}} + m_v^{\text{eff}}}$ is the effective reduced mass of the bound electron-hole system. The optical bandgap of the material E_{opt} is defined with respect to the ground state and is therefore different from the quasi-

*Ground and excited states of the excitons are often labelled in analogy to the Rydberg series as 1s, 2s, 3s, etc.

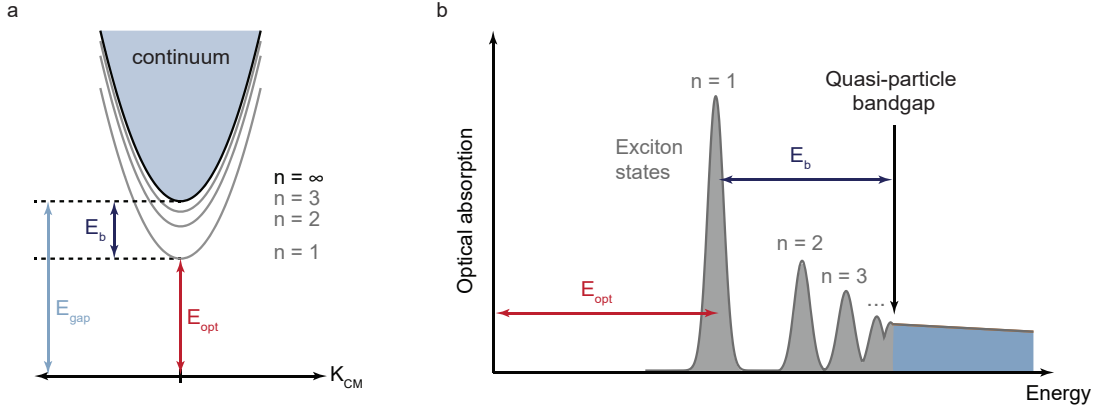


Figure 2.4. **Excitonic states in a two-dimensional semiconductor.** **a**, Excitonic dispersion as a function of the center-of-mass wavenumber \mathbf{K}_{CM} . The grey parabola depict the energy level scheme of the bound states with principal quantum number n analogous to the hydrogen atom. The exciton ground state ($n = 1$) and the excited states ($n > 1$) are indicated. **b**, Schematic illustration of the optical absorption including the series of excitonic states and their relative energies below the quasi-particle bandgap. Electronic bandgap E_{gap} (light blue), optical bandgap E_{opt} (red) and excitonic binding energy E_b (dark blue) are labelled. The image is adapted from Ref. [25]

particle bandgap E_{gap} . Using $\mu_{\text{eff}} \approx 0.22 m_0$ [21] and an effective dielectric constant $\epsilon_{\text{eff}} \approx 5$ [25], typical binding energies on the order of 0.5 eV can be estimated (compared to ~ 10 meV in conventional GaAs with $\mu_{\text{eff}} \approx 0.06 m_0$ [29]). Due to this large binding between electrons and holes, the optical properties in 2D TMDs are dominated by strong excitonic effects up to room temperature [1, 12, 13]. The large effective mass [21] together with the reduced dielectric screening further leads to an extremely small exciton radius, or Bohr radius, of $a_B = \frac{4\pi\epsilon_0\epsilon_{\text{eff}}\hbar^2}{\mu_{\text{eff}}e^2} \approx 0.5$ nm [12], suggesting that Coulomb effects play an important role in these systems. This will be discussed in more detail in Chapter 8.

2.3.2 Intralayer and interlayer excitons

Excitons in monolayer TMDs experience an extreme out-of-plane confinement of both electrons and holes. The bound electron-hole pairs are therefore called intralayer excitons as they are strongly localized within the layer. When two or more layers are stacked on top of each other, such as in bilayers (BLs), trilayers (TLs) etc., interlayer excitons can form, where electrons and holes reside in different layers (Fig. 2.5a) [31, 32]. Due to the spatial separation of electrons and holes, these excitons are often also referred to as indirect in real space. Figs. 2.5b,c illustrate the two possible situations for heterobilayers. On the one hand, the two neighboring layers can have a band offset leading to a type-II (staggered) band alignment, where the bottom of the CB and the top of the VB at the K point

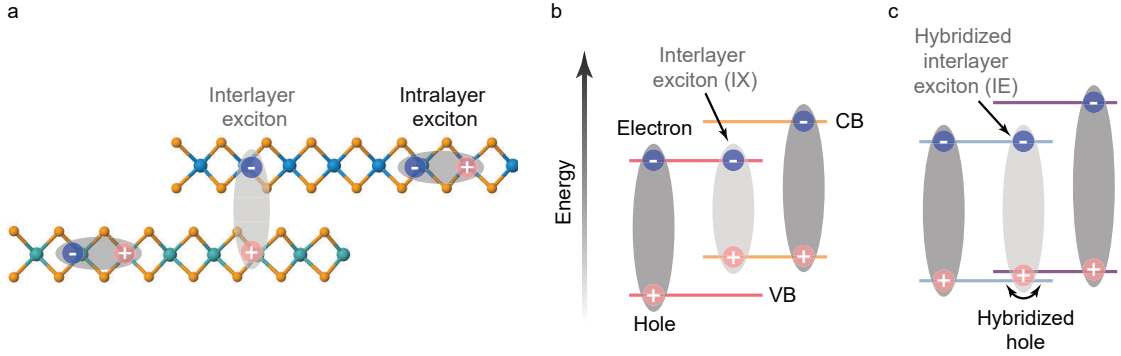


Figure 2.5. **Intralayer and interlayer excitons in heterobilayers.** **a**, Schematic of van der Waals heterobilayers. Intralayer excitons are Coulomb-bound electron-hole pairs within a single layer, while interlayer excitons form between electrons and holes residing in different layers. **b**, Electronic band diagrams of a type-II heterobilayer, where the CB minimum and the VB maximum are in separate layers. Interlayer excitons (IXs) form with the electrons and holes localized in the separate layers. **c**, Band alignment between two different layers, here with the VB delocalized over both layers (small VB offset between the layers). The hybridized hole state is indicated by a double-sided arrow. In this case, intralayer excitons are mixed with interlayer excitons (IE). Figure adapted from Ref. [30].

are located in different layers (Fig. 2.5b), such as in $\text{MoSe}_2/\text{WSe}_2$ heterobilayers [33–41]. Here, the interlayer exciton becomes the lowest-energy excitonic transition and is therefore bright in photoluminescence (PL) (see also Chapter 6). On the other hand, intralayer excitons can be mixed with interlayer excitons (Fig. 2.5c) [31, 42], due to hybridization of the electron states, such as in $\text{MoSe}_2/\text{WS}_2$ [43, 44] and WSe_2/WS_2 [45], or hybridization of the hole states, as observed for MoS_2/WS_2 [46] and $\text{MoSe}_2/\text{hBN}/\text{MoSe}_2$ heterostructures [47, 48]. This hybridization results in optical interlayer transitions with high oscillator strength. This is especially the case in homobilayer (2H-stacked bilayer) systems [49–51], as will be discussed in Chapter 7 in more detail. We will refer to interlayer excitons in heterobilayers as IXs and to interlayer excitons in hybridized systems as IEs.

2.3.3 Neutral and charged excitons

As described above, 2D TMDs support bound electron-hole pairs, or neutral excitons X^0 . In the presence of free carriers, the optically created electron-hole pairs (two-particle excitons) can interact with the excess electrons and bind into three-particle states X^- (trions) [1, 52]. For single-valley materials, the bound trion state consists of two electrons in a spin-singlet state and a hole. However, electrons in 2D TMDs have an additional valley degree of freedom τ , and different intravalley and intervalley

trion species can exist (see Chapter 8) [53]. In the exciton-polaron picture [54–56], the optically generated excitons are dressed by the interaction with electrons in the Fermi sea. When the interaction is attractive, the exciton resonance splits into a higher-energy exciton-polaron X^0 (corresponding to the neutral exciton) and a lower-energy exciton polaron X^- (corresponding to the trion in the single-particle limit). When the interaction is repulsive, only the X^0 appears in the optical response. The many-body physics associated with the formation of trions in monolayer MoS₂ will be discussed in Chapter 8, where we optically probe the 2DEG ground state by absorption and PL spectroscopy.

2.4 Optical selection rules and valley Zeeman effect

As described above, the broken inversion symmetry in monolayer TMDs and the large SOI lift the spin degeneracy into opposite directions for the two valleys. This leads to the valley-dependent optical selection rules: interband A and B transitions at the $+K$ and $-K$ point couple to right- (σ^+) and left-handed (σ^-) circularly polarized light,

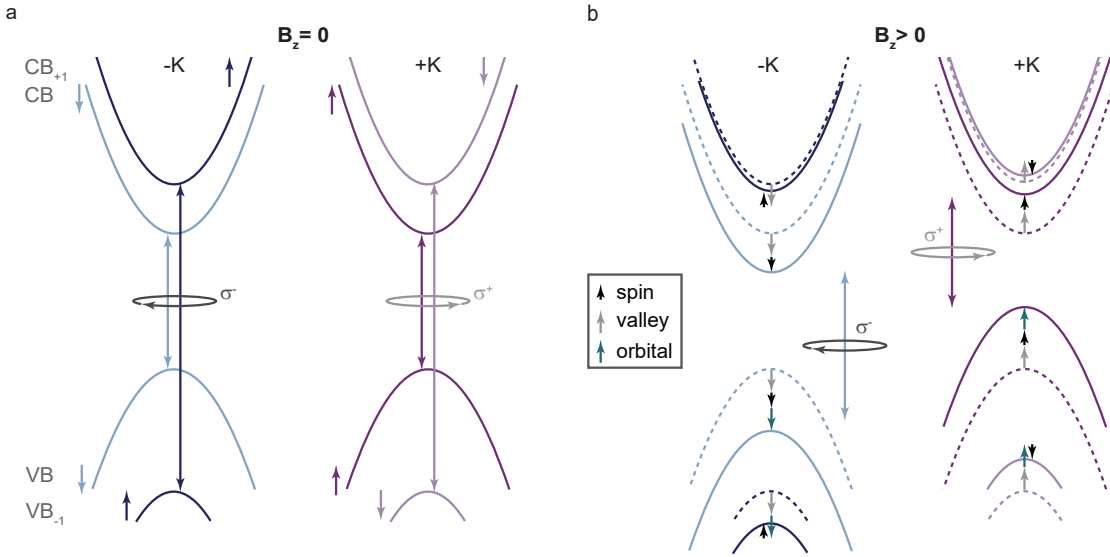


Figure 2.6. **Optical selection rules and valley Zeeman shift.** **a**, Band diagram of monolayer MoS₂ at the $+K$ and $-K$ valley and specific valley-dependent optical selection rules at $B_z = 0$. Dark blue/purple and light blue/purple arrows represent spin-up/spin-down in the $-K/+K$ valley. **b**, Relative shifts of the CBs and VBs in an applied magnetic field $B_z > 0$. Dashed lines correspond to the band positions at $B_z = 0$ as depicted in **a**. The spin, valley orbital and atomic orbital contributions are illustrated by separate black, grey and green arrows. The σ^+ (σ^-) polarized transition energy decreases (increases) in an applied magnetic field ($B_z > 0$), lifting the degeneracy of the two valleys.

respectively (Figs. 2.3a and 2.6a) [2, 8–10]. These spin- and valley-contrasting selection rules together with the direct-bandgap transition at $+K$ and $-K$ therefore allow for the optical generation and detection of valley polarization in monolayer TMDs.

At zero magnetic field ($B_z = 0$), the spin-allowed transitions in the two valleys are degenerate. Applying an out-of-plane magnetic field breaks the time-reversal symmetry and therefore lifts the degeneracy according to the valley Zeeman effect [57–59]. Fig. 2.6b depicts the Zeeman shift. The dashed lines indicate the bands at zero field ($B_z = 0$) as indicated in Fig. 2.6a. The total Zeeman shift contains contributions from spin Δ_s (black arrow), valley orbital Δ_v (grey arrow) and atomic orbital Δ_α (green arrow) magnetic moment [57]

$$\Delta_s = 2\mu_B B_z s_z \quad s_z = \pm \frac{1}{2} \quad (2.4)$$

$$\Delta_v = \alpha_{c,v} \tau \mu_B B_z \quad \tau = \pm 1 \quad (2.5)$$

$$\Delta_\alpha = m_z \mu_B B_z \quad m_z = \{0, \pm 2\}. \quad (2.6)$$

Here, s_z and τ are the spin and valley quantum numbers, and $\alpha_{c,v} \approx 0.375$ [21] is the valley g -factor for the CB and VB, respectively. While spin and valley orbital magnetic moments do not affect the optical transition energies, the atomic orbital moment has a significant contribution to the Zeeman shift. As mentioned earlier, the CBs are mainly composed of d_{z^2} orbitals ($m_z = 0$), whereas the VBs are mainly composed of $d_{x^2-y^2}$ states ($m_z = \pm 2$ for $\pm K$). This results in a net shift by $\mp 2\mu_B B_z$ for interband transitions in the $\pm K$ valley and a Zeeman splitting between the two valleys

$$\Delta E = E(\sigma^+) - E(\sigma^-) = \mp 4\mu_B B_z, \quad (2.7)$$

where $E(\sigma^+)$ and $E(\sigma^-)$ are the excitonic transition energies for intralayer excitons in the $+K$ and $-K$ valley, respectively.

3

Building high-quality opto-electronic devices with two-dimensional semiconductors

The ability to obtain two-dimensional (2D) crystals from layered materials such as graphite, hexagonal boron nitride (hBN) and transition metal dichalcogenides (TMDs), provides a new route for creating so-called van der Waals heterostructures (vdWHs) [60, 61]. Despite their atomic thickness, these 2D crystals have no dangling bonds [6], and layers with different lattice constants can be assembled even with a lattice mismatch. Stacking different combinations of 2D materials, artificial vdWHs can be realized with tailor-made properties.

In the following sections, we introduce the most important fabrication steps and techniques used for building our vdWH devices. First, the isolation of thin 2D materials is described, followed by a short introduction to methods for locating and characterizing them. Then, their assembly into vdWHs is presented. To complete a device, standard nanofabrication procedures are used, such as electron-beam lithography (EBL), reactive ion etching (RIE) and metallization with thermal deposition. Detailed fabrication recipes can be found in the Appendix A. Finally, we outline strategies for optimizing the sample quality in opto-electronic devices.

3.1 From 3D to 2D: preparation and identification

3.1.1 Exfoliation of 2D crystals

Due to their layered structure and weak interlayer van der Waals (vdW) forces, single- and few-layer flakes of, for example, graphite, hBN, and TMDs can be mechanically exfoliated from their bulk crystals by the so-called “Scotch tape” method [61]. Here, a piece of adhesive tape (“Scotch tape”) is used to break the weak interlayer bonding of the vdW crystals and to separate individual layers of material (see Fig. 3.1).

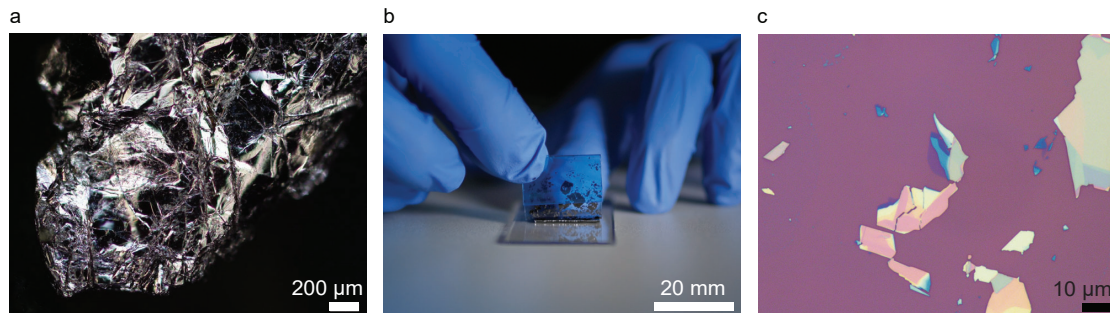


Figure 3.1. **From 3D to 2D: the “Scotch tape” method.** Images of **a**, a bulk MoS₂ crystal, **b**, MoS₂ flakes distributed over a piece of adhesive tape (filmstill by schwarzpictures.com) and **c**, thin MoS₂ flakes on a Si/SiO₂ chip after exfoliation.

Fig. 3.2 demonstrates our workflow for exfoliating various 2D materials (see Appendix A Table A.1 for sources of different bulk crystals). The goal is to obtain thin and relatively large-area flakes. First, we place the bulk crystal onto a piece of adhesive tape. We then fold and unfold the tape over the crystal, peeling off a number of flakes. We repeat this step until the material is densely spread over a large area on the tape, taking care not to overlay the flakes on top of each other. The folding technique has the disadvantage of fragmenting the flakes due to bending of the tape. To avoid this, the tape can be fixed to a hard, flat surface, and a second piece of tape can be used to exfoliate the flakes further. This step can be repeated with a fresh piece of tape until the initial tape is gradually covered with a thin “film” of the material – a good basis for later obtaining thin layers on the Si/SiO₂ substrate. As a last exfoliation step, we lightly press the tape with the exfoliated flakes onto a clean Si/SiO₂ substrate and leave both in contact for a few seconds, using a small weight to apply a uniform pressure. Slowly peeling the tape off finally results in the transfer of a few, thin flakes to the substrate.



Figure 3.2. **Mechanical exfoliation process.** Illustration of the technique for exfoliating two-dimensional materials using adhesive tape. The individual steps (a–j) are described in the text (filmstills by schwarzpictures.com).

3.1.2 Layer identification and characterization

The mechanical exfoliation technique generally produces flakes in a range of thicknesses, shapes and sizes, randomly distributed over the substrate. However, among these flakes only a small fraction of them are atomically thin and can thus be used as building blocks for our vdWHs. For initially locating and characterizing these flakes, we use techniques such as optical microscopy, Raman spectroscopy and atomic force microscopy (AFM).

Optical microscopy

After exfoliation, we first locate the interesting flakes under an optical microscope with a white light source. In general, 2D crystals with a thickness of less than ~ 15 nm are barely visible. Their visibility, however, can be increased when put onto an appropriate substrate (here Si/SiO₂) [62, 63]. The thin layers on the given substrate can be considered as a multilayered system, where interference effects appear due to multiple reflections at the different interfaces. Accordingly, choosing the right SiO₂ thickness can result in constructive interference of the light at the surface with the reflection from the back of the SiO₂ layer. This is the case for 2D crystals exfoliated onto Si substrates with a ~ 90 nm or a ~ 285 nm thick SiO₂ layer. Due to the resulting enhanced contrast, we can easily distinguish single- from few-layer flakes, and estimate the flake thickness from their color. Fig. 3.3 shows optical microscope images of different 2D materials (TMD, FLG, hBN), exfoliated onto a Si/SiO₂ (~ 285 nm) substrate. Under illumination with white light, mono- and bilayer TMDs appear in a transparent blue color (Fig.3.3a), while we typically choose FLG and hBN flakes with an intense blue and blue-green color

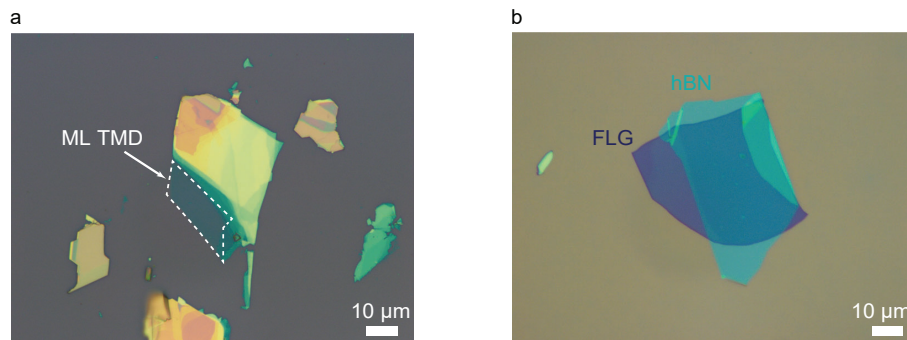


Figure 3.3. **Exfoliation of two-dimensional (2D) materials.** **a**, and **b**, Different 2D materials exfoliated onto Si wafers with a ~ 285 nm oxide layer. **a**, Monolayer (ML) TMD flakes (marked by a white dashed line) appear in transparent blue-green, while **b**, few-layer graphene (FLG) and hBN flakes with thicknesses of ~ 10 nm to 20 nm have an intense blue and blue-green color, respectively.

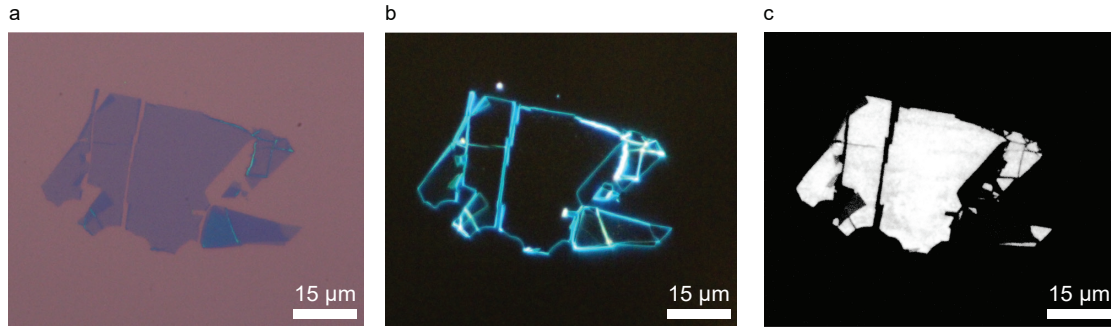


Figure 3.4. **Optical microscopy for selecting single-layer transition metal dichalcogenide (TMD) flakes.** Optical images of single-layer tungsten diselenide (WSe_2) under **a**, bright and **b**, dark field illumination. While bright field microscopy is used for the initial location of the flake, we use the dark field mode of our microscope to inspect the cleanliness of the flake. **c**, Luminescence image of the same flake using a tungsten halogen lamp. Bulk TMDs, are indirect bandgap semiconductors with negligible luminescence. When the crystals are thinned down to a single layer, however, a strong luminescence emerges, indicating an indirect-to-direct bandgap transition. This enables a clear distinction between single-layer and bilayer flakes.

(Fig. 3.3b), corresponding to a thickness of ~ 10 nm to ~ 20 nm (Fig. 3.3b).

For a quick inspection of the flake quality, we additionally use the dark field mode of our optical microscope. Dark field images are constructed from the light scattered by the sample, so that edges, cracks within the flake, tape residues and particles on the flake appear brighter than flat surfaces, and can thus be easily spotted (Fig. 3.4b). This aids us in selecting clean and homogeneous flakes for our devices.

Raman spectroscopy

Optical microscopy is a powerful tool for quickly and non-destructively locating and inspecting the thin exfoliated flakes. However, their thickness is only estimated by the contrast of the reflection spectra or the difference in color. For a more precise determination of the number of layers in 2D materials, Raman spectroscopy is widely used, as the vibrational properties of the material are very sensitive to the sample thickness. In the case of MoS_2 , for example, there are two main Raman-active peaks: the in-plane E_{2g}^1 mode at $\sim 382\text{ cm}^{-1}$, and the out-of-plane A_{1g} mode at $\sim 407\text{ cm}^{-1}$ in the bulk (Fig. 3.5a). The former red-shifts while the latter blue-shifts with increasing number of layers, and thus, we can use their frequency difference to identify the number of layers [64] (Figs. 3.5b,c).

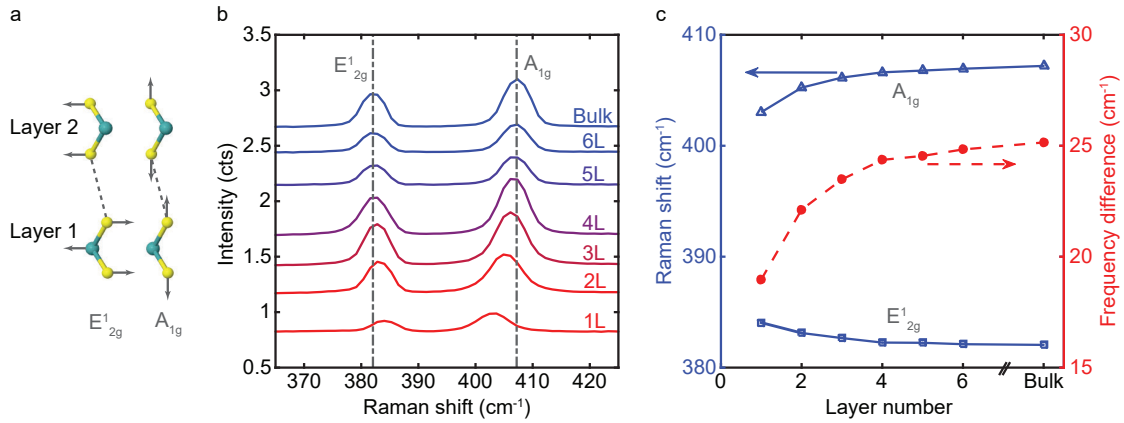


Figure 3.5. **Layer-dependent Raman spectroscopy** **a**, Schematic illustration of the in-plane E_{2g}^1 and out-of-plane A_{1g} vibrational modes. **b**, Raman spectra of MoS₂ for different number of layers at room temperature. The spectra are vertically offset for clarity; dashed lines indicate the position of the two vibrational modes E_{2g}^1 and A_{1g} for bulk MoS₂. **c**, Peak position shifts for the two Raman modes as a function the layer thickness, extracted from the spectra in panel **b**. The figure is adapted from Ref. [65].

3.2 Assembling van der Waals heterostructures

Once we have exfoliated all building blocks onto separate Si/SiO₂ chips and identified them with the techniques described above, we can design and build our vdWHs. For the assembly, we implemented a transfer method based on the work of P. J. Zomer *et al.* [66]. It uses a polymer stamp to stack flakes, assembling the structure from the top down, meaning the first flake to be picked up will be the top layer of the final stack. This has the advantage that only the top surface of the top layer will be in contact with the stamp, while the other layers will be protected from any contact with the polymer stamp and chemicals used during device fabrication. The stacking process can therefore be considered as dry and polymer free. However, in order to build vdWHs with clean interfaces, it is crucial to assemble the layers as soon as possible after their exfoliation. In principle, any vdWH design can be realized using this so-called dry-transfer technique. For simplicity, we describe the stacking procedure for a hBN/ML TMD/hBN heterostructure, as illustrated in Fig. 3.7.

The experimental set-up (see Fig. 3.6), also referred to as stacking station, consists of an optical microscope (Olympus TH4-200) equipped with large working distance optical objectives, a home-built heater, a three-axis micrometer stage to position the stamp and the substrate, as well as a tilt stage to stack at various angles. For the viscoelastic

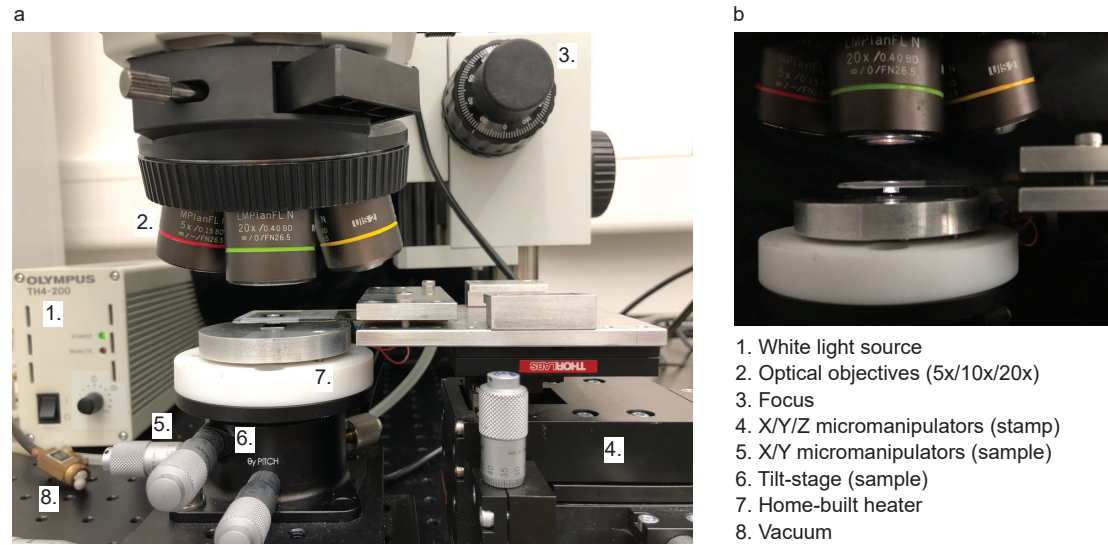


Figure 3.6. **Experimental set-up for stacking 2D materials into van der Waals heterostructures (stacking station).** **a**, Optical microscope and positioning stages. The individual components are labelled. **b**, Zoom into the transfer stamp fixed on a glass slide for better handling. The light from the microscope goes through the PDMS/PC stamp and illuminates the underlying sample.

stamp, we use a home-made polydimethylsiloxane (PDMS) block covered by a thin layer of polycarbonate (PC) which is affixed to a glass slide for better handling (see Appendix A for the preparation of the stamp).

To pick up the first layer of our vdWH stack, we place the substrate with the exfoliated top layer of our designed structure (here top hBN) on the sample stage. We then attach the glass slide to the three-axis manipulator with the stamp facing down towards the sample. We locate the first flake through the transparent stamp, place it under a clean area on the PC film, and pick it up (Fig. 3.7b). A detailed description of this process will be given for the transfer of the next layer (here ML TMD). After the successful pick-up of the first layer, we replace the substrate below the stamp by the Si/SiO₂ chip with the next layer (here ML TMD). Again, we locate the flake on the substrate (here ML TMD) through the transparent stamp, and align it with the already picked-up flake on the stamp (here top hBN) (Fig. 3.7c). We now carefully lower the stamp and finely readjust the position of the substrate with respect to the stamp in the X-Y-plane using the micromanipulators. Upon approaching, one side of the stamp touches the underlying substrate first (contact line in Fig. 3.7c₁), due to the substrate being initially tilted by a few degrees. At this point, we heat the stage to $T = 60^{\circ}\text{C}$, causing the PDMS to expand. This results in a lateral movement of the PC film across the flake (Fig. 3.7c₂), thus slowly

bringing the top layer (here top hBN) in contact with the flake on the substrate (here ML TMD). If the contact line stops moving, the Z-micromanipulator can be used to carefully lower the glass slide further. Once the contact line has passed both flakes

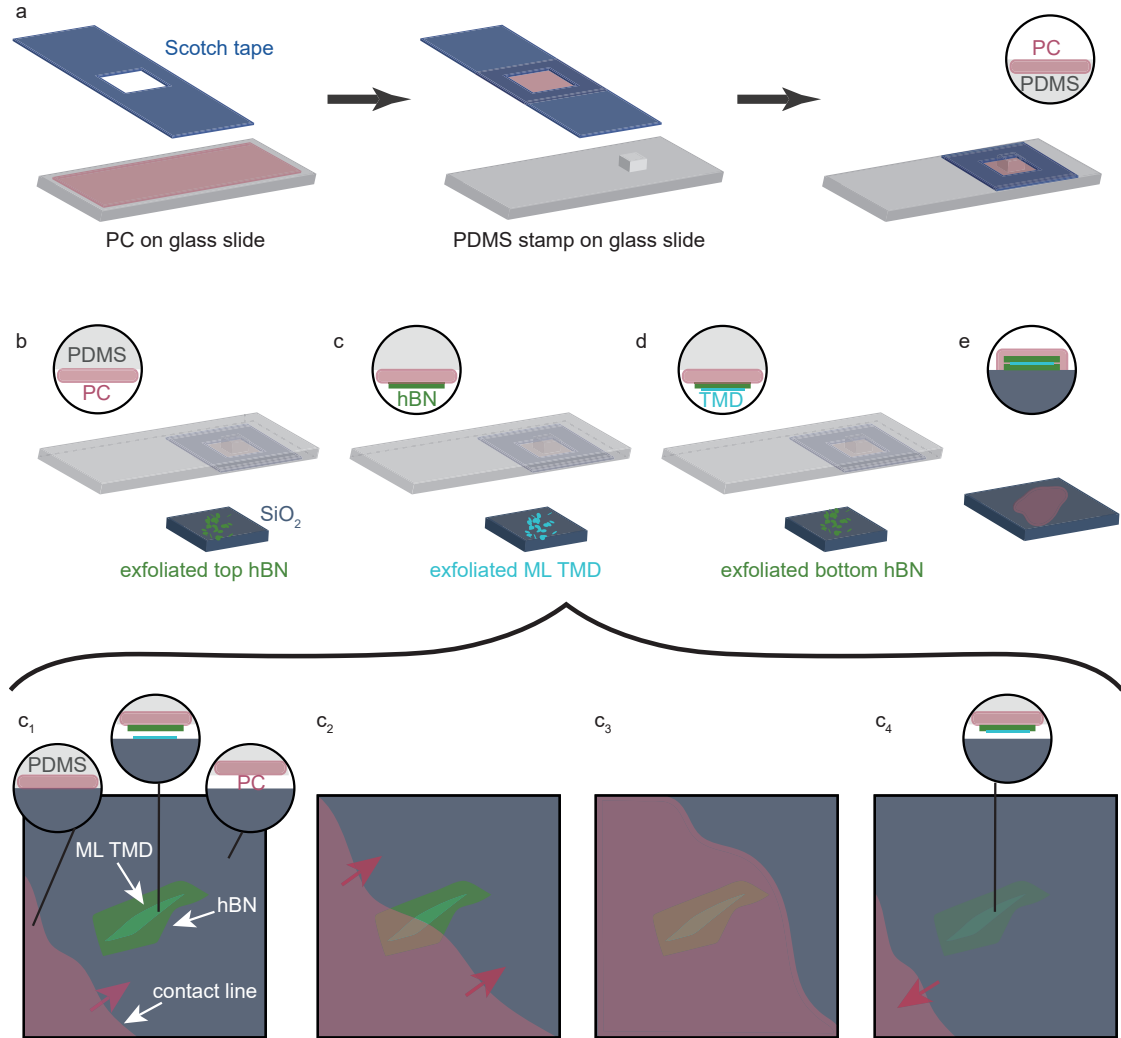


Figure 3.7. **Dry-stacking method for building van der Waals heterostructures (demonstrated for a hBN/ML TMD/hBN stack).** **a**, Preparation of the PDMS/PC stamp. **b**, First, the exfoliated top hBN is picked up from the Si/SiO₂ substrate, **c**, followed by the pick-up of the ML TMD flake. Insets **c**₁, to **c**₄, depict the detailed transfer process as described in the text. A change in contrast of the layers between **c**₁ and **c**₄ demonstrates that the ML TMD was successfully picked up by the top hBN. **d**, In a third step, the bottom hBN layer is picked up similarly by the ML TMD/hBN stack and **e**, the complete vdWH is released onto the pre-patterned substrate by melting the PC film. The circular insets illustrate the stamp and the picked-up flakes. The figure is adapted from Ref. [67].

(Fig. 3.7c₃), we increase the temperature of the transfer stage to $T = 85^\circ\text{C}$. During this process, due to the expansion of the PDMS, we constantly need to adjust the height of the stamp using the micrometer screws, to maintain the same contact between the stamp and the substrate. At $T = 85^\circ\text{C}$, we turn off the heating. While the substrate cools down, the PDMS contracts and hence, slowly retracts, which can be seen in the retreat of the contact line (Fig. 3.7c₄). Due to the stronger interaction between the ML TMD and the hBN compared to the interaction with the substrate, the flake gently peels off the substrate. We then elevate the stamp until it is completely out of contact with the underlying substrate. We note that the top hBN flake can sometimes show visible wrinkles after its pick-up, especially when it is very thin (Fig. 3.8a). If this is the case, we heat the sample stage to $T = 60^\circ\text{C}$ already before the stamp touches the underlying substrate. As the stamp gradually warms up, the PDMS/PC expands, and the wrinkles can be smoothed out (Fig. 3.8b). Only then, we bring the stamp in contact with the substrate.

To pick up the last layer (here bottom hBN), we use the exact same procedure as described above (Fig. 3.7d). For more complex heterostructures with a larger number of flakes, the pick-up step is simply repeated for all flakes until the desired stack is completed. We note that the alignment of the layers becomes trickier at each step. Naturally, also the risk of failure, e.g. rupturing, folding and misalignment of flakes, increases with every additional step, even though the general pick-up yield is very high.

In the last step (Fig. 3.7e), we release the complete stack from the PDMS/PC stamp

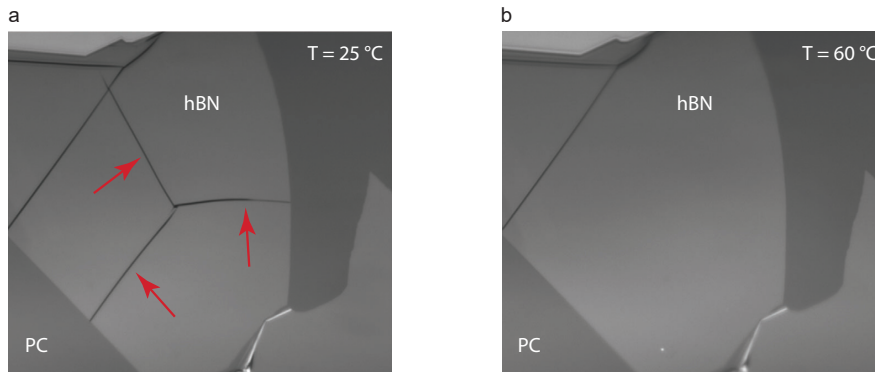


Figure 3.8. **Wrinkle removal by heating.** Optical image of a thin hBN flake picked up with a PDMS/PC stamp **a**, at $T = 25^\circ\text{C}$ and **b**, at $T = 60^\circ\text{C}$. The wrinkles, indicated by red arrows in **a** can be removed when the stamp is heated to $T = 60^\circ\text{C}$ for a few minutes before it is brought into contact with the underlying substrate.

onto a clean substrate, pre-patterned with alignment markers and an additional gate structure. Ideally, the heterostructure is positioned in the middle of four alignment markers, which is advantageous for subsequent nanofabrication processes. Similarly to the steps described before, we bring the heterostructure into contact with the underlying substrate. This time, however, we lower the transfer stage until almost the whole substrate is in contact with the stamp, and then heat it up to $\sim 185^\circ\text{C}$ for around five minutes. At this temperature, the PC film melts and can be detached from the PDMS by slowly lifting the glass slide with the stamp. Subsequently, we bake the heterostructure covered with the PC film for another ten minutes at $\sim 200^\circ\text{C}$ to ensure the adhesion of the heterostructure to the target substrate. Afterwards, the PC film is dissolved in chloroform for around one hour, and the sample is rinsed in IPA and blow-dried with N_2 .

During the stacking process, micro-bubbles can appear in the heterostructure due to contaminations, including air, water or hydrocarbons, trapped between the interfaces [68, 69]. We therefore thermally anneal the completed heterostructure under vacuum at $T = 100^\circ\text{C}$ for up to 12 hours. This step can remove polymer residues on the top and can allow bubbles to move and coalesce, resulting in larger homogeneous regions on the sample. We then acquire AFM images to map the clean areas, that is, areas without bubbles, in the heterostructure, and to measure the thickness of the different hBN layers. This is important for determination of the exact etching times (if necessary) and for the calculation of the electrostatics. To complete the device, we further process the heterostructure by shaping it into the final device geometry and fabricating electrical gates (Fig. 3.9). For these steps, standard electron-beam lithography (EBL), reactive ion etching (RIE) and metallization processes are used (see Appendix A for detailed

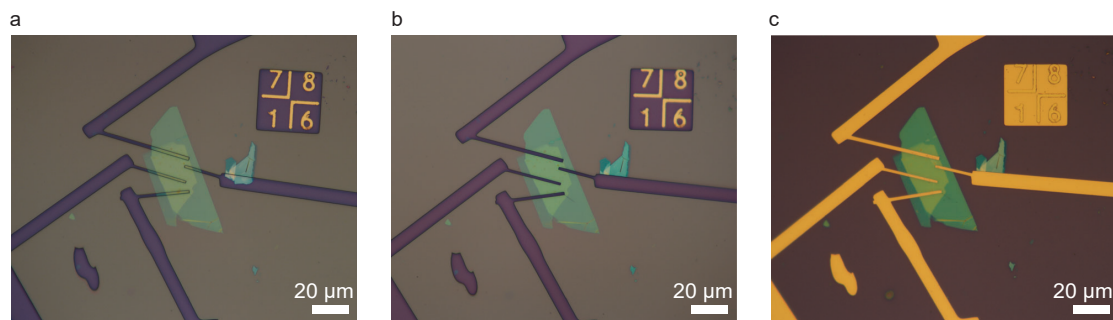


Figure 3.9. **Nano-fabrication steps for making contacts.** **a**, Electron-beam lithography (EBL), **b**, reactive ion etching (RIE) and **c**, metallization with thermal deposition for making contact to the monolayer TMD encapsulated in hBN. The figure is adapted from Ref. [65].

fabrication recipes). Finally, we connect the sample to the chip carrier by Au-wire bonding and test the electrical contacts.

3.3 Strategies for optimizing the sample quality in opto-electronic devices

3.3.1 Sample encapsulation

It is well-known that disorder can have a strong impact on the optical and transport properties of semiconductor systems. In the case of 2D materials, disorder can be attributed to many sources, including fluctuations of the material’s properties, such as chemical and structural compositions, strain and doping inhomogeneities [25, 70, 71]. Specifically, the presence of bubbles or wrinkles can lead to strain and localization of charge carriers within the sample. One disorder that can be particularly large in these 2D systems is the so-called dielectric disorder [71]. Fluctuations in the dielectric environment influence both the exciton binding energies and the bandgap, and can lead to large variations of the optical properties (energy, intensity, linewidth) [12, 25, 27, 71]. This is due to the fact that long-range Coulomb interactions are very sensitive to the environment.

A clear way to mitigate this effect and to access the intrinsic high optical quality of 2D TMDs is to create a homogeneous dielectric environment [71–73]. For 2D materials, hBN has proven to be an ideal material for encapsulation as it provides an atomically flat

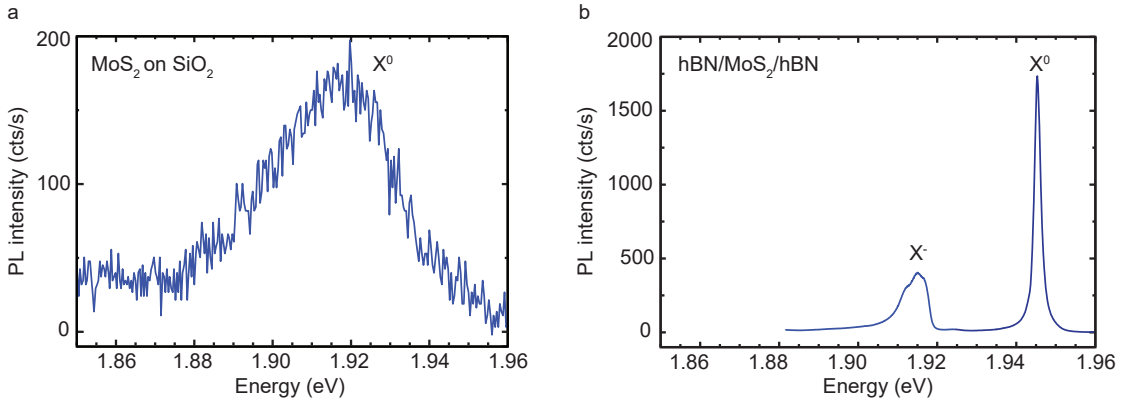


Figure 3.10. **Optical quality upon encapsulation with hexagonal boron nitride (hBN).** Photoluminescence (PL) spectrum for **a**, MoS₂ on SiO₂ and **b**, hBN/ML MoS₂/hBN on SiO₂. Encapsulation in hBN results in reduced optical linewidths for the neutral (X^0) and negatively charged (X^-) excitons in monolayer MoS₂. The X^0 linewidth reaches a value as low as ~ 1.8 meV at $T = 4$ K.

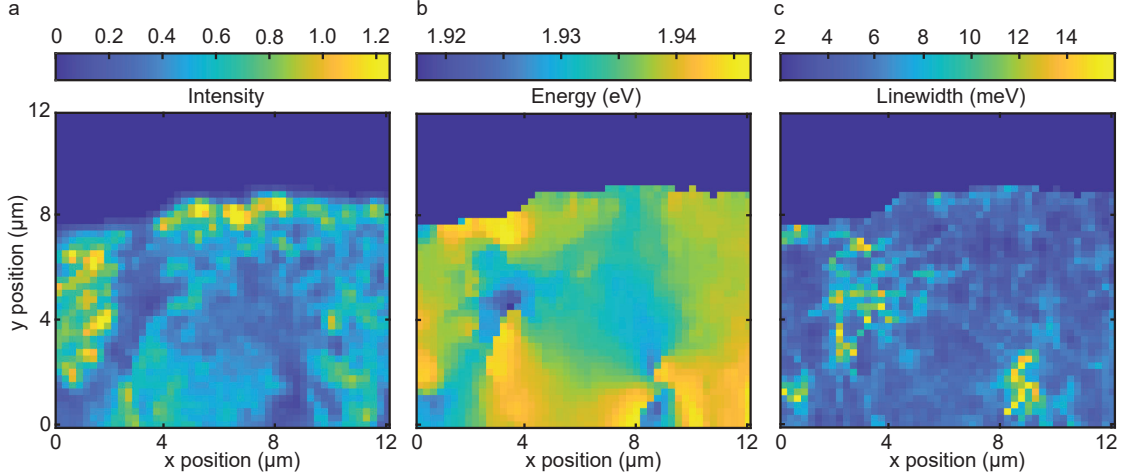


Figure 3.11. **Sample quality as a function of position.** **a**, Integrated photoluminescence (PL) intensity, **b**, energy and **c**, linewidth of the neutral exciton X^0 as a function of position in a gated hBN/MoS₂/hBN vdWH at zero carrier concentration ($T = 4$ K). Large homogeneous regions with high intensity, small energy fluctuations and narrow linewidth indicate the high optical quality of the device.

surface without dangling bonds and charge traps [74, 75]. While the top hBN protects the surface of the TMD layer, the bottom hBN separates the sample from the underlying Si/SiO₂ substrate, preventing possible transfer of charge and local field fluctuations, as well as surface roughness to the TMD layer. Fig. 3.10 shows the optical PL spectrum of monolayer MoS₂ on SiO₂ and MoS₂ encapsulated in hBN, respectively. When directly on SiO₂, the optical quality of MoS₂ is rather poor: the optical response shows a low emission efficiency and large optical linewidths (Fig. 3.10a). However, embedding the optically active 2D TMD layer between the inert, large-gap barrier hBN reduces the inhomogeneous broadening of the optical transitions and results in well-resolved neutral (X^0) and negatively charged exciton (X^-) peaks (Fig. 3.10b). The neutral exciton shows a remarkable bright and sharp PL emission with a narrow optical linewidth of ~ 1.8 meV approaching the ideal homogeneous limit [72]. Fig. 3.11 depicts the fitted integrated intensity, energy and linewidth of the X^0 resonance at zero carrier concentration over a large area ($12 \mu\text{m} \times 12 \mu\text{m}$) on a hBN/ML MoS₂/hBN vdWH. We can identify large homogeneous regions on the sample with narrow X^0 linewidth and small energy fluctuations. Combining the narrow linewidth with full control of the carrier concentration and/or electric field via external gates opens the way to create high-quality opto-electronic devices.

3.3.2 Device structure

We employ field-effect devices to control the carrier concentration n in our 2D TMD layer(s) and the electric field F_z across the vdWH. Fig. 3.12 shows the typical device geometries (single- and dual-gate devices) used within this thesis. In general, the optically active 2D layer(s) are encapsulated in insulating hBN for two main reasons. First, as described above, encapsulation in hBN results in a strong narrowing of the optical transitions [72]. Second, hBN represents a dielectric spacer that can withstand high breakdown fields up to ~ 1.5 MV/cm [76]. The FLG sheets serve as transparent gate electrodes for applying a “local” bias voltage.

Single-gate device

In the case of individual TMD monolayers, we use so-called single-gate devices to study their behavior upon electrostatic tuning of the carrier concentration n (see also Supplement in Ref. [56]). Fig. 3.12a is a schematic depiction of such a device, where either (i) p-doped silicon (Si) or (ii) FLG is used as back-gate. We can calculate the capacitances of our devices using simple electrostatics: the 2D TMD layer(s) and the p-doped Si or FLG act as two electrodes separated by the bottom hBN layers and in (i) additionally the SiO₂ substrate, with thicknesses d_{hBN} and d_{SiO_2} . Accordingly, the device capacitances per unit area can be estimated to be

$$(i) \ C = \frac{1}{\frac{d_{\text{hBN}}}{\epsilon_0 \epsilon_{\text{hBN}}} + \frac{d_{\text{SiO}_2}}{\epsilon_0 \epsilon_{\text{SiO}_2}}} \quad (ii) \ C = \frac{\epsilon_0 \epsilon_{\text{hBN}}}{d_{\text{hBN}}}, \quad (3.1)$$

with ϵ_0 the vacuum permittivity and ϵ_{hBN} the dielectric constant of hBN. By applying a gate voltage V_G to our global Si or “local” FLG back-gate, keeping the 2D layer(s) grounded, we can inject charge carriers into our device through

$$n = C \cdot V_G. \quad (3.2)$$

Dual-gate device*

Especially in bilayer systems, we need separate control over the charge and field distribution in order to investigate reliably the excitonic behavior. In these cases, we make use

*This section is partially adapted from the Supplement in N. Leisgang *et al.*, Nature Nanotechnology **15**, 901–907 (2020).

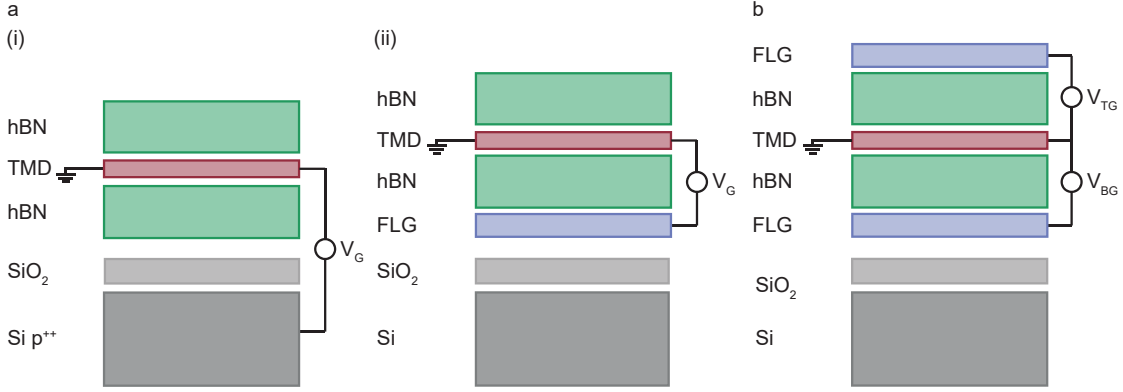


Figure 3.12. **Device structures.** Schematics of the van der Waals device designs used within this thesis. **a**, Single-gate device to control the carrier concentration in the 2D TMD layer(s). Here, (i) p-doped Si or (ii) FLG is used as a global or “local” back-gate, respectively. **b**, Dual-gate device with top and bottom few-layer graphene (FLG) gates to control independently the carrier concentration in the 2D TMD layer(s) and the electric field across the heterostructure. For both devices, hexagonal boron nitride (hBN) is used as a dielectric spacer around the 2D layer(s).

of a so-called dual-gate heterostructure design, as depicted in Fig. 3.12b. The presence of the (optically transparent) top and bottom electrical gates, in addition to the directly contacted TMD layer(s), allows us to control the total carrier density n of the TMD layer(s) as well as the electric field F_z across the heterostructure using the voltages V_{TG} and V_{BG} applied to the top and bottom gates.

We consider the electrostatic model schematically depicted in Fig. 3.12b. The TMD layer(s) are modelled as grounded conducting plates in between two insulating hBN layers. Upon electrical gating, top and bottom displacement fields, D_T and D_B , respectively, lead to a net carrier doping n of the TMD layer(s), as well as an imposed interlayer electric field D . By setting n and varying D , we can tune the interlayer electric field while keeping the carrier concentration in the TMD layer(s) constant. By varying n above or below zero, we can inject electrons or holes into the system and shift the Fermi level without changing the electric field across the heterostructure [77].

In our experiment, the displacement fields D_T and D_B are tuned independently by the top and bottom gate voltages, through the relations

$$D_T = C_T(V_{TG} - V_{TG}^0) \quad (3.3)$$

$$\text{and } D_B = -C_B(V_{BG} - V_{BG}^0) . \quad (3.4)$$

Here, V_{TG} and V_{BG} are the voltages applied to the top and bottom gates, and V^0 is the

effective offset voltage due to initial environmental carrier doping. To describe the capacitive system, we introduce the relevant geometric top and bottom gate capacitances per unit area as

$$C_T = \frac{\epsilon_0 \epsilon_{\text{hBN}}}{d_T} \quad \text{and} \quad C_B = \frac{\epsilon_0 \epsilon_{\text{hBN}}}{d_B} . \quad (3.5)$$

Here, d_T and d_B are the thicknesses of the top and bottom hBN layers as determined by AFM measurements, ϵ_0 is the vacuum permittivity and $\epsilon_{\text{hBN}} \approx 3.76$ [78] is the dielectric constant of hBN. In general, we use hBN layers with thicknesses between ~ 15 nm and ~ 40 nm, that is, thick enough to reduce the influence of charge fluctuations at the SiO₂ surface, but thin enough to minimize charge trapping in the hBN layers [79, 80].

Using the plate capacitor model, we can define the total applied electron density as

$$\begin{aligned} n &= n_T + n_B \\ &= \frac{1}{e} \left[C_T (V_{\text{TG}} - V_{\text{TG}}^0) + C_B (V_{\text{BG}} - V_{\text{BG}}^0) \right] , \end{aligned} \quad (3.6)$$

where n_T and n_B are the carrier densities in the top and bottom layers, and e is the electron charge. From Eq. 3.5 and 3.6, the net carrier doping can be calculated to be

$$n = \frac{1}{e} \frac{\epsilon_0 \epsilon_{\text{hBN}}}{d_T} \left[(V_{\text{TG}} - V_{\text{TG}}^0) + \frac{d_T}{d_B} (V_{\text{BG}} - V_{\text{BG}}^0) \right] . \quad (3.7)$$

Now we evaluate quantitatively the electric displacement in the system, assuming that there are no charges accumulated at the interfaces

$$\begin{aligned} D &= \frac{1}{2} \left[C_T (V_{\text{TG}} - V_{\text{TG}}^0) - C_B (V_{\text{BG}} - V_{\text{BG}}^0) \right] \\ &= \frac{1}{2} \epsilon_0 \epsilon_{\text{hBN}} \left[\frac{(V_{\text{TG}} - V_{\text{TG}}^0)}{d_T} - \frac{(V_{\text{BG}} - V_{\text{BG}}^0)}{d_B} \right] . \end{aligned} \quad (3.8)$$

The electric field across the TMD layer(s) can then be calculated to be

$$F_z = \frac{1}{2} \frac{\epsilon_{\text{hBN}}}{\epsilon_{2\text{D}} d_B} \left[(V_{\text{TG}} - V_{\text{TG}}^0) - \frac{d_T}{d_B} (V_{\text{BG}} - V_{\text{BG}}^0) \right] , \quad (3.9)$$

where we use $D = \epsilon_0 \epsilon_{2\text{D}} F_z$, with $\epsilon_{2\text{D}}$ being the dielectric constant of the TMD layer(s).

Fig. 3.13a maps the optical response of the neutral exciton in a homobilayer MoS₂ dual-gate device structure (see Appendix B) for different voltages applied to the top and bottom gates, V_{TG} and V_{BG} . From the calculations above, we can disentangle the response of the system to both the out-of-plane applied electric field across the het-

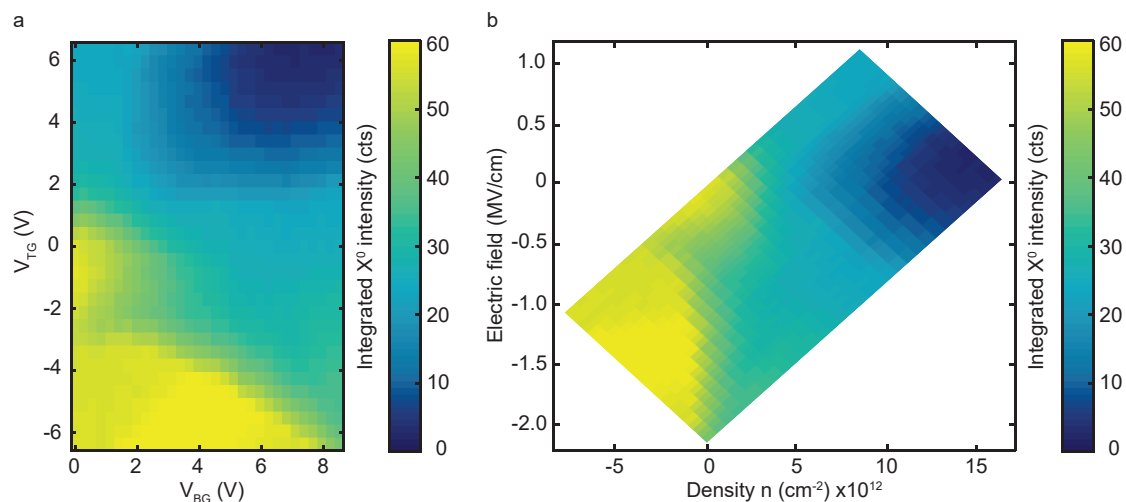


Figure 3.13. **Voltage map in a dual-gate device structure.** **a**, Absorption strength of the neutral exciton X^0 in homobilayer MoS₂ as a function of the top and bottom voltages, V_{TG} and V_{BG} . **b**, Transformation into the variables $F(V_{TG}, F_{BG})$ and $n(V_{TG}, F_{BG})$ using $d_T/d_B = 0.75$ as determined by AFM measurements.

erstructure (Eq. 3.9) and the induced change in carrier density (Eq. 3.7) by evaluating $F(V_{TG}, V_{BG})$ and $n(V_{TG}, V_{BG})$ (see Ref. [81]). From the nearly constant absorption at the X^0 exciton resonance along the vertical axis in Fig. 3.13b, we can confirm, in this case, that for the applied top and bottom gate voltages our gate operation scheme only varies the electric field F_z , while the carrier concentration in the TMD layers stays nearly constant. In general, tuning n in the device modifies both the intensity and lineshape of the excitons. On the other hand, by changing F_z , we can control their emission energies via the quantum confined Stark effect (QCSE).

4

Experimental methods: optical spectroscopy of two-dimensional semiconductors

Optical spectroscopy provides information about various properties of a semiconducting material, such as its optical bandgap, excitonic binding energies, absorption strengths, doping level and so on. In 2D TMDs, the optical probe is particularly powerful: the combination of spatial and polarization resolution can additionally reveal interesting spin and valley physics (see Chapter 2) [25, 70].

In this Chapter, we will briefly introduce the general concepts of light-matter interactions with a focus on linear and second-order nonlinear effects. We will then discuss the experimental methods used within this thesis, including absorption (or reflectivity), photoluminescence (PL) and second harmonic generation (SHG) spectroscopy, as well as the detailed measurement techniques and set-ups.

4.1 Concepts: light-matter interactions

In a simple classical picture, we can consider the optical properties of a material as the interaction of an electro-magnetic field with oscillating dipoles [82]. Within this approximation, the optical response of a material to an applied light field can be written as a power series of the polarization $\mathbf{P}(\omega)$ in terms of the optical field strength $\mathbf{E}(\omega)$ [82–84],

$$\mathbf{P}(\omega) = \mathbf{P}^{\text{L}}(\omega) + \mathbf{P}^{\text{NL}}(\omega) = \epsilon_0 \left[\chi^{(1)} \mathbf{E}(\omega) + \chi^{(2)} \mathbf{E}^2(\omega) + \chi^{(3)} \mathbf{E}^3(\omega) + \dots + \chi^{(k)} \mathbf{E}^k(\omega) \right], \quad (4.1)$$

where $\mathbf{P}^{\text{L}}(\omega)$ describes the linear optical response and $\mathbf{P}^{\text{NL}}(\omega)$ accounts for higher-order nonlinear terms, and ϵ_0 refers to the permittivity of free space. $\chi^{(k)}$ is the k^{th} -order optical susceptibility, a material-dependent $(k + 1)$ -rank tensor. It relates all possible combinations of the three cartesian coordinates (x, y, z) of the polarization with the

coordinates of the interacting electric fields. Using the Einstein summation convention, each component P_i ($i = x, y, z$) of the material polarization can equivalently be expressed as

$$P_i = \epsilon_0 \left[\chi_{ij}^{(1)} E_j + \chi_{ijk}^{(2)} E_j E_k + \chi_{ijkl}^{(3)} E_j E_k E_l + \dots \right]. \quad (4.2)$$

For weak electric fields, the polarization is linearly proportional to the electric field,

$$\mathbf{P}^L(\omega) = \epsilon_0 \boldsymbol{\chi}^{(1)} \mathbf{E}(\omega). \quad (4.3)$$

$\boldsymbol{\chi}^{(1)}$ ($\equiv \chi(\omega)$) is the well-known linear optical susceptibility, which describes conventional linear optical effects, such as absorption in a material. $\epsilon(\omega) = 1 + \chi(\omega)$ is the frequency-dependent dielectric response function.

On the other hand, if the applied light field is strong enough, or the nonlinear optical susceptibility is very large, higher-order terms ($k \geq 2$) become significant. This results in a polarization $\mathbf{P}(\omega)$ that oscillates at frequencies different from the the incoming light. Here, we will only focus on linear and second-order nonlinear optical effects, specifically SHG; higher-order nonlinear processes are not part of the experimental methods within this thesis.

4.1.1 Linear optical spectroscopy

The majority of the data presented within this thesis stem from linear optical processes which involve the lowest order of interaction between electro-magnetic waves and the elementary excitations, or resonances, within a semiconducting material. In this case, the strength of the incident field is weak enough so that the induced polarization depends only linearly on $\mathbf{E}(\omega)$ (Eq. 4.3) [28, 82, 85].

Absorption (or reflectivity) spectroscopy probes the optical transition energies and their relative oscillator strengths by illuminating the sample with a broadband light source or with a weak tunable laser (Fig. 4.1a). If an incident photon is resonant with an allowed transition, this photon will be absorbed by the material. If the energy of the incoming photon does not match the resonance condition, the material does not absorb such light. In photoluminescence (PL) spectroscopy, a monochromatic laser is used to excite electrons from the valence band (VB) to the conduction band (CB) with an energy above the material's bandgap (Fig. 4.1b). The electrons and holes subsequently relax towards the lowest energy states (ground states) via scattering processes before they recombine and emit a photon. In principle, the resulting PL emission spectra are more complicated than the absorption spectra due to complex relaxation pathways and

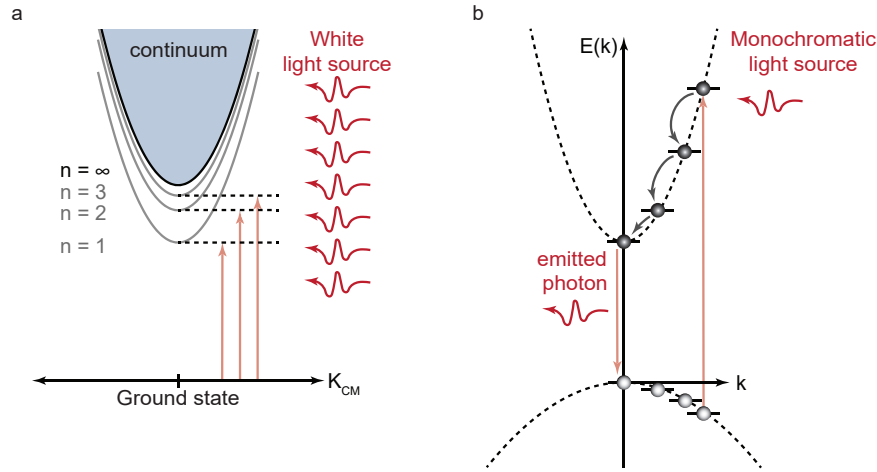


Figure 4.1. **Schematic illustration of the absorption and emission (photoluminescence) process in a direct bandgap semiconductor.** **a**, Absorption spectroscopy probes the optically allowed transitions (see also Chapter 2). The red wavy arrows illustrate the broadband light source. **b**, In photoluminescence (PL) spectroscopy, the semiconductor is excited by a monochromatic laser above the material’s bandgap. The photo-generated carriers rapidly relax towards the lowest energy state (indicated by the grey arrows for the electrons in the CB) and recombine, emitting a photon.

competing relaxation and radiation rates.

Determination of the optical susceptibility*

In the case of a weak incident field, the optical response of the probed material can be described by both the optical susceptibility $\chi(\omega)$ and the dielectric function $\epsilon(\omega)$ (Eq. 4.3). For strongly absorbing materials, these linear response functions can be determined via optical reflectivity measurements. In principle, this requires measuring both the reflectance R of a material at normal incidence, as well as its absorption coefficient. In practice, however, it is sufficient to measure R over a wide spectral range, and deduce the absorption coefficient, and thus $\chi(\omega)$ or $\epsilon(\omega)$, using the Kramers-Kronig relation [28]. As our vdWHs are multilayered structures, additional interference effects influence the optical reflectivity spectrum. In the following, we demonstrate how the resulting complicated reflectivity expression for such a multilayered system can be simplified and related to the characteristic dielectric response function of the system.

Let us first consider a thin layer that is placed on top of a thick glass substrate

*This section is partially adapted from the Supplement in J. G. Roch *et al.*, Nature Nanotechnology **14**, 432-436 (2019). The relation between differential reflectivity and optical susceptibility was derived by G.F. and J.G.R.

(Fig. 4.2a). Here, the thickness d of the layer is much smaller than the wavelength λ of the incident light. The Fresnel reflection coefficient of this three-layer system (Fig. 4.2a with air (1), thin layer (2), substrate (3)) can be calculated, for example by using the transfer matrix method [82], to be

$$\frac{E_r}{E_0} = \frac{r_{12} + r_{23} e^{-2i\beta}}{1 + r_{12}r_{23} e^{-2i\beta}} \equiv r_{123} , \quad (4.4)$$

where E_0 and E_r are the incident and the total reflected fields, respectively. $r_{ij} = \frac{n_i - n_j}{n_i + n_j}$ is the Fresnel coefficient between the two interfaces i and j with (complex) refractive indices n_i and n_j , and $\beta = \frac{2\pi n_2}{\lambda} \cos \varphi_2$ defines the phase change of the beam when passing through the thin layer. For the three-layer system, the reflectivity is then given by $R_{123} = |r_{123}|^2 \equiv R(d)$. While this value is rather difficult to determine experimentally, we can accurately measure the normalized change in the reflectivity

$$\frac{\Delta R}{R_0} = \frac{R(d) - R(0)}{R(0)} , \quad (4.5)$$

with $R(0) \equiv R_{13} = |r_{13}|^2$ the reflectivity of the two-layered system, that is, the reflectivity in the absence of the thin layer ($d = 0$).

Following Ref. [86], the differential reflectivity of the thin layer ($d \ll \lambda$) at normal incidence can then be expressed as

$$\frac{\Delta R}{R_0} = -\frac{8\pi d n_1}{\lambda} \operatorname{Im} \left(\frac{\epsilon_1 - \epsilon_2}{\epsilon_1 - \epsilon_3} \right) , \quad (4.6)$$

with $\epsilon_k = \epsilon'_k + i\epsilon''_k$ the complex dielectric constant of the k^{th} layer. In our case, the first medium is air and thus $n_1 = 1$. Making the assumption that glass (medium 3) does not absorb light, that is, $\epsilon_3 = \epsilon'_3$ ($\epsilon''_3 = 0$), and using the relation $\epsilon_2 = 1 + \chi^*$, we can show that the imaginary part of the optical susceptibility $\operatorname{Im}(\chi)$ of the thin layer can be directly related to the differential reflectivity via

$$\operatorname{Im}(\chi) = \frac{\lambda}{8\pi d} (1 - \epsilon'_3) \frac{\Delta R}{R_0} . \quad (4.7)$$

However, our vdWHs generally consist of more than three layers. Thus, additional reflections at different interfaces and multiple thin-film interferences within the individual layers (hBN, SiO₂, Si) contribute to the measured reflectivity spectrum (Fig. 4.2a). Such

*For simplicity, we will write $\chi_2 \equiv \chi$ when referring to the optical susceptibility of the thin layer (2).

optical interferences mostly affect the lineshape symmetry of the optical transitions. Following Ref. [87], we can use a finite phase factor $e^{-i\alpha(\omega)}$, with a frequency-dependent phase shift $\alpha(\omega)$, to account for such effects. For our complex multilayered system, we can then simply replace $\text{Im}(\chi) \equiv \chi''$ by

$$\tilde{\chi}'' = e^{-i\alpha} \chi'' , \quad (4.8)$$

accounting for all additional optical interferences within the system. Here we assumed that, to first order, the included phase shift $\alpha(\omega) = \alpha$ is frequency-independent within our spectral range of interest. Following Eq. 4.7, we effectively probe

$$\frac{\Delta R}{R_0} = \frac{8\pi d}{\lambda} \frac{1}{1 - \epsilon'_3} \tilde{\chi}'' \propto \tilde{\chi}'' , \quad (4.9)$$

in our experiments rather than the intrinsic susceptibility χ'' of the thin optically active layer. From the above definition (Eq. 4.8), $\chi'' = e^{i\alpha} \tilde{\chi}''$, which we can rewrite as

$$\chi'' = \sin(\alpha)\tilde{\chi}' + \cos(\alpha)\tilde{\chi}'' . \quad (4.10)$$

Together with the Kramers-Kronig relation [28]

$$\tilde{\chi}'(\omega) = -\frac{2}{\pi} \mathcal{P} \int_0^\infty \frac{\omega'}{\omega'^2 - \omega^2} \tilde{\chi}''(\omega') d\omega' , \quad (4.11)$$

we can now express the imaginary part of the optical susceptibility of the thin layer $\text{Im}(\chi) \equiv \chi''$ by the experimentally measured quantity $\frac{\Delta R}{R_0} \propto \tilde{\chi}''$ as

$$\chi'' = \frac{\lambda}{8\pi d} (1 - \epsilon'_3) \left[-\sin(\alpha) \frac{2}{\pi} \mathcal{P} \int_0^\infty \frac{\omega'}{\omega'^2 - \omega^2} \frac{\Delta R}{R_0}(\omega') d\omega' + \cos(\alpha) \frac{\Delta R}{R_0} \right] \quad (4.12)$$

and thus, transform the differential reflectivity into absorption.

To obtain the absorption spectrum, the reference spectrum R_0 turns out to be an important quantity. As the recorded spectra are broadband, small interference patterns appear in the raw reflectivity spectrum R due to internal reflections in the optical set-up. With the optimal R_0 , those cancel out completely on computing $\Delta R = R - R_0$, and the baseline of $\frac{\Delta R}{R_0}$ is zero (light-blue spectrum in Fig. 4.2c). This is an important basis for carrying out the Kramers-Kronig transformation. In the experiment, we have two possibilities to measure R_0 . In general, we can record the reference spectrum R_0 on any position within the sample without the thin optical layer. However, our vdWHs

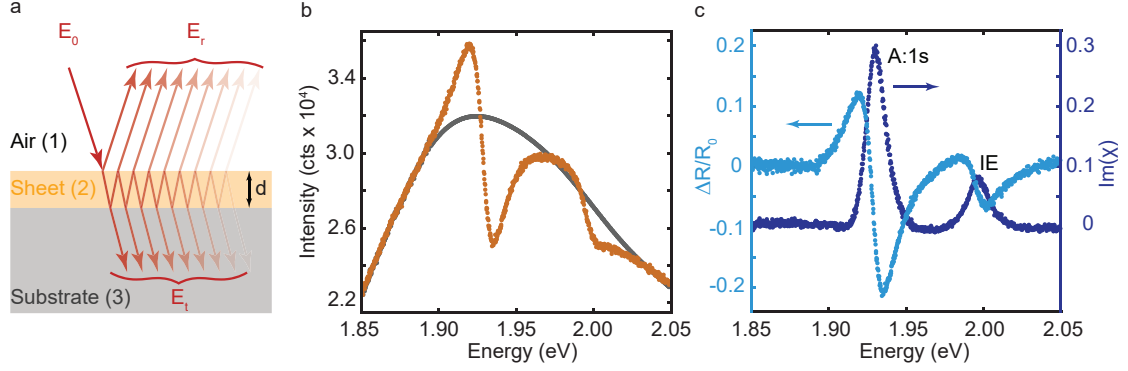


Figure 4.2. **Determination of the optical susceptibility** **a**, Multiple interferences from a thin layer (2) in air (1) placed on a thick glass substrate (3). E_0 is the incident electric field, E_r and E_t denote the total reflected and transmitted field, respectively. **b**, Raw reflectivity R (orange) and reference R_0 (grey) spectrum recorded on the same sample position ($T = 4\text{ K}$). R_0 is interpolated from the raw reflectivity spectrum at a high electron density $n \approx 11.5 \cdot 10^{12} \text{ cm}^{-2}$. **c**, Differential reflectivity $\frac{\Delta R}{R_0}$ (light blue) and corresponding absorption spectrum $\text{Im}(\chi)$ (dark blue) of the neutral exciton (A:1s) and the interlayer exciton (IE) in homobilayer MoS_2 at zero electron concentration. Using the reference spectrum and the Kramers-Kronig relation, the raw reflectivity data can be converted into the imaginary part of the optical susceptibility $\text{Im}(\chi)$. Here, a phase factor $\alpha = 67^\circ$ compensates for the multiple thin-film interferences within the vdW heterostructure.

consist of many layers, and moving around on the sample can slightly change the interference pattern. In addition, the intensity of the reflected light can differ from position to position, leading to a small offset on computing the differential reflectivity signal $\frac{\Delta R}{R_0}$. A more accurate approach is to obtain R_0 from the same spot on the sample as the reflectivity data are recorded. We know that varying the carrier concentration in our gated devices leads to significantly different reflectivity spectra. We therefore interpolate R_0 from the raw reflectivity spectrum at a high electron density where the oscillator strength is distributed over a large spectral range [88] (grey spectrum in Fig. 4.2b). As R and R_0 are acquired from the same spot on the sample, all interference patterns cancel on computing the reflection change ΔR . From the differential reflectivity spectrum $\frac{\Delta R}{R_0}$ (light-blue spectrum in Fig. 4.2c), we can subsequently transform $\frac{\Delta R}{R_0}$ using the Kramers-Kronig relation (Eq. 4.12) taking into account a phase shift α , and calculate the optical susceptibility of the thin film (dark-blue spectrum in Fig. 4.2c).

Figs. 4.2b,c show an example of the raw reflectivity (orange) and the differential reflectivity (light-blue) spectrum of the neutral exciton (A:1s) and interlayer exciton (IE) in homobilayer MoS_2 . In the absence of free electrons and external electric field, the excitonic absorption, that is, the imaginary part of the susceptibility $\text{Im}(\chi)$, is expected

to feature Lorentzian lineshapes. Consequently, we choose a value of α such that the transformed signal using Eq. 4.12* can be accurately described by a Lorentzian (dark-blue spectrum in Fig. 4.2c). As we assume that the phase shift α stays constant for changes in n and/or F_z , all differential reflectivity data recorded from the same spot on the sample can then be transformed using the same value for α .

4.1.2 Second harmonic generation[†]

Second-order nonlinear optical effects, including second harmonic generation and sum- and difference-frequency generation, are typically described by the second-order nonlinear optical susceptibility $\chi^{(2)}$ in Eq. 4.1. In a SHG process, two incident photons with the same frequency ω are converted into a single photon with frequency 2ω , as illustrated in Fig. 4.3a. Following Eq. 4.2, under an incident electric field $\mathbf{E}(\omega)$ with fundamental angular frequency ω , the second-order nonlinear polarization is determined by a third-rank electric susceptibility tensor [84, 89]

$$\chi^{(2)} : P_i(2\omega) = \epsilon_0 \chi_{ijk}^{(2)}(2\omega; \omega, \omega) E_j(\omega) E_k(\omega) \quad (4.13)$$

resulting in the creation of SHG. The second-order nonlinearities of a material can be probed by impinging intense linearly polarized light at angular frequency ω onto its surface and measuring the generated outgoing response at 2ω through an analyzer. By using different polarization combinations and/or by varying the orientation of the interface with respect to the incoming beam, different components of $\chi^{(2)}$ can be determined, giving information about the structural symmetry of the material as well as the strength of various nonlinear processes. Due to symmetry reasons, second-order (and other even-order) nonlinear optical interactions can only occur in non-centrosymmetric crystals, that is, crystals without an inversion symmetry[‡].

In the following section, we will demonstrate how the different crystal axes of 2D TMDs, that is, armchair and zigzag axes, can be identified through angular-resolved SHG.

*We note that the integral in Eq. 4.12 is only computed over the wavelength range corresponding to the experimental spectra.

[†]This section is partially adapted from N. Leisgang *et al.*, AIP Advances **15**, 105120 (2018).

[‡]We note that the SHG can be drastically enhanced when exciting on resonance with an excitonic transition [90], mediating SHG in inversion-symmetric crystals [91].

Determination of the crystallographic axes via angular-resolved SHG

As discussed in Chapter 2, the most commonly studied TMD crystal lattices in the bulk 2H-phase belong to the non-centrosymmetric D_{3h} ($\bar{6}m2$) point group*. The specific stacking arrangement of the individual layers results in an additional translational symmetry along the z -axis (perpendicular to crystal plane) for an even number of layers [92]. Considering this symmetry, the nonlinear optical response of the TMD crystals depends on the number of layers. While for an even number of layers, the second-order nonlinear susceptibility vanishes in principle ($\chi^{(2)} = 0$), for an odd number of layers, the absence of spatial inversion symmetry gives rise to a finite nonlinear response ($\chi^{(2)} \neq 0$). Following Refs. [84, 89, 93], the second-order nonlinear susceptibility tensor $\chi_{ijk}^{(2)}$ for materials with D_{3h} symmetry has four non-zero elements $\chi_{xxx}^{(2)} = -\chi_{xyy}^{(2)} = -\chi_{yyx}^{(2)} = \chi_{yxy}^{(2)} = |\chi^{(2)}|$,

$$\chi^{(2)} = \begin{pmatrix} \begin{pmatrix} 0 \\ \chi_{yyx}^{(2)} = -\chi_{xxx}^{(2)} \\ 0 \end{pmatrix} \\ \begin{pmatrix} \chi_{xyy}^{(2)} = -\chi_{xxx}^{(2)} \\ 0 \\ 0 \end{pmatrix} \\ \begin{pmatrix} 0 \\ 0 \\ 0 \end{pmatrix} \end{pmatrix} \begin{pmatrix} \chi_{yxy}^{(2)} = -\chi_{xxx}^{(2)} \\ 0 \\ 0 \end{pmatrix} \begin{pmatrix} 0 \\ \chi_{xxx}^{(2)} \\ 0 \\ 0 \\ 0 \end{pmatrix} \begin{pmatrix} 0 \\ 0 \\ 0 \\ 0 \\ 0 \end{pmatrix} \end{pmatrix}, \quad (4.14)$$

where x and y denote the armchair and zigzag direction, respectively. Using Eq. 4.13, the second-order nonlinear optical polarization of a non-centrosymmetric crystal with D_{3h} ($\bar{6}m2$) point group symmetry is then given by

$$\begin{pmatrix} P_x^{(2)}(2\omega) \\ P_y^{(2)}(2\omega) \\ P_z^{(2)}(2\omega) \end{pmatrix} = \epsilon_0 |\chi^{(2)}| \begin{pmatrix} E_x^2(\omega) - E_y^2(\omega) \\ -2E_x(\omega)E_y(\omega) \\ 0 \end{pmatrix}. \quad (4.15)$$

For a linearly polarized fundamental field applied along the real coordinates (x', y') , normally incident on the crystal,

$$E = E_{x'} + E_{y'} = E \cos(\phi) \hat{x} + E \sin(\phi) \hat{y}, \quad (4.16)$$

*Single layers (or more generally all odd number of layers) are described by a lower symmetry point group D_{3h} due to the reduced number of symmetry operations compared to the bulk crystal.

the second-order polarization in the crystal coordinate system is given by

$$\begin{pmatrix} P_x^{(2)}(2\omega) \\ P_y^{(2)}(2\omega) \\ P_z^{(2)}(2\omega) \end{pmatrix} = \epsilon_0 |\chi^{(2)}| \begin{pmatrix} E^2(\omega)(\cos^2 \phi - \sin^2 \phi) \\ -2E^2(\omega) \cos \phi \sin \phi \\ 0 \end{pmatrix}. \quad (4.17)$$

Here, ϕ describes the angle between real (x', y') and crystal (x, y) coordinates. Rotating the coordinate system (anticlockwise) by ϕ , that is, transforming $(x, y) \rightarrow (x', y')$,

$$\begin{aligned} x' &= x \cos \phi + y \sin \phi \\ y' &= -x \sin \phi + y \cos \phi \end{aligned} \quad (4.18)$$

and using Eq. (4.17), the second-order nonlinear polarization can be expressed in real coordinates by

$$\begin{pmatrix} P_{x'}^{(2)}(2\omega) \\ P_{y'}^{(2)}(2\omega) \\ P_{z'}^{(2)}(2\omega) \end{pmatrix} = \begin{pmatrix} P_x^{(2)}(2\omega) \cos \phi + P_y^{(2)}(2\omega) \sin \phi \\ -P_x^{(2)}(2\omega) \sin \phi + P_y^{(2)}(2\omega) \cos \phi \\ 0 \end{pmatrix} = \epsilon_0 |\chi^{(2)}| \begin{pmatrix} E^2(\omega) \cos 3\phi \\ E^2(\omega) \sin 3\phi \\ 0 \end{pmatrix}. \quad (4.19)$$

The response of the two orthogonal components of the SHG field $P_{x'}^{(2)}(2\omega)$ and $P_{y'}^{(2)}(2\omega)$ thus follow a $\cos 3\phi$ and $\sin 3\phi$ dependence, respectively. Since $E(2\omega) \propto P^{(2)}(2\omega)$, the intensity of the SHG signal with respect to the polarization of the fundamental field is

$$\begin{aligned} I_{x'}(2\omega) &\propto I_0(\omega) \cos^2 3\phi \\ I_{y'}(2\omega) &\propto I_0(\omega) \sin^2 3\phi. \end{aligned} \quad (4.20)$$

The corresponding two polar plots have a $\pi/3$ angular periodicity and are dephased by an angle $\pi/6$, representing the three-fold rotational symmetry of the crystallographic orientation with respect to the z -axis.

In our experiment, we excite the TMD crystal with linearly polarized intense light under normal incidence and analyze the SHG response with a rotatable linear polarizer oriented parallel to the fundamental polarization angle θ . This results in a six-fold SHG intensity pattern $I_{x'}(2\omega) \equiv I_{\parallel}^{\text{SHG}}$

$$I_{\parallel}^{\text{SHG}} \propto \cos^2 3(\theta - \theta_0), \quad (4.21)$$

where θ_0 is the angle between the armchair axis of the crystal and the defined “laboratory” axis (LAB) (Fig. 4.3). Here, $\theta - \theta_0 = \phi$ defines the angle between the orientation of the incident polarization and the armchair direction. The maxima of the measured

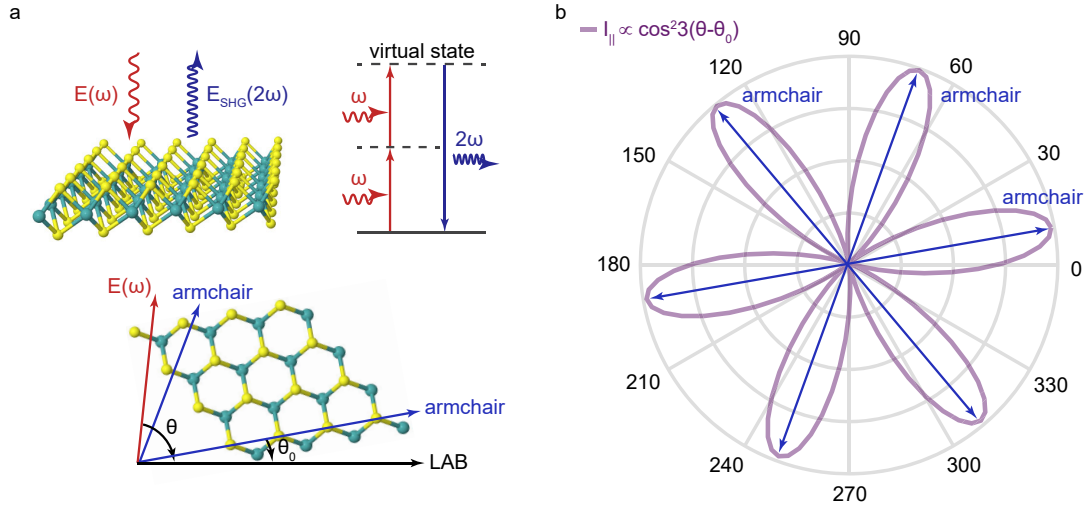


Figure 4.3. **Second harmonic generation (SHG) in transition metal dichalcogenide crystals.** **a**, Schematic representation of the SHG process under non-resonant excitation and orientation of the “laboratory” axis (LAB) in connection with the underlying crystal geometry. **b**, Polar plot of the calculated SHG intensity (parallel to the fundamental polarization angle) from a non-centrosymmetric crystal with D_{3h} ($\bar{6}m2$) point group symmetry (sketched in **a**) as function of the rotation angle, $I_{\parallel}^{\text{SHG}} \propto \cos^2 3(\theta - \theta_0)$.

angle-resolved SHG signal correspond to the armchair direction of the TMD crystal. This allows us to determine the initial lattice orientation of the underlying crystal by rotating the linear polarization in the experiment.

4.2 Microscope design for optical measurements

Our microscope is a modular system, developed to perform various opto-electronic experiments on vdWHs, either at room ($T = 300$ K) or at cryogenic temperature ($T = 4$ K). As illustrated in Fig. 4.4, the microscope system consists of three essential parts, namely the microscope head, the skeleton and the sample holder. With this design, we can easily switch between different optical characterization methods (PL, absorption/reflectivity, etc.) by simply exchanging, or modifying, the microscope head (see Sections 4.2.1 and 4.2.2).

Our free-beam confocal microscope heads are constructed with the following basic scheme (Fig. 4.4a): light excitation and detection are separated into the vertical arm and the lower horizontal arm, respectively. The upper horizontal arm is used for imaging the sample surface. Each arm is attached to the central cage, with the light being directed

via different beam-splitters (BSs). The vertical microscope arm links the external light source (laser, LED, etc.) with the microscope head via an optical fiber. The fiber is aligned with the optical axis of the microscope head using an x/y -translation stage, and the incoming light is collimated with an objective mounted in a z -translation stage. A tilt stage attached at the bottom of the excitation arm corrects for any misalignment of the incoming beam with respect to the optical axis of the microscope skeleton. The lower horizontal microscope arm is designed in a similar way to collect efficiently the light from the sample. The upper horizontal arm is implemented for imaging the the sample surface by focusing the reflected light from the sample onto a camera using an achromatic lens. This specific design structure of the microscope head is simple to align.

The microscope head is placed on top of the skeleton with the microscope objective. The sample itself is fixed onto a separate holder comprised of a set of $x/y/z$ -piezo nano-positioners, as well as a chip carrier with several electrical lines for contacting the sample (Fig 4.4b). For experiments at cryogenic temperatures we use a helium bath cryostat with a 9 T superconducting magnet. For this, the skeleton and sample holder are in-

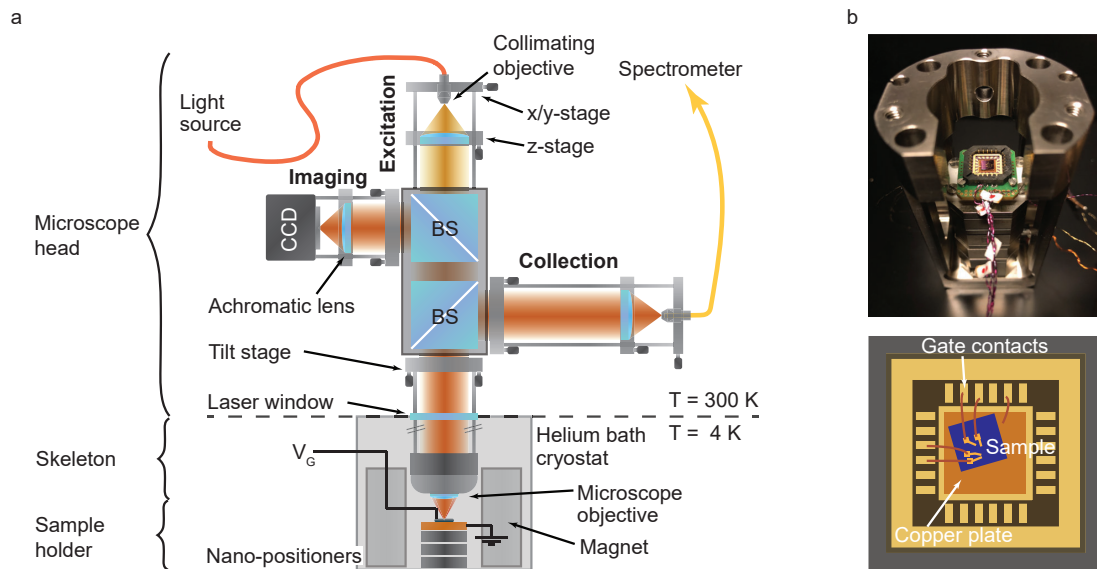


Figure 4.4. **Microscope set-up for opto-electronic experiments on vdWHs.** **a**, The sample and the microscope objective are inside a helium bath cryostat ($T = 4$ K), while the microscope head itself is located at room temperature ($T = 300$ K). For the general microscope head design, the three main parts, the excitation arm, the collection arm and the imaging arm are fixed to a central cage comprised of two beam-splitters (BSs). The microscope is connected to incoming light sources (laser, LED) and to the spectrometer using optical fibers. Microscope head, skeleton and sample holder are indicated in the sketch. **b**, Image of the sample holder (chip carrier and piezo-stack) and sketch of the chip carrier and electrical connections.

serted into a tube, evacuated and filled with ~ 25 mbar of helium exchange gas. We note that all optical elements, except the objective lens, remain under ambient conditions.

In the following Sections 4.2.1 and 4.2.2, we describe the three different microscope head designs for PL, absorption (or reflectivity) and SHG measurements in more detail. Different light sources (continuous-wave laser, LED, pulsed laser) are used for different applications. The optical components, such as lenses, microscope objectives and polarization optics, in the set-ups are selected for specific wavelength ranges depending on both excitation and emission wavelengths (see Appendix C for specifications).

4.2.1 Photoluminescence and reflectivity measurements*

We perform PL measurements using the microscope head, sketched in Fig. 4.5a. For this, we excite the sample either with an orange ($\lambda_{\text{exc}} = 594$ nm, $E_{\text{exc}} = 2.09$ eV) or a red ($\lambda_{\text{exc}} = 633$ nm, $E_{\text{exc}} = 1.96$ eV) HeNe laser[†]. The laser light is coupled into a single-mode (SM) fiber, with its output connected to our home-built microscope head. We use a bandpass filter (for orange light), or a laser line filter combined with a laser clean-up filter (for red light) to suppress any background luminescence originating from the fiber. The laser light is then sent through a linear polarizer (Lin. Pol.) and a computer controlled liquid crystal (LC). The LC can create a $+\lambda/2$ or $-\lambda/2$ retardance of the initial beam upon applying a bias voltage. This generates two perpendicular linear polarizations on demand. In combination with an achromatic quarter-wave plate retarder ($\lambda/4$), we can then switch between circularly polarized light with either right- (σ^+) or left- (σ^-) handed orientation, simply by controlling the voltage on the LC retarder. A high-NA microscope objective (see Appendix C) inside the helium bath cryostat ($T = 4$ K) then focuses the light to a diffraction-limited spot on the sample surface. In our vdWHs, homogeneous regions are typically around a few μm^2 in size (see Chapter 3). A small spot size is therefore crucial for recording optical spectra with transition linewidths close to the homogeneous limit. Piezo-electric nanositioners are used to control the position of the sample with respect to the focal spot. The emitted light from the sample is collected by the same objective, goes again through the $\lambda/4$, and is directed into the collection arm using a 90:10 BS. The combination of another LC and a linear polarizer is used in the collection arm to resolve the circular polarization of the emitted light. The orientation of the LCs in the excitation and collection arm with respect to the $\lambda/4$ plate

*The microscope heads for PL and reflectivity measurements were developed by J. G. Roch.

[†]Depending on the excitation source, the specific filters vary, but the structure of the microscope optics remains the same (see Appendix C for specifications).

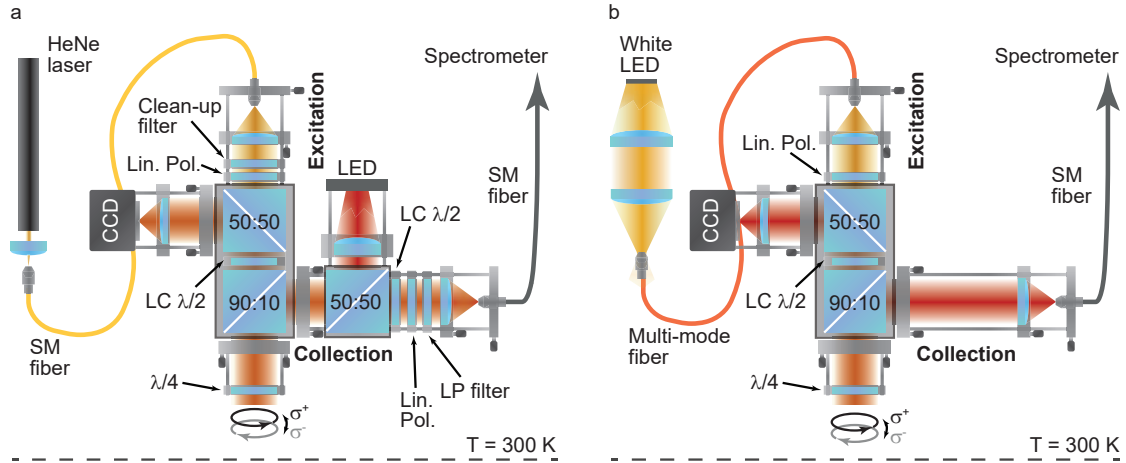


Figure 4.5. **Microscope head.** Design of the microscope head for **a**, photoluminescence (PL) and **b**, reflectivity measurements. In both cases, the microscope head remains under ambient condition, while optical access to the sample is provided by a sealed laser window. The vertical arm is used for excitation, and the optical signal, either PL or reflectivity, is detected via the horizontal arm. The 50:50 beam-splitter (BS) in the collection arm in **a**, together with a separate red LED, is used to image the sample with a CCD camera.

are calibrated in advance using linear polarizers. The light from the sample is then sent through a longpass (LP) filter, to remove any reflected laser light, and is coupled into a SM fiber at the end of the detection arm of our confocal microscope head. The spectra are recorded by a spectrometer equipped with a 300, 600 or 1500 grooves/mm grating and a nitrogen-cooled silicon charge-coupled device (CCD). For initial location of the sample, we temporarily insert a 50:50 BS for illuminating the sample with a red LED and detecting the image using the camera in the upper horizontal arm.

For reflectivity measurements, a slightly modified microscope head (Fig. 4.5b) is used compared to the above described set-up. Here, a broadband white LED (Osram warm white), which covers the full visible wavelength range, is coupled into a multi-mode fiber. Its light is then directed to the sample through nearly the same excitation arm as for the PL measurements. The reflected light is collected from a diffraction limited spot using a SM fiber and sent to the spectrometer. We note that, in contrast to PL measurements, there is no need to filter the polarization of the collected, that is, the reflected light.

4.2.2 Optical second harmonic generation measurements

We perform (polarization-resolved) second harmonic generation (SHG) experiments at room temperature using the confocal microscope set-up depicted in Fig. 4.6. A tunable,

mode-locked titanium sapphire (Ti:Sa) solid-state laser pumped with a semiconductor laser is used to create ultra-short transform-limited femto-second (fs) pulses with a repetition rate of 76 MHz. The optical laser pulse, centered at $\lambda_{\text{exc}} \approx 810$ nm, is coupled into a long optical single-mode fiber connecting the laser source to the microscope head. All the spectral components of the ~ 150 fs pulse are retained; dispersion in the optical fiber stretches the pulse to the pico-second domain at the sample (intensity FWHM 36 ± 10 ps). The incoming light is collimated by an aspheric lens and sent through a linear polarizer. The laser goes first through a longpass dichroic BS and then passes through an achromatic half-wave plate ($\lambda/2$) that rotates the initial polarization of the excitation laser. It is mounted in a computer-controlled stepper motor rotation stage providing both 360° endless rotation and single step rotations with an absolute accuracy of $\pm 0.14^\circ$. The laser is then focused to a spot size of about $1.5 \mu\text{m}$ on the sample by a microscope objective lens (NA = 0.65) at normal incidence. The generated SHG signal (at $\lambda_{\text{exc}}/2 \approx 405$ nm) is collected by the same objective and directed through the dichroic BS to the collection arm. The SHG signal parallel to the excitation polarization $I_{\text{SHG}}^{\parallel}$ is filtered using a polarizing beam-splitter (PBS) as an analyzer, aligned with the linear polarizer in the excitation arm. The SHG signal is then coupled into a single-mode fiber using an aspheric lens and sent to the spectrometer. Again, the left horizontal micro-

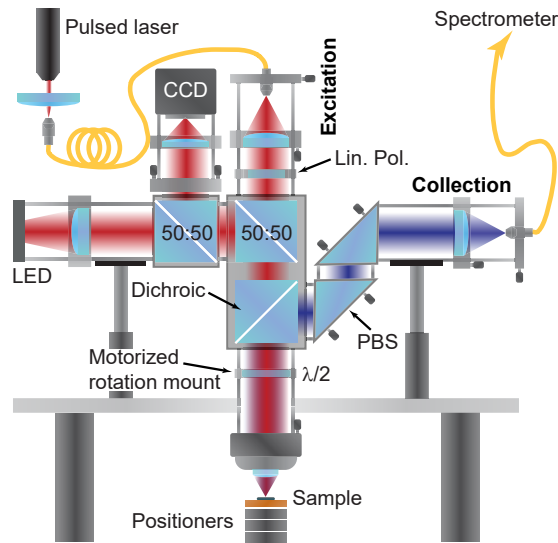


Figure 4.6. **Microscope set-up for (polarization-resolved) second harmonic generation measurements at room temperature.** The vertical arm is used for exciting the sample with a pulsed titanium sapphire (Ti:Sa) laser, while the second-harmonic signal is collected via the horizontal arm. The polarizing beam-splitter (PBS) aligned with the linear polarizer (Lin. Pol.) is used to filter out the desired signal. The red LED and x/y positioners help to locate the sample with a CCD camera.

scope arm provides the possibility of monitoring the sample surface using a red LED and a camera.

As the SHG set-up has to be optimized for two very distinct wavelength ranges in the excitation and collection arm, respectively, its alignment is rather challenging. Additionally, the SHG signal of single-layer TMDs is relatively weak compared to their PL response. To align the microscope, our simple solution is to use the microscope head in reversed direction, that is, sending light from a collimated blue laser diode ($\lambda = 405 \text{ nm}$) through the collection arm and detecting the PL signal from the sample using the excitation arm. In this way, we can operate the SHG set-up as a PL microscope and finely align our microscope head by optimizing the PL signal of the underlying sample.

5

Optical second harmonic generation in indium selenide

The content of this chapter is partially adapted from:

Nadine Leisgang, Jonas G. Roch, Guillaume Froehlicher, Matthew Hamer, Daniel Terry, Roman Gorbachev, and Richard J. Warburton,

“Optical second harmonic generation in encapsulated single-layer InSe”, AIP Advances 8, 105120 (2018).*

5.1 Summary

We report the observation of optical second harmonic generation (SHG) in single-layer indium selenide (InSe). We measure a second harmonic signal of $> 10^3$ cts/s under nonresonant excitation using a home-built confocal microscope and a standard pulsed pico-second laser. We demonstrate that polarization-resolved SHG serves as a fast, non-invasive tool to determine the crystal axes in single-layer InSe and to relate the sharp edges of the flake to the armchair and zigzag edges of the crystal structure. Our experiment determines these angles to an accuracy better than $\pm 0.2^\circ$. Treating the two-dimensional material as a nonlinear polarizable sheet, we determine a second-order sheet polarizability $|\chi_{\text{sheet}}^{(2)}| = (17.9 \pm 11.0) \times 10^{-20} \text{ m}^2 \text{ V}^{-1}$ for single-layer InSe, corresponding to an effective nonlinear susceptibility value of $|\chi_{\text{eff}}^{(2)}| \approx (223 \pm 138) \times 10^{-12} \text{ m V}^{-1}$ accounting for the sheet thickness ($d \approx 0.8 \text{ nm}$). We demonstrate that the SHG technique can also be applied to encapsulated samples to probe their crystal orientations. The method is therefore suitable for creating high quality van der Waals heterostructures with control over the crystal directions.

*The encapsulated InSe sample was fabricated by M.H. and D.T. N.L. performed the SHG measurements on InSe and analyzed the data. N.L. and S.S. measured the CVD-grown MoS₂ samples and interpreted the corresponding data.

5.2 Introduction to SHG in 2D materials

Since the isolation of graphene by mechanical exfoliation [5], leading, inter-alia, to the discovery of the quantum Hall effect in graphene [94], two-dimensional (2D) materials, such as atomic layers of transition metal dichalcogenides (TMDs) (e.g. MoS₂, MoSe₂, WS₂ and WSe₂) and III–IV compounds (e.g. GaS, GaSe) have attracted great attention in materials research on account of their tunable electronic and optical properties [4, 95]. The ability to combine the 2D layers with hexagonal boron nitride (hBN) and few-layer graphene offers an opportunity of creating high-performance, 2D opto-electronic devices [75, 96].

The desire to stack different 2D materials with precise control over the twist-angle [97–100] creates a need for a fast, non-invasive tool to probe the underlying crystal symmetries and crystallographic orientations. Nonlinear optical techniques, such as second harmonic generation (SHG), provide insight into the properties of surfaces or interfaces [89], particularly among non-centrosymmetric materials. SHG has been observed in single- and few-layer TMDs, such as MoS₂ [101, 102] and WS₂ [103], and has been used to align the crystal axes of various TMDs in order to create high-quality heterobilayers with strong interlayer exciton emission [33, 104]. However, TMD flakes with an

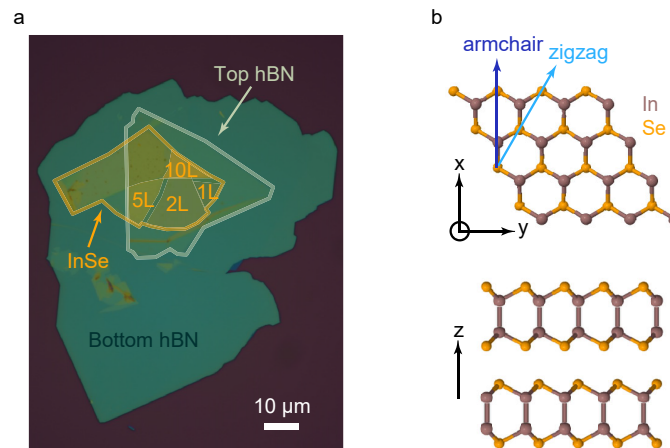


Figure 5.1. **Indium selenide (InSe).** **a**, Optical image of the InSe flake. The indicated layer thicknesses were determined by optical contrast and verified by atomic force microscopy and photoluminescence measurements. Second harmonic generation measurements were carried out on the parts of the InSe flake which are fully encapsulated in hBN. The device consists of SiO₂ (290 nm)/hBN (46 nm)/InSe/hBN (8 nm). **b**, Schematic of the InSe crystal structure (top and side view). Purple and orange spheres correspond to indium (In) and selenium (Se) atoms, respectively.

even number of layers exhibit inversion symmetry, resulting in a vanishing second-order nonlinearity ($\chi^{(2)} = 0$) which prevents the observation of SHG for all layer thicknesses.

Among the large family of van der Waals (vdW) crystals, indium selenide (InSe) has emerged as a promising 2D semiconductor due to its highly tunable optical response in the near-infrared to the visible spectrum [105] and its high electron mobilities at room and liquid-helium temperatures allowing the quantum Hall effect to be observed [106]. Similar to the TMDs, single-layer InSe belongs to the non-centrosymmetric D_{3h} ($\bar{6}m2$) point group with only one independent non-zero second-order nonlinear susceptibility tensor element. The susceptibility components satisfy $\chi_{xxx}^{(2)} = -\chi_{xyy}^{(2)} = -\chi_{yyx}^{(2)} = \chi_{yxy}^{(2)}$ with x along the armchair direction (Fig. 5.1b) [89]. In contrast, the specific stacking order in bulk and few-layer InSe breaks the mirror-plane symmetry characteristic of single-layer InSe, thus maintaining broken inversion symmetry for all layer thicknesses. This provides an opportunity to investigate nonlinearities in thin InSe films layer-by-layer. The dependence of polarization-resolved SHG on the crystallographic axes further opens up an optical means of characterizing the crystal structure and orientation of the thin InSe films. Indeed, observations of SHG in relatively thin InSe sheets (from 9 to 25 nm) with even and odd number of layers have been reported recently [107]. However, in the single-layer limit and under non-resonant condition, it remains elusive whether SHG signal can still be detected. In this chapter, we present SHG from encapsulated single- and few-layer InSe with the aim of determining the crystal axes and estimating the effective second-order nonlinear susceptibility of the single-layer.

5.3 SHG response of single- and few-layer InSe flakes

Fig. 5.1a shows an optical image of the sample used to investigate the SHG response of thin InSe flakes*. SHG spectroscopy was performed at room temperature using a home-built, confocal microscope set-up (see Chapter 4 for a detailed description of the experimental set-up). As shown in Fig. 5.2, an easy-to-measure SHG signal ($> 10^3$ cts/s) appeared at wavelength 405 nm when the laser beam (wavelength 810 nm) was focussed on encapsulated single- and few-layer InSe. Moreover, the SHG response could be observed for both even and odd number of layers. No observable SHG signal was measured on hBN. The integrated SHG signal increases by more than two orders of magnitude as the thickness of the InSe flake increases from 1 to 10 layers (Fig. 5.2b). Specifically, the SHG signal depends approximately quadratically on the layer thickness, i.e. $I_{\text{SHG}}(2\omega) \propto d^2$, as shown in Fig. 5.2b where the integrated SHG intensity $I_{\text{SHG}}(2\omega)$ of the

*The encapsulated InSe sample was fabricated by M.H. and D.T. at the University of Manchester.

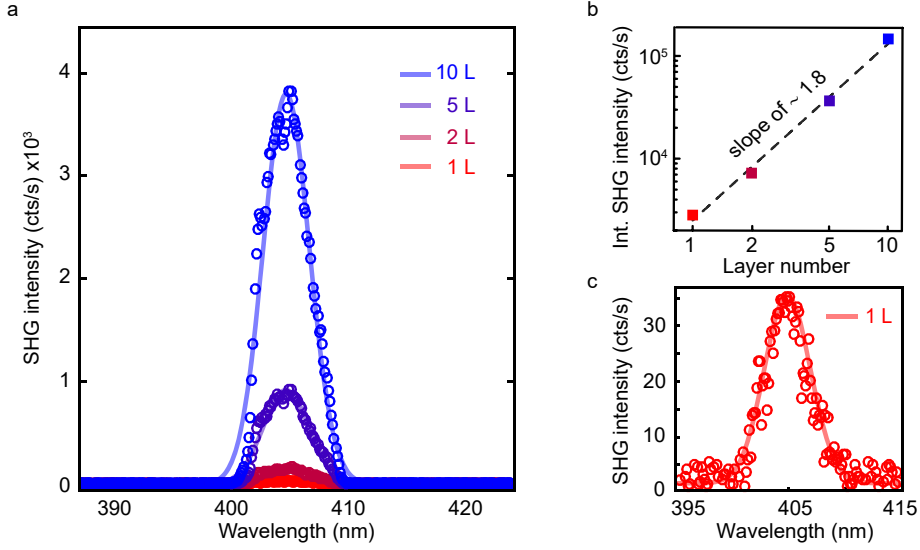


Figure 5.2. **Second harmonic generation (SHG) of encapsulated single- and few-layer InSe.** **a**, SHG spectra of single- and few-layer InSe at room temperature. **a**, Fitted data points (plotted on a double logarithmic scale) show the approximately quadratic increase (slope of ~ 1.8) of the integrated SHG with the number of layers. The error bars are smaller than the symbol size. **c**, SHG spectrum of encapsulated single-layer InSe.

InSe flakes is plotted versus the layer number N (with $d \approx N \times 0.8$ nm) on a logarithmic scale. Following Ref. [108], the dependence of the SHG intensity on the flake thickness is given by

$$I_{\text{SHG}}(2\omega) \propto (l_c |\chi_{\text{eff}}^{(2)}|)^2 \sin^2 \left(\frac{\pi d}{2l_c} \right) \quad (5.1)$$

where d is the flake thickness, $l_c = 2\pi/\Delta k \approx 20$ μm is the coherence length between the pump and the SH signal and $|\chi_{\text{eff}}^{(2)}|$ is the effective nonlinear susceptibility determined by the sample geometry and the non-zero components of the nonlinear sheet susceptibility tensor $\chi_{\text{sheet}}^{(2)}$ ($|\chi_{\text{eff}}^{(2)}| = |\chi_{\text{sheet}}^{(2)}|/d$). Thus, in the limit of atomically thin films (i.e. $d \ll l_c$), the SHG intensity $I_{\text{SHG}}(2\omega)$ is expected to increase quadratically with the number of layers, in good agreement with our observations (Fig. 5.2b).

5.4 Polarization-resolved SHG of single-layer InSe

The relatively strong SHG signal facilitates an investigation of the lattice symmetry and crystallographic orientation of the thin flakes. The SHG intensity $I_{\text{SHG}}(2\omega)$ is strongly dependent on the polarization angle $(\theta - \theta_0)$ between the laser polarization $\mathbf{E}(\omega)$ and the

armchair direction of the crystal defined in Fig. 5.3b (see Chapter 4). For polarization-resolved SHG, the laser polarization was rotated about the z -axis by a half-wave plate to vary θ , and the SHG signal $I_{\text{SHG}}^{\parallel}(2\omega)$ (SHG polarization parallel to the excitation polarization) was collected using an analyzer located in front of the detector. The polar plot for single-layer InSe in Fig. 5.3a shows a strongly varying 6-fold symmetry of $I_{\text{SHG}}^{\parallel}(2\omega) \propto \cos^2 3(\theta - \theta_0)$. This directly reveals the underlying symmetry and orientation of the single-layer InSe flake. The initial orientation of the sample with respect to the armchair direction of the crystal was determined to be $\theta_0 = 28.1^\circ \pm 0.2^\circ$. The sharp edges along which the single-layer InSe flake cleaved during exfoliation could therefore be clearly assigned to the armchair and zigzag crystal axes, respectively (Fig. 5.3b).

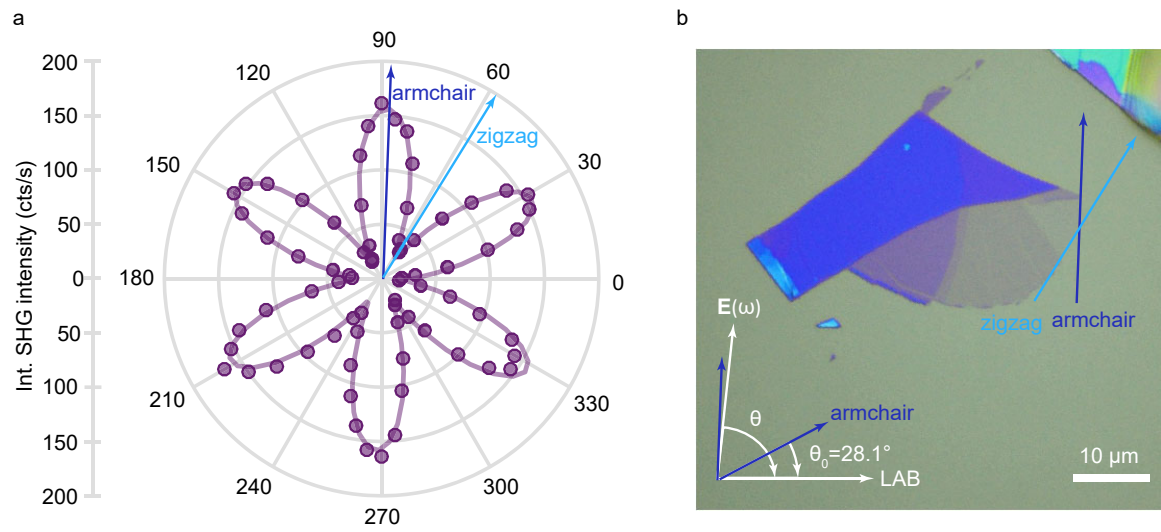


Figure 5.3. **Polarization-resolved second harmonic generation (SHG) of encapsulated single-layer InSe.** **a**, Polar plot of the “parallel” SHG intensity $I_{\text{SHG}}^{\parallel}(2\omega)$ of single-layer InSe as a function of rotation angle θ . Fitting the angular dependence to $I_{\text{SHG}}^{\parallel}(2\omega) \propto \cos^2 3(\theta - \theta_0)$ (solid purple line), the armchair direction (dark blue arrow) of the sample is determined as $\theta_0 = 28.1^\circ \pm 0.2^\circ$. This armchair direction is 30° from the zigzag direction (light blue arrow). **b**, Optical image of the InSe flakes before encapsulation. The armchair direction forms an angle θ_0 with respect to the “laboratory” axis (LAB). The indicated armchair (dark blue arrow) and zigzag (light blue arrow) edges were determined by polarization-resolved SHG performed on the encapsulated sample.

5.5 Second-order nonlinear sheet susceptibility

5.5.1 Relationship between generated second harmonics and nonlinear sheet susceptibility

To quantify the nonlinear response of single-layer InSe, we follow the formalism of Ref. [109]. SHG from a thin layer is treated as radiation from a nonlinear, polarizable sheet embedded in a dielectric medium, with boundary effects taken into account by Fresnel transmission coefficients.

We consider the simple case depicted in Fig. 5.4. The incoming pump light $\mathbf{E}(\omega)$ generates a nonlinear polarization wave at frequency 2ω within the polarizable sheet (a layer of radiating dipoles) on top of a substrate (Fig. 5.4a). Following Ref. [109], the nonlinear susceptibility of the thin layer can be modelled by a δ -function, with $\chi^{(2)} = \chi_{\text{sheet}}^{(2)} \cdot \delta(z)$, due to its atomic thickness, and the nonlinear polarizable sheet can be described by

$$\mathbf{P}_{\text{sheet}}^{(2)} = P_{\text{sheet}}^{(2)} \delta(z) e^{i(\mathbf{k}\mathbf{r} - \omega t)} \hat{\mathbf{r}}, \quad (5.2)$$

with \hat{x} - \hat{z} being the plane of incidence. The radiation field generated by $\mathbf{P}_{\text{sheet}}^{(2)}$ is then obtained from the solution of the wave equation

$$\nabla^2 \mathbf{E} + \frac{\epsilon}{c^2} \frac{\partial^2 \mathbf{E}}{\partial t^2} = -\frac{1}{\epsilon_0 c^2} \frac{\partial^2 \mathbf{P}_{\text{sheet}}^{(2)}}{\partial t^2}. \quad (5.3)$$

The \hat{p} - and \hat{s} -polarized components of the radiation field in medium 1 (air) coming from the nonlinear polarizable sheet at frequency ω_{sheet} are then given by

$$\mathbf{E}_p(\omega_{\text{sheet}}) = \frac{ik_1}{2\epsilon_1 k_{1z}} (k_{1z} t_{xx} P_{\text{sheet},x}(\omega_{\text{sheet}}) \hat{x} + k_x t_{zz} P_{\text{sheet},z}(\omega_{\text{sheet}}) \hat{z}) e^{i(\mathbf{k}\mathbf{r} - \omega t)} \quad (5.4)$$

$$\mathbf{E}_s(\omega_{\text{sheet}}) = \frac{ik_1^2}{2\epsilon_1 k_{1z}} t_{yy} P_{\text{sheet},y}(\omega_{\text{sheet}}) \hat{y} e^{i(\mathbf{k}\mathbf{r} - \omega t)}.$$

$P_{\text{sheet},x}$, $P_{\text{sheet},y}$, $P_{\text{sheet},z}$ are the nonlinear sheet polarization components induced at the interface, and ϵ_1 is the dielectric constant of medium 1 (air). Here, we have used $\mathbf{E}(\omega_{\text{sheet}}) = \mathbf{t} \cdot \mathbf{E}_0(\omega_{\text{sheet}})$, where $\mathbf{E}_0(\omega_{\text{sheet}})$ accounts for the radiation from the polarizable sheet in the absence of any boundary surfaces. $\mathbf{t} = (t_{xx}, t_{yy}, t_{zz})$ are the macroscopic local field correction factors, or Fresnel transmission coefficients, relating the field components in medium 1 (air) to the corresponding ones in the polarizable sheet

$$t_{xx} \equiv \left(\frac{E_p}{E_{p,0}} \right)_x, \quad t_{yy} \equiv \left(\frac{E_s}{E_{s,0}} \right)_y, \quad t_{zz} \equiv \left(\frac{E_p}{E_{p,0}} \right)_z. \quad (5.5)$$

For normal incidence on the sample (along \hat{z}), the P_z -terms are negligible and $E_p = E_s \equiv E$ ($t_{xx} = t_{yy} \equiv t$). The radiated field from the thin sheet back into medium 1 (air) is then given by [109]

$$E(\omega_{\text{sheet}}) = \frac{i\omega_{\text{sheet}}}{2c\epsilon_0} t_{\text{out}}(\omega_{\text{sheet}}) P_{\text{sheet}}(\omega_{\text{sheet}}) e^{i(k_1 z - \omega_{\text{sheet}} t)} \quad (5.6)$$

with

$$P_{\text{sheet}}(\omega_{\text{sheet}}) = \epsilon_0 |\chi_{\text{sheet}}^{(2)}| E_{\text{sheet}}^2(\omega) = \epsilon_0 |\chi_{\text{sheet}}^{(2)}| (t_{\text{in}}(\omega) E(\omega))^2. \quad (5.7)$$

$t_{\text{in}}(\omega)$ relates the incident field in the sheet $E_{\text{sheet}}(\omega)$ to the input field in free space $E(\omega)$ (Fig 5.4b), and $|\chi_{\text{sheet}}^{(2)}|$ is the second-order nonlinear sheet susceptibility.

Now, considering the case where $P_{\text{sheet}}(\omega_{\text{sheet}})$ is the nonlinear polarization at $\omega_{\text{sheet}} = 2\omega$ induced by an incoming field at ω from medium 1 (air), the generated second harmonic field amplitude can be written as

$$E_{\text{SHG}}(\omega_{\text{sheet}} = 2\omega) = \frac{2\omega}{2c} t_{\text{out}}(2\omega) |\chi_{\text{sheet}}^{(2)}| t_{\text{in}}^2(\omega) E^2(\omega). \quad (5.8)$$

Relating the field amplitude (in air) to an optical intensity by $I = 2c\epsilon_0 E^2$ leads to a

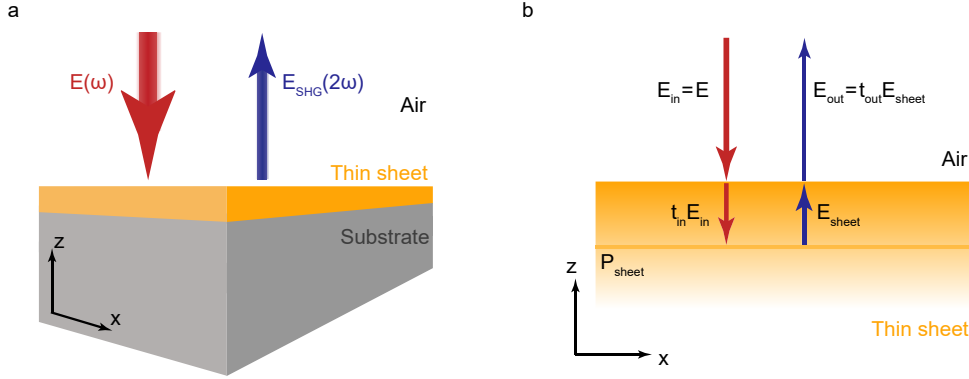


Figure 5.4. **Second harmonic generation from a thin sheet.** **a**, Illustration showing the second harmonic generated field from a nonlinear polarizable sheet under intense light illumination. $E(\omega)$ and $E_{\text{SHG}}(2\omega)$ denote the incoming field and the generated second harmonic field. **b**, Simplified geometry of the SHG from a thin polarizable sheet P_{sheet} at normal incidence. Incoming field E_{in} , generated radiation field within the layer E_{sheet} and field transmitted back into air are related by Fresnel transmission coefficients t_{in} and t_{out} .

second harmonic intensity

$$I_{\text{SHG}}(2\omega) = \frac{\omega^2}{2c^3\epsilon_0} t_{\text{out}}^2(2\omega) |\chi_{\text{sheet}}^{(2)}|^2 t_{\text{in}}^4(\omega) I^2(\omega) \quad (5.9)$$

which further needs to be converted into a time-averaged power P , as measured experimentally. For a pulsed laser with pulse duration Δt and repetition rate $1/T$, the peak intensity (determining the nonlinear effect), can be expressed by

$$I_{\text{peak}} = \frac{P_{\text{peak}}}{\pi w^2/2} \quad \text{with } P_{\text{peak}} = P \frac{T}{\Delta t}, \quad (5.10)$$

with P_{peak} being the peak power and w being the size of the focused fundamental spot on the sample. Since the second-order nonlinear polarization is generated proportional to the square of the fundamental light intensity, the shape and duration of the emitted second harmonic field is reduced by a factor of $\sqrt{2}$. This leads to

$$P_{\text{SHG}}(2\omega) = \frac{\sqrt{2}\omega^2}{4c^3\epsilon_0} \frac{T}{\Delta t \pi w^2} t_{\text{out}}^2(2\omega) |\chi_{\text{sheet}}^{(2)}|^2 t_{\text{in}}^4(\omega) P^2(\omega) \quad (5.11)$$

for the generated harmonic signal $P_{\text{SHG}}(2\omega)$ as a function of the average input power $P(\omega)$. Finally, for a fixed input power, the second order nonlinear sheet susceptibility can be estimated via

$$|\chi_{\text{sheet}}^{(2)}| = \left(\frac{4c^3\epsilon_0}{\sqrt{2}\omega^2} \frac{\Delta t \pi w^2}{T} \frac{1}{t_{\text{out}}^2(2\omega) t_{\text{in}}^4(\omega)} \frac{P_{\text{SHG}}(2\omega)}{P^2(\omega)} \right)^{\frac{1}{2}}. \quad (5.12)$$

For better comparison, we can describe the nonlinear sheet susceptibility by an effective bulk-like nonlinear susceptibility

$$|\chi_{\text{eff}}^{(2)}| = \frac{|\chi_{\text{sheet}}^{(2)}|}{d} \quad (5.13)$$

including the thickness of the nonlinear material $d \approx N \times 0.8 \text{ nm}$, where N is the number of layers and $\sim 0.8 \text{ nm}$ is the thickness of a single layer. Thus, the second harmonic intensity depends quadratically on the number of layers

$$\begin{aligned} I_{\text{SHG}}(2\omega) &= \frac{\omega^2}{2c^3\epsilon_0} t_{\text{out}}^2(2\omega) |\chi_{\text{sheet}}^{(2)}|^2 t_{\text{in}}^4(\omega) I^2(\omega) \\ &\propto d^2 |\chi_{\text{eff}}^{(2)}|^2 I^2(\omega). \end{aligned} \quad (5.14)$$

5.5.2 Experimental estimate of the nonlinear sheet susceptibility

As derived above, the second-order susceptibility $|\chi_{\text{sheet}}^{(2)}|$ of InSe can be extracted from measurements of the intensity of the SHG with respect to the driving intensity via Eq. 5.14. Experimentally, due to the nonlinear nature of the second harmonic process, the estimation of $|\chi_{\text{sheet}}^{(2)}|$ (Eq. 5.12) relies on the accurate determination of many experimental parameters, such as the shape and duration of the fundamental pulse, the shape and size of the focused fundamental spot on the sample, and the relation between the measured spectral counts and the actual SHG power, as well as the above introduced local field correction factors (Fresnel transmission coefficients). In our experiment, $t_{\text{in}}(\omega)$ and $t_{\text{out}}(2\omega)$ at normal incidence, accounting for the dielectric environment, are determined by the transfer matrix method (“Essential Macleod”) (see Appendix D for simulations).

Relating the laser intensity $I(\omega)$ and the SHG intensity $I_{\text{SHG}}(2\omega)$ in Eq. (5.12) to the experimentally measured time-averaged power values, we obtain $|\chi_{\text{sheet}}^{(2)}| = (17.9 \pm 11.0) \times 10^{-20} \text{ m}^2 \text{ V}^{-1}$ for single-layer InSe. To compare to other nonlinear optical bulk materials, we estimate an effective bulk-like nonlinear susceptibility $|\chi_{\text{eff}}^{(2)}| = (223 \pm 138) \times 10^{-12} \text{ m V}^{-1}$ by including the thickness of the 2D material ($d \approx 0.8 \text{ nm}$). This value is similar to the strong second-order optical susceptibility measured for single- and few-layer GaSe [110].

5.6 Conclusion and outlook

5.6.1 Nonlinear response of single- and few-layer InSe

In conclusion, we report an observation of SHG in single-layer InSe under nonresonant excitation with respect to the optical transition at 1.25 eV, yielding a nonlinear sheet susceptibility with an estimated value of $|\chi_{\text{eff}}^{(2)}| \approx 223 \text{ pm V}^{-1}$. Quantitative characterization of the nonlinear response of single- and few-layer InSe reveals the expected quadratic dependence of the SHG signal on the number of layers. The crystalline symmetry was probed by polarization-resolved SHG where the “petal” direction with maximum signal is parallel to the in-plane In-Se or Se-In (armchair) direction. This allowed for a fast and precise ($\pm 0.2^\circ$) assignment of the sharp edges of the InSe flake to its crystal axes, demonstrating that SHG serves as useful tool for the determination of the orientation of the material’s crystallographic axes. This is not only the case for InSe, but also for other TMD monolayers which exhibit a broken inversion symmetry.

5.6.2 Accessing the crystal structure and orientation in TMDs

The ability to distinguish different crystallographic axes, even in encapsulated samples, can be exploited to improve the quality of vdWHs by stacking various 2D materials with precise twist-angle control. Especially, when building heterostructures from individual TMD monolayers, the relative alignment (twist-angles) of the crystals with different lattice constants has a significant impact on the quality of the coupling between the layers, as well as moiré and reconstruction effects [48, 100, 111, 112]. In TMD multilayers, the layer-dependent SHG response can be used further to determine the stacking order [113]. Fig. 5.5a presents an optical microscope image of MoS₂ bilayers with 2H (180° twist-angle) and 3R (0° twist-angle) stacking grown by chemical vapor deposition (CVD) onto a Si/SiO₂ substrate. For conventional centrosymmetric 2H-phase TMDs, the SHG

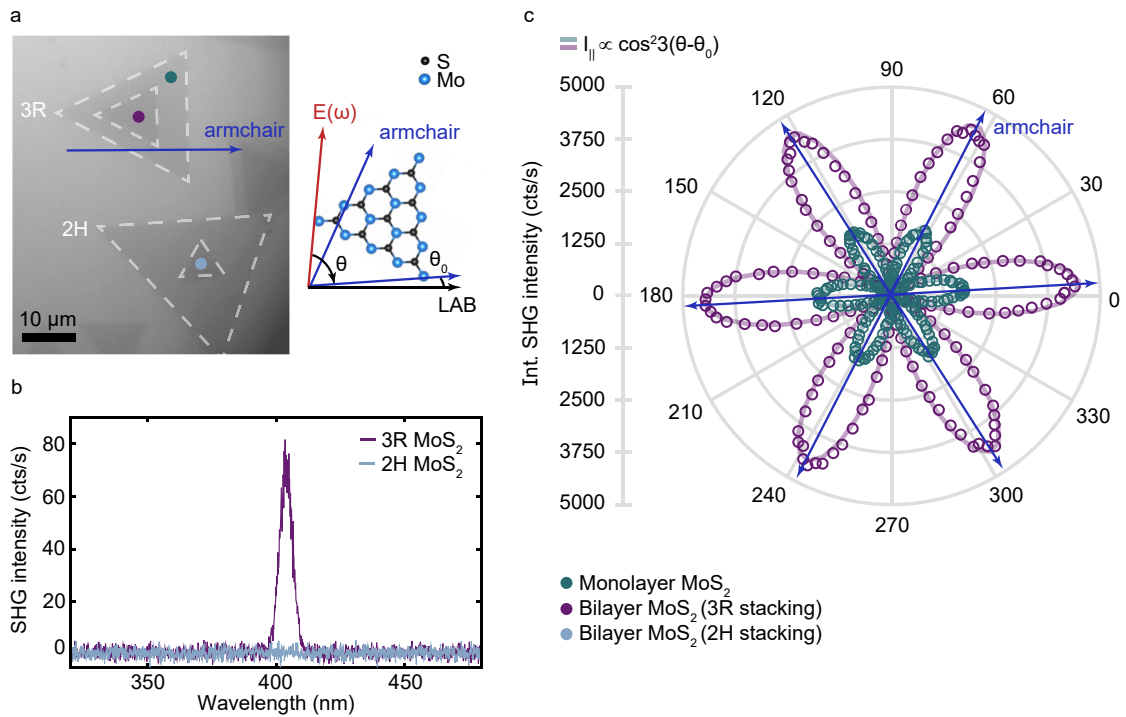


Figure 5.5. **Second harmonic generation (SHG) in MoS₂ bilayers with 2H- and 3R-stacking.** **a**, Optical microscope image of 2H and 3R CVD-grown MoS₂ bilayers (left). Colored dots indicate the positions for the SHG measurements in **b** and **c**. Schematic representation of the crystallographic orientation (right). **b**, SHG signal of 2H- and 3R-stacked bilayer MoS₂ at room temperature. A strong SHG response is observed for 3R-stacking (purple), while no signal can be detected for 2H-stacking (light-blue) (inversion symmetry restored) (see also Chapter 2). **c**, Polar plot of the polarized SHG signal of CVD-grown 3R-bilayer MoS₂ (purple) revealing the same symmetry as in the single layer (green).

signal is quenched for an even number of layers due to the lack of inversion symmetry. Therefore, no SHG signal can be detected for the natural 2H-stacking order* (Fig 5.5b). On the other hand, in the 3R-stacking, the individual layers are stacked with 0° twist-angle with respect to each other. Consequently, the non-centrosymmetric nature of the single layer is preserved for all number of layers. The polar plot of 3R MoS₂ bilayer in Fig. 5.5c directly reveals the stacking order and the crystallographic orientation of the bilayer. SHG spectroscopy therefore allows a clear distinction between 3R- and 2H-stacked bilayers and serves as an efficient tool for determining the crystallographic orientation in TMD layers.

*We emphasize that the SHG response is recorded under off-resonant excitation with respect to the optical transitions in bilayer MoS₂. Excitation on resonance with an excitonic transition can drastically enhance the SHG signal [90], and SHG can even be observed in 2H-stacked bilayer MoS₂ when tuned into resonance with the interlayer exciton transition around 2.00 eV (at zero electric field) [91].

6

Quantum confined Stark effect in a MoS₂ monolayer van der Waals heterostructure

The content of this chapter is partially adapted from:

Jonas G. Roch, Nadine Leisgang, Guillaume Froehlicher, Kenji Watanabe, Takashi Taniguchi, Peter Makk, Christian Schönenberger, and Richard J. Warburton,

“Quantum confined Stark effect in a MoS₂ monolayer van der Waals heterostructure”, Nano Letters **18**, 1070–107 (2018).*

6.1 Summary

The optics of dangling-bond-free van der Waals heterostructures containing transition metal dichalcogenides are dominated by excitons. A crucial property of a confined exciton is the quantum confined Stark effect (QCSE). Here, such a heterostructure is used to probe the QCSE by applying a uniform vertical electric field across a molybdenum disulfide (MoS₂) monolayer. The photoluminescence emission energies of the neutral and charged excitons shift quadratically with the applied electric field provided the electron density remains constant, demonstrating that the exciton can be polarized. Stark shifts corresponding to about half the homogeneous linewidth were achieved. Neutral and charged exciton polarizabilities of $(7.8 \pm 1.0) \times 10^{-10} \text{ D}\cdot\text{m}\cdot\text{V}^{-1}$ and $(6.4 \pm 0.9) \times 10^{-10} \text{ D}\cdot\text{m}\cdot\text{V}^{-1}$ at relatively low electron density ($\sim 10^{12} \text{ cm}^{-2}$) have been extracted, respectively. These values are one order of magnitude lower than the previously reported values but in line with theoretical calculations. The methodology presented here is versatile and can be applied to other semiconducting layered materials.

*J.G.R. and N.L. fabricated the gated monolayer MoS₂ devices. J.G.R. and N.L. measured the main (QCSE) device and analyzed the corresponding data. J.G.R. and G.F. investigated the reference sample. N.L. and L.S. fabricated the heterobilayer devices and performed and analyzed the measurements on interlayer excitons in MoSe₂/WSe₂ heterobilayers at low temperature.

6.2 Introduction

The recent emergence of optically active layered semiconductors [3, 7], such as molybdenum disulfide (MoS₂), and of the so-called van der Waals heterostructures (vdWHs) [60, 61], pave the way toward engineered quantum structures. Excitons in MoS₂ and other transition metal dichalcogenides (TMDs) have particularly large exciton binding energies [12], such that excitons dominate the optical properties, even at room temperature. Therefore, the fundamental properties of the excitons need to be elucidated. A basic feature of semiconductor nanostructures is the quantum confined Stark effect (QCSE), the change in optical response on applying an electric field perpendicular to the layers [114]. On the one hand, the QCSE characterizes the sensitivity of the exciton energy to charge noise as charge noise results in a fluctuating electric field within the device. The QCSE is therefore important in optimizing and understanding optical linewidths. On the other hand, the QCSE can be exploited to trap and manipulate excitons on the nanoscale by applying a locally varying vertical electric field [115, 116].

6.2.1 Concept of the quantum confined Stark effect in monolayer MoS₂

When a static electric field is applied perpendicular to a MoS₂ monolayer (z -axis), electrons and holes will tend to move apart to decrease their electrostatic potential energy. The resulting energy shift ΔE of the exciton energy is known as the QCSE and is given by

$$\Delta E = -\mu_z F_z - \beta_z F_z^2, \quad (6.1)$$

where F_z is the component of the electric field, μ_z the excitonic dipole moment and β_z the excitonic polarizability along the z -direction. Owing to the reflection symmetry about the molybdenum plane, $\mu_z = 0$ in a MoS₂ monolayer embedded in a symmetric dielectric environment [117] such that the QCSE is expected to be quadratic in F_z . Measurement of the Stark shift of the A exciton in a MoS₂ monolayer has been reported [118]. However, the experiment was performed on monolayers encapsulated in standard oxides (aluminium and silicon oxides) which have poor optical quality and, most probably, contain a significant density of charge traps [119]. Lately, a theoretical study [120] has predicted β_z to be more than one order of magnitude below the reported experimental value. An unambiguous measure of the QCSE in MoS₂ is therefore missing. A particular challenge is that the exciton energies depend strongly on the electron density in the MoS₂ monolayer (see Chapter 8) [121]. Furthermore, the description of the optical excitations in the high-density regime has a strong many-electron flavor: the

quasi-particles are no longer the simple excitons [122, 123]. These considerations mean that the QCSE should be measured at a low and constant electron density.

6.2.2 A high-quality MoS₂ monolayer van der Waals heterostructure

High-quality MoS₂ monolayers, obtained by encapsulation in hexagonal boron nitride (hBN), are used to determine precisely the QCSE of the neutral X^0 and negatively charged X^- A excitons. The photoluminescence (PL) spectra of these samples show narrow linewidths (~ 8 meV), close to the ideal limit ($1 - 2$ meV [72]), allowing the X^0 and X^- to be identified unambiguously. Both spectral features shift when applying an electric field. However, at the same time, the ratio between the integrated intensities of X^- and X^0 varies. The change in this ratio signifies a change in the electron density, which, in turn, shifts the emission energies (see Chapter 8). To separate carefully QCSE and doping contributions to the energy shifts, additional measurements were performed on a directly contacted MoS₂ device. These measurements quantify precisely both the X^- to X^0 intensity ratio and the exciton energy shifts as a function of the electron density. We use this information to find a region in the encapsulated device where the electric field can be changed at a constant and relatively low electron density*. In this

*We note that independent control of the carrier concentration n and the electric field F_z in the device was lacking at this point.

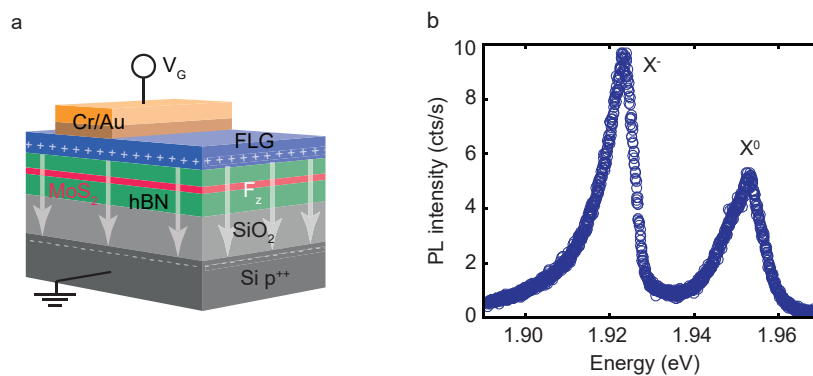


Figure 6.1. **Monolayer MoS₂ van der Waals heterostructure.** **a**, Three-dimensional schematic view of the device used to measure the quantum confined Stark effect. The device consists of a MoS₂ monolayer sandwiched between two layers of hBN and covered by a FLG top electrode, deposited onto a highly p-doped Si/SiO₂ substrate. A voltage V_G is applied between the Si substrate and the top electrode to create a uniform electric field F_z across the MoS₂. **b**, Typical PL spectrum recorded without an applied gate voltage $V_G = 0$ V at $T = 4$ K ($E_{exc} = 2.09$ eV, $I_{exc} < 2$ kW/cm²). The neutral X^0 and negatively charged X^- exciton are labelled.

region, we demonstrate a clear QCSE. We determine excitonic polarizabilities typically one order of magnitude smaller than the values reported in Ref. [118] but in good agreement with calculations in Ref. [120].

6.3 Energy tuning of excitons in monolayer MoS₂

The QCSE was measured using the encapsulated device with geometry as depicted in Fig. 6.1a: two thick hBN layers are used as dielectric spacers and the top few-layer graphene (FLG) acts as a transparent electrode (see Appendix B for a description of the fabrication process). Applying a DC voltage V_G between the FLG and the highly doped bottom Si substrate creates a uniform electric field in the MoS₂ monolayer, oriented perpendicular to the basal plane of the sample. Fig. 6.2a shows typical PL spectra recorded at 4 K over a voltage loop as illustrated in Fig. 6.2b: V_G varies from the initial state (S_1) at -85 V to $+85$ V (S_3) via S_2 (0 V) and then back to S_1 via S_4 (0 V). Two prominent features can be clearly identified (see Fig. 6.1b): a low-energy peak near 1.92 eV and a high-energy peak near 1.95 eV attributed to the negatively charged X^- and the neutral X^0 A excitons [1, 72], respectively. The emission energies of X^- and X^0 change with V_G , as seen in Fig. 6.3a, where the X^0 energy has been plotted. However, as demonstrated in the color map in Fig. 6.2a, the intensities of the X^- and X^0 features also vary with V_G . The ratio between the integrated PL intensities of X^- and X^0 , $I(X^-)/I(X^0)$ (Fig. 6.3b), cannot be explained by the QCSE as it depends on the gate voltage sweep direction. Instead, the change in relative intensity arises from a change

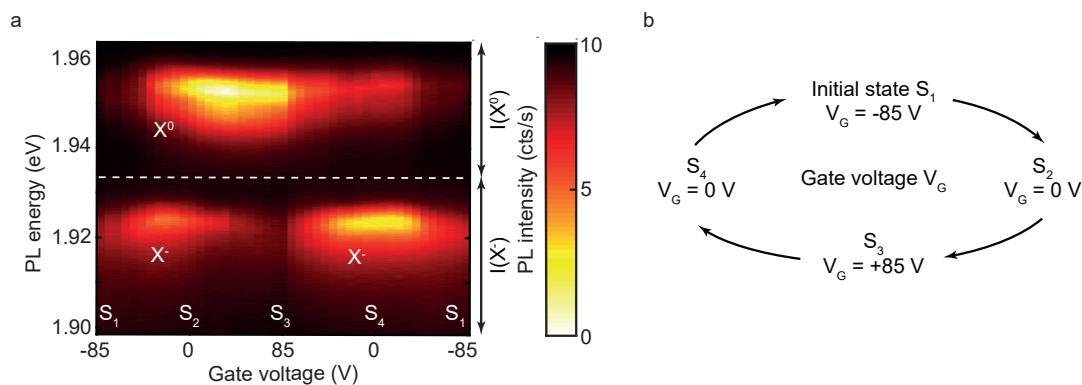


Figure 6.2. **Electrical tunability in monolayer MoS₂.** **a**, Color map of the PL spectra of MoS₂ as a function of V_G . The neutral X^0 and negatively charged X^- excitons and the four states defined in **b** are labelled. **b**, The gate voltage V_G in the device is varied along a loop from state S_1 (-85 V) to S_3 ($+85$ V) and back, reaching $V_G = 0$ twice (states S_2 and S_4).

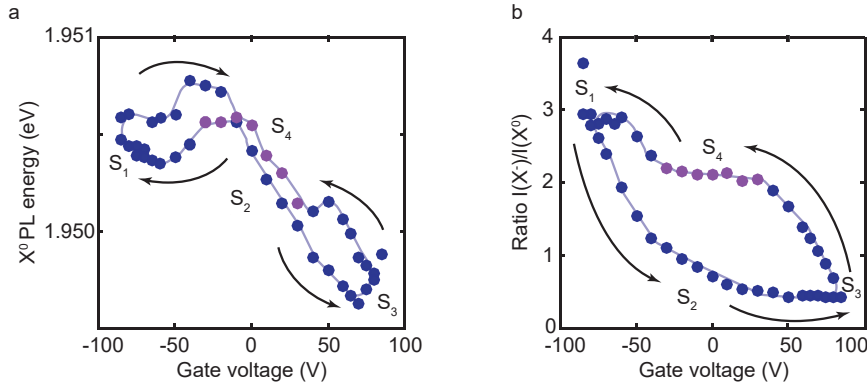


Figure 6.3. **Hysteresis in monolayer MoS₂.** **a**, Emission energy of X^0 as a function of V_G . The experimental data points extracted from the spectra in 6.2a are represented by circles where the purple circles correspond to the data used to measure the Stark shift. The solid line is a guide to the eye and the black arrows indicate the changes made to V_G . **b**, Ratio between the integrated intensity of the X^- and X^0 features extracted from the data in 6.2a as a function of V_G . The range of integration is indicated by the black double-headed arrows in 6.2a.

in the electron density [124]. The noticeable hysteresis appearing in Fig. 6.3 reflects the fact that the electron density depends on the direction of the voltage sweep. The hysteresis, not the focus of the present investigation, arises as a combined consequence of photodoping effects [80, 125], tunneling [126] from the FLG top gate through the insulating hBN top layer, and, possibly, charge trapping [127] at the SiO₂/hBN interface.

6.3.1 Charge control in a gated monolayer MoS₂ heterostructure

To monitor the electron density and its relation to $I(X^-)/I(X^0)$, a reference sample consisting of an encapsulated yet contacted MoS₂ monolayer was fabricated. In this case, the MoS₂ layer is directly contacted by a FLG sheet. This is a capacitive device and as such the electron density in the sample is expected to change linearly with the applied gate voltage [1]. This expectation was confirmed experimentally by measuring the energetic separation between the X^0 and X^- features in the PL spectra: we find a linear dependence of the X^0 and X^- energy separation with gate voltage (see Fig. 6.4b). At low electron densities, the energetic separation between X^0 and X^- scales linearly with the Fermi level, as ionization of X^- requires that an electron is moved up to the Fermi level [1, 128]. Given the linear dependence of Fermi energy on electron density for a 2D system, the PL itself demonstrates that the reference sample charges as a

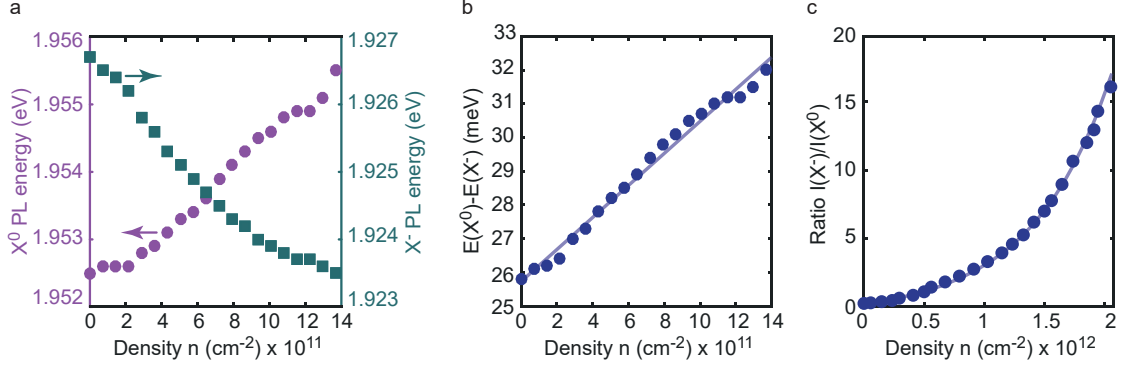


Figure 6.4. **Directly contacted MoS₂ device (reference sample).** **a**, Variation of the photoluminescence energy (PL) of X^0 (purple circles, left axis) and X^- (green squares, right axis) as a function of the electron density. **b**, Separation between the emission energy of the neutral $E(X^0)$ and negatively charged $E(X^-)$ excitons as a function of the electron density in the MoS₂ monolayer. **c**, Ratio between the integrated intensity of the X^- and X^0 PL features as a function of the electron density.

capacitive device (with a capacitance $\sim 12 \text{ nF cm}^{-2}$). It is noteworthy that the X^0 and X^- emission energies show opposite dependences on the electron density (Fig. 6.4a): X^0 blue-shifts while X^- red-shifts with increasing electron density [121]. As in the main sample, the reference sample shows hysteresis effects on ramping the voltage up and down. The voltage at which the electron density is close to zero changes depending on the history of the device. Despite this, we find a robust relationship between the intensity ratio $I(X^-)/I(X^0)$ and the X^0 , X^- splitting, equivalently the electron density. Fig. 6.4c plots $I(X^-)/I(X^0)$ as a function of the electron density extracted from the PL spectra recorded at various gate voltages on the reference sample. The monotonic increase of this ratio with the electron density can be well-described by a phenomenological exponential fit. This means that the ratio of $I(X^-)$ to $I(X^0)$ provides a highly sensitive tool with which to monitor any changes in the electron density. Of course, spatial inhomogeneities and sample-to-sample variations [72, 129] may also influence $I(X^-)/I(X^0)$, but for a particular location on a particular sample, this ratio is a very useful probe of the electron density. We exploit this feature but determine the absolute electron density from the energetic difference $E(X^0) - E(X^-)$ because this is a robust quantity without the sample-to-sample variations.

6.3.2 Polarizability of neutral and charged excitons

We return to the main sample. Using the energetic difference $E(X^0) - E(X^-)$ along the voltage loop displayed in Fig. 6.3a, we find a total variation of the electron density

of $\sim 10^{12} \text{ cm}^{-2}$. To isolate the QCSE contribution to the exciton energy, it is important to identify regions where the gate voltage can be swept without changing the ratio $I(X^-)/I(X^0)$, which, as explained above, is extremely sensitive to changes in the electron density. Inspection of the $I(X^-)/I(X^0)$ data in Fig. 6.3b shows that there are no significant changes in MoS₂ electron density around S₃ and S₄. These two regions are therefore good candidates for measuring the QCSE in MoS₂. Between S₂ and S₃, the ratio of $I(X^-)$ to $I(X^0)$ is small and corresponds to a region where MoS₂ has a low electron density ($\lesssim 10^{12} \text{ cm}^{-2}$). In this region, the X^- signal is weak and evaluation of the ratio $I(X^-)/I(X^0)$ becomes unreliable. It is therefore difficult to attest that the Fermi level in this region remains absolutely constant. Moreover, it is in this range of Fermi energy that photo-induced doping from the hBN layers occurs leaving charged defects in the hBN that potentially induce electric field screening [80]. The region around S₃ is therefore problematic with regards to the QCSE. The region around S₄, between +30 V and -30 V, exhibits a stronger X^- feature, and the ratio of $I(X^-)$ to $I(X^0)$ can therefore be reliably measured. From this ratio, the electron density is evaluated to remain constant to within 5%. Using the energetic difference $E(X^0) - E(X^-)$, the electron density is estimated to be of $(1.5 \pm 1.0) \times 10^{12} \text{ cm}^{-2}$. The large uncertainty arises through spatial inhomogeneities in $E(X^0) - E(X^-)$, a feature of both the main and reference samples.

Fig. 6.5b displays the change in X^- and X^0 emission energies, $\Delta E(X^-)$ and $\Delta E(X^0)$

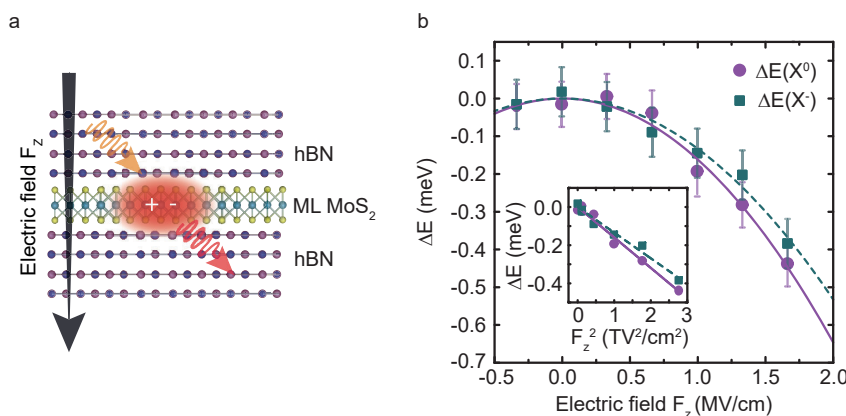


Figure 6.5. **Exciton polarizability.** **a**, Schematic depiction of a polarizable exciton in monolayer MoS₂. **b**, Neutral X^0 (purple circles) and negatively charged X^- (green squares) Stark shift as a function of the applied electric field F_z , extracted from the measurements in Fig. 6.2a and Fig. 6.3. The solid purple and dashed green lines are parabolic fits. The inset shows the same data points as a function of the squared electric field F_z^2 in order to highlight the quadratic dependence of the Stark shift.

respectively, in the region around S₄. F_z was determined by dividing V_G by the electrode-to-electrode distance of 300 nm and adding a constant built-in electric field of 0.66 MV/cm. This value was chosen such that $\Delta E(X^-)$ and $\Delta E(X^0)$ vanish at $F_z = 0$, that is, it is assumed that $\mu_z = 0$. This built-in electric field arises from space charge within the layers of the heterostructure. Both $\Delta E(X^-)$ and $\Delta E(X^0)$ exhibit a quadratic dependence on F_z , equivalently a linear dependence on F_z^2 , as shown in Fig. 6.5b. This is the signature of a QCSE. We argue that the experiment reveals a QCSE and not a residual effect of any small changes in electron density. First, for each point the measurement error in $I(X^-)/I(X^0)$ results in an electron density variation which leads to possible changes in $\Delta E(X^-)$ and $\Delta E(X^0)$, even without a QCSE. However, these changes (shown by the error bars in Fig. 6.5b) are considerably smaller than the $\Delta E(X^-)$ and $\Delta E(X^0)$ values observed experimentally: the uncertainties in electron density cannot account for the shifts in X^- and X^0 emission energies. Second, both X^0 and X^- red-shift around S₄ yet a change in electron density would result in $\Delta E(X^-)$ and $\Delta E(X^0)$ values of opposite sign (see Fig. 6.4a). (Note that X^0 and X^- are measured simultaneously.) From a fit to a second order polynomial, $\Delta E(X^-)$ and $\Delta E(X^0)$ versus F_z , excitonic polarizabilities of

$$\begin{aligned}\beta_z(X^-) &= (6.4 \pm 0.9) \times 10^{-10} \text{ D}\cdot\text{m}\cdot\text{V}^{-1} \\ \beta_z(X^0) &= (7.8 \pm 1.0) \times 10^{-10} \text{ D}\cdot\text{m}\cdot\text{V}^{-1}\end{aligned}$$

are deduced at an electron density of $(1.5 \pm 1.0) \times 10^{12} \text{ cm}^{-2}$. These values are nearly one order of magnitude lower than the previously reported values [118]. It is striking that the polarizabilities of the neutral and charged excitons are almost the same yet the emission energies are quite different on account of the different Coulomb interactions. The experiment itself therefore implies that Coulomb interactions in the excitons, equivalent to screening by the electron gas, is unimportant in determining the QCSE. This in turn allows us to compare the experimental result to a single-particle theory. The excitonic polarizabilities have been theoretically calculated with a finite barrier quantum well model [120]. Using barriers of 2.8 eV [126] for both electron and hole, a quantum well thickness of 0.65 nm and effective electron and hole masses of 0.35 bare electron mass [1], an exciton polarizability of $7.5 \times 10^{-10} \text{ D}\cdot\text{m}\cdot\text{V}^{-1}$ is deduced. This is in good agreement with the experimental values reported here and strengthens the claim that the measured QCSE is dominated by single-particle energy shifts. This point can be understood by considering the highly anisotropic nature of the confinement. In the vertical direction, the confinement is dominated by single particle effects, that is, confinement in a deep potential well. In the lateral direction, the exciton is much more polarizable [120, 130].

In detail, the experiment shows that the trion is slightly less polarizable than the

neutral exciton, as shown in Fig. 6.5b. This can be explained, at least qualitatively, by a subtle change in the Coulomb interactions. Specifically, in the X^- complex there is an additional decrease in the exciton binding energy with electric field. This is induced by the localization of the two electrons on one side of the monolayer and the hole on the other side, increasing the electron-electron repulsion, decreasing the electron-hole interaction [131], thus leading to a decrease in the trion binding energy.

6.4 Conclusion and outlook

6.4.1 QCSE in monolayer MoS₂

In conclusion, the QCSE of excitons has been extracted from PL measurements on a high-quality MoS₂ monolayer embedded in a vdWH. As the electron density in the monolayer is observed to vary with electric field, a careful data analysis exploiting reference measurements on a directly contacted MoS₂ device was performed. Regions were identified in which the electron density in the monolayer remains constant as the electric field is varied. Having ruled out any contribution of a changing electron density to the exciton energy shift, a QCSE was unambiguously identified. The small exciton polarizability is in line with theoretical computation [120]. The maximum QCSE achieved here corresponds to just half the homogeneous linewidth despite the fact that large electric fields were applied. The methodology used here to determine the QCSE in MoS₂ can be used also in other semiconducting monolayers, where similar values of the polarizability should be obtained owing to the extreme out-of-plane confinement of both electrons and holes (Fig. 6.5a). The insensitivity of the exciton to an electric field in MoS₂ has profound implications on its optical properties. On the one hand, we believe that the minute QCSE renders the exciton energy insensitive to charge noise. This, along with the superfast radiative decay, explains the observation of optical linewidths close to the homogeneous limit in MoS₂ vdWHs [72]. On the other hand, electrical control of the exciton based on the QCSE would require larger polarizabilities or a non-zero dipole moment as observed for interlayer excitons (or spatially indirect excitons) in bilayer systems for several combinations of TMDs [33, 36, 38, 39, 46, 98, 132, 133].

6.4.2 Electrical control of interlayer excitons in MoSe₂/WSe₂ heterobilayers

In type-II semiconducting heterostructures, such as MoSe₂/WSe₂ heterobilayers (Fig. 6.6a), the conduction band (CB) and valence band (VB) edges are located in different layers

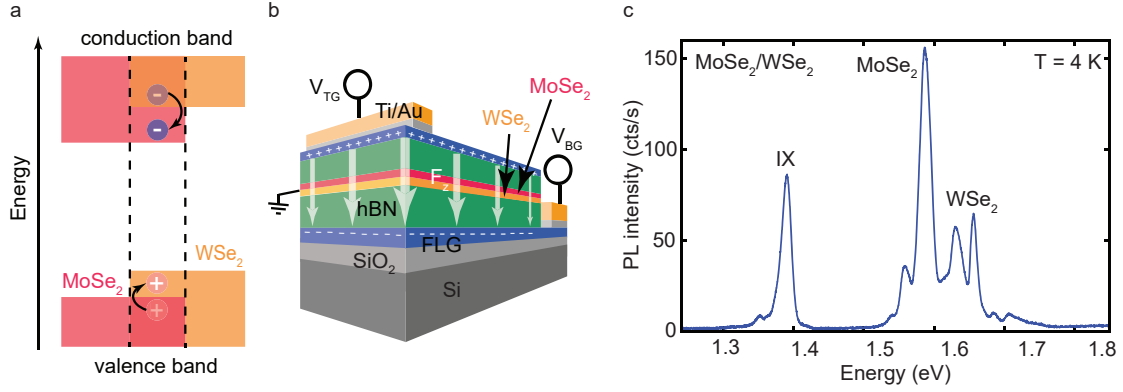


Figure 6.6. **Interlayer excitons in a MoSe₂/WSe₂ type-II van der Waals heterostructure.** **a**, Band alignment of the heterobilayer, consisting of n-doped MoSe₂ and p-doped WSe₂. **b**, Schematic depiction of the dual-gate device structure for independent control of the carrier concentration and the electric field F_z within the vdWH. Voltages are applied to the top and bottom FLG gates (V_{TG} and V_{BG}), while the two monolayers, encapsulated in hBN, are grounded. **c**, PL spectrum from the heterostructure area at $T = 4$ K ($E_{exc} = 2.09$ eV, $I_{exc} = 1.6$ kW/cm²). The interlayer exciton (IX) forming between the two layers appears at an emission energy below the intralayer excitons in MoSe₂ and WSe₂.

and interlayer excitons (IXs) form* with the hole residing in the WSe₂ and the electron residing in the MoSe₂ layer (Fig. 6.6a) [33, 36]. Fig. 6.6c shows the PL spectrum from a MoSe₂/WSe₂ vdWH at $T = 4$ K. At high energies, emission from the (neutral and charged) intralayer excitons in the MoSe₂ and WSe₂ monolayers can be observed in the overlap region. Compared to the monolayer regions, the PL signal is significantly quenched, indicating an efficient charge transfer between the layers. Additionally, an emission feature appears about 200 meV below the intralayer exciton energies, which can be attributed to the IX. Keeping the carrier concentration constant and at a low value while applying an electric field across the dual-gate device[†], we can linearly tune the IX energy by as much as $\Delta E_{IX} \approx 80$ meV through the QCSE (Fig. 6.7a). Fig. 6.7b plots the IX transition energy extracted from Fig. 6.7a as a function of F_z . According to Eq. 6.1

$$\Delta E_{IX} = -\mu_{IX} F_z = -e \cdot d \cdot F_z, \quad (6.2)$$

*The realization of IXs is strongly dependent on the stacking orientation, and thus precise control of the twist angle between the constituent monolayers is required (see Appendix B for the alignment of the individual layers).

[†]In contrast to the single-gate device used to measure the QCSE in monolayer MoS₂, the dual-gate device structure allows us to separate the effects of electrostatic doping and electric field (see Chapter 3).

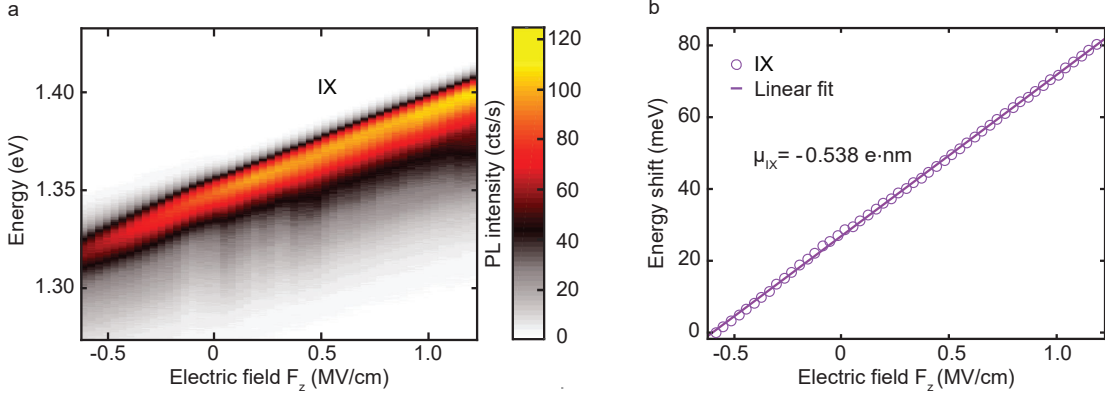


Figure 6.7. **Electrical control of interlayer excitons in a MoSe₂/WSe₂ van der Waals heterostructure.** **a**, Color map for the electrical field dependence of the interlayer exciton (IX) photoluminescence (PL) at $T = 4 \text{ K}$ ($E_{\text{exc}} = 2.09 \text{ eV}$, $I_{\text{exc}} = 0.14 \text{ kW/cm}^2$). **b**, IX energy peak position as a function of the applied electric field F_z measured on the heterostructure region of the device depicted in Appendix B. The solid line is a linear fit to the data, and a dipole moment of $\mu_{IX} = -0.538 \text{ e}\cdot\text{nm}$ can be extracted.

we can extract a dipole moment of $\mu_{IX} = -0.538 \text{ e}\cdot\text{nm}$ and, consequently, a distance of $d \approx 0.54 \text{ nm}$ between the spatially separated electrons and holes.

The unique combination of high electrical tunability and large binding energies of interlayer excitons in MoSe₂/WSe₂ heterobilayers provides an interesting platform for exploring opto-electronic phenomena and studying exciton-exciton interactions. First, the reduced overlap of the electron and hole wavefunctions leads to enhanced lifetimes compared to the intralayer excitons of up to $1 \mu\text{s}$ [36, 134], allowing for long lateral diffusion before recombination [135]. Second, as composite bosons, they are promising candidates for creating a Bose-Einstein condensate (BEC) of excitons [136, 137]: a collective, macroscopic quantum state of matter. The concept of interlayer (or indirect) excitons is well-known from conventional coupled GaAs quantum wells, which have been widely explored for the realization of an exciton BEC [138–140]. However, the weak exciton binding energy in these systems makes it difficult to reach condensed phases of excitons above a few Kelvin and limits the possibility of manipulating of the Bose-Einstein gas system. In contrast, TMDs feature excitons with extremely large binding energies, implying a very small Bohr radius. This provides the possibility to achieve a high exciton density and, in turn, a many-body state, a BEC, up to 100 K in TMD heterobilayer systems [41, 136, 141]. Third, in contrast to intralayer excitons in monolayers, interlayer excitons can experience a strong trapping potential in a locally varying electric

field via their large dipole moment [116, 142]. This is desirable for various quantum applications [143]: the trapping of a single exciton results in the emission of a single photon.

7

Giant Stark splitting of an exciton in bilayer MoS₂

The content of this chapter is partially adapted from:

Nadine Leisgang*, Shivangi Shree*, Ioannis Paradisanos*, Lukas Sponfeldner*, Cedric Robert, Delphine Lagarde, Andrea Balocchi, Kenji Watanabe, Takashi Taniguchi, Xavier Marie, Richard J. Warburton, Iann C. Gerber, and Bernhard Urbaszek, **“Giant Stark splitting of an interlayer exciton in bilayer MoS₂”**, *Nature Nanotechnology* **15**, 901–907 (2020).

*These authors contributed equally.

7.1 Summary

Transition metal dichalcogenides (TMDs) constitute a versatile platform for atomically thin opto-electronics devices and spin-valley memory applications. In monolayer TMDs the optical absorption is strong, but the transition energy can not be tuned as the neutral exciton has essentially no out-of-plane static electric dipole (see Chapter 6) [144, 145]. In contrast, interlayer exciton transitions in heterobilayers are widely tunable in applied electric fields, but their coupling to light is substantially reduced (see Chapter 6). In this work, we show tuning over 120 meV of interlayer excitons with a high oscillator strength in bilayer MoS₂ due to the quantum confined Stark effect [114]. We optically probed the interaction between intra- and interlayer excitons as they were energetically tuned into resonance. Interlayer excitons interact strongly with intralayer B excitons as demonstrated by a clear avoided-crossing, whereas the interaction with intralayer A excitons is substantially weaker. Our observations are supported by density functional theory

*N.L. fabricated device 1; S.S. and I.P. fabricated device 2 and sample 3. N.L. and L.S. performed optical spectroscopy measurements on device 1; S.S. and I.P. measured device 2 and sample 3. N.L., S.S., I.P. and L.S. analyzed the optical spectra and interpreted the results. I.C.G. performed and interpreted the DFT GW+BSE calculations.

(DFT) calculations, which include excitonic effects. In MoS₂ trilayers, our experiments uncovered two types of interlayer excitons with and without in-built electric dipoles. Highly tunable excitonic transitions with large in-built dipoles and oscillator strengths will result in strong exciton-exciton interactions and therefore hold great promise for non-linear optics with polaritons.

7.2 Introduction

The optical properties of TMDs, such as MoS₂ and WSe₂, are governed by excitons, Coulomb-bound electron-hole pairs [12, 25]. High-quality van der Waals heterostructures (vdWHs) show close-to-unity, gate-tunable reflectivity of a single MoSe₂ layer [146, 147], variation of the transition energies of interlayer excitons over a broad wavelength range in heterobilayers [33, 148] and valley polarized exciton currents [135].

In heterobilayers, the interlayer exciton is formed with the electron either in the top or in the bottom layer depending on the initial stacking [33]. Reports on interlayer excitons in heterobilayers rely mostly on photoluminescence emission [33, 135, 148–150] as the interlayer absorption is very weak. In 2H-stacked MoS₂ homobilayer the situation is different. First, a strong feature in the absorption up to room temperature was observed in earlier studies on MoS₂ bilayers [51, 151–154] and interpreted as an interlayer exciton, as theoretically predicted by Deilmann and Thygesen [49]. It was proposed that the strong oscillator strength of the interlayer exciton originates from a strong admixture with the B-intralayer transition (see the discussion in previous calculations [49, 51]). Second, in principle, two energetically degenerate interlayer excitons can form in which the electron resides in either the top or the bottom layer [77], whereas the hole is delocalized [155] (see Fig. 7.1).

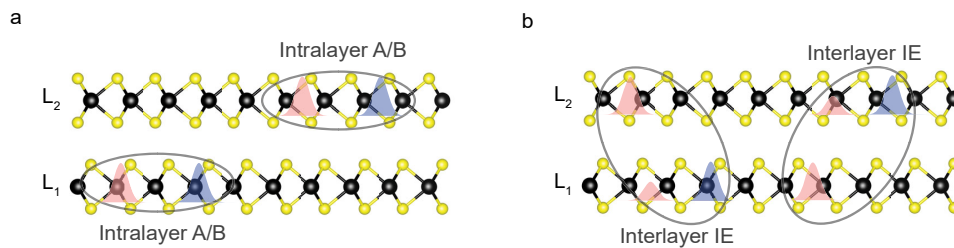


Figure 7.1. **Schematics of intralayer and interlayer excitons in homobilayer MoS₂.** Intralayer A and B resonances correspond to excitons where the electron and the hole reside in the same layer. Intralayer excitons can form in each of the two layers, denoted by the subscript L₁ (L₂) for layer 1 (layer 2). The interlayer exciton IE consists of an electron confined in one layer and a hole delocalized over both layers. The figure is adapted from Ref. [51].

Here, we investigate excitons in bilayer MoS₂ with both a strong light-matter interaction and a high tunability in external electric fields. Our experiments focused on momentum-direct intralayer and interlayer excitons that originate from valence and conduction bands (VBs and CBs, respectively) around the K point.

7.3 Experimental methods

We performed experiments as a function of the out-of-plane electric field in 2H-stacked bilayer MoS₂ independently in two different research laboratories using devices 1 and 2, with a geometry as depicted in Fig. 7.2a. Two hexagonal boron nitride (hBN) flakes are used as dielectric spacers, and few-layer graphene (FLG) at the top and bottom acted as transparent electrodes (see Appendix B for a description of the fabrication process and optical images of the devices). In device 1, a direct Ti/Au contact was added to the MoS₂ to operate the system in a dual-gate device scheme by grounding the bilayer, which allowed independent control of the applied electric field and the carrier concentration. A DC voltage was applied to the top and bottom gates (V_{TG} and V_{BG}) to create a uniform electric field in the MoS₂, oriented perpendicular to the bilayer. The optical reflectivity was measured at low temperature ($T = 4\text{ K}$) using a home-built confocal microscope and a weak, incoherent light source (see Chapter 4). The imaginary part of the optical susceptibility $\text{Im}(\chi)$, a measure of the absorption, was deduced from the differential reflectivity signal $\Delta R/R_0$, $\Delta R = R - R_0$, using a Kramers-Kronig relation, where R is the reflectivity spectrum obtained on the MoS₂ flake and R_0 is the reference spectrum (see Chapter 4 for a detailed description).

7.4 Stark effect tuning of interlayer excitons in bilayer MoS₂

We integrated the MoS₂ bilayers in devices 1 and 2 with top and bottom gates to apply a static out-of-plane electric field F_z . Fig. 7.2c and Fig. 7.3a show the color map of typical absorption spectra as a function of the electric field F_z , recorded on device 2 and device 1. Three prominent transitions can be clearly identified at zero electric field ($F_z = 0\text{ MV/cm}$): the intralayer A and B excitons (A:1s and B:1s) near 1.93 eV and 2.10 eV, respectively, and the interlayer A exciton (IE) at 2.00 eV [51]. On applying an external electric field F_z , the IE splits into two well-separated branches, as shown in Fig. 7.2b for $F_z = -0.5\text{ MV/cm}$. Using the area under the peaks in Fig. 7.2b as a rough measure of the relative absorption strength (we take A:1s as 100%), we see that at $F_z = 0\text{ MV/cm}$ the IE is about 30% compared with the intralayer A:1s. Remarkably, at finite electric field $F_z = -0.5\text{ MV/cm}$, the absorption strength does not vanish but

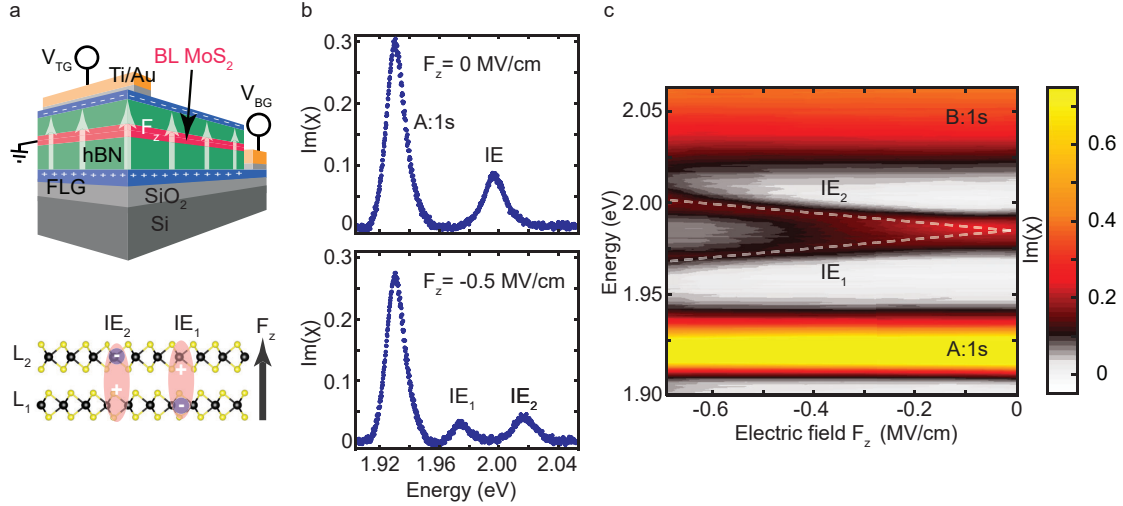


Figure 7.2. **MoS₂ bilayer van der Waals heterostructure (vdWH) in an applied electric field at $T = 4$ K.** **a**, Three-dimensional schematic of device 1, which consists of a MoS₂ homobilayer encapsulated between two hexagonal boron nitride (hBN) flakes. Few-layer graphene (FLG) serves as the top and bottom gates, and a direct Ti/Au contact to the MoS₂ is used to ground the bilayer. Voltages to the top and bottom gates (V_{TG} and V_{BG}) are applied to create a uniform electric field F_z across the device. The structural model of 2H-stacked bilayer MoS₂ and applied electric field direction is depicted below. **b**, Typical absorption spectra recorded without ($F_z = 0$ MV/cm) (top) and with ($F_z = -0.5$ MV/cm) (bottom) an applied electric field, extracted from Fig. 7.3a. **c**, Color map of the absorption spectra of a bilayer MoS₂ vdWH (device 2) showing the Stark shift of the interlayer excitons at small electric fields. The intralayer A:1s and B:1s and the two branches of the interlayer A resonances (IE_1 and IE_2) are labelled.

remains rather strong, with a combined 24% from $IE_1 + IE_2$ relative to the A:1s. Our experiments clearly show that the absorption peak IE, initially at 2.00 eV, corresponds to interlayer exciton resonances with out-of-plane oriented electric dipoles: the carriers clearly do not reside within the same layer. For the intralayer excitons, however, the energy shift with an applied electric field is negligible, as in the case for excitons in monolayers [144, 145]. As F_z is increased, the energy difference between the IE_1 and IE_2 states reaches a value of ~ 120 meV, which covers a wide spectral range that spans the entire energy range between the intralayer A and B excitons.

For small-to-moderate electric fields, before a noticeable interaction between the interlayer states and the A and B excitons, we observed a linear energy shift with F_z for both peaks, IE_1 and IE_2 , which suggests a first-order Stark shift caused by the static electric dipole moments across the MoS₂ bilayer (Fig. 7.3). In Fig. 7.3b we plot the transition energies extracted from Fig. 7.3a as a function of the applied field F_z and

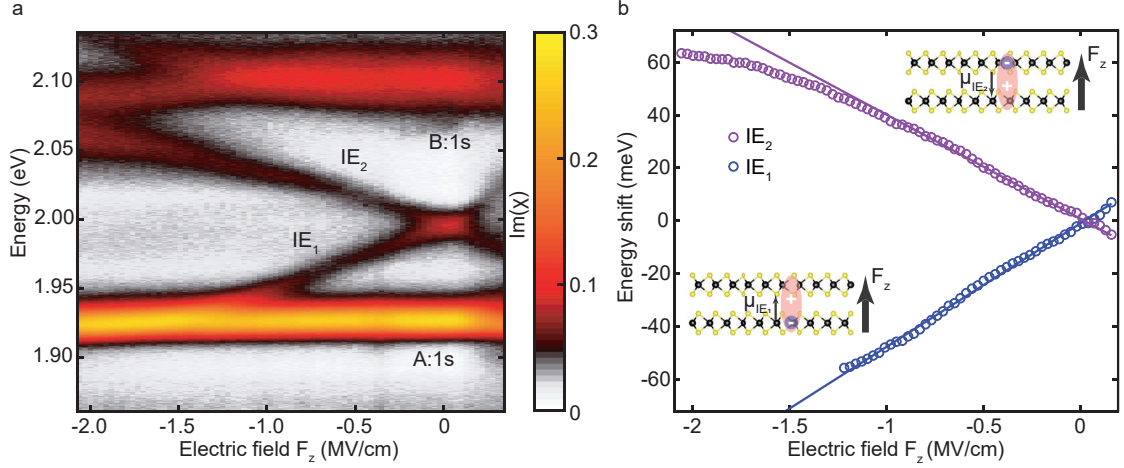


Figure 7.3. **Giant Stark shift in a MoS₂ bilayer van der Waals heterostructure (vdWH) at $T = 4$ K.** **a**, Color map of the absorption spectra of device 1 as a function of the electric field F_z applied perpendicular to the vdWH. **b**, Stark shift of the IEs as a function of F_z , extracted from the spectra in **a**. The solid blue and purple lines are linear fits to the experimental data points at small-to-moderate electric fields ($F_z = 0.1$ MV/cm to $F_z = -1$ MV/cm). Insets: schematics of the interlayer excitons in homobilayer MoS₂. An electron localized in one layer interacts with a hybridized hole state to form an interlayer exciton. The direction of the dipole moment depends on the location of the electron, either in the bottom (μ_{IE_1}) or top (μ_{IE_2}) layer.

show a linear fit. We extract large dipole moments of $\mu_{\text{IE}_1} = (0.47 \pm 0.01) e \cdot \text{nm}$ and $\mu_{\text{IE}_2} = (-0.39 \pm 0.01) e \cdot \text{nm}$ with e being the electron charge. Applying higher electric fields in our experiment, we discovered that the shifts deviate from a simple linear Stark shift, which reflects, as discussed below, very different interactions of the interlayer excitons with the A- and B-intralayer excitons. For the analysis of device 2, shown in Fig. 7.2c, we extracted a dipole value with a lower bound of about $0.3 e \cdot \text{nm}$.

In terms of the magnitude, the large extracted dipole moments are similar to results on interlayer excitons in MoSe₂/WSe₂ heterobilayers, as determined by photoluminescence (see Chapter 6) [33, 135, 148, 156]. For comparison with other homobilayer systems, interlayer excitons have very different characteristics, which depend on the TMD material [157, 158]. For WSe₂ bilayers, reports on interlayer excitons focus on indirect transitions in momentum space linked to the indirect band gap energetically below the direct K - K transitions [159, 160]. In the case of MoSe₂, K - K interlayer excitons are observed with similarities to the case of MoS₂, but with substantially lower oscillator strength [47, 48, 50]. This is mainly due to the larger VB spin-orbit splitting of MoSe₂ compared with that of MoS₂, which makes hole delocalization over both layers, and hence the formation of interlayer excitons, less favourable [155]. Signatures of interlayer excitons

in bulk 2H MoSe₂ have been reported, but the same study did not find K - K interlayer exciton signatures for bulk 2H WSe₂ [161].

7.5 Zeeman splitting of interlayer excitons

Magneto-optics is a powerful tool for line identification and transition energy tuning [156]. Applying a magnetic field B_z perpendicular to the sample plane lifts the degeneracy (valley Zeeman effect) and allows the measurement of the intra- and inter-layer exciton g -factors.

Zeeman splitting at zero electric field

Fig. 7.4a shows the polarization-resolved absorption spectra (σ^+ and σ^- polarization) of bilayer MoS₂ without (middle) and with (top, bottom) an externally applied magnetic field in our experiment. At $B_z = 0$ T, there is no difference between the two circular

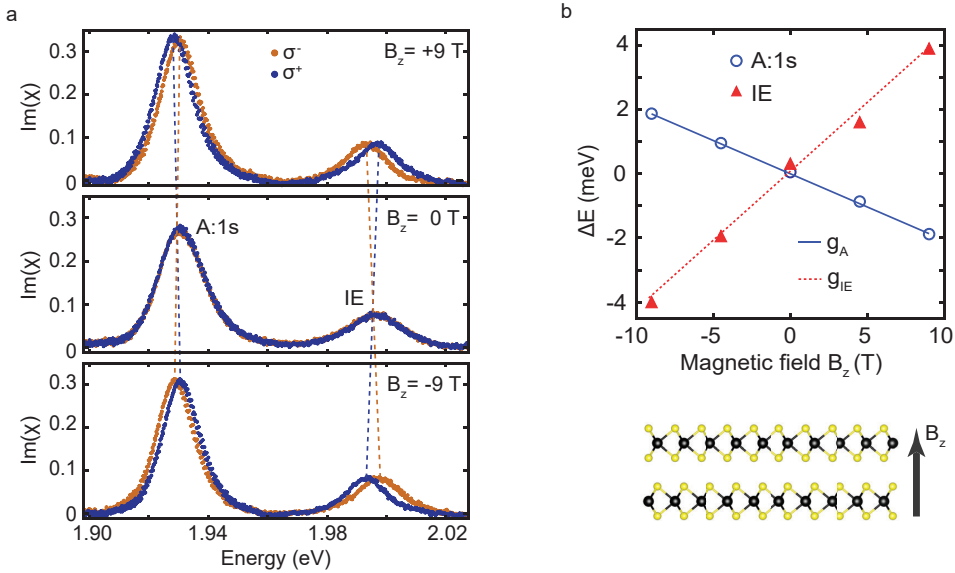


Figure 7.4. **Magneto-optics of bilayer MoS₂ (device 1) at zero electric field ($F_z = 0$ MV/cm).** **a**, Polarization-resolved absorption spectra for bilayer MoS₂ without (middle) and with (top, bottom) a magnetic field ($B_z = 0$ T and $B_z = \pm 9$ T) applied perpendicular to the layers. The orange and blue curves correspond to σ^- and σ^+ polarization. Intra- and interlayer A excitons (A:1s and IE) are labelled. **b**, Energy difference ΔE between the two circular polarizations for the intralayer (blue) and interlayer (red) excitons at different magnetic fields B_z . The g -factors of the two transitions are extracted from linear fits. The intralayer A exciton has a negative g -factor, $g_A = -3.6 \pm 0.1$, while the interlayer excitonic g -factor is approximately twice as large with opposite sign, $g_{IE} = 7.4 \pm 1.1$. The errors in the g -factors represent a 95% confidence interval that is calculated from the uncertainty of the fitting parameter.

polarizations, while at $B_z = \pm 9$ T, the degeneracy is lifted. For a more detailed analysis of the Zeeman splitting, magneto-optical measurements were performed for different magnetic field values (at $F_z = 0$ MV/cm), presented in Fig. 7.4b. The intralayer exciton A:1s, which exhibits a negligible Stark shift, shows a negative Zeeman splitting of about 2 meV at $B_z = +9$ T. As the magnetic field direction is reversed in Fig. 7.4 (see also Fig. 7.5b), it changes sign. The Zeeman splitting for the interlayer exciton IE is about 4 meV at $B_z = +9$ T, and the sign is opposite with respect to the intralayer exciton. The Zeeman splittings of the two excitonic transitions are defined as

$$\begin{aligned}\Delta E_A &= E_A(\sigma^+) - E_A(\sigma^-) = g_A \mu_B B_z \\ \Delta E_{IE} &= E_{IE}(\sigma^+) - E_{IE}(\sigma^-) = g_{IE} \mu_B B_z\end{aligned}\quad (7.1)$$

with $E(\sigma^+)$ and $E(\sigma^-)$ being the transition energies for the two circular polarizations, g_A and g_{IE} are the excitonic g -factors, and $\mu_B = 58 \mu\text{eV}/\text{T}$ is the Bohr magneton. From the data presented in Fig. 7.4, we deduce a negative Landé g -factor of around -3.6 for the intralayer exciton A:1s and a positive g -factor of about $g_{IE} \approx 7.4$ for the interlayer exciton [151]. These g -factors, g_A and g_{IE} , are obtained from linear fits of ΔE versus B_z , divided by μ_B in Fig. 7.4b. The larger Zeeman splitting of interlayer excitons with opposite sign compared to intralayer excitons has been observed for other multilayer

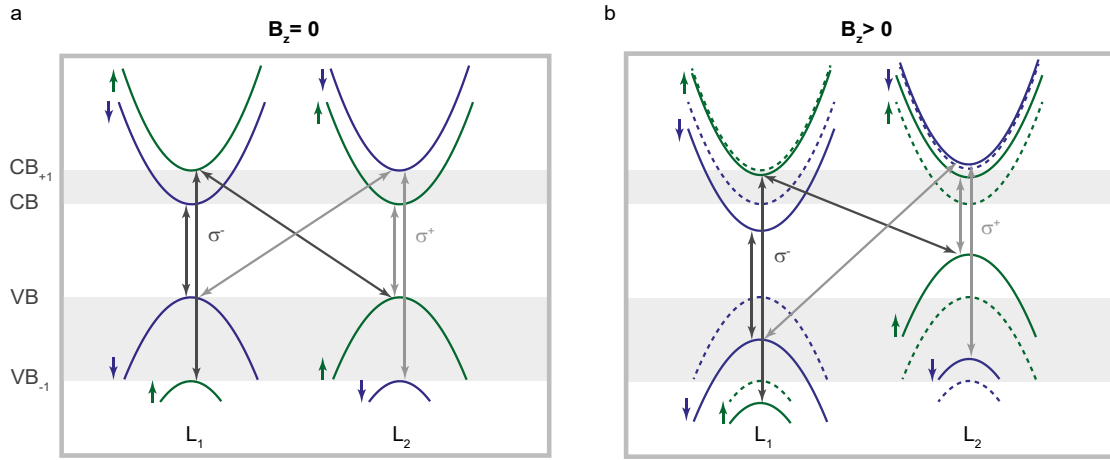


Figure 7.5. **Band diagram and optical selection rules in homobilayer MoS₂.** Optical selection rules for the transitions at **a**, $B_z = 0$ and **b**, $B_z > 0$ between the spin-orbit split valence bands (VB, VB₋₁) and conduction bands (CB, CB₊₁). Vertical and diagonal arrows indicate intralayer (A:1s, B:1s) and interlayer (IE) transitions with σ^+ (grey) and σ^- (black) polarization. For clarity, we only plot the transitions at the $+K$ point. The dashed lines in **b** indicate the band positions without an applied magnetic field.

systems [162].

A simplistic picture of the bandstructure and the optical selection rules in homobilayer MoS₂ at the $+K$ point is presented in Fig. 7.5. An applied magnetic field ($B_z > 0$) shifts the bands by the Zeeman shift due to the contributions of spin, valley and orbital effects (see Chapter 2 for monolayer MoS₂). For intralayer excitons, the spin and valley contributions to the Zeeman splitting for an optical transition within the same layer cancel, at least partially, and the total Zeeman shift is dictated by the orbital contribution. Interlayer transitions originate predominantly from the CB₊₁ and VB in the different layers. Consequently, the valley contribution is additive and the orbital contribution has an opposite sign compared to the intralayer case, resulting in a larger Zeeman splitting with opposite sign [163, 164], as observed in our measurements (Fig. 7.5).

Differential reflectivity contrast

Fig. 7.6a maps the differential reflectivity contrast, constructed as the difference between the differential reflectivity spectra recorded for σ^+ and σ^- polarization ($\Delta R/R_0(\sigma^+) - \Delta R/R_0(\sigma^-)$), at $B_z = +9$ T when applying an external electric field across the MoS₂ bilayer. As can be deduced from our polarization-resolved absorption measurements at zero electric field, dips in the reflectivity contrast spectra correspond to excitonic resonances with negative g -factors ($g < 0$), positive values are related to resonances exhibiting a positive g -factor ($g > 0$). Fig. 7.6b compares the absorption (top) and differential reflectivity contrast spectrum (bottom) at zero electric field ($F_z = 0$ MV/cm), extracted from the color map in Fig. 7.6a along the blue dashed line. The intralayer A:1s and B:1s exciton resonances (with negative g -factors) and the interlayer exciton (IE) resonance (with positive g -factor) can be identified. Additionally, a transition ~ 30 meV below the intralayer B:1s exciton (at $F_z = 0$ MV/cm) can be observed, labelled as BIE. This small feature, highlighted by the black dashed square in Fig. 7.6a, can be uncovered in the reflectivity contrast plot, as the difference in reflectivity between σ^+ and σ^- polarization is nearly zero for the intralayer B exciton. This is due to the fact that the B-exciton transition is spectrally broad and its Zeeman splitting is small compared to its linewidth. The positive g -factor of the BIE transition as well as its tunability with electric field clearly indicate an interlayer character [151]. However, with increasing electric field, the BIE resonance loses oscillator strength and, thus, cannot be observed for higher field values than $F_z = -0.2$ MV/cm.

For interlayer excitons, Stark effect tuning over tens of meV could in principle be

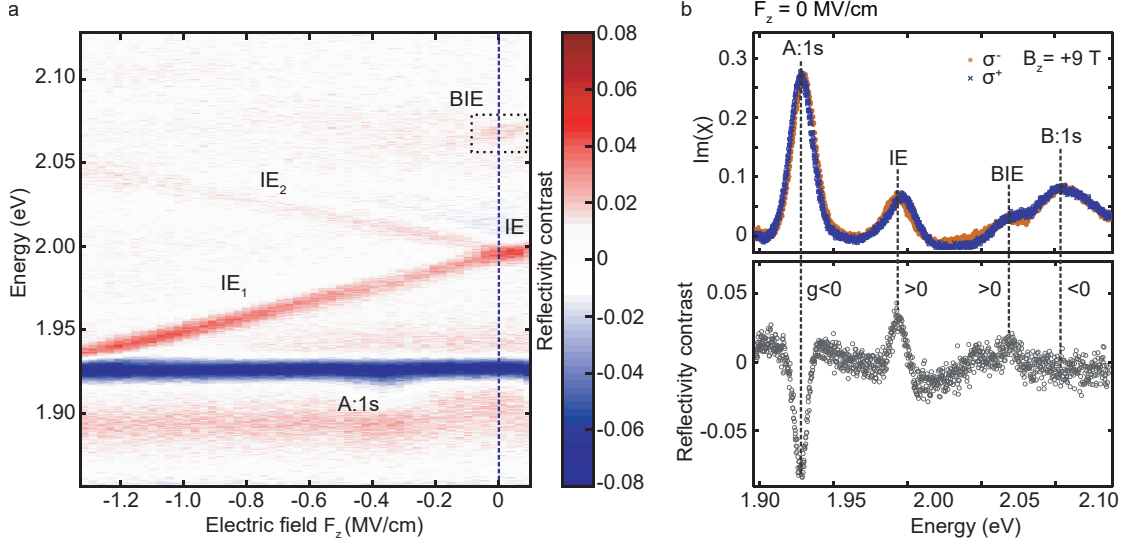


Figure 7.6. **Absorption and differential reflectivity contrast in a magnetic field ($B_z = +9$ T).** **a**, Color map of the differential reflectivity contrast between σ^+ and σ^- polarization ($\Delta R/R_0(\sigma^+) - \Delta R/R_0(\sigma^-)$) at $B_z = +9$ T on applying an external electric field across the MoS₂ bilayer (device 1). A negative value, corresponding to a dip in the differential reflectivity contrast spectrum, reflects a negative g -factor, while a positive value reflects a positive g -factor. In this panel, we can also observe a transition ~ 30 meV below the intralayer B exciton (at $F_z = 0$ MV/cm), labelled as BIE. **b**, Absorption (top) and differential reflectivity contrast spectrum (bottom) at zero electric field ($F_z = 0$ MV/cm). The bottom panel shows the data extracted along the blue dashed line in **a** ($F_z = 0$ MV/cm). The intralayer A and B excitons (A:1s and B:1s) and the two interlayer resonances (IE and BIE) are labelled.

combined with an additional magnetic field splitting of the two interlayer Zeeman states [164]. Our knowledge about interlayer versus intralayer magneto-optics is crucial for the analysis and discussion of our bilayer and trilayer results.

7.6 Tuning interlayer and intralayer excitons into resonance

Owing to the very large tunability shown in Fig. 7.2c and Fig. 7.3a for the interlayer transition energy, we were able to tune the interlayer excitons into resonance with the A- and B-intralayer excitons. The interactions were very different. This can be directly seen by comparing Fig. 7.7a ($IE_1 \leftrightarrow A$) with 7.8a ($IE_2 \leftrightarrow B$).

7.6.1 IE-A interaction

In Fig. 7.7a, the IE_1 transition merges with the A-exciton line at around -1.3 MV/cm; at the highest electric fields in these experiments, the absorption contrast of IE_1 decreases

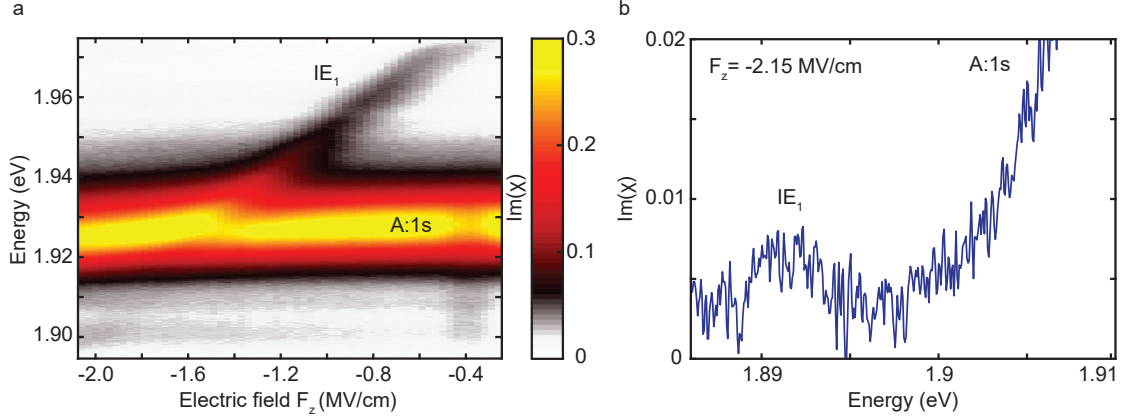


Figure 7.7. **Electric-field dependence in a magnetic field ($B_z = +9$ T): $IE_1 \leftrightarrow A$.** **a**, Color map of the absorption spectra (σ^+ polarization) centered around the intralayer A exciton, showing a very small avoided-crossing with IE_1 . **b**, Spectrum at $F_z = -2.15$ MV/cm showing the IE_1 below the A exciton. The measurement was recorded on the same device 1, albeit in a second cooldown cycle and opposite polarization (σ^- polarization).

(a consequence of the large change to the dielectric constant induced by the strong A exciton), and falls below the noise. This points to a small avoided-crossing of the weak IE_1 exciton with the strong A exciton. On the one hand, the IE-A coupling is clearly less than the linewidth of the A exciton – if this were not the case then a clear avoided-crossing would be visible. On the other hand, the coupling is not zero – there is clearly a change in the dispersion of the A exciton at the electric fields where the IE and A excitons are close in energy. This point can best be probed on samples with a smaller linewidth. Our estimate for the coupling of the IE-A excitons on the present sample is 5 ± 3 meV. Fig. 7.7b shows that the IE_1 can indeed be tuned below the A exciton, becoming the lowest-energy transition.

7.6.2 IE-B interaction

For the B exciton, we can distinguish two resonances associated with intralayer excitons in the two different layers L_1 and L_2 , labelled as B_{L1} and B_{L2} (Figs. 7.8a,b). B_{L1} shows a nearly constant transition energy and integrated absorption strength in the plotted electric field range (Figs. 7.8c,d). Tuning IE_2 energetically close to resonance with B_{L2} indicates a strong coupling. There are two experimental signatures for strong coupling between B_{L2} and IE_2 . First, we observe a clear avoided-crossing in Fig. 7.8c on plotting the transition energies as a function of the applied field. Second, B_{L2} and IE_2 exchange strength – B_{L2} is initially strong, but then weakens; IE_2 is initially weak, but then

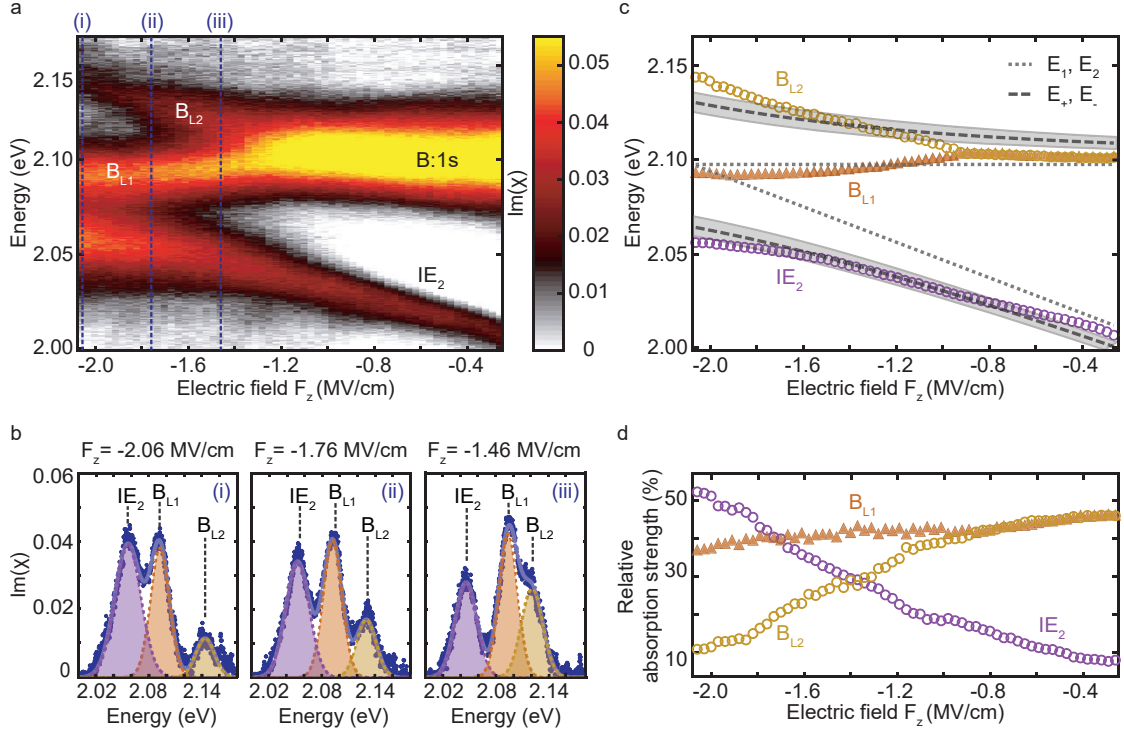


Figure 7.8. **Electric-field dependence in a magnetic field ($B_z = +9$ T): $IE_2 \leftrightarrow B$.** **a**, Color map of the absorption spectra (σ^+ polarization) centered around the intralayer B exciton. B_{L1} and B_{L2} are the intralayer excitons that reside in layers 1 (L_1) and 2 (L_2), respectively. The dashed vertical lines show spectra reproduced in **b**. **b**, Spectra from the data of **a** with a three-peak fit that determines the transition energies and the relative absorption strengths (plotted in **c,d**). **c**, Peak positions versus applied electric field extracted from the spectra shown in **a**. The transitions IE_2 and B_{L2} show a clear avoided-crossing. The dotted lines show the peak energy evolution expected without coupling. Here, E_1 is the mean energy of B_{L2} , and E_2 is set to be the unperturbed energy of IE_2 . The dashed lines are a fit to B_{L2} (E_+) and IE_2 (E_-) (Eq. 7.3) using a coupling energy W of 33 ± 5 meV; the shaded area corresponds to the uncertainty in W . **d**, Evolution of the integrated absorption strength of IE_2 , B_{L2} and B_{L1} confirms the mixing of IE_2 and B_{L2} ; here 100% corresponds to the sum of these three transitions.

strengthens to become the dominant exciton at large electric fields. This can be clearly seen on plotting the evolution of the absorption strength in Fig. 7.8d.

The avoided-crossing of IE_2 and B_{L2} (Fig. 7.8c) can be modelled by a simple two-level system, taking into account the effect of the externally applied electric field F_z . The corresponding Hamiltonian of the coupled system with interaction W can be written as

$$H = \begin{pmatrix} E_1 & W \\ W & E_2 \end{pmatrix}, \quad (7.2)$$

where the two resonances E_1 and E_2 are described as a function of F_z^* . Diagonalizing the modified Hamiltonian and solving for the eigenenergies E_{\pm} of the coupled system gives

$$E_{\pm} = \frac{1}{2}(E_1 + E_2) \pm \sqrt{\frac{(E_1 - E_2)^2}{4} + |W|^2}. \quad (7.3)$$

Using this simple model, we can fit the data (dashed lines in Fig. 7.8c) and extract a coupling energy $W = 33 \pm 5$ meV. We note that the two-level model describes the energies around the avoided-crossing quite well, but does not capture the intensities of the resonances.

The strong coupling between IE_2 and B_{L2} can be qualitatively described using Fig. 7.9. Intralayer A excitons (B excitons) form between the highest valence band VB (second highest VB_{-1}) state and the lowest conduction band CB (second-lowest CB_{+1}) state (Fig. 7.9a). For the interlayer excitons IE_1 (IE_2), the hole contribution comes from the VB state of L_2 (L_1), partially hybridized with VB_{-1} of L_1 (L_2), while the well-localized electron lies in the CB_{+1} state of the other layer L_1 (L_2) (Fig. 7.9b). The avoided-crossing of IE_2 and B_{L2} (Fig. 7.8a), is a consequence of the mixing between interlayer states and intralayer B-states. As IE_2 shares the same CB state only with B_{L2} and not with B_{L1} , there is an avoided-crossing between IE_2 and the B:1s resonance in L_2 (B_{L2}), but not the B:1s resonance in L_1 (B_{L1}). This intuitive explanation of the avoided-crossing agrees well with the theoretical calculations, summarized in Appendix E Table E.1 demonstrating

* E_1 remains constant, while E_2 shifts linearly with $-0.47 e \cdot \text{nm}$ as a function of F_z .

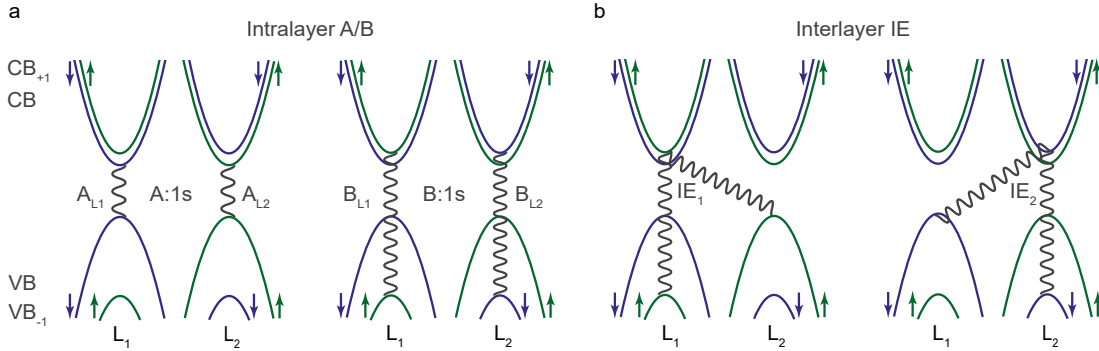


Figure 7.9. **Band diagram of intralayer and interlayer excitons in homobilayer MoS₂ at the K point.** **a**, Intralayer resonances A:1s and B:1s and **b**, interlayer excitons IE_1 and IE_2 . The lowest conduction bands (CB and CB_{+1}) and the two highest valence bands (VB and VB_{-1}) are labelled. Wavy lines connect the states involved for the formation of the different excitonic complexes at the K point. The figures are adapted from Ref. [51].

the decomposition of the oscillator strengths for intralayer and interlayer excitons.

7.6.3 GW+BSE modelling of excitons in MoS₂ bilayers

The main observations of the experiments on devices 1 and 2 are (1) the splitting and very large energy shifts of the IE transitions in an applied electric field, (2) the avoided-crossing of the IE₂ with the B-intralayer exciton, and (3) the small avoided-crossing of the IE₁ with the A-intralayer exciton. The high oscillator strength and large Stark shift of the interlayer exciton were initially discussed by Deilmann and Thygesen [49] using GW+BSE calculations (GW, one-body Green's function G and the dynamically screened Coulomb interaction W ; BSE, Bethe-Salpeter equation). The target here is – also using GW+BSE calculations – to develop a semi-quantitative understanding for the observed effects (1) and (2) by calculating the mixing of intra- and interlayer exciton components as a function of F_z . The approach is based on the inclusion of the applied electric field as a perturbation in the bandstructure calculations, similar to the approach in [49, 165, 166]. Note that only free-standing 2H MoS₂ bilayers are considered in the calculations, that is, placed in vacuum, as the aim is to qualitatively reproduce the main trends. When applying an electric field, the relevant CBs and VBs at the K point shift down in energy for L₁ with respect to L₂, marked as ΔE_{Stark} (see Fig. 7.10a for the electric field configuration and Fig. 7.10b for a bandstructure schematic). A more realistic GW picture of this effect on the bandstructure is given in Appendix E DFT calculations. From the sketch in Fig. 7.10b, it is thus clear that the IE transitions will split in energy: transitions that involve the L₂ VBs and the CBs in L₁ will decrease in energy, whereas transitions that involve the L₁ VBs and L₂ CBs will increase in energy.

After including excitonic effects, the calculated absorption (Fig. 7.11) looks very similar to our measurements at small electric fields (Fig. 7.2c). Fig. 7.10c demonstrates how the IE transition energy changes, roughly linearly, with the applied electric field. At large electric field values of 5 MV/cm, we see two main groups of transitions: at the low energy side, the IE₁ close to the A-exciton energy, and at the high energy side, the IE₂ close to the B exciton as in Deilmann and Thygesen [49]. The calculations show relative IE oscillator strengths (versus A:1s) reasonably close to that of experiments, despite neglecting the environmental dielectric constant variations. We refrain to comment on any higher electric field values in the calculations, as the initial assumption to treat the electric field as a perturbation, in comparison with other energy splittings in the bandstructure, reaches its limits.

The exact nature and mixing of the absorption peaks, as calculated in Fig. 7.11, contain information on the evolution of the exciton states with electric field (Appendix E

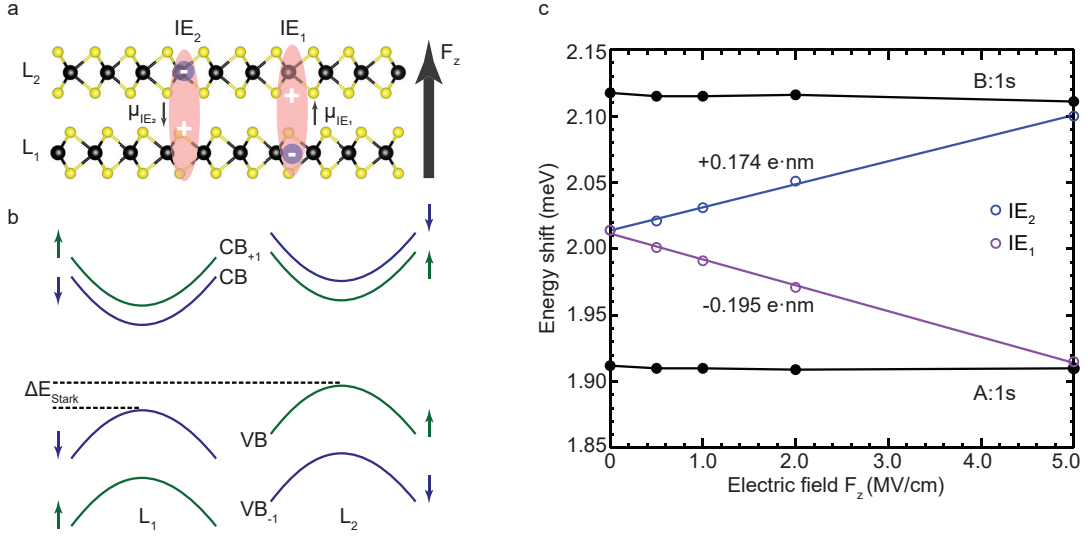


Figure 7.10. **Beyond DFT calculations of the electric field effects on the bandstructure and excitonic properties of a 2H MoS₂ bilayer.** **a**, Structural model of the 2H bilayer stacking and electric field direction. **b**, Schematic of the bandstructure modification due to the application of F_z showing a global shift, ΔE_{Stark} , between the distinct bandstructures of the two layers (see Appendix E for detailed results on GW bandstructure calculations). The lowest conduction bands (CB and CB₊₁) and the two highest valence bands (VB and VB₋₁) are indicated. **c**, Evolution of the excitonic peak positions with respect to the electric field, and the corresponding dipole moment estimates for IE₁ and IE₂ excitons.

Tables E.1 and E.2). We can use this knowledge to analyze the results in Fig. 7.7a and Fig. 7.8a in particular: for finite electric fields, the intralayer A exciton contains a very small IE component that remains small as the field increases. Our theory indicates very little mixing between the A-intralayer exciton and the IE exciton, consistent with the experiments in Fig. 7.7a. Concerning interactions with the intralayer B exciton, the IE exciton is mixed with the intralayer B exciton as they share the same valence states. This was suggested in [51] to explain the surprisingly high oscillator strength of the IE transitions. From the calculations, it becomes apparent that the mixing between the higher energy IE branch and the B exciton becomes stronger as the electric field amplitude is increased (see Appendix E DFT calculations for a detailed description of each component). We suggest that this clear admixture of the IE-exciton with the B exciton in the calculations is the origin of the observed avoided-crossing between IE₂ and B_{L2}, shown in Figs. 7.8a,c, as well as the enhancement of the absorption strength of IE₂, shown in Fig. 7.8d. The GW+BSE calculations therefore capture the main experimental findings, and aid our understanding of the interactions of the IE exciton with

the intralayer A- and B-exciton resonances, and the observed IE Stark shift.

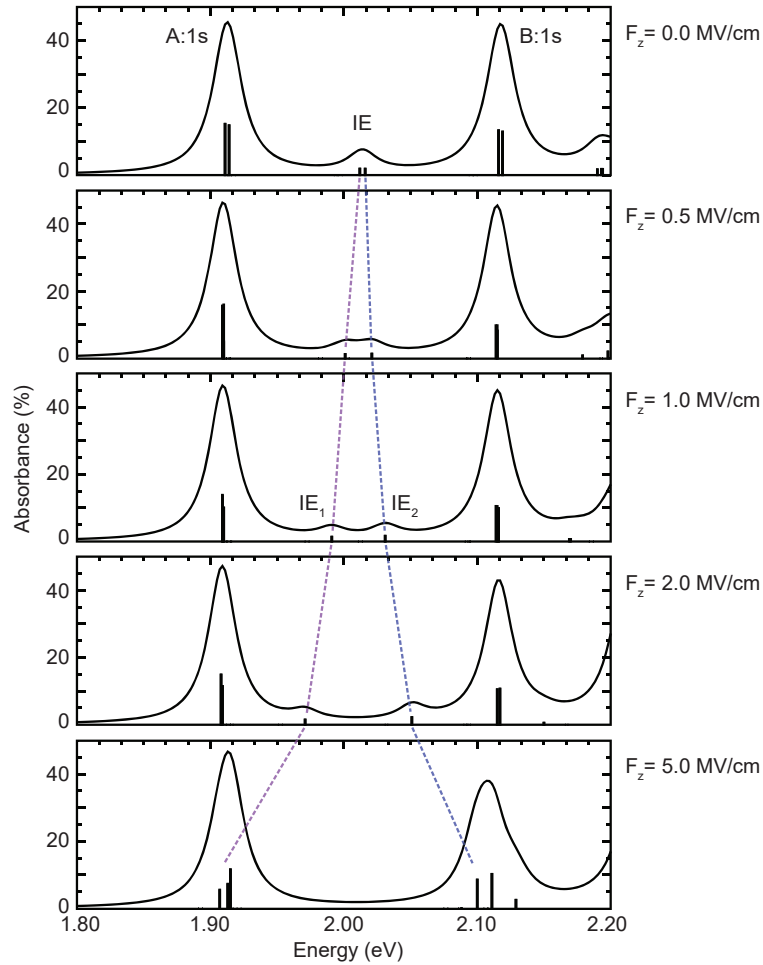


Figure 7.11. **Beyond DFT calculations of the absorption spectra of a 2H MoS₂ bilayer as a function of the applied electric field F_z .** DFT-GW-BSE calculations determine both the energy position and absorption strength that correspond to the exciton transitions shown with vertical black lines. The numerical precision of the calculations is estimated to be on the order of ± 5 meV (see computational settings in Appendix E DFT calculations) such that any splitting below this value does not have any physical significance. For comparison with the experiment, an artificial broadening on the order of 10 meV is introduced for each transition. This results in the spectra shown with solid black lines; the three main transitions A:1s (intralayer A), IE (interlayer) and B:1s (intralayer B) are labelled.

7.7 Interlayer excitons in MoS₂ trilayers

The combined approach using experiments and theory was applied to uncover and manipulate novel exciton species in a more complex system, namely MoS₂ homotrilayers. In contrast to inversion symmetric MoS₂ bilayers, trilayers could be advantageous in non-linear optics due to the broken inversion symmetry that gives rise to a non-vanishing second-order non-linear susceptibility. In the trilayer system, additional types of interlayer excitons were discovered as compared with the bilayer in our experiment: at zero electric field, two different interlayer transitions appear in the absorption, labelled IE* and IE in Fig. 7.12a. The absorption measurements as a function of the electric field lead to a surprising observation: whereas IE splits into two branches (IE₁ and IE₂) as for the bilayer studies, IE* does not show any measurable splitting and, hence, a negligible or, at least, a very small in-built electric dipole moment.

Interestingly, the same behavior can be observed in the GW+BSE calculations in Fig. 7.13b. The different behavior of IE and IE* in applied electric fields can be explained by analyzing their microscopic origin in the calculations (Appendix E). The schematic in Fig. 7.13a shows these excitons to have very distinct characteristics. For the IE, two degenerate states form at zero electric field, that is, IE₁ and IE₂. For IE₁, the electron is localized in the bottom layer and the hole is delocalized between the middle and bottom layers. For IE₂, the electron is localized in the top layer and the hole is delocalized between the middle and top layers. As such, IE₁ and IE₂ have a finite dipole

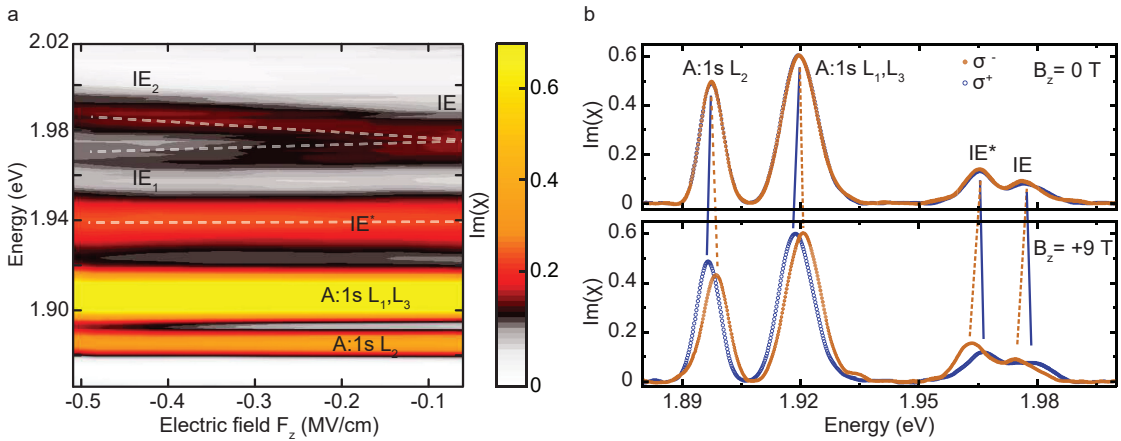


Figure 7.12. **MoS₂ trilayer in an applied electric and magnetic field.** **a**, Color map of the absorption spectra in device 2. **b**, Magneto-optics on device 3 with a small Zeeman splitting for intralayer excitons (A:1s) and large Zeeman splitting for interlayer excitons IE and IE* without (top) and with (bottom) magnetic fields of $B_z = +9$ T perpendicular to the monolayer plane.

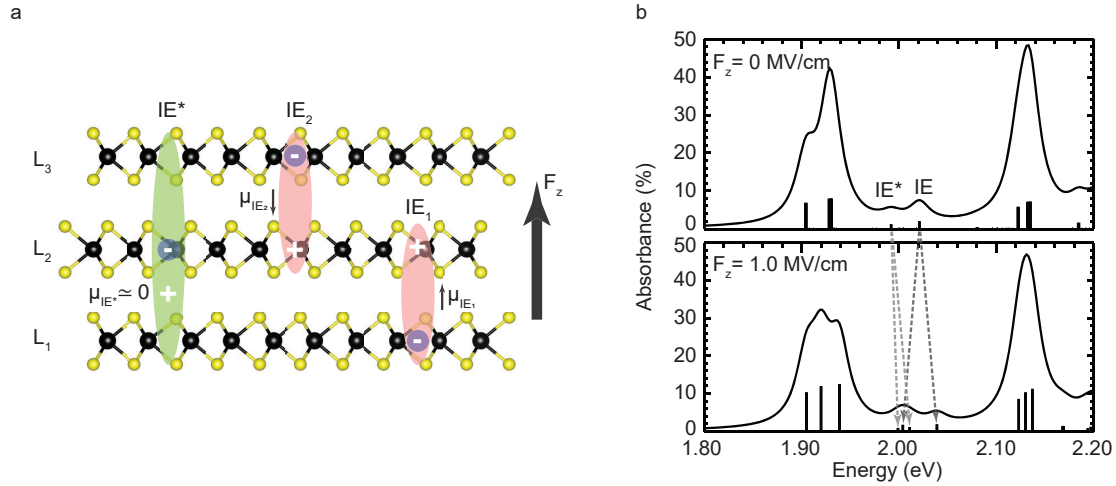


Figure 7.13. **Theoretical description of MoS₂ trilayer in an applied electric field.** **a**, Schematic of the studied 2H-stacked trilayer representing the microscopic origin of IE and IE*. **b**, Theoretical absorption spectra of 2H MoS₂ freestanding trilayer without (top) and with (bottom) an electric field. See Appendix E DFT calculations for a detailed discussion of the trilayer bandstructure and the effect of the electric field on it. The Stark shifts of IE and IE* are indicated by grey arrows.

moment, similar to the interlayer excitons in bilayers. We extract a dipole moment of $|\mu| \approx 0.15 e \cdot \text{nm}$. This smaller value with respect to the bilayer can have its origin in the different dielectric environment and a more localized hole wavefunction. The admixture of intralayer excitons with interlayer excitons does not change substantially over the investigated electric field range (Appendix E Table E.2).

For the IE* at slightly lower energy, the situation is different with respect to the IE: the electron is localized in the middle layer and the hole is delocalized over all three layers. This results in a negligible in-built electric dipole moment of IE* which translates into a non-resolvable Stark splitting of the transition in the measurements. The absence of a clear Stark shift might place the interlayer nature of the IE* into question. To answer this, magneto-optics were performed, shown in Fig. 7.12b. The intralayer excitons show a Zeeman splitting on the order of 2 meV at $B_z = +9$ T, while for IE and IE* the Zeeman splitting is on the order of 4 meV, with opposite sign compared to that of the intralayer transitions. This confirms the interlayer character of these peaks. These results lead to an unusual situation for interlayer excitons: a strong splitting in magnetic fields, but a very small Stark shift in electric fields.

7.8 Conclusion and outlook

In Chapter 6, we demonstrated that monolayer MoS₂ has a strong optical response, but the transition energy is not tunable via the QCSE, as the intralayer exciton has essentially no permanent out-of-plane electric dipole. In contrast, interlayer exciton transitions in heterobilayers are widely tunable in an applied electric field. However, their observation mostly relies on PL measurements. We showed that homobilayer MoS₂ combines the best of both worlds, a polarizable yet strong optical dipole. In its natural bilayer form, interlayer excitons form with high oscillator strength and large electrical tunability over 120 meV (see also [164, 167]). Owing to their very large opposing dipole moments, we were able to bring the interlayer excitons energetically close to resonance with the intralayer states. The interaction of the blue-shifted interlayer exciton with the intralayer B exciton showed clear signatures of strong coupling. In contrast, the interaction of the red-shifted interlayer exciton with the intralayer A exciton showed only a weak coupling. This allows us to conclude that the interlayer exciton has a strong B-exciton component in its wave function, but a much smaller A-exciton component. We expect that at even higher fields than those in these experiments, the interlayer exciton will lie lower in energy than that of the A exciton and will recover its absorption strength once it is sufficiently red-detuned from the A exciton. This will represent an advantageous scenario for applications: the ground-state exciton is long-lived and possesses both a large in-built electric dipole moment and a strong absorption.

For opto-electronics, the highly tunable excitons with an in-built dipole found here in MoS₂ bilayers are promising to explore coupling to optical cavity modes, where excitons and photons can couple to form polaritons [168, 169]. Very recently, optical non-linearities at a single polariton level have been detected in III-V semiconductors [170, 171]. To build on these promising proof-of-principle experiments, further work on excitonic systems with stronger exciton-exciton interactions is desirable.

8

Spin-polarized electrons in monolayer MoS₂

The content of this chapter is partially adapted from:

Jonas G. Roch, Guillaume Froehlicher, Nadine Leisgang, Peter Makk, Kenji Watanabe, Takashi Taniguchi, and Richard J. Warburton,

“Spin-polarized electrons in monolayer MoS₂”, Nature Nanotechnology 14, 432–436 (2019).*

8.1 Summary

Coulomb interactions are crucial in determining the ground state of an ideal two-dimensional electron gas (2DEG) in the limit of low electron densities [172]. In this regime, Coulomb interactions dominate over single-particle phase-space filling. In silicon and gallium arsenide, electrons are typically localized at these low densities. In contrast, in transition metal dichalcogenides (TMDs), Coulomb correlations in a 2DEG can be anticipated at experimentally relevant electron densities. Here, we investigate a 2DEG in a gated monolayer of the TMD molybdenum disulfide by optical absorption and photoluminescence spectroscopy. The optical probe of the 2DEG is particularly powerful: it is local and highly spin- and valley-selective [10]. In a magnetic field of +9.00 T and at electron concentrations up to $n \simeq 5 \times 10^{12} \text{ cm}^{-2}$, we present evidence of itinerant ferromagnetism in monolayer MoS₂. Out of the four available conduction bands [17, 21], only two are occupied. These two bands have the same spin but different valley quantum numbers. Our results suggest that only two bands are occupied even in the absence of a magnetic field. The spin-polarization increases with decreasing 2DEG density, suggesting

*G.F., J.G.R. and N.L. fabricated the device for absorption measurements. J.G.R. and G.F. carried out the absorption measurements and analyzed the optical absorption data. J.G.R. developed the exciton-polaron theory. N.L. and H.M. fabricated the device for photoluminescence (PL) measurements. N.L. performed the PL measurements and analyzed the data. N.L. and D.M. interpreted the results.

that Coulomb interactions are a key aspect of the symmetry breaking. We propose that exchange couplings align the spins [173]. The Bohr radius is so small [12] that even electrons located far apart in phase-space interact with each other [173].

8.2 Introduction

A two-dimensional electron gas (2DEG) is formed when the movement of free electrons is limited to two spatial dimensions. As the electron density n increases, single-particle effects (phase-space filling) increase more rapidly than the Coulomb interactions. The importance of Coulomb interactions is encoded in the Wigner-Seitz parameter, $r_s = \frac{1}{\sqrt{\pi n}} \frac{1}{a_B}$. Coulomb interactions dominate at large values of r_s [172].

Monolayer transition-metal dichalcogenides (TMDs), such as MoS₂, MoSe₂, WS₂ and WSe₂, represent a natural host for a 2DEG. There are two inequivalent conduction band valleys at the $+K$ and $-K$ points of the Brillouin zone. The large electron effective mass [21] and the weak dielectric screening result in an extremely small Bohr radius [12], ~ 0.5 nm. The immediate consequence is that r_s is pushed towards relatively large values at experimentally relevant electron concentrations. We focus on monolayer MoS₂. Monolayer MoS₂ has a graphene-like structure with Mo and S sub-lattices [7, 10] (see Chapter 2). The band edges are located at the $+K$ and $-K$ points; an energy gap of about 2.0 eV separates the conduction band (CB) from the valence band (VB). Spin degeneracy is lifted by spin-orbit coupling. In each valley, the two CBs are split by $\Delta_c \approx 3$ meV [17, 21, 174] and the two VBs are split by $\Delta_v \approx 150$ meV [17]. In MoS₂, the upper VB has the same spin as the lower CB [1]. Optical absorption promotes an electron from a VB state to a CB state with strict selection rules [10]: a circularly polarized σ^+ photon couples the VB and the CB with spin $|\uparrow\rangle$ at the $+K$ point; a σ^- photon couples the VB and the CB with spin $|\downarrow\rangle$ at the $-K$ point (see Chapter 2). We note that MoS₂ is a special TMD as the spin-orbit splitting in the CB is small compared with typical 2DEG Fermi energies [17]. There are four available bands: $+K_\uparrow$, $+K_\downarrow$, $-K_\uparrow$ and $-K_\downarrow$.

8.3 Experimental methods

Here, we use a gated monolayer MoS₂ van der Waals heterostructure (vdWH)* (see Appendix B). A monolayer of MoS₂ forms a planar capacitor with respect to a conductive substrate. The carrier density n in the monolayer is determined by a voltage V_G applied

*We employ two different devices for the absorption and PL measurements.

to the capacitor (see Chapter 3). The MoS₂ monolayer is encapsulated in hexagonal boron nitride (hBN): this allows close-to-ideal optical linewidths [72] and Shubnikov-de Haas oscillations [175] to be observed at low temperature. We measure both the optical susceptibility and the photoluminescence (PL) response at cryogenic temperatures ($T = 4\text{ K}$).

8.4 Optical absorption in gated monolayer MoS₂

In this section, we probe the 2DEG ground state in MoS₂ by measuring the susceptibility at optical frequencies. This probe is particularly powerful. First, it is a local measurement: signal is gleaned from a few-hundred-nanometer diameter spot on the sample. On this length scale, close-to-ideal optical linewidths have been demonstrated [72, 129], yet there are clearly inhomogeneities on larger length scales even with state-of-the-art material. Secondly, the measurement represents a weak perturbation to the ground state: in our experiments, there is, on average, less than one photo-created excitation (an exciton, an electron-hole pair) at a time. Thirdly, the optical probe is valley- and spin-selective via the polarization of the light [10].

Fig. 8.1 shows the local optical susceptibility $\text{Im}(\chi)$ as a function of electron concentration n at various values of the perpendicular magnetic field B_z . We focus initially on the susceptibility at $B_z = +9.00\text{ T}$ for $n \leq 6 \times 10^{12}\text{ cm}^{-2}$. At low electron density, the peak labelled X^0 dominates the susceptibility for both σ^+ and σ^- polarization. This resonance corresponds to the creation of a neutral exciton. As n increases, the X^0 blue-shifts (on account of bandgap renormalization), broadens and weakens, eventually disappearing into the noise. With σ^+ polarization, as X^0 weakens, two resonances emerge, labelled X_{LE}^- and X_{HE}^- . These two resonances are red-shifted with respect to X^0 . In the opposite photon polarization, σ^- , as n increases the X^0 resonance blue-shifts and weakens but for low to modest n there are no X^- features.

8.4.1 Exciton-polaron theory

The excitons injected into the 2DEG by our optical probe interact with the electrons in the Fermi sea. Theory has been developed to describe an exciton interacting either with a spin-degenerate Fermi sea at the Γ -point of the Brillouin zone [54, 176] or a spin-polarized Fermi sea [123], and successfully stress-tested against experiments on quantum wells [54] and monolayer MoSe₂ [122]. When the exciton-electron interaction is attractive, the exciton resonance splits into two exciton-polarons [122, 123]. The upper

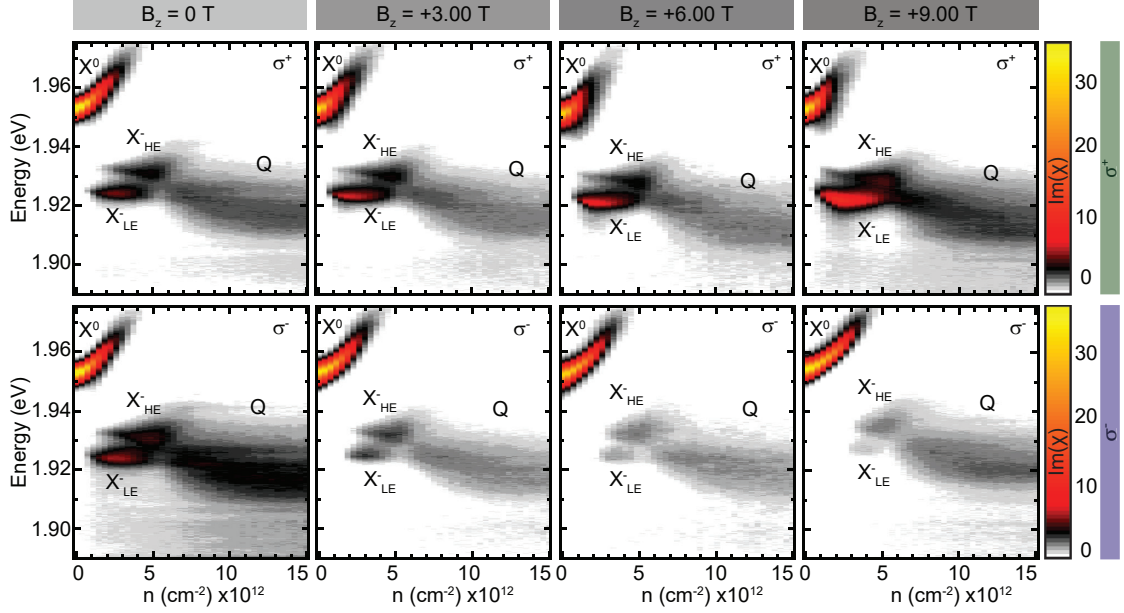


Figure 8.1. **Optical susceptibility of a gated monolayer of MoS₂.** The optical reflectivity is measured from a 400 nm diameter region on the device at low temperature ($T = 4$ K) using a confocal microscope and ultra-weak, incoherent light source (see Chapter 4). The imaginary part of the optical susceptibility is deduced from the reflectivity by accounting for optical interferences [56, 88] (see Chapter 4). At the optical resonance, the reflectivity contrast is very large, 60%; equivalently, the susceptibility is 30. The color maps show the optical susceptibility as a function of the photon energy (vertical axis) and electron concentration n (horizontal axis) in a perpendicular magnetic field B_z of 0, +3.00, +6.00 and +9.00 T with σ^+ polarized light (top panels) and with σ^- polarized light (bottom panels).

exciton-polaron corresponds to X^0 ; the lower exciton-polaron corresponds to X^- (and becomes the trion in the single-particle limit [1, 177, 178]). On the other hand, when the exciton-electron interaction is repulsive, only the X^0 appears in the susceptibility with a tail on the high-energy side (see Appendix F). In these theories, the interaction is attractive only if the electron in the exciton and the electron in the Fermi sea have opposite spins, a spin-singlet. The interaction is repulsive for parallel spins, a spin-triplet.

We apply the exciton-polaron theory to the MoS₂ susceptibility. With σ^+ photons, we observe not one but two lower exciton-polarons, X_{LE}^- and X_{HE}^- . This implies that the exciton interacts attractively with two Fermi seas, the energy splitting arising from different exciton-electron scattering cross-sections. With σ^- photons, the spectra follow the exciton-polaron theory for a repulsive exciton-Fermi sea interaction. Only the upper exciton-polaron is visible in the spectrum. For both σ^+ and σ^- photons, the details of the measured spectra match the exciton-polaron theory (see Appendix F).

8.4.2 Stable spin-polarization in a magnetic field

The comparison of the optical susceptibility results to the exciton-polaron theory leads to the conclusion that at $B_z = +9.00$ T, of the four bands only two are occupied, both with spin $|\downarrow\rangle$, that is, the $-K_\downarrow$ and $+K_\downarrow$ bands. A photon-generated electron-hole pair with electron spin $|\uparrow\rangle$ interacts attractively with spin $|\downarrow\rangle$ electrons from two different bands. This conclusion on the number of occupied bands can be verified via another feature of the susceptibility spectra. In the limit of large hole masses, the energetic separation between the upper and lower exciton-polarons is simply $\delta E = E(X^0) - E(X^-) = E_b + E_F$ where E_b is the trion binding energy and E_F is the Fermi energy [128], a result demonstrated experimentally on CdTe quantum wells [179]. For the equal hole and electron masses of MoS₂, this result applies at $E_F \geq 20$ meV. The gradient $d\delta E/dE_F$ increases from 1.0 to 2.0 as $E_F \rightarrow 0$. Our experimental data lie mostly in the high- E_F regime (see Supplement in [56]). This enables us to determine E_F from the optical spectra. As E_F is linked to n by the two-dimensional density of states, we can determine how many bands are populated. Taking an electron effective mass of $m_e^{\text{eff}} = 0.44m_0$ [21], the measured $d\delta E/dn$ (Fig. 8.2b) implies that 1.9 ± 0.1 bands are occupied at $B_z = +9.00$ T (see Supplement in [56]). It is worth adding that despite the large value of $B_z = +9.00$ T, no hints of Landau levels are observed in the low electron concentration regime, similarly to monolayer MoSe₂ [88] and WSe₂ [180]. Even at $B_z = +9.00$ T, Coulomb interactions

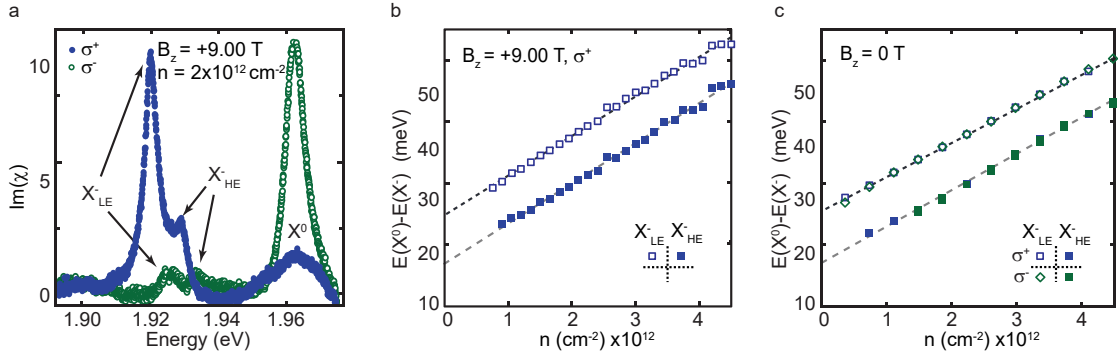


Figure 8.2. **Analysis of the optical susceptibility of a gated monolayer of MoS₂.** **a**, Imaginary part of the optical susceptibility $\text{Im}(\chi)$ at $B_z = +9.00$ T and $n = 2.0 \times 10^{12} \text{ cm}^{-2}$ for both σ^+ and σ^- photons. For σ^+ , two trion resonances (X_{LE}^- and X_{HE}^-) dominate the spectrum. (LE, low-energy; HE, high-energy.) For σ^- , X^0 dominates and has a high-energy tail. **b**, Energetic difference $E(X^0) - E(X^-)$ for the two trions at $B_z = +9.00$ T as a function of n . Linear fits give slopes of 6.1×10^{-15} and $6.3 \times 10^{-15} \text{ eVcm}^2$ for X_{LE}^- and X_{HE}^- , respectively. **c**, As in **b**, but at $B_z = 0$ T. Linear fits give 5.6×10^{-15} and $5.9 \times 10^{-15} \text{ eVcm}^2$ for X_{LE}^- and X_{HE}^- , respectively. The trion binding energies are 17 meV (X_{LE}^-) and 25 meV (X_{HE}^-).

are indeed so strong that the exciton is in the weak-field regime [58]. The experiment would therefore suggest that Landau quantization is not crucial for the spontaneous spin-polarization.

For $n \geq 6 \times 10^{12} \text{ cm}^{-2}$, X_{LE}^- and X_{HE}^- weaken and the susceptibility is dominated by a broad, red-shifted peak labelled Q (Fig. 8.1), which can be attributed to a Mahan-like exciton [181]. We speculate that the absence of a marked contrast between σ^+ and σ^- polarization signals that the 2DEG is no longer spin-polarized [181, 182].

We turn now to the magnetic field dependence. At $B_z = 0 \text{ T}$, the X_{LE}^- and X_{HE}^- features are equally strong for both σ^+ and σ^- photons (Fig. 8.1). As B_z increases, the X_{LE}^- and X_{HE}^- gradually disappear for σ^- photons. At $B_z = 0 \text{ T}$, the gradients $d\delta E/dn$ (Fig. 8.2c) change by less than 10% with respect to $B_z = +9.00 \text{ T}$, suggesting that even in this limit, only two bands are occupied. Given the equivalence of the spectral signatures at $B_z = 0 \text{ T}$ with respect to those at $B_z = +9.00 \text{ T}$ (Fig. 8.1), the same two bands are occupied, the two with the same spin but different valley indices. We speculate that in the absence of a magnetic field, small fluctuating “puddles” of spin $|\uparrow\rangle$ and spin $|\downarrow\rangle$ electrons form, resulting in a zero net magnetization [181]. Applying an external magnetic field $B_z = +9.00 \text{ T}$ in the experiment favors the magnetization to lie either in the “up” or “down” direction, stabilizing the spin-polarization.

8.5 Photoluminescence in gated monolayer MoS₂

The observation that two lower-energy exciton-polaron branches (trions) form for excitons created at the $+K$ point, while the interaction appears to be repulsive for excitons created at the $-K$ point, suggests that only the two CBs with spin $|\downarrow\rangle$ are filled.

We now probe the ground state of the electrons in monolayer MoS₂ by measuring the PL response as a function of the electron density. A laser with photon energy 1.959 eV is used to excite the MoS₂ close to resonance with the X^0 optical transition. Specifically, our experiment is designed to excite the MoS₂ with either right-handed (σ^+) or left-handed (σ^-) circularly polarized light and to detect both, the σ^+ and σ^- PL response in a magnetic field ($B_z = +9.00 \text{ T}$). Owing to the robust optical selection rules in monolayer TMDs (Fig. 8.3), this probe is highly spin- and valley-selective. Crucially, the cross-polarized emission channels give information on intervalley exchange mechanisms.

Our PL spectra reveal Lorentzian shaped lines approaching the ideal homogeneous limit. The general behavior of the emission as a function of electron density is compa-

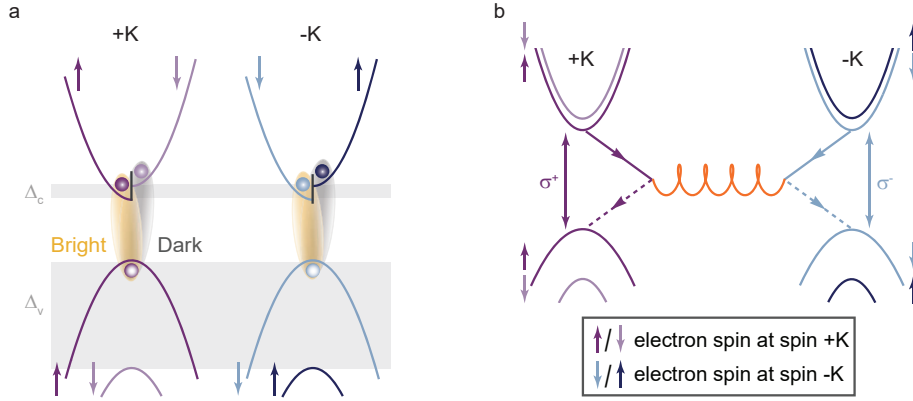


Figure 8.3. **Monolayer MoS₂**. **a**, Bandstructure of monolayer MoS₂. The colors (light/dark purple, light/dark blue) correspond to the electron spin states (spin | ↓)/ spin | ↑) at the + K and $-K$ point. Photoluminescence (PL) results from the radiative recombination of bright excitons with same electron spins. The very small spin-orbit (SO) splitting in the conduction band $\Delta_c \approx -3$ meV [21] results in approximate degeneracy of the bright (yellow) and dark (grey) excitons within their linewidth. **b**, Electron-hole exchange diagram. Here, the exciton from the + K valley scatters into the exciton in the $-K$ valley via the annihilation channel, flipping the spins of both electron and hole. Due to the valley-dependent optical selection rules, σ^+ (σ^-) circularly polarized light addresses the transition at the + K ($-K$) point of the Brillouin zone. The conduction electron (valence hole) wave function is shown by solid (dashed) lines. The orange wavy line corresponds to the long-range Coulomb interaction; the + K ($-K$) valley is indicated with purple (blue) color.

table with our absorption measurements. At charge neutrality ($n \simeq 0$), a sharp peak, labelled as X^0 , dominates the spectrum in all four combinations of circular polarization (Fig. 8.4). Applying a gate voltage to the electrode, effectively tuning n , the X^0 shifts to higher energies and weakens, eventually disappearing into the noise. For moderate, but large-enough n , red-shifted resonances emerge in the spectrum. With σ^+ collection, the optical spectrum consists of three peaks, labelled as T_1 , T_2 and T_3 . When light is collected with the opposite polarization, σ^- , only one peak, T_4 , is visible in the PL data. At $n \approx 4.0 \cdot 10^{12} \text{ cm}^{-2}$ *, a broad feature appears below the trion peaks, labelled as Q , and quickly gains intensity at even higher electron densities. Similar to absorption, there is no clear contrast between the different polarization channels for the Q -peak.

The optical response at $n \simeq 0$ arises from the recombination of tightly bound electron-hole pairs, neutral excitons. At small electron densities, an optically excited exciton can trap an electron from the Fermi sea due to the attractive charge-dipole interaction [183].

*The carrier density is determined via $n = C \cdot V_G$ (see Chapter 3), where $C = 97.9 \pm 4.9 \text{ nFcm}^{-2}$ is the capacitance of the device and V_G is the voltage applied to the FLG back-gate.

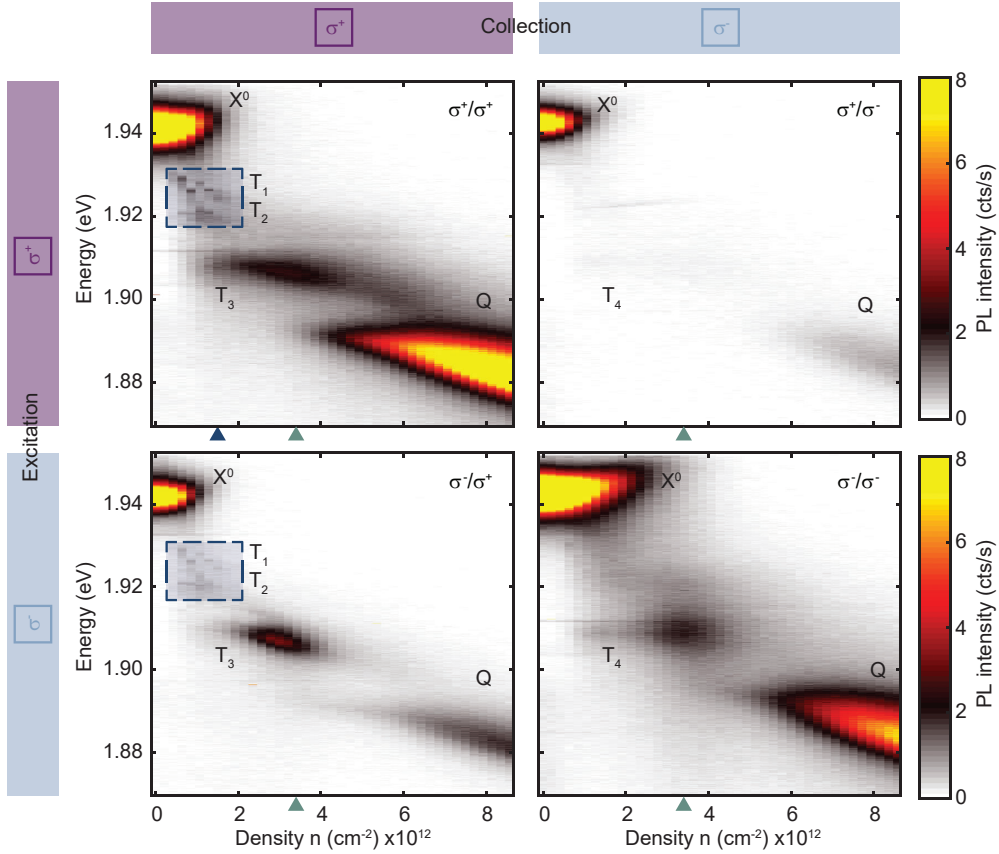


Figure 8.4. **Helicity-resolved photoluminescence (PL) of gated monolayer MoS₂.** The color maps show the optical PL response ($T = 4\text{K}$) as a function of the photon energy (vertical axis) and the electron density n (horizontal axis) in a perpendicular magnetic field ($B_z = +9.00\text{T}$) for all four polarization combinations (excitation/collection). The diagonal panels correspond to the co-polarized channels σ^+/σ^+ and σ^-/σ^- , while the top (bottom) off-diagonal panel shows the signal in the cross-polarized σ^+/σ^- (σ^-/σ^+) channel. X^0 denotes the neutral exciton, T_1 and T_2 (marked with a blue dashed square), T_3 and T_4 correspond to different trion states. Q labels the peak appearing at high n densities, previously interpreted as a Mahan exciton [181]. We note that the neutral exciton resonance is saturated for better visibility of the trion resonances, reaching up to 45 cts/s at $n \simeq 0$ in the σ^-/σ^- polarization.

The resulting bound state is known as the negatively charged exciton, or trion [184], which is similar in spirit to the negative hydrogen ion [185, 186]. Such a physical picture is only valid for small Fermi energies $E_F \lesssim E_T$, where E_T is the trion binding energy. In monolayer MoS₂, the trion binding energy is around 20–40 meV (with radius of 10–20 Å [187, 188]), depending on temperature and underlying substrate [1, 187–194]. Increasing the Fermi energy, that is, increasing the gate voltage in our experiment, the

trion resonance strengthens, while the exciton resonance broadens and loses its amplitude due to the scattering with itinerant electrons and relaxation to the trion state [54]. At high Fermi energies $E_F \gtrsim E_T \sim 30$ meV [190, 191, 193], where $n \gtrsim 1/a_T^2$, $a_T \sim 20$ Å is the trion size, the exciton interacts with many electrons at the same time and the simple trion picture is not longer accurate. Instead, the exciton is dressed by the electron-hole pairs of the fluctuating Fermi sea, forming a collective exciton-polaron quasiparticle [55, 122, 123, 188, 195, 196].

8.5.1 Exciton valley depolarization in monolayer MoS₂

PL arises from the radiative recombination of bright excitons at the $+K$ or $-K$ point (Fig. 8.3a). These excitons must have the same electron spins in order to be created by, or recombine into, photons. The optical selection rules ensure that normally incident σ^+ (σ^-) circularly polarized light can only create an exciton in the $+K$ ($-K$) valley (Fig. 8.3b). Conversely, one can measure the valley polarization of the photo-excited electrons, because σ^+ (σ^-) photons originate from the recombination of excitons in the $+K$ ($-K$) valley. In our experiment, the valley polarization η of the optically excited electrons can be estimated from the neutral exciton intensities detected in the circular polarization of the same I_{co} (σ^+/σ^+) and opposite helicity I_{cross} (σ^+/σ^-) compared to the excitation light (see Appendix F)

$$\eta = \frac{I_{\text{co}} - I_{\text{cross}}}{I_{\text{co}} + I_{\text{cross}}} \approx 42.7\%. \quad (8.1)$$

This number indicates a significant bright exciton transition between the $+K$ and $-K$ valley in our monolayer MoS₂ vdWH. This is strong evidence of an electron-hole exchange mechanism.

Assuming that electron-hole exchange is the only significant mechanism, and applying a rate equation model,

$$\frac{\tau_{eh}}{\tau_R} \simeq 2 \left(\frac{\eta}{\eta - 1} \right). \quad (8.2)$$

Taking a typical value for the radiative lifetime, $\tau_R \simeq 4$ ps [190, 197], the measured value of η allows the electron-hole exchange time to be estimated as $\tau_{eh} \simeq 6$ ps. This is similar to other estimates of the exciton-valley relaxation time [198]. The electron-hole exchange is caused by the long-range Coulomb interaction (Fig. 8.3b) [199–201]. This mechanism is similar to the Bir-Aronov-Pikus mechanism of the electron spin relaxation due to the interaction with holes [202]. Here, we do not consider exciton-exciton interactions [203, 204], due to the low laser power and therefore small exciton densities in our experiment.

8.5.2 Trion states in monolayer MoS₂

Experimental observations

The optical response of monolayer MoS₂ strongly depends on the doping. We focus on the PL at small-to-moderate electron densities, that is, where the negatively charged trions are present. Different sample positions, labelled as P1, P2 and P3, are investigated, marked by white circles on the position-dependent PL map (σ^-/σ^- polarization, $n = 0$) (Fig. 8.5b) recorded from the region indicated by the white dashed square in the optical image on Fig. 8.5a. P1, P2 and P3 represent clean spots on the sample, reflected by high intensities and narrow optical linewidths of the X^0 ($\Gamma = 2.8 - 4.1$ meV) at $n \simeq 0$. We present here the data obtained on position P1 (see Appendix F for P2 and P3).

In the σ^+/σ^+ and σ^-/σ^+ configurations, as the X^0 transition weakens, three resonances emerge, labelled as T_1 , T_2 and T_3 . We note that the different trion states are very close in energy, that is, the energy difference between them is on the order of a few meV. This makes it rather difficult to distinguish them experimentally. A clear observation of the two trions T_1 and T_2 in our experiment (Fig. 8.6a) is probably related to the high sample quality. In the two polarization channels with σ^- collection, as the carrier density increases, the X^0 blue-shifts and weakens, but only one trion feature appears, labelled as T_4 .

Fig. 8.6c plots the linewidth of the low-energy trions as a function of the electron density. The trion T_3 in σ^+/σ^+ and σ^-/σ^+ polarization shows a non-monotonic behavior

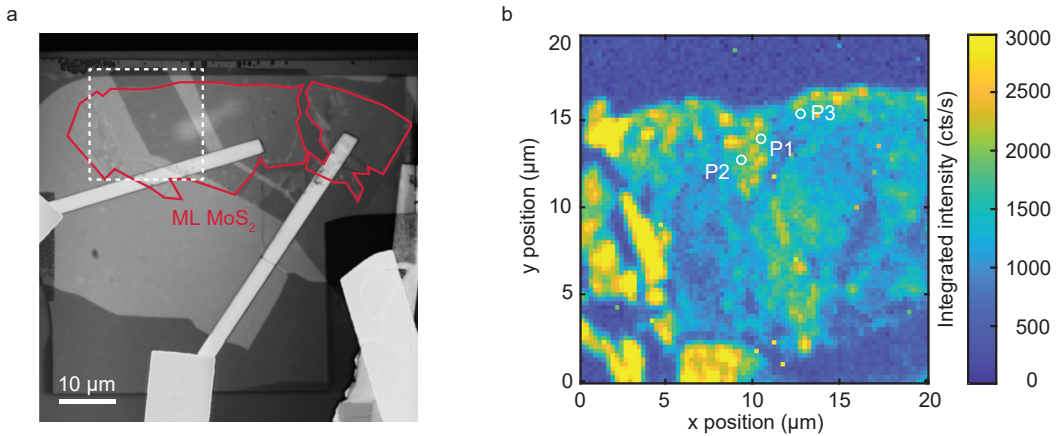


Figure 8.5. **Sample positions.** **a**, Optical image of the device structure. The monolayer (ML) MoS₂ region is marked in red. **b**, Total integrated PL intensity (σ^-/σ^- channel, $n \simeq 0$) from the region marked by the white dashed square in **a** ($T = 4$ K). The different sample positions P1, P2 and P3 are indicated by white circles.

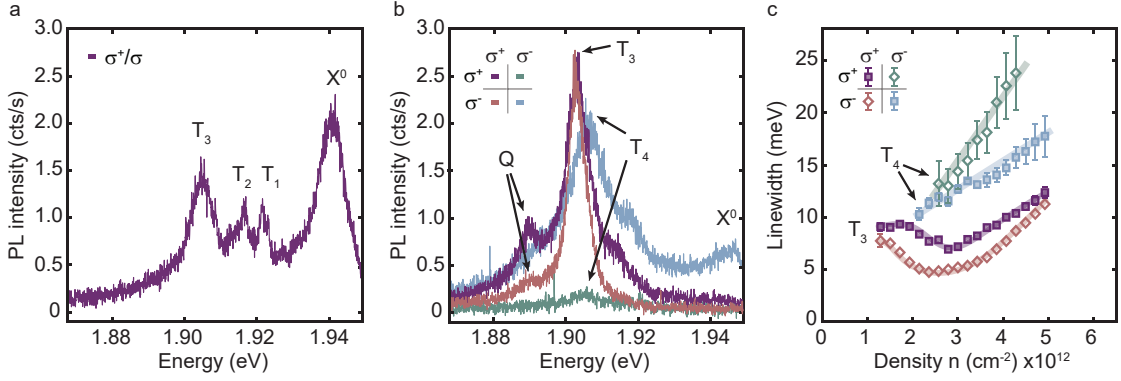


Figure 8.6. **Analysis of the photoluminescence (PL) response of gated monolayer MoS₂.** **a**, PL signal at $B_z = +9.00$ T and $n = 1.5 \cdot 10^{12} \text{ cm}^{-2}$ in σ^+/σ^+ polarization (indicated by a blue triangle in Fig. 8.1). The two trion states T_1 and T_2 are clearly visible. **b**, Optical spectra at $n = 3.4 \cdot 10^{12} \text{ cm}^{-2}$ in all four polarization combinations (indicated by green triangles in Fig. 8.1). Neutral exciton X^0 , low-energy trions T_3 and T_4 , as well as the Q -peak are labelled. **c**, Linewidths of the low-energy trion states versus n . For σ^+/σ^+ and σ^-/σ^+ , the trion linewidth shows a non-monotonic behavior. For σ^-/σ^+ and σ^-/σ^- , the linewidth increases linearly as a function of n . The error bars represent a 95% confidence interval that is calculated from the uncertainty in the Lorentzian fit (see Appendix F).

in its linewidth, whereas the one in σ^+/σ^- and σ^-/σ^- polarization has a linewidth which increases nearly linearly with n . This difference already points to the fact that T_3 and T_4 correspond to different trion states.

Theoretical description of three-particle trion states

We use the few-particle trion picture to interpret our experimental results (see Appendix F for a detailed description). This approach is valid as long as the Fermi wavelength $\sim 1/k_F$, k_F is the Fermi momentum, is much larger than the trion size $a_T \sim 20 \text{ \AA}$ [187, 188, 205]. This is the case for low electron densities in our experiment.

For single-valley materials, two electrons in the trion bound state have to form a spin singlet due to the Pauli exclusion principle [54]. However, in monolayer MoS₂, electrons have an additional valley degree of freedom τ . This results in the intravalley $|S_d\rangle$ and intervalley $|S_i\rangle$ spin singlet trions as well as in the intervalley spin triplet $|T_s\rangle$ trions (see

Appendix F) [53]

$$|S_d\rangle = |\tau K\rangle_1 |\tau K\rangle_2 \frac{|\uparrow\rangle_1 |\downarrow\rangle_2 - |\downarrow\rangle_1 |\uparrow\rangle_2}{\sqrt{2}}, \quad (8.3)$$

$$|S_i\rangle = \frac{|+K\rangle_1 |-K\rangle_2 + |-K\rangle_1 |+K\rangle_2}{\sqrt{2}} \frac{|\uparrow\rangle_1 |\downarrow\rangle_2 - |\downarrow\rangle_1 |\uparrow\rangle_2}{\sqrt{2}}, \quad (8.4)$$

$$|T_s\rangle = \frac{|+K\rangle_1 |-K\rangle_2 - |-K\rangle_1 |+K\rangle_2}{\sqrt{2}} \chi_s. \quad (8.5)$$

Here, we only present the electron component of the trions, $\tau = \pm 1$ labels the valley, and χ_s , $s \in \{-1, 0, 1\}$ is the triplet spinor

$$\chi_+ = |\uparrow\rangle_1 |\uparrow\rangle_2, \quad (8.6)$$

$$\chi_0 = \frac{|\uparrow\rangle_1 |\downarrow\rangle_2 + |\downarrow\rangle_1 |\uparrow\rangle_2}{\sqrt{2}}, \quad (8.7)$$

$$\chi_- = |\downarrow\rangle_1 |\downarrow\rangle_2. \quad (8.8)$$

These trion states have different energies due to k -dependent Coulomb interactions, SO splitting in the conduction band and different effective masses of the SO split bands.

8.5.3 Evidence of full spin-polarization in a magnetic field

In this work, we are able to resolve three trion peaks in the σ^+/σ^+ and σ^-/σ^+ channels (Fig. 8.6a), while the σ^-/σ^- and σ^+/σ^- channels contain only a single trion peak. In the following, we show that this PL picture is only possible in case of an electron Fermi sea which is fully spin-polarized with spin $|\downarrow\rangle$ projection (in accordance with our absorption measurements).

Let us first consider the excitation by circular light with σ^+ polarization. Due to the optical selection rules, this results in the optical absorption in the $+K$ valley [2, 10]. The bright excitons excited during this process consist of a CB electron with spin $|\uparrow\rangle$ and a VB hole with spin $|\downarrow\rangle$ (Fig. 8.3). (This means that the valence band is filled with electrons with spin $|\uparrow\rangle$.) Accordingly, we fix the electron component of the photo-excited exciton to

$$|ex_+\rangle = |+K\rangle |\uparrow\rangle. \quad (8.9)$$

Let us assume that our MoS₂ monolayer is an itinerant ferromagnet with only spin $|\downarrow\rangle$ Fermi seas filled in each valley. Binding an $|+K\rangle |\downarrow\rangle$ electron to the exciton (Eq. 8.9), we create the $|S_d\rangle$ trion (Eq. 8.4) (see Appendix F for details). On the other hand, if the

photo-excited exciton binds to an $| - K \rangle | \downarrow \rangle$ electron, this creates a superposition of the $|S_i\rangle$ and $|T_0\rangle$ states

$$\frac{|+K\rangle_1 | \uparrow \rangle_1 | -K\rangle_2 | \downarrow \rangle_2 - | -K\rangle_1 | \downarrow \rangle_1 | +K\rangle_2 | \uparrow \rangle_2}{\sqrt{2}} = \frac{|S_i\rangle + |T_0\rangle}{\sqrt{2}}, \quad (8.10)$$

where $|S_i\rangle$ and $|T_0\rangle$ are the eigenstates of the three-body problem (Eqs. (8.3), (8.5)) (see also Appendix F). According to our analysis, this state is optically bright: optical excitation results in both a peak at the $|S_i\rangle$ energy and a separate peak at the $|T_0\rangle$ energy (Fig. 8.6a). This coincides with our observations. The trion T_3 appears as a strong low-energy peak while the other two peaks T_1 and T_2 appear and disappear at similar electron densities.

As discussed earlier, long-range Coulomb interactions can cause an exciton to be transferred from one valley to the other, flipping the spins of both electron and hole (Fig. 8.3b). In other words, if an exciton is created with σ^+ polarization, there is a certain possibility to detect a σ^- photon due to valley- and spin-depolarization. In our experiment, a valley polarization of $\eta \approx 42.7\%$ suggests that this effect is significant. This implies that, at finite electron density, the $|+K\rangle | \uparrow \rangle$ exciton, which can bind to an $|+K\rangle | \downarrow \rangle$ electron forming $|S_d\rangle$, can scatter into the $| - K \rangle | \downarrow \rangle$ exciton, which can bind to an $|+K\rangle | \downarrow \rangle$ electron to form the triplet $|T_- \rangle$ trion (see Fig. 8.7a and Appendix F). This trion can radiatively recombine emitting a σ^- photon.

In our experiment, the difference in the linewidth for the low-energy trions T_3 (in σ^+/σ^+) and T_4 (in σ^+/σ^-) as a function of density, $\Gamma(n)$, in Fig. 8.6c points to the different nature of the two transitions. A large $d\Gamma/n$ for T_4 with respect to T_3 suggests the triplet character. We note that T_4 only appears as a very broad faint peak in the σ^+/σ^- channel. The strong X^0 response compared to the weak response at $n > 1 \times 10^{12} \text{ cm}^{-2}$ in the σ^+/σ^- channel is strong evidence for the electron-hole exchange. Once a Fermi sea is established the process is suppressed – the optically generated exciton cannot be transferred to the $-K$ valley due to the presence of a $| - K \rangle | \downarrow \rangle$ Fermi sea.

Following a similar analysis, the state in Eq. 8.10 cannot be exchanged into an optically bright exciton (Fig. 8.7b): binding of an $| - K \rangle | \downarrow \rangle$ exciton to an $| - K \rangle | \downarrow \rangle$ electron would imply an intravalley triplet trion with same spin and valley quantum number. This process is not possible due to the Pauli exclusion principle (Fig. 8.7b).

Next, let us consider excitation with σ^- polarized light. Here, the electron component

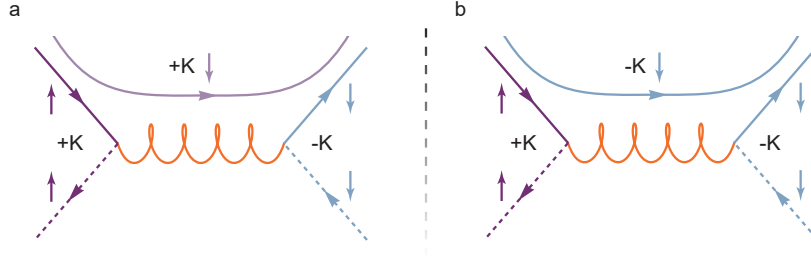


Figure 8.7. **Electron-hole exchange diagrams.** **a**, Electron-hole exchange diagram resulting in the exchange of the direct $|S_d\rangle$ trion, created by σ^+ polarized light, to the triplet $|T_-\rangle$ trion. This state can recombine, sending out a σ^- photon. **b**, Electron-hole exchange diagram showing that the trion state in Eq. 8.10 does not contribute to the σ^+/σ^- channel. The resulting state has to be the intravalley spin triplet trion, which is known to be unbound [54]. Here, the $+K$ ($-K$) valley is shown in purple (blue); electron spins are indicated by arrows. The orange wavy line illustrates the long-range Coulomb interaction.

of the exciton is

$$|ex_-\rangle = | -K\rangle | \downarrow \rangle. \quad (8.11)$$

Such excitons can only bind $| +K\rangle | \downarrow \rangle$ electrons from the fully spin-polarized Fermi sea, forming $|T_-\rangle$ trions (see Appendix F). This is consistent with our observations from the σ^-/σ^- channel; only one trion T_4 is visible in the optical spectrum. Again, we can use $\Gamma(n)$ as a diagnostic tool to identify the states in our data. Comparing the density dependence of the linewidths of the low-energy resonances in the σ^+/σ^- and σ^-/σ^- channels (Fig. 8.6c), we can indeed confirm that they correspond to the same trion resonance identified as the triplet trion $|T_-\rangle$.

Finally, we consider the electron-hole exchange of optically excited excitons from the $-K$ to the $+K$ valley. This corresponds to the change of the electron component of the excitons from Eq. 8.11 to Eq. 8.9. In this case, we expect the PL picture in the σ^-/σ^+ channel to be qualitatively similar to the one in the σ^+/σ^+ channel, that is, the appearance of the states in Eq. 8.10 and the direct singlet trion $|S_d\rangle$ (Eq. 8.4). Indeed, the trion peak T_3 has a very characteristic non-monotonic linewidth dependence as a function of the electron density (Fig. 8.6c). This allows us to identify it in both channels with σ^+ collection, σ^+/σ^+ and σ^-/σ^+ .

Now, what would happen if the other two Fermi seas, namely $| \pm K\rangle | \uparrow \rangle$, were filled? First, the $| -K\rangle | \uparrow \rangle$ Fermi sea would result in the appearance of the $|S_d\rangle$ trion in the σ^-/σ^- channel. Even though the energies of T_3 and T_4 in our experiment are

quite similar, their linewidths are very different. Therefore, we would still be able to distinguish them. Similarly, the $|S_d\rangle$ trion would appear in the σ^+/σ^- channel after electron-hole exchange. In our optical data, we have no evidence of the T_3 peak in the σ^+/σ^- channel. Second, the $|+K\rangle|\uparrow\rangle$ Fermi sea would give rise to the mixed bright-dark trion states in the σ^-/σ^- and σ^+/σ^- channels. We also do not see any signatures of T_1 and T_2 in these channels.

8.6 Conclusion and outlook

The conclusion of our experimental (absorption and PL) and theoretical analysis is unambiguous: out of four possible bands two are occupied. This spin-polarization of the MoS₂ 2DEG can be qualitatively understood by exchange [206] and the strong intervalley Coulomb scattering [173]. At low temperature, the “first” injected electrons populate the band with lowest energy. Intravalley and intervalley exchange will then favour population of the bands with the same electron spin: the small CB spin-orbit splitting implies a moderate cost in kinetic energy. These results highlight a very particular feature of TMDs. The Bohr radius is only slightly larger than the lattice constant such that the two-body Coulomb interaction connecting an electron at the $+K$ point with an electron at the $-K$ point (far apart in phase-space) is comparable to the two-body Coulomb interaction between two electrons close together in phase-space [173].

At first sight, the spin-polarization mimics Stoner ferromagnetism. However, the Stoner mechanism is based on a mean-field theory which is invalid in two-dimensions for which ferromagnetic order is excluded by the Mermin-Wagner theorem [207]. However, the CB spin-orbit splitting, which is small but non-zero, establishes an in-built quantization axis such that a spontaneous symmetry-breaking is feasible, Mermin-Wagner notwithstanding.

9

Conclusion and outlook

In two-dimensional (2D) transition metal dichalcogenides (TMDs), excitons exhibit strong light-matter interactions as a consequence of the pronounced Coulomb interaction between electrons and holes. Within this thesis, we have demonstrated that the excitons are additionally highly tunable through charge density and electric field control via external electrical gates.

Fig. 9.1 depicts the progress in controlling excitons in 2D semiconducting TMDs, demonstrating their potential for interaction-driven physics and opto-electronic applications when combined in *“layered structures with just the right layers”**.

Using a gated van der Waals heterostructure (vdWH), we demonstrated that excitons in monolayer MoS₂ can be polarized (Chapter 6). However, the corresponding energy shifts are quite small. To control excitons effectively via the QCSE larger polarizabilities or a non-zero out-of-plane electric dipole moment are required. Interlayer excitons were realized in a MoSe₂/WSe₂ heterobilayer, where the bound electrons and holes reside in different layers. Applying an electric field at close-to-zero carrier concentration, these interlayer excitons could be tuned over a spectral range of around 80 meV (Chapter 6). However, while these excitons exhibit a large permanent electric dipole moment, they are only weakly coupled to light, and their observation mostly relies on PL emission.

To obtain a polarizable yet strong optical dipole, homobilayer MoS₂ was integrated in a dual-gate device structure. We discovered interlayer excitons with high oscillator strength and large electrically tunability over 120 meV. By applying an electric field, the degeneracy of the two exciton configurations was lifted and interlayer excitons could be

* *“What could we do with layered structures with just the right layers? What would the properties of materials be if we could really arrange the atoms the way we want them?”*
— Richard P. Feynman, “There’s Plenty of Room at the Bottom” (1959).

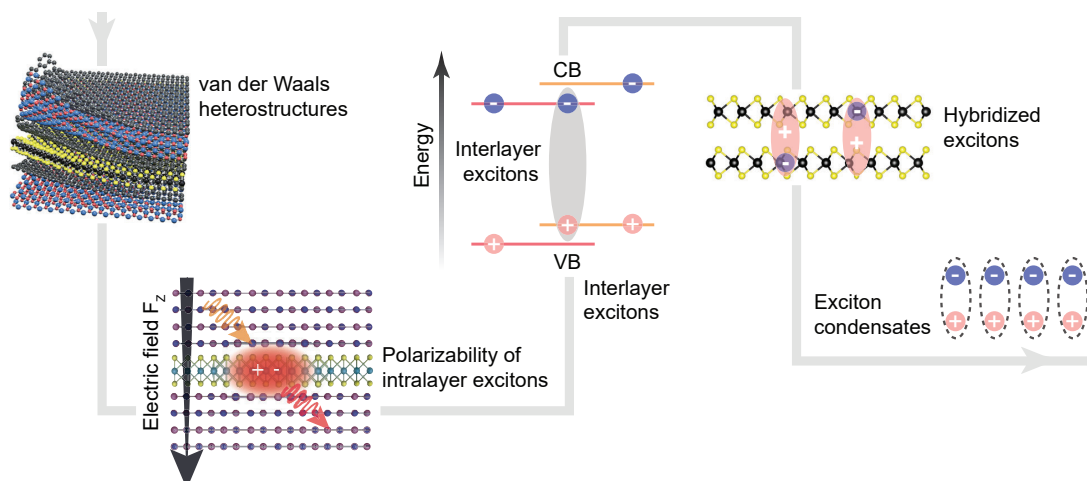


Figure 9.1. **Progress in controlling excitons in 2D semiconducting transition metal dichalcogenide van der Waals heterostructures (vdWHs).** Creating designer materials to realize excitons with strong light-matter interactions and strong exciton-exciton interactions. The figure of the vdWH is adapted from Ref. [208].

tuned energetically close to resonance with the intralayer states. We demonstrated that the interlayer excitons interact with both intralayer excitons confined to the single layers (Chapter 7).

In general, exciton-exciton interactions in semiconductors lead to many interesting phenomena such as nonlinear optical and condensation effects, as has been widely studied in III–V quantum wells. 2D TMDs, especially bilayer systems with large exciton dipoles, provide a promising alternative to conventional III–V quantum wells. On the one hand, excitons in 2D TMDs are very robust, which makes them stable even at room temperature. On the other hand, the interactions can be engineered by utilizing the unique spin-, valley-, layer- and twist-degrees of freedom. This makes these systems an interesting platform for exploring exotic quantum phenomena, such as macroscopic condensation in ensembles of interacting excitons [41, 136, 141]. At the few-exciton level, the repulsion between excitons can be employed to confine single excitons in potential traps [170, 171]. Here, semiconducting TMDs offer many technological advantages. Unlike III–V semiconductors, they are atomically flat without dangling bonds, and active elements can be positioned close to the surface.

Equipping monolayer MoS_2 with electrical gates allows electrons to be injected, creating a two-dimensional electron gas (2DEG). Optically probing the interaction between excitons with the electrons from the underlying Fermi sea, we found evidence that the

electrons have the same spin. Two of the possible four bands are occupied – the two with the same spin but in different valleys. This is a striking result: the creation of a spontaneous spin-polarization in a 2DEG (Chapter 8). To confirm the presence of the spin-polarized state in monolayer MoS₂, the magnetic signal could be directly probed with a sensitive spectrometer [209], such as magnetic nanowires (NWs) [210]. The combination of high magnetic force sensitivity, nanometer resolution, and the ability to operate in high-field configurations makes these scanning magnetic force sensors ideal candidates to measure subtle magnetization textures. We further point out that full spin-polarization is achieved here at rather large external magnetic fields. One possibility to stabilize the spin-polarizations at lower magnetic fields is the use of a magnetic substrate [211]. In turn, patterning this substrate may allow a textured spin-polarization to be generated.

Appendices

A

Supplementary information to Chapter 3: “Building high-quality opto-electronic devices with two-dimensional semiconductors”

In Chapter 3 the most important fabrication techniques are introduced. This Appendix provides more details of our fabrication recipes.

A.1 Building blocks for van der Waals heterostructures

A.1.1 Two-dimensional crystals

In Table A.1 below, we list the different 2D materials and the sources of their bulk crystals used within this thesis.

| 2D material | Type | Source |
|--------------------|----------------|---|
| MoS ₂ | Natural | SPI Supplies |
| MoSe ₂ | Synthetic | HQ Graphene |
| WSe ₂ | Synthetic | HQ Graphene |
| InSe | Bridgman-grown | A. Patané, School of Physics and Astronomy, University of Nottingham |
| hBN | Synthetic | K. Watanabe and T. Taniguchi [212] |
| Graphite | Natural | NGS Nanographit, HQ Graphene, or Graphene Supermarket |

Table A.1. Sources of different bulk crystals used for exfoliation of 2D materials.

A.1.2 Exfoliation material

For the mechanical exfoliation of the different 2D crystals, we generally use one of the two tapes (#1 or 2) listed in Table A.2. For exfoliating single-layers of TMDs, we sometimes additionally employ thin “Gelfilm” (#3) – a viscoelastic material based on polydimethylsiloxane (PDMS) – to transfer the flakes from the tape (#1 or 2) to the Si/SiO₂ substrate. This additional step tends to reduce the amount of tape residues and results in the exfoliation of only a few, but very thin flakes on the substrate.

| # | Product name | Product number | Source |
|---|--------------|----------------|----------------|
| 1 | Nitto tape | ELP BT-150P-LC | Nitto |
| 2 | Blue tape | 1005R-6.0 | Ultron Systems |
| 3 | Gelfim | WF-25-X4 | Gel-Pak |

Table A.2. **Sources of various tapes used for exfoliation.**

A.1.3 Substrates

As described in Chapter 3, 2D crystals are exfoliated onto Si substrates with either a ~ 80 nm or ~ 285 nm thick oxide layer to increase their optical contrast. Table A.3 provides more details of the substrate characteristics used for exfoliation and device fabrication.

| Characteristics | Specifications |
|--------------------------------|--|
| Substrate material | Silicon $\langle 100 \rangle$, 500–550 μm thick |
| SiO ₂ capping layer | 0 \pm 5% nm silicon oxide 285 \pm 5% nm silicon oxide |
| Doping level | Undoped or p ⁺⁺ -doped |
| Resistivity | > 10 ⁴ Ω cm |

Table A.3. **Substrate characteristics.** Specifications of the Si/SiO₂ substrates used for exfoliation and device fabrication.

Substrate cleaning

1. First, we dice the wafer into appropriate sizes (10 mm × 10 mm).
2. We then clean the pieces with acetone and IPA under sonication for around 5 min each and blow-dry them with N₂.
3. Optionally, we do an additional O₂ plasma treatment after the general cleaning procedure, which tends to reduce the amount of tape residues on the substrate when exfoliating.

A.2 Assembly of van der Waals heterostructures

In the following, we present a detailed protocol for building vdWHs (see Chapter 3). The first part describes the preparation of the polymer stamp used to pick up the layers. Next, we explain our general stacking procedure for assembling the devices. In the last part, we introduce a slightly modified recipe used when placing vdWHs close to the chip edge.

A.2.1 Polymer stamp

Our pick-up procedure uses an elastic polymer stamp, consisting of a home-made polydimethylsiloxane (PDMS) block covered by a thin layer of polycarbonate (PC). The preparation of the two components (Table A.4), as well as the fabrication of the stamp are described below.

| Polymer | Specifications | Source |
|----------------------------------|--|---------------|
| Polydimethylsiloxane (PDMS) | 184 Silicone elastomer kit (base and curing agent) | Sylgard |
| Poly(Bisphenol-A-carbonate) (PC) | Analytical standard (pellets) $M_W = 28.2$, $M_n = 17.0$ | Sigma-Aldrich |

Table A.4. **Polymers used for the transfer stamp.**

Polydimethylsiloxane (PDMS)

1. We mix the “silicone elastomer base” and the “silicone elastomer curing agent” with a ratio of 10:1 by weight.

2. We pour the viscoelastic material (~ 11 g) into a clean petri dish.
3. To let the bubbles settle down, we leave the covered petri dish for around 30 min at room temperature.
4. We then bake the mixture for around 55 min at $T = 65^\circ\text{C}$ in a pre-heated oven.

Polycarbonate (PC)

1. We mix 0.8 g of PC with 20 ml of chloroform.
2. Under continuous stirring for around 12 h, the PC should dissolve.
3. To create a thin film of PC, we put a drop of liquid PC onto a clean glass slide. We use a second glass slide to disperse the solution uniformly by pressing/ sliding the two glass slides against each other. We then let the two films dry in air.

Preparation of the PDMS/PC stamp

1. We first cut a small piece of PDMS ($5\text{ mm} \times 5\text{ mm} \times 3\text{ mm}$), which we clean in IPA under sonication for around 5 min.
2. We place the PDMS block onto its side on top of a clean glass slide and UVO-clean it for around 5 min. Next, we flip the PDMS block, make sure it is in full contact with the glass slide and UVO-clean it for another 3 min. These UVO-steps improve the adhesion between the PDMS block and the glass slide, as well as later between the PDMS block and the PC film.
3. Now, we cut a window ($12.5\text{ mm} \times 12.5\text{ mm}$) into a piece of commercial “Scotch tape”, which we then use to pick up the thin PC film from the glass slide.
4. To finish the stamp, we transfer the PC film onto the PDMS block and fix it with additional “Scotch tape”.

Once the stamp is prepared, we attach it to the micromanipulator in the stacking station with the stamp facing downwards and start our pick-up procedure.

A.2.2 Heterostructure assembly techniques

General stacking procedure

1. We start with the pick-up of the top layer of our vdWH.

- (i) We locate the flake – priorly exfoliated onto a Si/SiO₂ substrate – through our transparent PDMS/PC stamp, and place it under a clean area of the stamp.
 - (ii) We now carefully lower the stamp and bring it in contact with the underlying substrate, which is held in place by a vacuum chuck. Due to a small tilt of the substrate with respect to the stamp, one side of the stamp touches the underlying substrate first.
 - (iii) Upon approaching the flake of interest, we heat the stage to $T = 60^{\circ}\text{C}$, which results in the lateral movement of the PC film across the flake.
 - (iv) Once the stamp is in full contact with the flake, we raise the temperature to $T = 85^{\circ}\text{C}$. During this process, we constantly need to adjust the height of the stamp using the Z-micromanipulator to maintain the same contact between the stamp and the substrate.
 - (v) At $T = 85^{\circ}\text{C}$, we turn off the heater. The PDMS contracts with decreasing temperature, and the PC film slowly detaches from the underlying substrate. This results in the pick-up of the flake.
2. We repeat the above described pick-up procedure (step 1) for all flakes according to our initial device design.
 3. We release the vdW stack onto the final substrate (pre-patterened with markers, gates, etc.). For this, we set the stacking angle to be as flat as possible, guaranteeing better alignment precision.
 - (i) We carefully align the vdW stack on the PDMS/PC stamp to the desired position on our final substrate and bring both in contact at $T = 80^{\circ}\text{C}$.
 - (ii) We then heat the sample stage to $T = 185^{\circ}\text{C}$ in order to melt the PC film with the vdW stack onto the underlying substrate.
 - (iii) When lifting the glass slide using the Z-micromanipulator, the PC film detaches from the PDMS stamp. To ensure the adhesion of the vdW stack to the substrate, we subsequently bake the chip for another 10 minutes at $T = 200^{\circ}\text{C}$.
 4. We now dissolve the PC in chloroform for around one hour. Afterwards, we rinse the sample in IPA and blow-dry it with N₂.
 5. As a last step, we anneal the finished vdW stack under vacuum at $T = 100^{\circ}\text{C}$ for up to 12 hours.

If we plan to place the TMD flake(s) on top of a contact, or if we need to pattern contacts before encapsulation, we pick up the bottom part first and transfer it to the final substrate (step 1.–5.). We then pattern the small contacts to the TMD flake(s) following standard EBL and metallization procedures (as described below). In a next step, we pick up the top part using a new stamp following the same procedure as before.

Modified stacking procedure at the chip edge

1. We start with the pick-up of the top layer of our vdWH (see Section “General stacking procedure”).
2. We repeat the above described pick-up procedure for all flakes according to our design (see Section “General stacking procedure”).
3. We transfer the vdW stack to the final substrate.
 - (i) Here, we use an additional aluminum plate with two vacuum holes to extend the stage vacuum. We place the final substrate on one of the holes and its cleaved counterpart on the other hole.
 - (ii) We now make use of the thermal expansion of aluminum. We heat the sample stage to $T = 190^\circ\text{C}$ and align the two well-cleaved edges of both chips as close as possible. We then let the stage cool down to $T = 175^\circ\text{C}$. With decreasing temperature, the expanded aluminum plate slightly contracts, effectively moving the two chips closer together.
 - (iii) We align the vdW stack on the PDMS/PC stamp to the desired position on our final substrate (pre-patterened with markers, gates, etc.) and bring both in contact at $T = 175^\circ\text{C}$. In this step, we have to constantly adjust the alignment between the stamp and the final substrate, since the PDMS gradually expands when lowering the stamp due to the proximity to the heated stage. We note that, once in contact with the underlying substrate, the PC film starts to melt, and we can barely correct for any misalignment.
 - (iv) When the vdW stack is in full contact with the substrate, we wait for around 10 minutes to ensure that the PC film is completely melted.
 - (v) Carefully lifting the glass slide using the Z-micromanipulator, the PC film detaches from the PDMS stamp.
 - (vi) To increase the adhesion of the vdW stack to the substrate, we bake the chip for another 10 minutes at $T = 190^\circ\text{C}$. For this step, we turn off the vacuum

to avoid any movement of the chips due to the expansion of the underlying aluminum plate.

4.–5. See Section “General stacking procedure”.

Also here, it is possible to first only transfer the bottom part to the substrate, place the contacts, and then stack the top part onto the pre-patterned structure.

A.2.3 Spin-coating 2D materials for pick-up

With the described assembly technique, we are also able to pick up pre-patterned flakes. This provides the great possibility to shape the exfoliated flakes prior to their encapsulation according to a specific device architecture. Furthermore, we can pre-pattern e.g. graphene flakes used as gate electrodes.

In principle, patterning 2D materials using standard nanofabrication processes, including electron beam lithography (EBL) and reactive ion etching (RIE), is straight forward (see Appendix A.3 for details). However, most EBL resists require baking at around $T = 180 - 200^\circ\text{C}$. Since 2D materials become difficult to pick up once heated above $T = 100^\circ\text{C}$, we developed a “wet-transfer” technique of PMMA onto a Si/SiO₂ chip with exfoliated flakes. Here, the idea is to not have to bake the chip with the exfoliated flakes as is required for direct PMMA spin-coating. This gives us the ability to still be able to pick up the 2D flakes after patterning. The detailed process is described below. We note that for this procedure, the flakes need to be directly exfoliated onto a chip with markers, which is necessary for the alignment in the subsequent EBL process.

1. We first cut a piece of Si/SiO₂ wafer (30 mm×40 mm) and clean it in acetone and IPA.
2. The next part involves two separate spin-coating steps. First, we spin-coat a film of dextran onto the clean wafer.
 - Spin parameters: speed 2000 rpm; acceleration time 4 s; spinning time 40 s
 - Baking parameters: 3 min at $T = 150^\circ\text{C}$

We then spin-coat a thin film (~ 90 nm) of positive-tone PMMA resist (AR-P 672.02) on top.

- Spin parameters: speed 4000 rpm; acceleration time 4 s; spinning time 40 s
 - Baking parameters: 5 min at $T = 180^\circ\text{C}$
3. For the final “wet-transfer” of PMMA onto a chip with exfoliated flakes, we proceed as follows:

- (i) First, we fill a clean petri dish with DI water.
- (ii) We then cut a square – slightly larger than the chip with the exfoliated flakes – into the spin-coated wafer using a razor blade.
- (iii) Next, we let the chip slowly slide into the water and wait until the dextran dissolves. This results in a thin film of PMMA floating on the water surface.
- (iv) We pick up the chip with the exfoliated flakes, flip it upside down and let it carefully drop onto the floating PMMA film.
- (v) We then take the chip out of the water, turn it and bake it for around 5 min at $T = 90^\circ\text{C}$ on a hot-plate.

Following this procedure, we can pattern the flakes using standard nano-fabrication processes as described in the next Appendix A.3, and subsequently pick them up using the dry-transfer technique as described above (Section A.2.2).

A.3 Nanofabrication processes

To create opto-electronic devices, we need to integrate 2D TMD layers and FLG flakes within the vdWH with good electrical contacts. This requires multiple additional steps in the fabrication process, such as EBL, RIE and metal deposition, as described in detail below.

A.3.1 Base structure fabrication: pre-patterning substrates

We place our vdWHs onto Si/SiO₂ substrates (either p⁺⁺-doped or undoped) with a defined marker grid, which is required for the alignment in the following EBL steps and for locating the structure in our optical set-up. This is done either by UV-lithography or laser writing techniques. The markers are in general arranged in a square pattern with a separation of $\sim 200\ \mu\text{m}$.

Markers on Si/SiO₂ substrates using UV-lithography

1. First, we spin-coat a full 3-inch Si wafer ($\sim 285\ \text{nm}$ oxide) with $\sim 1\ \mu\text{m}$ of optical resist (AZ 1512).
 - Spin parameters: speed 6000 rpm; acceleration time 6 s; spinning time 45 s
 - Baking parameters: 60 s at $T = 100^\circ\text{C}$
2. We expose the wafer with a marker-grid to UV light (wavelength $\sim 365\ \text{nm}$) for around 1 s.

3. We then develop the structure with MIF 726 for around 17 s, and stop the process with DI water.
4. Subsequently, we treat the wafer with an O₂ plasma (20 sccm) for 30 s.
 - Plasma parameters: gas flow 20%; pressure 40 mTorr; power 60 W
5. We metallize the marker structure by thermal deposition of Ti (5 nm)/Au (45 nm).
6. Finally, we perform the lift-off in warm acetone ($T = 50^{\circ}\text{C}$).

Markers and structures on Si/SiO₂ substrates using laser-writing

1. We spin-coat a 2-inch Si wafer (~ 285 nm oxide) with ~ 480 nm positive photoresist (Microposit S1805).
 - Spin parameters: speed 4500 rpm; acceleration time 3 s; spinning time 40 s
 - Baking parameters: 2 min at $T = 125^{\circ}\text{C}$
2. We laser-write (Laser-writer uPG101) a pre-defined structure onto the wafer: power 65% of 4 mW; focus -15.
3. Subsequently, we develop the wafer with MF-319 ($< 2.5\%$ TMAH in H₂O) for 55 s. Afterwards, we rinse the wafer in DI water and blow-dry it with N₂.
4. We metallize the marker structure by thermal deposition of Ti/Au with the desired thickness.
5. Finally, we perform the lift-off in warm acetone ($T = 50^{\circ}\text{C}$).

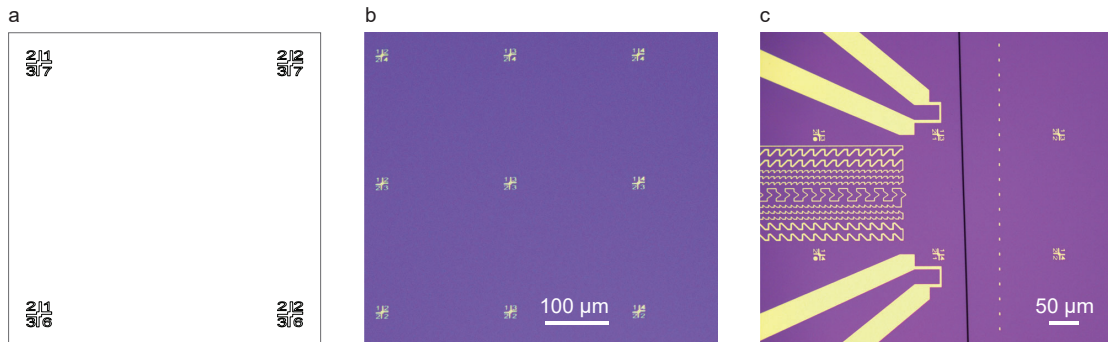


Figure A.1. **Pre-patterning substrates.** **a**, Design for alignment markers. **b**, Metallized Ti/Au markers on a Si/SiO₂ substrate. **c**, Pre-patterning structure for a gated vdWH device. The dotted vertical line is used as a guide to the eye for cleaving.

A.3.2 Electron-beam lithography for contacts and etching

1. We spin-coat the sample with a positive-tone PMMA resist (AR-P 672.045).
 - Spin parameters: speed 4000 rpm; acceleration time 4 s; spinning time 40 s
 - Baking parameters: 3 min at $T = 180^{\circ}\text{C}$
2. We expose the sample with a highly-focused electron beam (E-beam) using a pre-designed nanostructure.
 - EBL parameters: working distance 17.7 mm; acceleration voltage 20 kV; dose $550 \mu\text{C}/\text{cm}^2$
3. After exposure, we develop the structure in an IPA/DI water mixture (7/3) for 60 s at $T = 5^{\circ}\text{C}$.

A.3.3 Reactive ion etching

In this context, reactive ion etching is used to shape vdWHs and to define side contacts. Etching parameters for different 2D materials are listed in the Table A.5 below.

| Gas | Gas flow (sccm) | Process pressure (mTorr) | RF (power) (W) | Etching rate (nm/min) | | | | |
|------------------------------------|--------------------|--------------------------------|----------------------|--------------------------|------|-------|-------------------|-------|
| | | | | SiO ₂ | PMMA | hBN | Graphite | TMDs |
| O ₂ | 20 | 40 | 60 | negl. | 100 | 20 | several layers | – |
| CHF ₃ /O ₂ | 40/4 | 60 | 60 | 14 | < 10 | 20 | 4 | 19 |
| Ar/O ₂ | 22/8 | 25 | 30 | – | 70 | – | 10 | – |
| SF ₆ /Ar/O ₂ | 20/5/5 | 25 | 50 | 30 | 80 | > 300 | – | > 170 |

Table A.5. Plasma parameters for etching.

A.3.4 Metallization of contacts

1. For metallizing the contacts defined by EBL, we evaporate Ti (5 nm)/Au (45 nm) or Cr (5 nm)/Au (45 nm) for top contacts, or Ti (10 nm)/Au (20 nm) for contacts within the vdWHs.
 - Evaporation rates: 0.7 to 0.85 Å/s for Ti; 0.85 to 1.05 Å/s for Cr or Au
2. We then slowly lift-off the excess material by leaving the device in warm acetone ($T = 50^\circ\text{C}$) for a few hours.
3. As a last step, we anneal the sample under vacuum for more than 12 hours at $T = 100^\circ\text{C}$.

Table A.7 provides an overview of the individual steps and parameters for fabricating a gated vdWH device (see also Fig. A.3 for illustration).

A.3.5 Device connection

1. To finish the device, we carefully cleave the chip to a smaller size ($\sim 6\text{ mm} \times 6\text{ mm}$), in order for it to fit into the chip carrier.
2. We then glue the sample onto the (conductive) 20-terminal chip carrier using silver paint. When using a p^{++} -doped Si substrate as a global back-gate, silver paint ensures the electrical contact between the substrate and the chip carrier.
3. We connect the fabricated gate electrodes on the sample to the chip carrier using an Au-wire bonder at $T = 80^\circ\text{C}$ (see Table A.6 for bonding parameters).

| | Search | Power | Time | Force | Tail | Tear |
|------------------------|---------------|--------------|-------------|--------------|-------------|-------------|
| 1. Bond (chip carrier) | 1.20 | 2.42 | 4.0 | 3.0 | | |
| 2. Bond (sample) | 1.20 | 2.19 | 4.0 | 2.0 | 2.5 | 5.0 |

Table A.6. **Bonding parameters.**

4. The chip carrier can now be easily plugged into the corresponding chip socket in the measurement set-up (see Chapter 4).

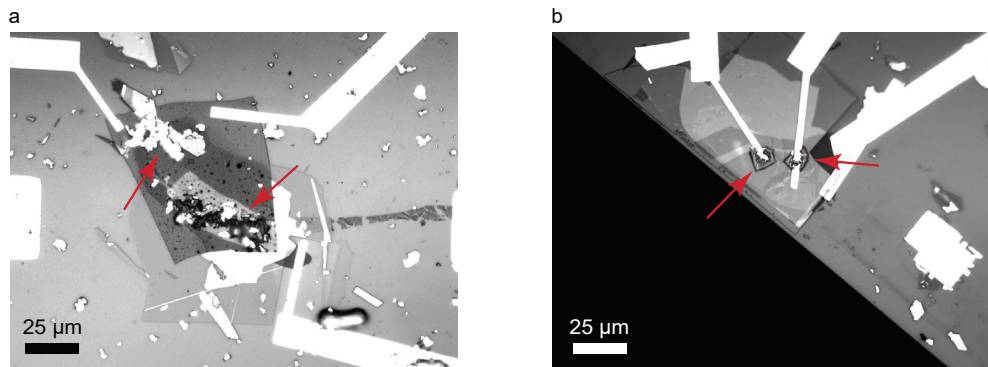


Figure A.2. **Device damage.** Optical images demonstrating the damage **a**, to the hBN by applying too high voltages and **b**, to the gold contacts by electrical discharge. Destroyed regions are indicated by red arrows.

When handling the finished device, it is very important to always keep everything on the same ground, since electrostatic discharge can easily blow up the device (see Fig. A.2).

| # | Step | Parameters |
|----|--|--|
| 1 | Pre-patterning Si/SiO ₂ substrate with alignment markers | Section A.3.1 |
| 2 | Exfoliation of individual flakes onto cleaned Si/SiO ₂ substrates | Table A.1, A.2 and A.3 |
| 3 | VdWH assembly/ stacking | Pick-up at $T = 60 - 85^{\circ}\text{C}$ PC melting at $T = 180 - 185^{\circ}\text{C}$ for ~ 10 min Baking at $T = 190^{\circ}\text{C}$ for ~ 10 min Dissolving in chloroform for ~ 1 h Rinsing in IPA Blow-drying with N ₂ |
| 4 | Annealing | Under vacuum at $T = 100^{\circ}\text{C}$ for 12 hours |
| 5 | Spin-coating | PMMA (AR-P 672.045) speed 4000 rpm; acceleration time 4 s; spinning time 40 s Baking at $T = 180^{\circ}\text{C}$ for 3 min |
| 6 | E-beam exposure | Section A.3.2: working distance 17.7 mm; voltage 20 kV; dose 500 $\mu\text{C}/\text{cm}^2$ |
| 7 | Etching | Table A.5 |
| 8 | Development | 60 s in IPA/DI water (7/3) at $T = 5^{\circ}\text{C}$ N ₂ blow-dry |
| 9 | Metallization | 5 nm/45 nm (top gates) or 5 nm/10 nm (gates within vdWH) of Ti/Au |
| 10 | Metal lift-off | Chip immersed in warm acetone for ~ 3 h |

Table A.7. List of general fabrication parameters for a gated vdWH device.

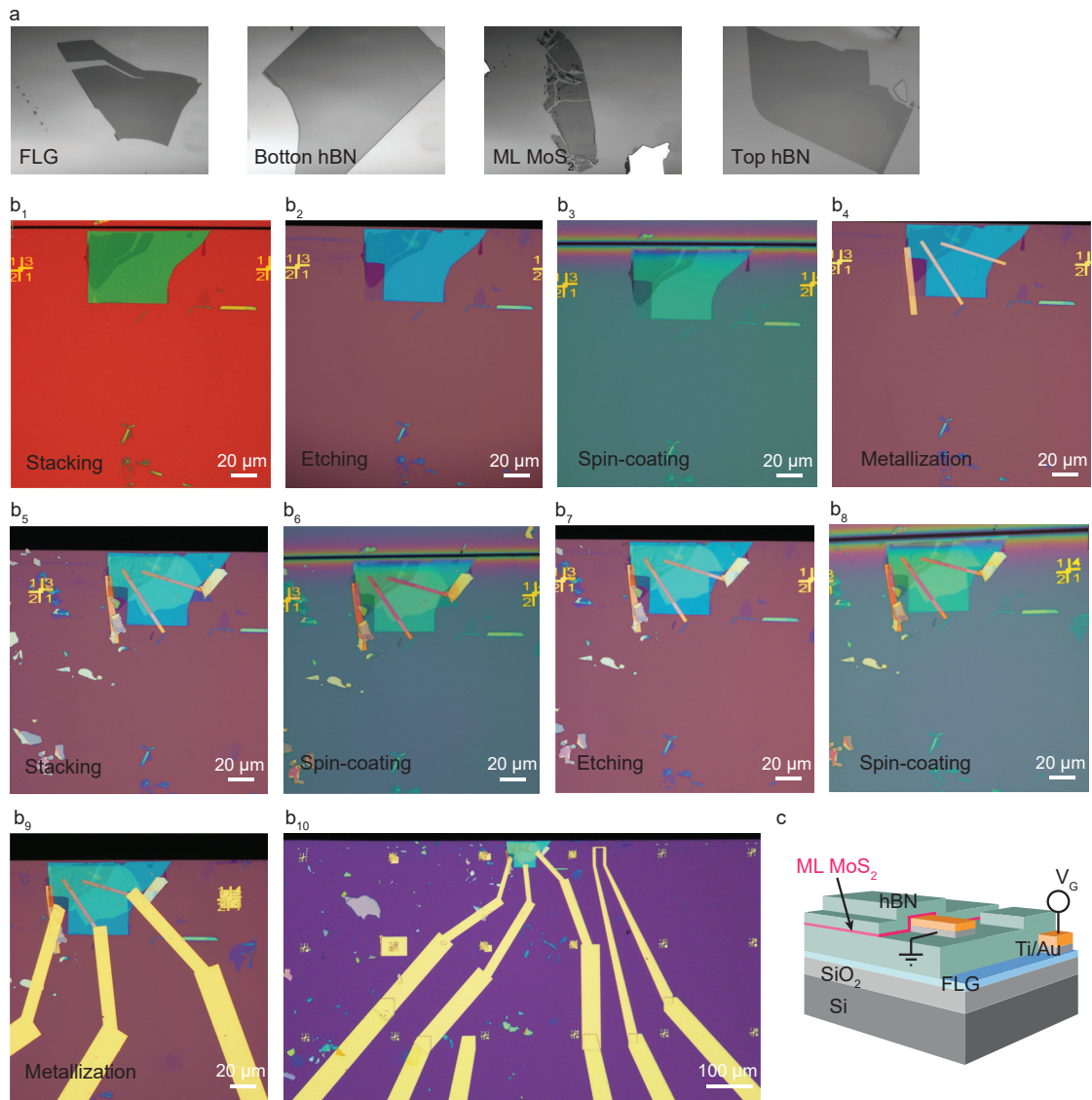


Figure A.3. **Detailed illustration of the fabrication procedure for building a gated vdWH.** **a**, Individual 2D flakes as building blocks of the vdWH obtained by mechanical exfoliation. **b**, Stacking sequence to build the heterostructure from the top-down. Different nano-fabrication steps are indicated. **c**, Sketch of the device structure consisting of monolayer MoS₂ encapsulated by two insulating hBN sheets. A voltage V_G can be applied to the FLG sheet to induce charge carriers into the MoS₂.

B

Details of samples and opto-electronic devices

There are a few important samples and devices that are essential for the results presented in this thesis. In this Appendix B, we provide some specific fabrication and device details*.

B.1 Encapsulated indium selenide sample

This sample was used to study optical second harmonic generation (SHG) in single- and few-layer indium selenide (InSe) (see Chapter 5).

Thin unprotected InSe films have optical properties which deteriorate over time, interpreted as a gradual degradation of the crystal due to interaction with oxygen and water

*The information within this section are partially adapted from the Methods Sections in the corresponding publications.

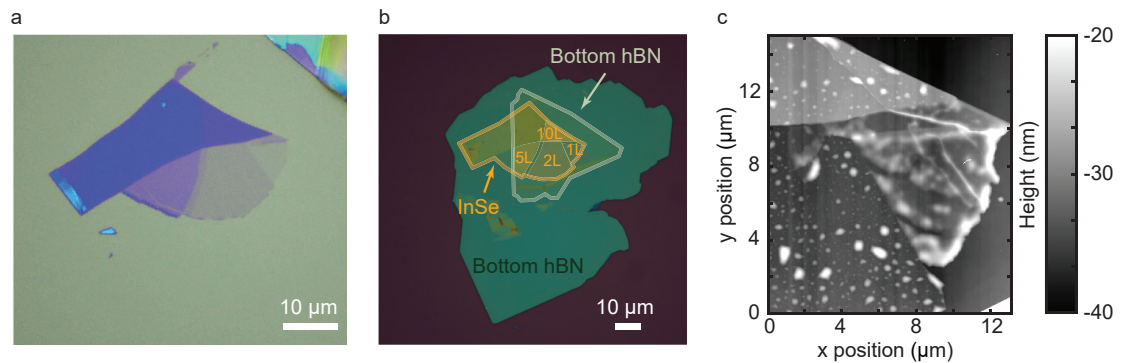


Figure B.1. **Encapsulated indium selenide sample.** Optical image of the indium selenide (InSe) flakes **a**, before and **b**, after encapsulation in hBN. **c**, AFM was used to determine the thicknesses of the InSe and hBN flakes.

in the atmosphere [106, 213]. Thus, to protect the material from the interaction with the environment, we employed exfoliation and subsequent encapsulation of single- and few-layer InSe in an inert (argon) atmosphere. The resulting InSe structures are stable under ambient conditions even in the single-layer limit [214]. InSe flakes were mechanically exfoliated from a Bridgman-grown rhombohedral γ -InSe bulk crystal (Fig. B.1a). The exfoliated InSe layers were picked up by a hBN crystal (8 nm) and deposited onto a large, relatively thick hBN flake (46 nm) prepared on a Si wafer with 290 nm thick SiO₂ (Fig. B.1b). The sample was annealed at 150°C for 1 hour so that contaminations, such as hydrocarbons trapped between the flakes, agglomerate through the self-cleaning mechanism [215]. InSe layers of different thickness and single-layer steps (≈ 0.8 nm) were identified by AFM measurements (Fig. B.1c) after encapsulation.

B.2 Monolayer MoS₂ vdWH device for measuring the QCSE

For the study of the quantum confined Stark effect (QCSE) in monolayer MoS₂ (see Chapter 6), we fabricated two separate devices, a field-effect device (Fig. B.2) and a directly contacted MoS₂ device (reference sample). Both devices were assembled by

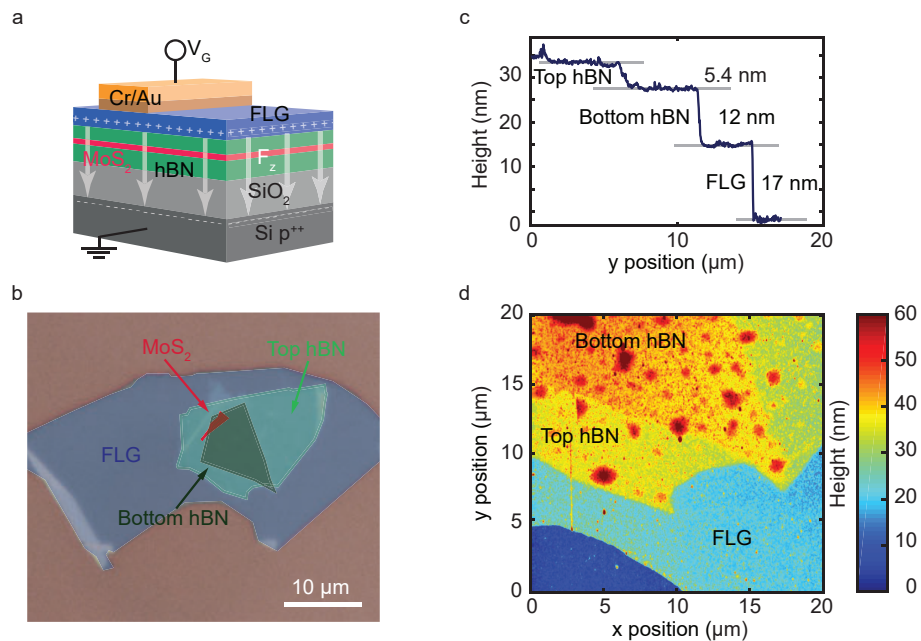


Figure B.2. **Monolayer MoS₂ vdWH device for measuring the QCSE.** **a**, Three-dimensional schematic and **b**, optical microscope image of the device structure. The different layers are labelled and artificially highlighted. **c**, and **d**, AFM was used to determine the thicknesses of the hBN and FLG flakes.

stacking 2D materials via the dry-transfer technique described in Appendix A.2.2. All layers were mechanically exfoliated from bulk crystals (see Appendix Table A.1). MoS₂ monolayers were treated by a bis(trifluoromethane)sulfonimide (TFSI) solution following Ref. [216] before full encapsulation between hBN layers. Few-layer graphene (FLG) was employed as a top transparent electrode or as a contact electrode to the MoS₂ [217]. Metal contacts to the FLG were patterned by EBL and subsequent metal deposition of Au (45 nm)/ Cr (5 nm). The flake thickness of each layer was characterized by a combination of optical contrast, AFM, PL, and Raman spectroscopy. The field-effect device consists of SiO₂ (300 nm), hBN (5.4 nm), MoS₂ (0.65 nm), hBN (12 nm), and FLG (17 nm) (Figs. B.2c,d).

B.3 Gated MoSe₂/WSe₂ heterobilayer devices

Two different gated MoSe₂/WSe₂ heterobilayer devices (see schematic in Fig. B.3a) were fabricated to study the tunability of interlayer excitons (IXs) in applied electric fields (see Chapter 6). Figs. B.3c,d show optical micrograph images of the vdWHs. We determined the crystallographic axes of the individual TMD monolayers with the help of angle-resolved SHG prior to their assembly. Fig. B.3b plots the SHG intensity in monolayer MoSe₂ (green) and WSe₂ (purple), respectively. Both signals show a minimum and a maximum upon rotation by 60°, revealing the initial orientation of the individual crystals with respect to their armchair axis. When stacking, we then aligned the layers along the same crystal direction to maximize the coupling efficiency, which is essential for the formation of IXs. The vdWHs are assembled using the fabrication methods described above (Appendix A). Direct gold contacts allow to tune the carrier concentration n in the individual flakes. FLG sheets on the top and bottom of the stack serve as local gates to apply an electric field F_z across the device.

B.4 Homobilayer MoS₂ devices

Three separate structures were fabricated for exploring the QCSE in homobilayer MoS₂ (see Chapter 7): device 1 was prepared at the University of Basel, and device 2 and sample 3 were assembled at LPCNO Toulouse. vdWHs were fabricated by stacking 2D materials via dry-transfer techniques. For device 1, a PDMS stamp with a thin PC film was used to pick up individual layers from top to bottom. All flakes were previously mechanically exfoliated from bulk crystals on SiO₂ (285 nm)/Si substrates (see Appendix Table A.1). Metal contacts to the MoS₂ and FLG were patterned by EBL and subsequent metal deposition of Ti (5 nm)/Au (45 nm) (see Appendix A). For device

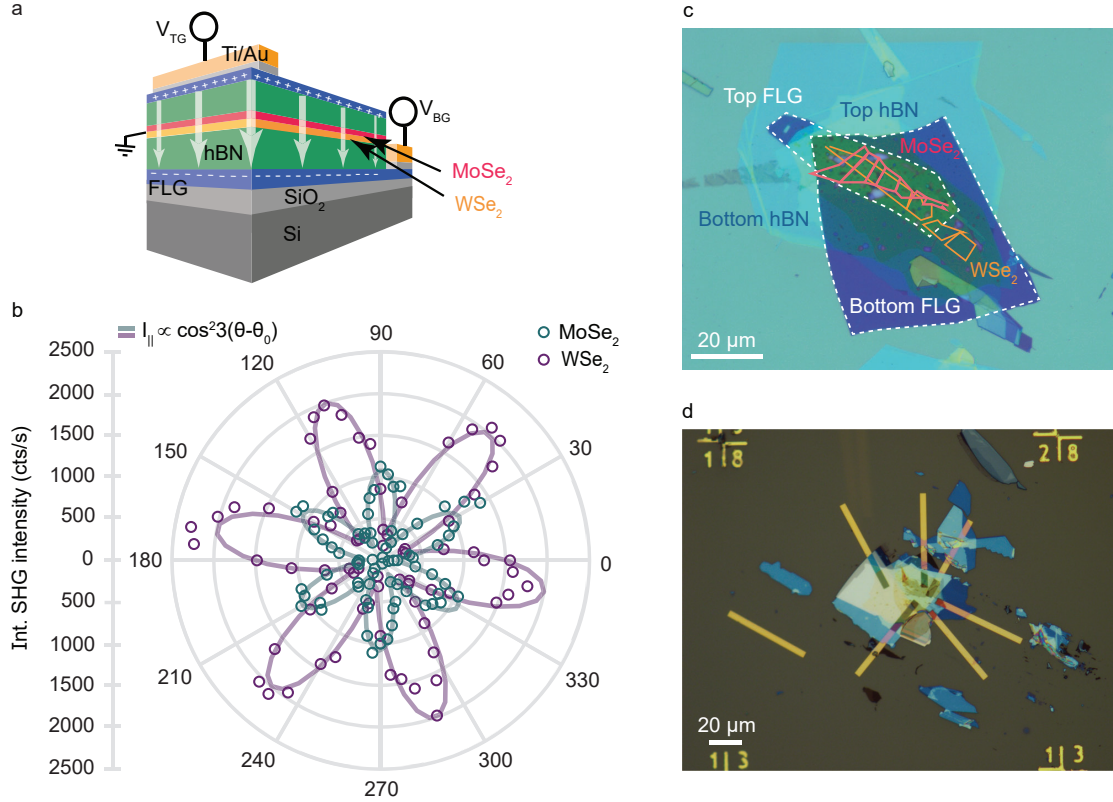


Figure B.3. **Gated MoSe₂/WSe₂ heterobilayer device.** **a**, Three-dimensional schematic of the device structure. The device consists of two monolayers of TMDs (MoSe₂ and WSe₂) encapsulated between two insulating hBN layers. The monolayers are individually contacted and FLG flakes on both sides serve as transparent gate electrodes. **b**, Angle-resolved SHG of the individual monolayers before stacking. The initial rotation of the flakes with respect to the armchair axis is measured to be $\theta_0 = 29.0^\circ$ for MoSe₂ and $\theta_0 = -10.8^\circ$ for WSe₂, respectively. **c**, and **d**, are optical images of the two heterobilayer structures investigated within this thesis.

2, 2H-stacked MoS₂ crystals, synthetic hBN [212] and natural graphite were subjected to micromechanical cleavage on Nitto Denko tape [6], then exfoliated again on a PDMS stamp placed on a glass slide for optical inspection. Sequential deterministic stamping of the selected flakes was then applied to build the complete stack, aligned according to the position of the Au contacts pre-patterned onto the substrate. Sample 3, consisting of bilayer (BL) and trilayer (TL) MoS₂, was assembled following the same transfer steps as device 2.

Optical images of the devices 1 and 2, and sample 3 are shown in Figs. B.4d,e,f. For the determination of the electric field values in the gated devices, the thicknesses of the individual hBN layers in device 1 and 2 were measured by AFM ($d_T = 16.2$ nm

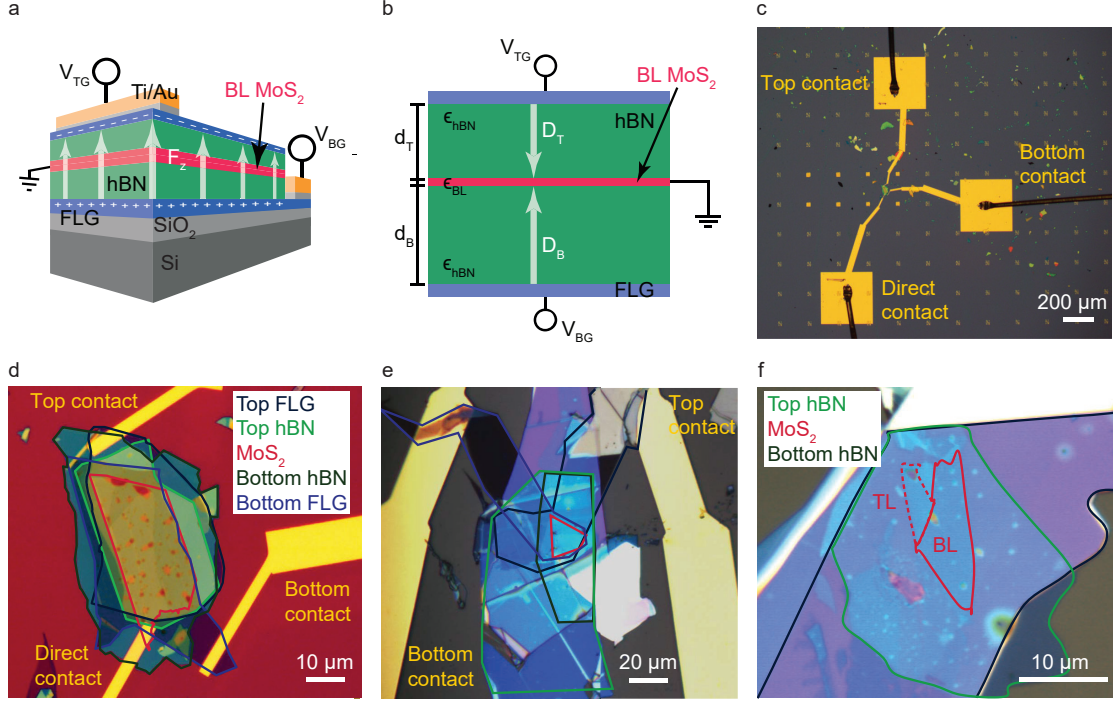


Figure B.4. **Homobilayer MoS₂ device and sample structure.** **a**, Three-dimensional schematic of device 1, which consists of a MoS₂ homobilayer encapsulated between two hBN flakes. FLG serves as the top and bottom gates, and a direct Ti/Au contact to the MoS₂ is used to ground the bilayer. Voltages to the top and bottom gates (V_{TG} and V_{BG}) are applied to create a uniform electric field F_z across the device. **b**, Schematic of the corresponding electrostatic model. **c**, Optical image of the gated device structure (device 1) with 5x magnification. Contacts to the individual layers are connected to the chip carrier through wire-bonding. Microscope images of the electrical gated **d**, device 1 and **e**, device 2, and **f**, sample 3, consisting of bilayer (BL) and trilayer (TL) MoS₂.

and $d_B = 21.5$ nm for device 1, and $d_T = 13$ nm and $d_B = 4$ nm for device 2). For device 1, we made use of the so-called dual-gate device scheme (Figs. B.4a,b), which allows independent control of the carrier density in the MoS₂ bilayer and the electric field across the heterostructure using the voltages applied to the top and bottom gates, V_{TG} and V_{BG} , (see Chapter 4).

B.5 Gated monolayer MoS₂ devices

In Chapter 8, we employed two different devices to probe the spin-polarization in monolayer (ML) MoS₂ by optical absorption (device 1) and PL spectroscopy (device 2). We fabricated device 1 following the general stacking procedure described in Section A. Here, FLG was used as a contact electrode with Cr (5 nm)/Au (45 nm) metal contacts to inject

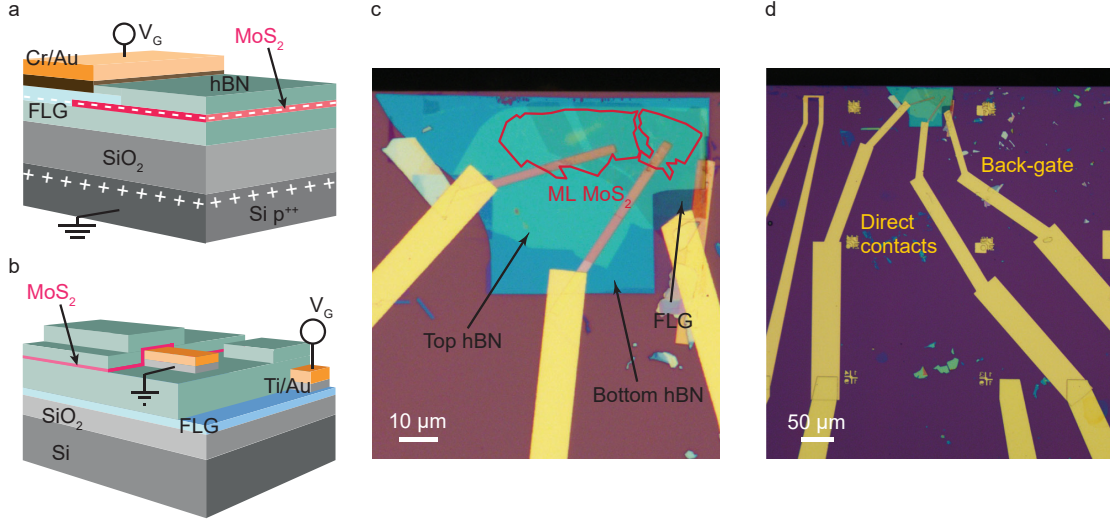


Figure B.5. **Gated monolayer MoS₂ devices.** **a**, and **b**, Three-dimensional schematics of device 1 and device 2, consisting of monolayer (ML) MoS₂ encapsulated between two hBN flakes. FLG serves as a gate electrode to inject charge carriers into the MoS₂. **c**, and **d**, are optical images of the device structure (device 1). The monolayer region is highlighted and the different layers are indicated. For device 1, the ML MoS₂ is grounded through direct contacts, while a voltage V_G is applied to the FLG back-gate.

charge carriers into the encapsulated MoS₂ monolayer on a p⁺⁺-doped silicon substrate (see schematic in Fig. B.5a). For device 2 (see schematic in Fig. B.5b), we employed the modified stacking procedure described in Appendix A (see also Fig. A.3 for a detailed illustration of the device fabrication). Here, the stacking sequence was divided into two steps. First, we placed the FLG back-gate and the bottom hBN layer onto an undoped SiO₂ (285 nm)/Si substrate with pre-patterned alignment markers and big metal leads, Ti (5 nm)/Au (55 nm). Bottom metal contacts were then patterned by EBL and subsequent metal deposition of Ti (10 nm)/Au (20 nm). In a second step, monolayer MoS₂ and a capping hBN layer were placed on top of the initial vdW stack. To improve the contact to the MoS₂, we annealed our device in vacuum at $T = 100^\circ\text{C}$ for more than 12 hours. Figs. B.5c,d show optical images of device 2. The monolayer MoS₂ region is highlighted with red color. In this device design, FLG is used as a “local” back-gate, while the MoS₂ monolayer is grounded by direct metal contacts. Charge carriers were injected into the two devices through $n = C \cdot V_G$ (see Chapter 3), with $C = 11.1 \pm 0.5 \text{ nFcm}^{-2}$ for device 1 and $C = 97.9 \pm 4.9 \text{ nFcm}^{-2}$ for device 2.

C

Supplementary information to Chapter 4: “Experimental methods: optical spectroscopy of two-dimensional semiconductors”

C.1 Components of the optical set-ups

Optical measurements were performed using the home-built microscope set-ups described in Chapter 4. Here, we provide a detailed list of the optical components (Table C.1) in our set-ups (Fig C.1).

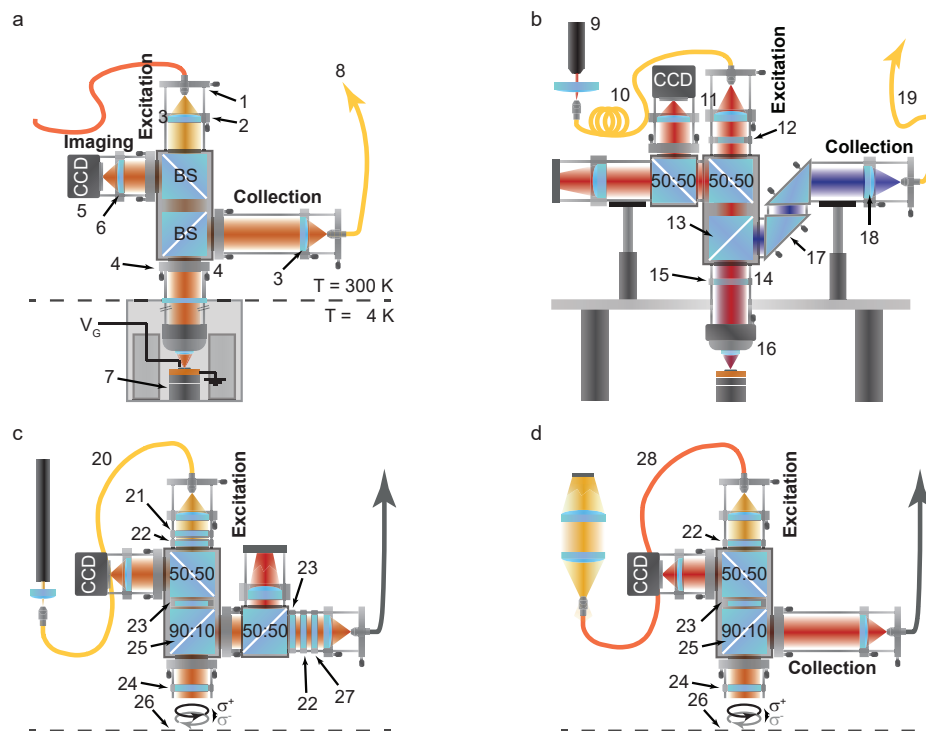


Figure C.1. **Optical elements.** Components for **a**, the general microscope set-up, for **b**, the SHG set-up and for the microscope heads to perform **c**, PL and **d**, absorption measurements.

| # | Element | Part number |
|----|--|---|
| 1 | x/y -translation stage | Thorlabs CP1XY |
| 2 | z -translation stage | Thorlabs SM1Z |
| 3 | Objective | Nikon 10x/NA=0.25 |
| 4 | Tilt stage | Thorlabs KC1-T/M |
| 5 | Camera | Allied Vision Technologies Guppy (Pro) F-503B |
| 6 | Achromatic lens | Thorlabs AC254-200-B-ML, $f = 200$ mm |
| 7 | $x/y/z$ -piezo nano-positioners | Attocube, ANP \times 10 and ANPz101 |
| 8 | Spectrometer | Princeton Instruments, Acton SpectraPro SP-2500 |
| 9 | Mode-locked Ti:Sa laser | Coherent MIRA900 |
| 10 | Single-mode (SM) fiber | Thorlabs HP780, $\lambda = 780 - 970$ nm |
| 11 | Aspheric lens | Thorlabs C280TME-B, $f = 18.4$ mm, NA = 0.15 |
| 12 | Linear polarizer (Lin. Pol.) | Thorlabs LPVIS050-MP2, $\lambda = 550 - 1500$ nm, transm. 80.1%, extinction ratio $> 10^7$ at $\lambda = 810$ nm |
| 13 | Longpass dichroic beamsplitter (BS) | Thorlabs DMLP650R, $\lambda = 650$ nm cut-on, transm. 97.4% at $\lambda = 810$ nm, refl. 98.2% at $\lambda = 405$ nm |
| 14 | Achromatic half-wave ($\lambda/2$) plate | Thorlabs AHWP10M-600, $\lambda = 400 - 800$ nm |
| 15 | Motorized rotation stage | Thorlabs K10CR1/M |
| 16 | Microscope objective lens | Olympus 40x, NA = 0.65 |
| 17 | Polarizing beam-splitter (PBS) | Thorlabs PBSW-405, $\lambda = 405$ nm |
| 18 | Aspheric lens | Thorlabs C560TME-A, $f = 13.8$ mm, NA = 0.18 |
| 19 | Single-mode (SM) fiber | Thorlabs SM300, $\lambda = 320 - 430$ nm |
| 20 | Single-mode (SM) fiber | Thorlabs HP630, $\lambda = 600 - 770$ nm |
| 21 | Bandpass filter or Laser line filter and Laser clean-up filter | Chroma ET580/25X, $\lambda = 580 \pm 25$ nm Thorlabs FL05632.8-1, $\lambda = 632.8 \pm 10$ nm and Semrock MaxLine, $\lambda = 632.8$ nm |
| 22 | Linear polarizer (Lin. Pol.) | Thorlabs LPVISB050-MP2, $\lambda = 500 - 720$ nm |
| 23 | Computer-controlled liquid crystal (LC) | Thorlabs LCC1411-A, $\lambda = 350 - 700$ nm |
| 24 | Superachromatic quarter-wave ($\lambda/4$) plate retarder | Thorlabs SAQWP05M-700, $\lambda = 325 - 1100$ nm |
| 25 | 90:10 beamsplitter (BS) | Thorlabs BS028 |
| 26 | Microscope objectives | Microthek 20x/NA = 0.45, 40x/NA = 0.65 or 60x/NA = 0.85 |
| 27 | Longpass (LP) filter | Semrock Razor Edge Long Pass E-Grade, $\lambda = 633$ nm |
| 28 | Multi-mode fiber | Thorlabs FT030 |
| 29 | Blue laser diode | Thorlabs CPS405, $\lambda = 405$ nm |

Table C.1. List of the optical elements used within the different microscope heads depicted in Fig. C.1.

D

Supplementary information to Chapter 5: “Optical second harmonic generation in indium selenide”

D.1 Electric field simulations

In Chapter 5, we introduced local field correction factors in our estimation of the non-linear sheet susceptibility to account for the dielectric environment. In the following, we simulate this effect, that is, the electric field transmitted from air towards the InSe flake and the generated SH field transmitted back to air using the simulation software “Essential MacLeod”. In our case, the single- and few-layer InSe flakes are encapsulated in hBN placed on a Si/SiO₂ substrate. In order to determine the local field correction factors $t_{\text{in}}(\omega)$ and $t_{\text{out}}(2\omega)$, we consider the stacking of thin films (single-layer InSe encapsulated in hBN and the SiO₂ layer underneath) on top of a semi-infinite Si film: Si substrate/SiO₂ (290 nm)/bottom hBN (46 nm)/InSe/top hBN (8 nm). The single InSe layer is modelled by a thin homogeneous film of thickness ~ 0.8 nm, characterized by a real refractive index n_{InSe} , ranging from 2.335 at 810 nm (1.531 eV) to 2.887 at 405 nm (3.061 eV) [218]. The SiO₂ layer of thickness $d_{\text{SiO}_2} = 290$ nm is optically characterized by a wavelength-dependent real refractive index n_{SiO_2} ranging from 1.453 at 810 nm to 1.470 at 405 nm [219], while the refractive index of hBN $n_{\text{hBN}}(\lambda)$, ranging from $2.212+i\cdot 0.000048$ at 1 eV to $2.568+i\cdot 0.047$ at 405 nm (4 eV), is taken from Ref. [220]. We consider a semi-infinite silicon substrate underneath, with a wavelength-dependent complex refractive index $n_{\text{Si}}(\lambda)$ [221]. Under normal light incidence, the fraction of light transmitted from air towards the InSe flake $t_{\text{in}}(\omega)$ and the fraction of the generated SH light in the InSe transmitted back $t_{\text{out}}(2\omega)$ can be simulated by “Essential MacLeod” (see

Fig. D.1), which is based on transfer matrix methods, to be

$$t_{\text{in}}(\omega) = 58.88 \% \pm 0.06 \% \quad \text{at } \lambda = 810 \text{ nm}$$

$$t_{\text{out}}(2\omega) = 29.55 \% \pm 0.04 \% \quad \text{at } \lambda = 405 \text{ nm}.$$

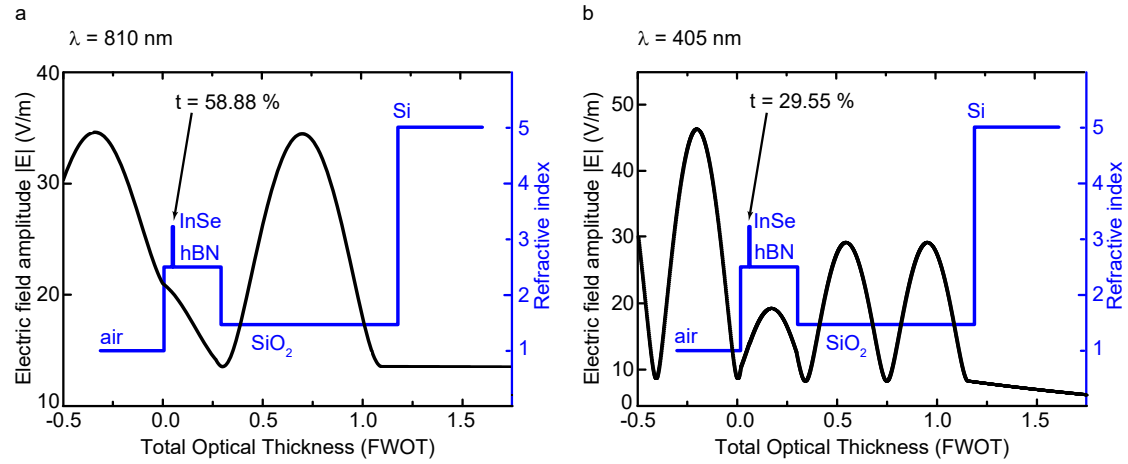


Figure D.1. Simulation of the electric field **a**, transmitted from air towards the InSe flake $t_{\text{in}}(\omega)$ and **b**, the generated second harmonic field in the InSe transmitted back to air $t_{\text{out}}(2\omega)$.

E

Supplementary information to Chapter 7: “Giant Stark splitting of an exciton in bilayer MoS₂”

E.1 Data acquisition details

Experiments were performed independently in two different research laboratories using devices 1 and 2. The reflectivity spectra of device 1 were recorded with the reflectivity set-up described in Chapter 4 using a microscope objective with $NA = 0.45$. In order to evaluate the differential reflectivity $\Delta R/R_0$, we compare the reflectivity spectrum R obtained from the MoS₂ flake at a given electric field F_z with a reference spectrum R_0 . Sweeping the gate voltages V_{TG} and V_{BG} so that only the carrier concentration n_{tot} in the device is varied leads to significantly different reflectivity spectra. For device 1, we thus interpolate the reference spectrum R_0 from the raw reflectivity spectrum at a high electron density $n_{tot} \approx 11.5 \cdot 10^{-12} \text{ cm}^{-2}$, where the oscillator strength is distributed over a large spectral range [88]. Using Kramers-Kronig relation, the measured differential reflectivity data $\Delta R/R_0$ can be converted into the imaginary part of the optical susceptibility $\text{Im}(\chi)$ (see also Chapter 4 for a more detailed description).

For device 2*, low temperature reflectance measurements were performed in a home-built micro-spectroscopy setup constructed around a closed-cycle, low vibration attoDry cryostat with a temperature controller ($T = 4 \text{ K}$ to $T = 300 \text{ K}$). For reflectivity, a halogen lamp with a stabilized power supply is used as a white light source, initially focused onto a pin-hole that is imaged on the sample. The reflected light is then dispersed by spectrometer and detected by a Si-CCD camera. Here, the differential reflectivity is defined as $\Delta R/R_0$, where R is the intensity reflection coefficient of the sample with the MoS₂ layers and R_0 is obtained from the same structure without the MoS₂. We note that the overall shape and amplitude of the differential reflectivity signal depends on

*Measurements on device 2 were performed at LPCNO Toulouse by S.S. and I.P.

thin-film interferences in the hBN layers [222].

E.2 Beyond DFT calculations*

Below, we provide details of the DFT GW+BSE calculations presented in Chapter 7.

E.2.1 Computational details

The atomic structures, the quasi-particle bandstructures and optical spectra have been obtained from DFT calculations using the VASP package [223, 224]. The projector-augmented wave scheme [225, 226] has been used to treat core electrons. The lattice parameter value is set to 3.22 Å for all the runs. A grid of $15 \times 15 \times 1$ k -points has been used, in conjunction with a vacuum height of 21.9 Å, for all the calculation cells. The geometry’s optimisation process has been performed at the PBE-D3 level [227] in order to include van der Waals interactions between layers. All the atoms were allowed to relax with a force convergence criterion below 0.005 eV/Å. Heyd-Scuseria-Ernzerhof (HSE) hybrid functional [228–230] has been used as approximation of the exchange-correlation electronic term, including SOC, to determine eigenvalues and wave functions as input for the full-frequency-dependent GW calculations [231] performed at the G_0W_0 level. The application of the electric field is done at this step, just before the GW calculation process, considering that at small/moderate electric field values, its application is only a small perturbation to the bandstructures. An energy cutoff of 400 eV and a Gaussian smearing of 0.05 eV width have been chosen for partial occupancies, when a tight electronic minimisation tolerance of 10^{-8} eV was set to determine, with a good precision, the corresponding derivative of the orbitals with respect to k needed in quasi-particle bandstructure calculations. The total number of states included in the GW procedure is set to 1280, in conjunction with an energy cutoff of 100 eV for the response function, after a careful check of the direct band gap convergence (smaller than 0.1 eV as a function of k -points sampling). Bandstructures have been obtained after a Wannier interpolation procedure performed by the WANNIER90 program [232]. All optical excitonic transitions have been calculated by solving the Bethe-Salpeter Eq. [233, 234], using the twelve highest valence bands and the sixteen lowest conduction bands to obtain eigenvalues and oscillator strengths on all systems. From these calculations, the absorbance values are reported by using the imaginary part of the complex dielectric function. With this computational setting a good agreement is obtained in terms of A and B peak positions, as

*This section is partially adapted from the Supplement in N. Leisgang *et al.*, Nature Nanotechnology **15**, 901–907 (2020). DFT GW+BSE calculations were performed by I.C.G.

well as for oscillator strength values, with the well-converged results of Qui *et al.* [235] for MoS₂ MLs.

E.2.2 Bandstructure modifications due to the electric field

As can be seen in Fig. E.1, moderate electric field application on a free standing 2H MoS₂ bilayer shifts bandstructures from the two distinct layers by decreasing valence bands and conduction band energies for the layer L₁ lying at the highest electrostatic potential value while L₂ bands are upshifted. Mind that similar results were already reported in previous works using standard DFT calculations only [236–238], confirmed here by our GW series of calculations.

In Fig. E.2, the bandstructures of the trilayer case are reported. Interestingly, without electric field, L₁ and L₃ valence bands, more specifically VB and VB₋₁, are both mixtures of Mo d_{xy} , $d_{x^2-y^2}$ with in-plane S p orbitals coming from both L₁ and L₃ layers. Thus, when making transitions implying those states (solid black lines in Fig. E.2), holes will be delocalized over the top and bottom layers at the same time. By suppressing symmetry, with the application of an electric field, VB and VB₋₁ become more relocalized one each of the layers. Since our calculation cell is symmetric in the (Oz) direction, and since L₂ is located in the middle of it, its corresponding electrostatic potential is 0. This explains the absence of band shifts for the L₂ bands.

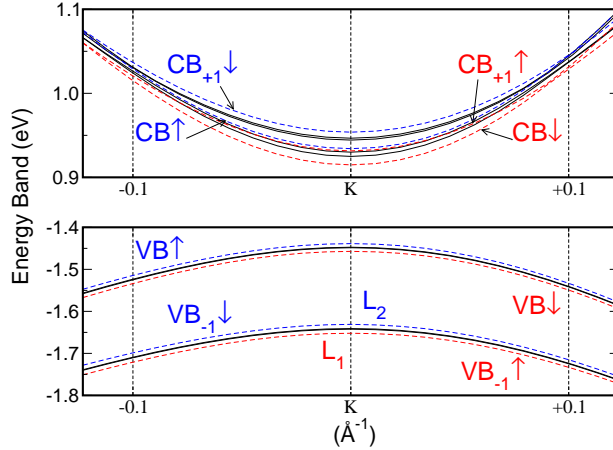


Figure E.1. **Valence and conduction band shifts induced by an electric field.** G_0W_0 bandstructure of 2H MoS₂ bilayer in the vicinity of the K point, without (black lines) and with an applied electric field $F_z = 1$ MV/cm value (dashed lines). L₁ bands are in red, while L₂ bands are depicted in blue.

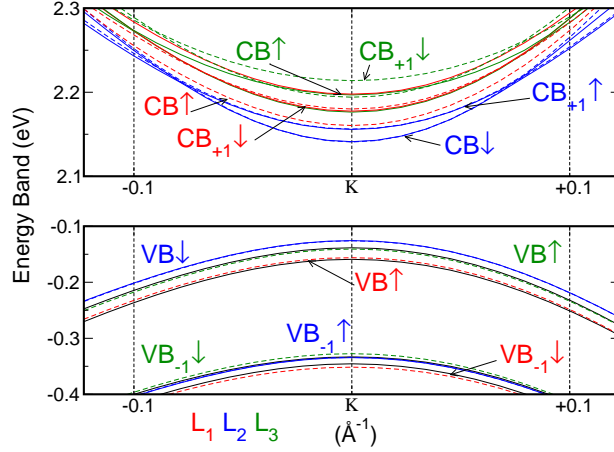


Figure E.2. **Valence and conduction bands shifts induced by an electric field.** G_0W_0 bandstructure of 2H MoS₂ trilayer in the vicinity of K point, without (solid lines) and with an applied electric field $F_z = 1$ MV/cm value (dashed lines). L_1 bands are in red, L_2 bands are blue and L_3 band are depicted in green.

E.2.3 Decomposition of the exciton oscillator strength with respect to single-particle transitions

Bilayer case

From Table E.1, one can see that the A exciton is not completely of pure intralayer exciton character, since a small amount (around 5%) of the oscillator strength is coming from the VB_{-1} of the other layer. This mixing does not vary with respect to the electric

| Exciton | A | IE_1 | IE_2 | B |
|--------------------|---|--|--|---|
| | $VB_{\uparrow}^{L_2} \rightarrow CB_{\uparrow}^{L_2}$ | $VB_{\uparrow}^{L_2} \rightarrow CB_{+1,\uparrow}^{L_1}$ | $VB_{\downarrow}^{L_1} \rightarrow CB_{+1,\downarrow}^{L_2}$ | $VB_{-1,\downarrow}^{L_2} \rightarrow CB_{+1,\downarrow}^{L_2}$ |
| 0.0 (MV/cm) | 5% | 13% | 13% | 17% |
| 0.5 (MV/cm) | 6% | 12% | 14% | 18% |
| 1.0 (MV/cm) | 5% | 11% | 15% | 19% |
| 2.0 (MV/cm) | 5% | 10% | 18% | 23% |

Table E.1. **Decomposition of the oscillator strengths for 2H MoS₂ bilayer at the K point.** Identification of the main electron-hole pairs related to the excitonic peaks are indicated in the first line. The percentage of the second most important contribution to the oscillator strength is given for four different electric field values; its physical nature is indicated in the second line for $F_z = 0$ MV/cm. CB and VB denote conduction band and valence band. L_1 and L_2 indicate transitions in layer 1 and 2, respectively.

field. Note that no delocalization of the electron is observed, as expected in this case, due to symmetry of the conduction band d_{z^2} nature [15, 155, 239]. Interestingly, for the B-peak, originating mainly from $\text{VB}_{-1,\uparrow}^{\text{L}_1} \rightarrow \text{CB}_{+1,\uparrow}^{\text{L}_1}$ and $\text{VB}_{-1,\uparrow}^{\text{L}_2} \rightarrow \text{CB}_{+1,\uparrow}^{\text{L}_2}$ transitions, the interlayer contributions ($\text{VB}_{\uparrow}^{\text{L}_2} \rightarrow \text{CB}_{+1,\uparrow}^{\text{L}_1}$ and $\text{VB}_{\downarrow}^{\text{L}_1} \rightarrow \text{CB}_{+1,\downarrow}^{\text{L}_2}$) are already large for zero electric field and increase with enhanced electric field values. This means that the delocalization of the hole, even in the B excitons, becomes more pronounced with electric field. In contrast, the intralayer contribution to IE_1 tends to decrease with increasing electric field, while it increases for IE_2 , explaining the anticrossing regime observed between IE_2 and B lines.

Trilayer case

In Table E.2, the percentages of the second main electron-hole pair contribution to the first excitonic peaks are given for the trilayer case in the absence of an electric field. A- peaks are related to two different transitions, namely A:1s L_2 and A:1s L_1, L_3 , as can be observed from magneto-optics measurements, reported previously [51]. The contribution from the other layers to these oscillator strengths remains modest. The IE^* peak clearly results from interlayer transitions, in which the electron lies in L_2 , while the hole is delocalized over L_1 and L_3 (mediated by a small amount of intralayer L_2 coupling with good spin parity). For IE , the hole is almost exclusively in L_2 . It couples with an electron largely localized in L_1 and in lesser extent in L_3 . A first B-like exciton (B:1s

| Exciton | A:1s L_2 | A:1s L_1, L_3 | IE^* |
|--------------------|--|---|--|
| | $\text{VB}_{\downarrow}^{\text{L}_2} \rightarrow \text{CB}_{\downarrow}^{\text{L}_2}$ | $\text{VB}_{\uparrow}^{\text{L}_{1,3}} \rightarrow \text{CB}_{\uparrow}^{\text{L}_{1,3}}$ | $\text{VB}_{\uparrow}^{\text{L}_{1,3}} \rightarrow \text{CB}_{+1,\uparrow}^{\text{L}_2}$ |
| 0.0 (MV/cm) | 6% | 7% | 10% |
| | $\text{VB}_{-1,\downarrow}^{\text{L}_{1,3}} \rightarrow \text{CB}_{\downarrow}^{\text{L}_2}$ | $\text{VB}_{-1,\uparrow}^{\text{L}_2} \rightarrow \text{CB}_{\uparrow}^{\text{L}_{1,3}}$ | $\text{VB}_{-1,\uparrow}^{\text{L}_2} \rightarrow \text{CB}_{+1,\uparrow}^{\text{L}_2}$ |
| 1.0 (MV/cm) | 4% | 8% | 12% |
| | $\text{VB}_{-1,\downarrow}^{\text{L}_{1,3}} \rightarrow \text{CB}_{\downarrow}^{\text{L}_2}$ | $\text{VB}_{-1,\uparrow}^{\text{L}_2} \rightarrow \text{CB}_{\uparrow}^{\text{L}_{1,3}}$ | $\text{VB}_{-1,\uparrow}^{\text{L}_2} \rightarrow \text{CB}_{+1,\uparrow}^{\text{L}_2}$ |

| Exciton | IE | B:1s L_2 | B:1s L_1, L_3 |
|--------------------|--|--|---|
| | $\text{VB}_{\downarrow}^{\text{L}_2} \rightarrow \text{CB}_{+1,\downarrow}^{\text{L}_{1,3}}$ | $\text{VB}_{-1,\uparrow}^{\text{L}_2} \rightarrow \text{CB}_{+1,\uparrow}^{\text{L}_2}$ | $\text{VB}_{-1,\downarrow}^{\text{L}_{1,3}} \rightarrow \text{CB}_{+1,\downarrow}^{\text{L}_{1,3}}$ |
| 0.0 (MV/cm) | 13% | 13% | 23% |
| | $\text{VB}_{\downarrow}^{\text{L}_2} \rightarrow \text{CB}_{+1,\downarrow}^{\text{L}_{1,3}}$ | $\text{VB}_{\uparrow}^{\text{L}_{1,3}} \rightarrow \text{CB}_{+1,\uparrow}^{\text{L}_2}$ | $\text{VB}_{\downarrow}^{\text{L}_2} \rightarrow \text{CB}_{+1,\downarrow}^{\text{L}_{1,3}}$ |
| 1.0 (MV/cm) | 12% | 10% | 23% |
| | $\text{VB}_{\downarrow}^{\text{L}_2} \rightarrow \text{CB}_{+1,\downarrow}^{\text{L}_{1,3}}$ | $\text{VB}_{\uparrow}^{\text{L}_{1,3}} \rightarrow \text{CB}_{+1,\uparrow}^{\text{L}_2}$ | $\text{VB}_{\downarrow}^{\text{L}_2} \rightarrow \text{CB}_{+1,\downarrow}^{\text{L}_{1,3}}$ |

Table E.2. **Decomposition of the oscillator strengths for 2H MoS₂ trilayer at the K point without and with electric field.** Identification of the two main electron-hole pairs related to excitonic peaks and percentage of the second contribution to the total oscillator strength.

L₂), composed of the corresponding L₂ VB and CBs, appears in the spectrum with a small contribution from delocalized holes over L_{1,3}. Additional B-like transitions (B:1s L₁, L₃), implying L₁ and L₃ VBs and CBs, also contribute to the spectrum. The effect of the electric field on the oscillator strength is also provided for an electric field value of $F_z = 1.0 \text{ MV/cm}$. Interestingly, only IE* and B:1s L₂ show significant changes in their transition composition: for both of them the intralayer contribution is reinforced by the application of the electric field, mainly due to the degeneracy lift of L₁ and L₃ VBs.

F

Supplementary information to Chapter 8: “Spin-polarized electrons in monolayer MoS₂”

In Chapter 8, we investigate a two-dimensional electron gas (2DEG) in a gated monolayer of MoS₂ by probing the interaction of excitons with the underlying Fermi sea through optical absorption and photoluminescence (PL) spectroscopy.

F.1 Optical absorption in gated monolayer MoS₂

This section provides a detailed description of the exciton-polaron theory used to interpret the optical susceptibility in monolayer MoS₂ as a function of the electron density.

F.1.1 Theory of the trion absorption in a 2DEG*

In this picture, photo-excited excitons are dressed by the interaction with excess electrons in the Fermi sea. As a consequence, the exciton resonance splits into a lower-energy attractive exciton-polaron branch (corresponding to the trion X^- in the single-particle limit) and a higher-energy repulsive exciton-polaron branch (normally identified as the exciton X^0 branch) [122, 240]. These two interactions, where either an exciton captures an electron and creates a X^- (attractive interaction) or an electron scatters off an exciton (repulsive interaction), contribute to the self-energy (Ξ) in the 2D exciton optical susceptibility [54, 123, 176, 241]

$$\chi(\hbar\omega) = -2|d_{cv}|^2 \frac{|\psi(\mathbf{r} = 0)|^2}{\hbar\omega + i\gamma - E(X^0) - \Xi}. \quad (\text{F.1})$$

*This section is partially adapted from the Supplement in J. G. Roch *et al.*, Nature Nanotechnology **14**, 432-436 (2019). J.G.R. developed the theory for this section.

$E(X^0)$ is the exciton energy, γ accounts for optical broadening, d_{cv} is the intervalley optical dipole moment and ψ is the exciton wavefunction.

When the Fermi level is smaller than the trion binding energy $E_F < E_b(X^-)$, the self-energy Ξ can be written as [123]

$$\Xi(\hbar\omega) = \int_0^\infty g_{2D} f_{FD}(\epsilon) T(\hbar\omega + \epsilon) d\epsilon, \quad (\text{F.2})$$

where $f_{FD}(\epsilon)$ is the Fermi-Dirac distribution describing the occupation of the Fermi sea, $g_{2D} = \frac{m_c^{\text{eff}}}{2\pi\hbar^2}$ is the 2D density of states (without spin-degeneracy), m_c^{eff} is the effective electron mass in the conduction band and $T(\epsilon)$ is the two-particle T -matrix.

Under the assumption that electrons in the Fermi sea only interact with excitons composed of electrons with opposite spin (singlet collision) to form a bound state (singlet trion), the T -matrix elements are [123]

$$T_s(\hbar\omega) = \frac{2\pi\hbar^2}{\mu_T} \frac{1}{\ln\left(\frac{-E_b(X^-)}{\hbar\omega - E(X^0) + i\gamma}\right)}, \quad (\text{F.3})$$

where μ_T is the reduced exciton-electron mass. μ_T can be written as

$$\frac{1}{\mu_T} = \frac{1}{m_c^{\text{eff}}} + \frac{1}{m_v^{\text{eff}} + m_c^{\text{eff}}}, \quad (\text{F.4})$$

with m_v^{eff} being the effective electron mass in the valence band.

Suris [54, 176] derived a model for the absorption of a 2DEG considering the effect of both singlet and triplet collisions. He assumes that, in a singlet collision, the exciton-electron interaction has a bound state corresponding to the singlet trion. On the other hand, in a triplet collision, there are no bound states of the exciton-electron interaction. This comes from the fact that triplet trions are unbound in the absence of magnetic fields [242].

In his model [54, 176], the two types of interactions are introduced by separating the T -matrix into two parts, $T = \frac{1}{2}T_s + \frac{3}{2}T_t$, with T_s accounting for singlet interactions and T_t for triplet interactions in the scattering process of an electron from an exciton. As these scattering matrix elements T_s are in agreement with those of Eq. F.3, we generalize the results from Ref. [123] for the case of singlet and triplet interactions inspired by Refs. [54, 176]. The T -matrix elements accounting for triplet interactions can then be

written as [54, 176]

$$T_t(\hbar\omega) = \frac{2\pi\hbar^2}{\mu_T} \frac{1}{\ln\left(\frac{-E_b(X^0)}{\hbar\omega - E(X^0) + i\gamma} \frac{E_b(X^0)}{\alpha E_b(X^-)}\right)}, \quad (\text{F.5})$$

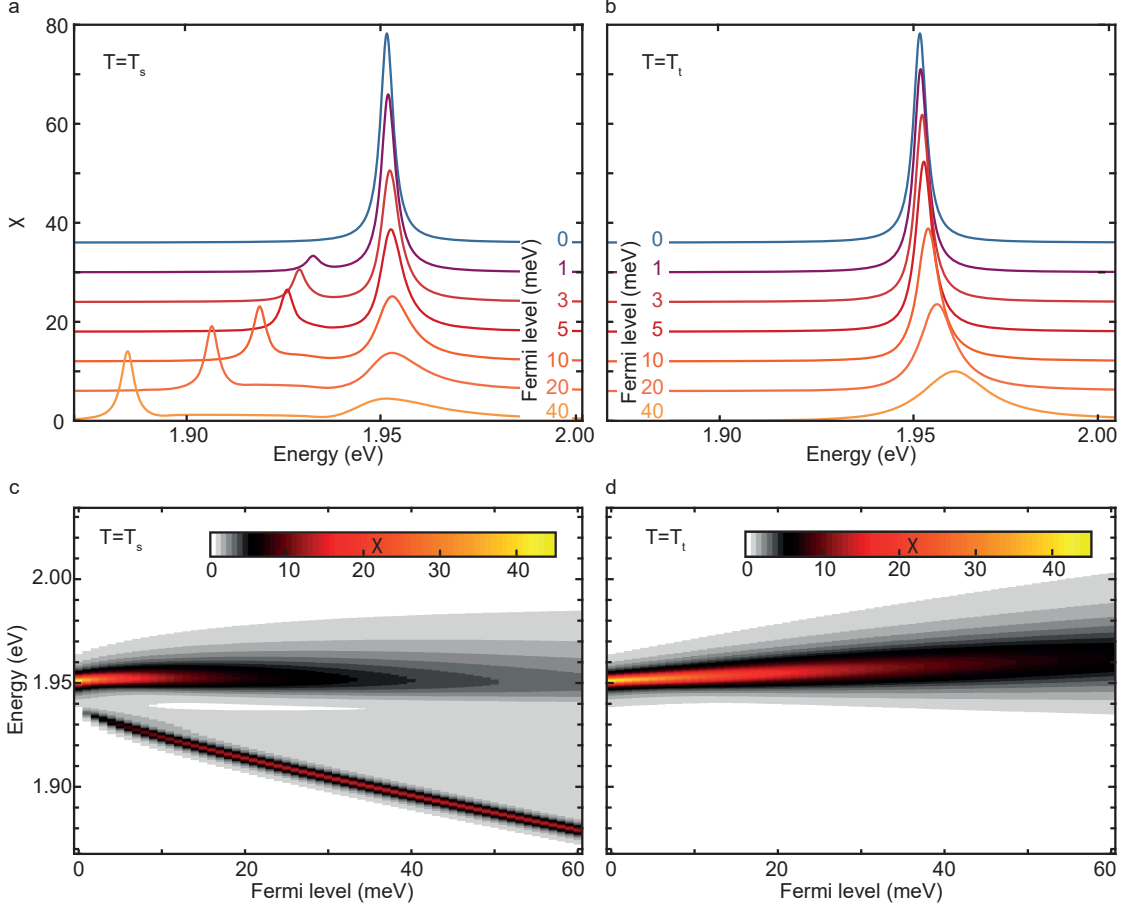


Figure F.1. **Suris model of the 2DEG optical susceptibility.** Optical susceptibility χ of an exciton simulated following Eq. F.2. The exciton interacts with a fully spin-polarized Fermi sea. **a**, The electrons of the photo-generated excitons have opposite spin to that of the electrons of the Fermi sea. Excitons interact attractively with electrons (singlet collisions). As a consequence, a low energy peak emerges around 1.9 eV, while the X^0 stays around 1.95 eV. **b**, The electrons of the photo-generated excitons have the same spin as the electrons of the Fermi sea. Therefore, the excitons experience a repulsive interaction with the electrons (triplet collisions). The X^0 peak becomes more asymmetric toward the high-energy side with increasing electron density (or Fermi level). **c**, Color map of the optical susceptibility χ in the case of singlet collisions for different Fermi levels and different photon energies. **d**, Same as in **c** but for triplet collisions. The simulations presented here were obtained using $m_c^{\text{eff}} = 0.44$ [21], $m_v^{\text{eff}} = 0.5$ [243], $E_b(X^0) = 260$ meV, $E_b(X^-) = 17$ meV, $E(X^0) = 1.952$ eV, $\alpha = 1$ and $\gamma = 2.0$ meV.

where $\alpha \approx 1$ is a number.

Fig. F.1 shows the contributions of the different T -matrix components to the optical susceptibility χ . In Figs. F.1a,c, we plot the optical susceptibility resulting from the singlet scattering ($T = T_s$). A sharp peak around 1.9 eV emerges at a finite Fermi level. It corresponds to the X^- or, more precisely, to the attractive polaron. The X^0 resonance at 1.95 eV (repulsive polaron) is also influenced by the interaction. It loses quickly in amplitude and the lineshape becomes asymmetric as the Fermi level increases. When only triplet scattering ($T = T_t$) is allowed (Figs. F.1b,d), no low-energy peak appears in the spectrum as there are no bound triplet trions. However, the X^0 resonance is modified by the presence of the Fermi sea. Its amplitude decreases, and the resonance shifts to higher energies with increasing Fermi level. In addition, the X^0 lineshape is modified by the presence of electrons: as the Fermi level increases, a long tail evolves on its high-energy side, and the X^0 peak becomes less and less Lorentzian. Comparing Fig. F.1a and Fig. F.1b shows that an attractive exciton-electron interaction is responsible for a sharp low-energy resonance (X^- , or attractive polaron), while a repulsive exciton-electron interaction tends to create a high-energy tail to the high-energy resonance (X^0 , or repulsive polaron). This prediction of the polaron model is in good agreement with our experimental optical absorption data presented in Chapter 8.

F.2 Photoluminescence in gated monolayer MoS₂

To identify the trion states in the different circular-polarization channels in PL, we use the few-particle trion picture.

F.2.1 Trion states in monolayer MoS₂

The existence of two degenerate valleys $+K$ and $-K$ in the bandstructure results in distinct states for the two- and three-particle excitations, respectively. As momentum has to be conserved, only electron-hole pairs (two-particle excitons) with close-to-zero momentum can be created under light excitation. However, the three-particle trion states are fundamentally different as the excess electron has an additional valley degree of freedom. In the following, we derive the eigenstates of the three-particle trion problem.

Eigenstates of the interacting three-body (trion) problem

The quantum states of trions can be obtained by solving the eigenvalue problem of the three-particle Hamiltonian. This calculation, however, is a non-trivial task. Nevertheless, the total spin projection s_z is a good quantum number, meaning it is conserved. Therefore, we can equivalently write down the eigenstates of s_z , that is, the wavefunctions corresponding to the spin values. In a system with two spin- $\frac{1}{2}$ particles (here, two electrons), each particle can either have spin $|\uparrow\rangle$ or spin $|\downarrow\rangle$. Consequently, the system has four basis states,

$$|\uparrow\rangle_1|\uparrow\rangle_2, |\uparrow\rangle_1|\downarrow\rangle_2, |\downarrow\rangle_1|\uparrow\rangle_2, |\downarrow\rangle_1|\downarrow\rangle_2, \quad (\text{F.6})$$

where we used the single-particle states to label the basis states. For the total spin projected on z , s_z , this gives us one state with $s_z = 0$,

$$\left. \frac{|\uparrow\rangle_1|\downarrow\rangle_2 - |\downarrow\rangle_1|\uparrow\rangle_2}{\sqrt{2}} \right\} \text{singlet state}, \quad (\text{F.7})$$

as well as three states with $s_z = 1$,

$$\left. \begin{array}{l} |\uparrow\rangle_1|\uparrow\rangle_2 \\ \frac{|\uparrow\rangle_1|\downarrow\rangle_2 + |\downarrow\rangle_1|\uparrow\rangle_2}{\sqrt{2}} \\ |\downarrow\rangle_1|\downarrow\rangle_2 \end{array} \right\} \text{triplet states}. \quad (\text{F.8})$$

We note that the singlet state is antisymmetric, while the triplet states are symmetric.

Now, since MoS₂ is a two-valley semiconductor, we have an additional valley degree of freedom τ . Analogous to the spin states, this gives us four possible orbital states, one antisymmetric state

$$\frac{|+K\rangle_1|-K\rangle_2 - |-K\rangle_1|+K\rangle_2}{\sqrt{2}} \quad (\text{F.9})$$

and three symmetric states

$$|+K\rangle_1|+K\rangle_2 \quad (\text{F.10})$$

$$\frac{|+K\rangle_1|-K\rangle_2 + |-K\rangle_1|+K\rangle_2}{\sqrt{2}} \quad (\text{F.11})$$

$$|-K\rangle_1|-K\rangle_2. \quad (\text{F.12})$$

Let us now construct the wavefunctions, taking into account the spin part s_z and the valley, or orbital, part τ . According to Fermi statistics, the total wavefunctions have to be antisymmetric under particle exchange.

For $s_z = 0$, the spin state is antisymmetric, and thus, following Fermi statistics, the orbital state has to be symmetric. This leads to following possibilities for the trion states

$$|S_d\rangle = | + K\rangle_1 | + K\rangle_2 \frac{|\uparrow\rangle_1 |\downarrow\rangle_2 - |\downarrow\rangle_1 |\uparrow\rangle_2}{\sqrt{2}}, \quad (\text{F.13})$$

$$\text{or } |S_d\rangle = | - K\rangle_1 | - K\rangle_2 \frac{|\uparrow\rangle_1 |\downarrow\rangle_2 - |\downarrow\rangle_1 |\uparrow\rangle_2}{\sqrt{2}}, \quad (\text{F.14})$$

which represent the intravalley spin singlet trions in either the $+K$ or $-K$ valley. Similarly, we can construct the other possible states by forming antisymmetric total wavefunctions from the possible spin- and valley states

$$|S_i\rangle = \frac{| + K\rangle_1 | - K\rangle_2 + | - K\rangle_1 | + K\rangle_2}{\sqrt{2}} \frac{|\uparrow\rangle_1 |\downarrow\rangle_2 - |\downarrow\rangle_1 |\uparrow\rangle_2}{\sqrt{2}}, \quad (\text{F.15})$$

$$|T_s\rangle = \frac{| + K\rangle_1 | - K\rangle_2 - | - K\rangle_1 | + K\rangle_2}{\sqrt{2}} \chi_s, \quad (\text{F.16})$$

where χ_s , $s \in \{-1, 0, 1\}$ is the triplet spinor

$$\chi_+ = |\uparrow\rangle_1 |\uparrow\rangle_2, \quad (\text{F.17})$$

$$\chi_0 = \frac{|\uparrow\rangle_1 |\downarrow\rangle_2 + |\downarrow\rangle_1 |\uparrow\rangle_2}{\sqrt{2}}, \quad (\text{F.18})$$

$$\chi_- = |\downarrow\rangle_1 |\downarrow\rangle_2. \quad (\text{F.19})$$

$|S_i\rangle$ and $|T_s\rangle$ are the intervalley spin singlet and the spin triplet trions, respectively.

Optical excitation of the trion states under circular polarization

Let us now investigate which trion states we can create under optical excitation with circularly-polarized light. The optical selection rules for the absorption ensure that normally incident σ^+ or σ^- circularly polarized light can only create an exciton in the $+K$ or $-K$ valley.

For σ^+ , the electron component of the bright exciton (A exciton) can be written as

$$|ex_+\rangle = | + K\rangle |\uparrow\rangle. \quad (\text{F.20})$$

In general, that is, without assuming any spin-polarization, such exciton has the option to bind to electrons from different Fermi seas

$$|+K\rangle|\downarrow\rangle, |-K\rangle|\downarrow\rangle, |-K\rangle|\uparrow\rangle. \quad (\text{F.21})$$

We note that binding to an $|+K\rangle|\uparrow\rangle$ electron is not possible due to the Pauli exclusion principle. This results in the formation of following states

$$|+K\rangle|\downarrow\rangle \xrightarrow{\text{trion}} |+K\rangle_1|+K\rangle_2 \frac{|\uparrow\rangle_1|\downarrow\rangle_2 - |\downarrow\rangle_2|\uparrow\rangle_1}{\sqrt{2}} \quad (\text{F.22})$$

$$|-K\rangle|\downarrow\rangle \xrightarrow{\text{trion}} \frac{|+K\rangle_1|\uparrow\rangle_1|-K\rangle_2|\downarrow\rangle_2 - |-K\rangle_2|\downarrow\rangle_2|+K\rangle_1|\uparrow\rangle_1}{\sqrt{2}} \quad (\text{F.23})$$

$$|-K\rangle|\uparrow\rangle \xrightarrow{\text{trion}} \frac{|+K\rangle_1|-K\rangle_2 - |-K\rangle_2|+K\rangle_1}{\sqrt{2}} |\uparrow\rangle_1|\uparrow\rangle_2. \quad (\text{F.24})$$

These states correspond to the intravalley spin singlet trion $|S_d\rangle$ when binding to the $|+K\rangle|\downarrow\rangle$ electron (Eqs. F.22 and F.13), and the intervalley spin-triplet trion $|T_+\rangle$ if a spin $|\uparrow\rangle$ electron from the $-K$ valley is involved (Eqs. F.24 and F.16), that is, $|-K\rangle|\uparrow\rangle$. Now, let us have a closer look at the state created when binding to an electron from the spin $|\downarrow\rangle$ Fermi sea in the opposite valley, that is, $|-K\rangle|\downarrow\rangle$. Comparing Eq. F.23 to the sum of Eq. F.16 and Eq. F.15

$$\begin{aligned} |T_0\rangle + |S_i\rangle &= \frac{|\uparrow\rangle_1|\downarrow\rangle_2}{\sqrt{2}} \sqrt{2} |+K\rangle_1|-K\rangle_2 \\ &\quad + \frac{|\downarrow\rangle_2|\uparrow\rangle_1}{\sqrt{2}} (-\sqrt{2}) |-K\rangle_2|+K\rangle_1 \\ &= |+K\rangle_1|\uparrow\rangle_1|-K\rangle_2|\downarrow\rangle_2 - |-K\rangle_2|\downarrow\rangle_2|+K\rangle_1|\uparrow\rangle_1 \end{aligned} \quad (\text{F.25})$$

yields that binding to a $|-K\rangle|\downarrow\rangle$ electron results in a superposition of the two intervalley trion states $|T_0\rangle$ and $|S_i\rangle$

$$|-K\rangle|\downarrow\rangle \xrightarrow{\text{trion}} \frac{|T_0\rangle + |S_i\rangle}{\sqrt{2}}. \quad (\text{F.26})$$

Accordingly, excitation with σ^- polarized light creates an exciton at the $-K$ valley

$$|ex_-\rangle = |-K\rangle|\downarrow\rangle, \quad (\text{F.27})$$

which can bind to an electron

$$| - K \rangle_2 | \uparrow \rangle_2, | + K \rangle_2 | \uparrow \rangle_2, | + K \rangle_2 | \downarrow \rangle_2 \quad (\text{F.28})$$

to form a three-particle trion state

$$| - K \rangle_2 | \uparrow \rangle_2 \xrightarrow{\text{trion}} | S_d \rangle \quad (\text{F.29})$$

$$| + K \rangle_2 | \uparrow \rangle_2 \xrightarrow{\text{trion}} \frac{| T_0 \rangle + | S_i \rangle}{\sqrt{2}} \quad (\text{F.30})$$

$$| + K \rangle_2 | \downarrow \rangle_2 \xrightarrow{\text{trion}} | T_- \rangle. \quad (\text{F.31})$$

F.2.2 Valley polarization

The valley-contrasting selection rules introduced in Chapter 2, together with the direct-bandgap transitions at the two degenerate K valleys, allow for the optical creation and detection of valley polarization in monolayer MoS₂. The degree of valley polarization η can be quantified by

$$\eta = \frac{I_{\text{co}} - I_{\text{cross}}}{I_{\text{co}} + I_{\text{cross}}} \quad (\text{F.32})$$

from the helicity-resolved PL intensities I_{cross} and I_{co} . Fig. F.2a presents the helicity-resolved PL spectra (σ^+ and σ^- components) of monolayer MoS₂ at $B_z = +9.00$ T, excited by σ^+ or σ^- polarized light. At charge neutrality ($n \simeq 0$), the spectra consist

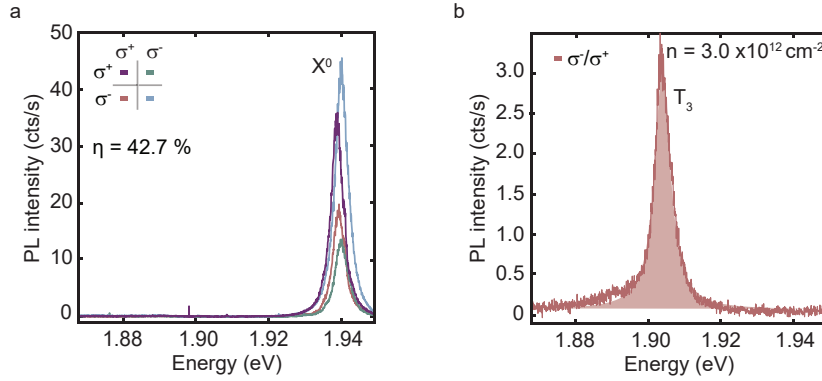


Figure F.2. **Analysis of the optical response of a monolayer MoS₂ in an external magnetic field.** **a**, Photoluminescence (PL) spectra at $n \simeq 0$ in all four circular polarizations ($T = 4$ K). Lorentzian fits to the neutral exciton X^0 reveal a valley polarization of $\eta = 42.7\%$ in our gated monolayer MoS₂. **b**, Single spectrum of a negatively charged trion in σ^-/σ^+ polarization measured on monolayer MoS₂ at $n = 3.0 \cdot 10^{12} \text{ cm}^{-2}$. The colored Lorentzian displays a fit to the corresponding T_3 line.

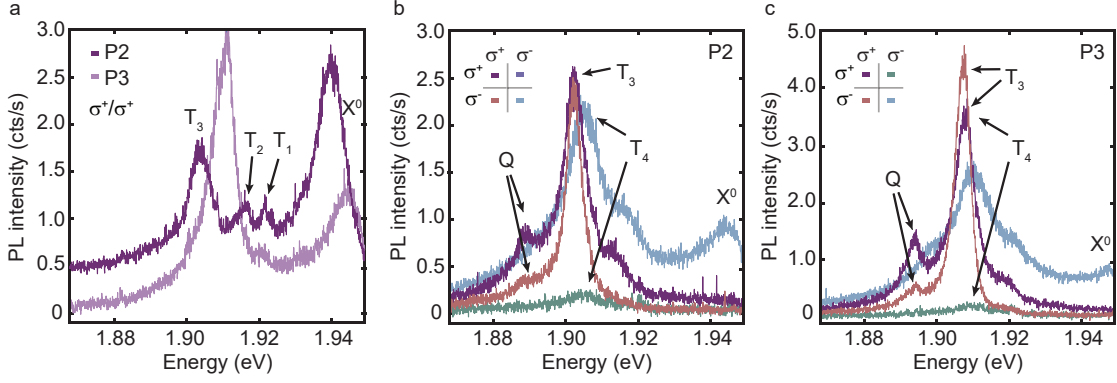


Figure F.3. **Optical photoluminescence (PL) spectra at different positions on the sample.** **a**, PL signal at $B_z = +9.00$ T and $n = 1.5 \cdot 10^{12} \text{ cm}^{-2}$ in σ^+/σ^+ polarization for different positions on the sample, position P2 (dark purple) and position P3 (light purple). The spectrum at position P2 is plotted with an offset of 0.5 cts/s for clarity. Optical spectra at $n = 3.4 \cdot 10^{12} \text{ cm}^{-2}$ in all four polarization channels for **b**, position P2 and **c**, position P3. The neutral exciton X^0 , the different trion states T_1 , T_2 , T_3 and T_4 , as well as the Q -peak are indicated. The similarity with the data on P1 (Chapter 8) demonstrates the reproducibility of the full spin-polarization in monolayer MoS₂.

of a strong, narrow transition line corresponding to the neutral exciton X^0 . These spectra further demonstrate a symmetric valley polarization (at $n \simeq 0$) for excitation with opposite helicity, that is, $\eta = 42.7\%$ under σ^+ excitation and $\eta = -42.9\%$ under σ^- excitation in our experiment.

F.2.3 Data reproducibility

As discussed in Chapter 8, different sample positions, labelled as P1, P2 and P3, were investigated to verify the reproducibility of the data obtained on position P1. Figs. F.3 and F.4 show the PL data for the four possible circular polarization combinations (excitation/collection) in a perpendicular magnetic field of $B_z = +9.00$ T for different positions on the sample P2 and P3. The neutral exciton linewidths and intensities are comparable to the data shown in Chapter 8 (position P1). Fig. F.4 presents the optical PL response in the different polarization channels for position P2 (F.4a) and position P3 (F.4b): the diagonal panels correspond to the co-polarized channels σ^+/σ^+ and σ^-/σ^- , while the top (bottom) off-diagonal panel shows the signal in the cross-polarized σ^+/σ^- (σ^-/σ^+) channel. At all positions, electron charging is demonstrated. With increasing carrier concentration, the intensity of the neutral exciton (X^0) is transferred to the negatively charged trions, while at high $n \approx 4.0 \cdot 10^{12} \text{ cm}^{-2}$ a broad peak, labelled as Q , appears at all positions on the sample. Furthermore, the presence and absence of

the trion states for the different polarization combinations (Figs. F.3b,c), as described in the Chapter 8, demonstrates the reproducibility of the spin-polarization of the 2DEG in monolayer MoS₂.

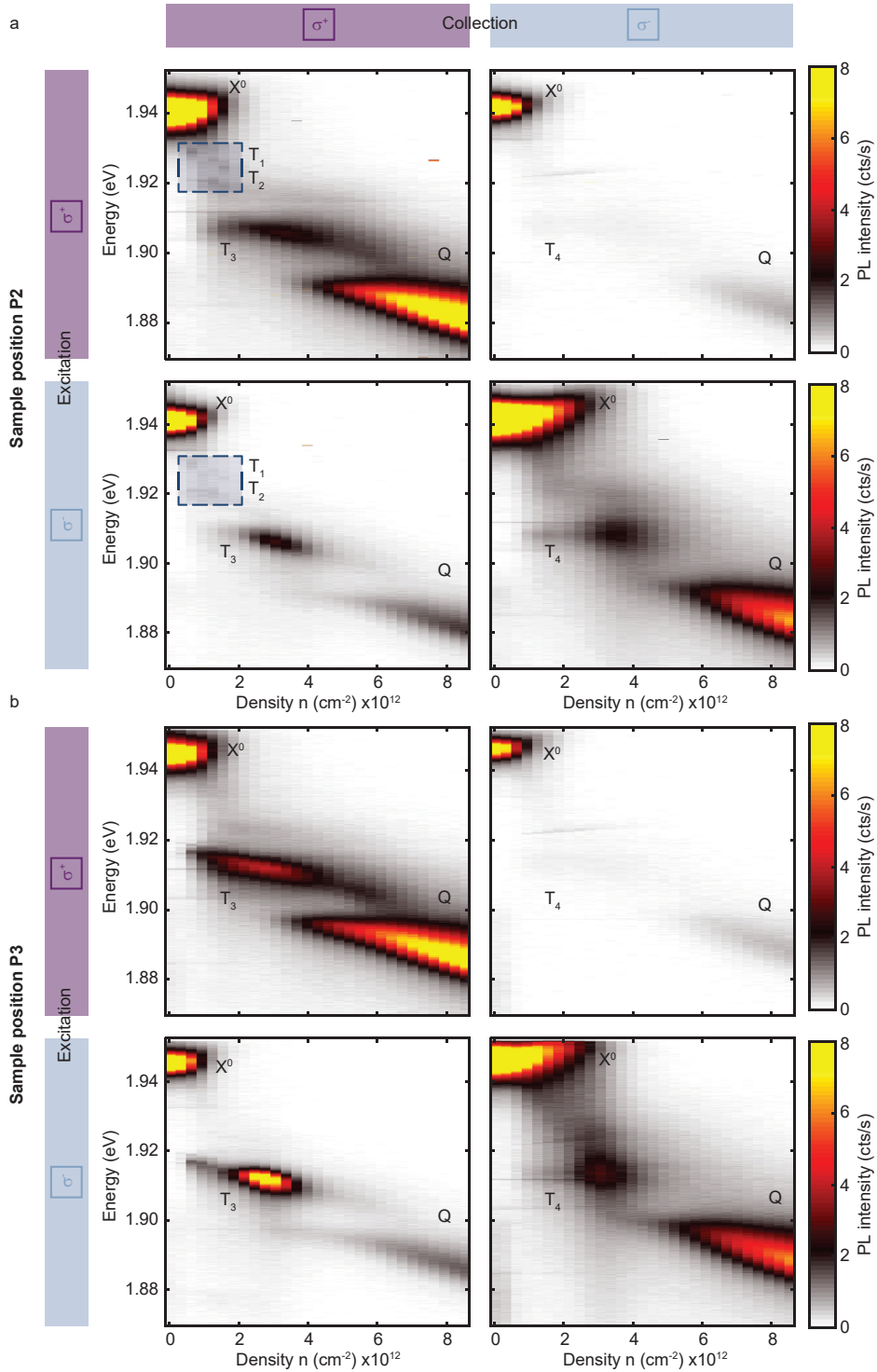


Figure F.4. **Optical photoluminescence (PL) from monolayer MoS₂ in a magnetic field at different positions.** The color maps show the PL response ($T = 4$ K) as a function of the photon energy (vertical axis) and the electron density n (horizontal axis) for all four polarization combinations obtained from different positions on the sample, labelled as P2 (top) and P3 (bottom). The data presented in Chapter 8 are extracted from position P1.

References

- [1] K. F. Mak, K. He, C. Lee, G. H. Lee, J. Hone, T. F. Heinz, and J. Shan, *Tightly bound trions in monolayer MoS₂*, [Nature Materials](#) **12**, 207 (2013).
- [2] K. F. Mak, K. He, J. Shan, and T. F. Heinz, *Control of valley polarization in monolayer MoS₂ by optical helicity*, [Nature Nanotechnology](#) **7**, 494 (2012).
- [3] A. Splendiani, L. Sun, Y. Zhang, T. Li, J. Kim, C.-Y. Chim, G. Galli, and F. Wang, *Emerging photoluminescence in monolayer MoS₂*, [Nano Letters](#) **10**, 1271 (2010).
- [4] K. F. Mak and J. Shan, *Photonics and optoelectronics of 2D semiconductor transition metal dichalcogenides*, [Nature Photonics](#) **10**, 216 (2016).
- [5] K. S. Novoselov, A. K. Geim, S. V. Morozov, D. Jiang, Y. Zhang, S. V. Dubonos, I. V. Grigorieva, and A. A. Firsov, *Electric field effect in atomically thin carbon films*, [Science](#) **306**, 666 (2004).
- [6] K. S. Novoselov, A. K. Geim, S. V. Morozov, D. Jiang, M. I. Katsnelson, I. V. Grigorieva, S. V. Dubonos, and A. A. Firsov, *Two-dimensional gas of massless Dirac fermions in graphene*, [Nature](#) **438**, 197 (2005).
- [7] K. F. Mak, C. Lee, J. Hone, J. Shan, and T. F. Heinz, *Atomically thin MoS₂: a new direct-gap semiconductor*, [Physical Review Letters](#) **105**, 136805 (2010).
- [8] H. Zeng, J. Dai, W. Yao, D. Xiao, and X. Cui, *Valley polarization in MoS₂ monolayers by optical pumping*, [Nature Nanotechnology](#) **7**, 490 (2012).
- [9] T. Cao, G. Wang, W. Han, H. Ye, C. Zhu, J. Shi, Q. Niu, P. Tan, E. Wang, B. Liu, and J. Feng, *Valley-selective circular dichroism of monolayer molybdenum disulphide*, [Nature Communications](#) **3**, 887 (2012).
- [10] D. Xiao, G.-B. Liu, W. Feng, X. Xu, and W. Yao, *Coupled spin and valley physics in monolayers of MoS₂ and other group-VI dichalcogenides*, [Physical Review Letters](#) **108**, 196802 (2012).

- [11] W. Zhang, K. Tanaka, Y. Hasegawa, K. Shinokita, K. Matsuda, and Y. Miyauchi, *Bright and highly valley polarized trions in chemically doped monolayer MoS₂*, [Applied Physics Express](#) **13**, 035002 (2020).
- [12] A. Chernikov, T. C. Berkelbach, H. M. Hill, A. Rigosi, Y. Li, O. B. Aslan, D. R. Reichman, M. S. Hybertsen, and T. F. Heinz, *Exciton binding energy and nonhydrogenic Rydberg series in monolayer WS₂*, [Physical Review Letters](#) **113**, 076802 (2014).
- [13] A. Ramasubramaniam, *Large excitonic effects in monolayers of molybdenum and tungsten dichalcogenides*, [Physical Review B](#) **86**, 115409 (2012).
- [14] G.-B. Liu, D. Xiao, Y. Yao, X. Xu, and W. Yao, *Electronic structures and theoretical modelling of two-dimensional group-VIB transition metal dichalcogenides*, [Chemical Society Reviews](#) **44**, 2643 (2015).
- [15] A. Kormányos, G. Burkard, M. Gmitra, J. Fabian, V. Zólyomi, N. D. Drummond, and V. Fal'ko, *$\mathbf{k} \cdot \mathbf{p}$ theory for two-dimensional transition metal dichalcogenide semiconductors*, [2D Materials](#) **2**, 022001 (2015).
- [16] Z. Y. Zhu, Y. C. Cheng, and U. Schwingenschlögl, *Giant spin-orbit-induced spin splitting in two-dimensional transition-metal dichalcogenide semiconductors*, [Physical Review B](#) **84**, 153402 (2011).
- [17] G.-B. Liu, W.-Y. Shan, Y. Yao, W. Yao, and D. Xiao, *Three-band tight-binding model for monolayers of group-VIB transition metal dichalcogenides*, [Physical Review B](#) **88**, 085433 (2013).
- [18] K. Zollner, P. E. F. Junior, and J. Fabian, *Strain-tunable orbital, spin-orbit, and optical properties of monolayer transition-metal dichalcogenides*, [Physical Review B](#) **100**, 195126 (2019).
- [19] E. S. Kadantsev and P. Hawrylak, *Electronic structure of a single MoS₂ monolayer*, [Solid State Communications](#) **152**, 909 (2012).
- [20] J. Klinovaja and D. Loss, *Fermionic and Majorana bound states in hybrid nanowires with non-uniform spin-orbit interaction*, [The European Physical Journal B](#) **88**, 62 (2015).
- [21] A. Kormányos, V. Zólyomi, N. D. Drummond, and G. Burkard, *Spin-orbit coupling, quantum dots, and qubits in monolayer transition metal dichalcogenides*, [Physical Review X](#) **4**, 011034 (2014).

- [22] W. S. Yun, S. W. Han, S. C. Hong, I. G. Kim, and J. D. Lee, *Thickness and strain effects on electronic structures of transition metal dichalcogenides: 2H-MX₂ semiconductors (M=Mo, W; X=S, Se, Te)*, [Physical Review B](#) **85**, 033305 (2012).
- [23] W. Zhao, R. M. Ribeiro, M. Toh, A. Carvalho, C. Kloc, A. H. Castro Neto, and G. Eda, *Origin of indirect optical transitions in few-layer MoS₂, WS₂, and WSe₂*, [Nano Letters](#) **13**, 5627 (2013).
- [24] W. Yao, D. Xiao, and Q. Niu, *Valley-dependent optoelectronics from inversion symmetry breaking*, [Phys. Rev. B](#) **77**, 235406 (2008).
- [25] G. Wang, A. Chernikov, M. M. Glazov, T. F. Heinz, X. Marie, T. Amand, and B. Urbaszek, *Colloquium: excitons in atomically thin transition metal dichalcogenides*, [Reviews of Modern Physics](#) **90**, 021001 (2018).
- [26] A. V. Stier, N. P. Wilson, G. Clark, X. Xu, and S. A. Crooker, *Probing the influence of dielectric environment on excitons in monolayer WSe₂: insight from high magnetic fields*, [Nano Letters](#) **16**, 7054 (2016).
- [27] A. Raja, A. Chaves, J. Yu, G. Arefe, H. M. Hill, A. F. Rigosi, T. C. Berkelbach, P. Nagler, C. Schüller, T. Korn, C. Nuckolls, J. Hone, L. E. Brus, T. F. Heinz, D. R. Reichman, and A. Chernikov, *Coulomb engineering of the bandgap and excitons in two-dimensional materials*, [Nature Communications](#) **8**, 15251 (2017).
- [28] C. Klingshirn, *Semiconductor Optics* (Springer, Berlin Heidelberg New York), 3rd edition (2007).
- [29] W. Nakwaski, *Effective masses of electrons and heavy holes in GaAs, InAs, AlAs and their ternary compounds*, [Physica B: Condensed Matter](#) **210**, 1 (1995).
- [30] B. Urbaszek and A. Srivastava, *Materials in flatland twist and shine*, [Nature](#) **567**, 39 (2019).
- [31] T. Deilmann, M. Rohlfing, and U. Wurstbauer, *Light-matter interaction in van der Waals heterostructures*, [Journal of Physics: Condensed Matter](#) **32**, 333002 (2020).
- [32] Y. Jiang, S. Chen, W. Zheng, B. Zheng, and A. Pan, *Interlayer exciton formation, relaxation, and transport in TMD van der Waals heterostructures*, [Light: Science and Applications](#) **10**, 72 (2021).

- [33] P. Rivera, J. R. Schaibley, A. M. Jones, J. S. Ross, S. Wu, G. Aivazian, P. Klement, K. Seyler, G. Clark, N. J. Ghimire, J. Yan, D. G. Mandrus, W. Yao, and X. Xu, *Observation of long-lived interlayer excitons in monolayer MoSe_2 - WSe_2 heterostructures*, [Nature Communications](#) **6**, 6242 (2015).
- [34] P. Rivera, K. L. Seyler, H. Yu, J. R. Schaibley, J. Yan, D. G. Mandrus, W. Yao, and X. Xu, *Valley-polarized exciton dynamics in a 2D semiconductor heterostructure*, [Science](#) **351**, 688 (2016).
- [35] P. Nagler, M. V. Ballottin, A. A. Mitioglu, F. Mooshammer, N. Paradiso, C. Strunk, R. Huber, A. Chernikov, P. C. M. Christianen, C. Schüller, and T. Korn, *Giant magnetic splitting inducing near-unity valley polarization in van der Waals heterostructures*, [Nature Communications](#) **8**, 1551 (2017).
- [36] B. Miller, A. Steinhoff, B. Pano, J. Klein, F. Jahnke, A. Holleitner, and U. Wurstbauer, *Long-lived direct and indirect interlayer excitons in van der Waals heterostructures*, [Nano Letters](#) **17**, 5229 (2017).
- [37] A. T. Hanbicki, H.-J. Chuang, M. R. Rosenberger, C. S. Hellberg, S. V. Sivaram, K. M. McCreary, I. I. Mazin, and B. T. Jonker, *Double indirect interlayer exciton in a $\text{MoSe}_2/\text{WSe}_2$ van der Waals heterostructure*, [ACS Nano](#) **12**, 4719 (2018).
- [38] A. Ciarrocchi, D. Unuchek, A. Avsar, K. Watanabe, T. Taniguchi, and A. Kis, *Polarization switching and electrical control of interlayer excitons in two-dimensional van der Waals heterostructures*, [Nature Photonics](#) **13**, 131 (2019).
- [39] L. A. Jauregui, A. Y. Joe, K. Pistunova, D. S. Wild, A. A. High, Y. Zhou, G. Scuri, K. De Greve, A. Sushko, C.-H. Yu, T. Taniguchi, K. Watanabe, D. J. Needleman, M. D. Lukin, H. Park, and P. Kim, *Electrical control of interlayer exciton dynamics in atomically thin heterostructures*, [Science](#) **366**, 870 (2019).
- [40] K. L. Seyler, P. Rivera, H. Yu, N. P. Wilson, E. L. Ray, D. G. Mandrus, J. Yan, W. Yao, and X. Xu, *Signatures of moiré-trapped valley excitons in $\text{MoSe}_2/\text{WSe}_2$ heterobilayers*, [Nature](#) **567**, 66 (2019).
- [41] L. Sigl, F. Sigger, F. Kronowetter, J. Kiemle, J. Klein, K. Watanabe, T. Taniguchi, J. J. Finley, U. Wurstbauer, and A. W. Holleitner, *Signatures of a degenerate many-body state of interlayer excitons in a van der Waals heterostack*, [Physical Review Research](#) **2**, 042044 (2020).

- [42] W.-T. Hsu, B.-H. Lin, L.-S. Lu, M.-H. Lee, M.-W. Chu, L.-J. Li, W. Yao, W.-H. Chang, and C.-K. Shih, *Tailoring excitonic states of van der Waals bilayers through stacking configuration, band alignment, and valley spin*, *Science Advances* **5**, eaax7407 (2019).
- [43] E. M. Alexeev, D. A. Ruiz-Tijerina, M. Danovich, M. J. Hamer, D. J. Terry, P. K. Nayak, S. Ahn, S. Pak, J. Lee, J. I. Sohn, M. R. Molas, M. Koperski, K. Watanabe, T. Taniguchi, K. S. Novoselov, R. V. Gorbachev, H. S. Shin, V. I. Fal'ko, and A. I. Tartakovskii, *Resonantly hybridized excitons in moiré superlattices in van der Waals heterostructures*, *Nature* **567**, 81 (2019).
- [44] L. Zhang, Z. Zhang, F. Wu, D. Wang, R. Gogna, S. Hou, K. Watanabe, T. Taniguchi, K. Kulkarni, T. Kuo, S. R. Forrest, and H. Deng, *Twist-angle dependence of moiré excitons in $WS_2/MoSe_2$ heterobilayers*, *Nature Communications* **11**, 5888 (2020).
- [45] Y. Tang, J. Gu, S. Liu, K. Watanabe, T. Taniguchi, J. Hone, K. F. Mak, and J. Shan, *Tuning layer-hybridized moiré excitons by the quantum-confined Stark effect*, *Nature Nanotechnology* **16**, 52 (2021).
- [46] J. Kiemle, F. Sigger, M. Lorke, B. Miller, K. Watanabe, T. Taniguchi, A. Holleitner, and U. Wurstbauer, *Control of the orbital character of indirect excitons in MoS_2/WS_2 heterobilayers*, *Physical Review B* **101**, 121404 (2020).
- [47] Y. Shimazaki, I. Schwartz, K. Watanabe, T. Taniguchi, M. Kroner, and A. İmamoğlu, *Strongly correlated electrons and hybrid excitons in a moiré heterostructure*, *Nature* **580**, 472 (2020).
- [48] J. Sung, Y. Zhou, G. Scuri, V. Zólyomi, T. I. Andersen, H. Yoo, D. S. Wild, A. Y. Joe, R. J. Gelly, H. Heo, S. J. Magorrian, D. Bérubé, A. M. M. Valdivia, T. Taniguchi, K. Watanabe, M. D. Lukin, P. Kim, V. I. Fal'ko, and H. Park, *Broken mirror symmetry in excitonic response of reconstructed domains in twisted $MoSe_2/MoSe_2$ bilayers*, *Nature Nanotechnology* **15**, 750 (2020).
- [49] T. Deilmann and K. S. Thygesen, *Interlayer excitons with large optical amplitudes in layered van der Waals materials*, *Nano Letters* **18**, 2984 (2018).
- [50] J. Horng, T. Stroucken, L. Zhang, E. Y. Paik, H. Deng, and S. W. Koch, *Observation of interlayer excitons in $MoSe_2$ single crystals*, *Physical Review B* **97**, 241404 (2018).

- [51] I. C. Gerber, E. Courtade, S. Shree, C. Robert, T. Taniguchi, K. Watanabe, A. Balocchi, P. Renucci, D. Lagarde, X. Marie, and B. Urbaszek, *Interlayer excitons in bilayer MoS₂ with strong oscillator strength up to room temperature*, [Physical Review B](#) **99**, 035443 (2019).
- [52] J. S. Ross, S. Wu, H. Yu, N. J. Ghimire, A. M. Jones, G. Aivazian, J. Yan, D. G. Mandrus, D. Xiao, W. Yao, and X. Xu, *Electrical control of neutral and charged excitons in a monolayer semiconductor*, [Nature Communications](#) **4**, 1474 (2013).
- [53] Y. V. Zhumagulov, A. Vagov, D. R. Gulevich, P. E. Faria Junior, and V. Perebeinos, *Trion induced photoluminescence of a doped MoS₂ monolayer*, [The Journal of Chemical Physics](#) **153**, 044132 (2020).
- [54] R. Suris, V. Kochereshko, G. Astakhov, D. Yakovlev, W. Ossau, J. Nürnberger, W. Faschinger, G. Landwehr, T. Wojtowicz, G. Karczewski, and J. Kossut, *Excitons and trions modified by interaction with a two-dimensional electron gas*, [Physica Status Solidi \(b\)](#) **227**, 343 (2001).
- [55] D. K. Efimkin and A. H. MacDonald, *Exciton-polarons in doped semiconductors in a strong magnetic field*, [Physical Review B](#) **97**, 235432 (2018).
- [56] J. G. Roch, G. Froehlicher, N. Leisgang, P. Makk, K. Watanabe, T. Taniguchi, and R. J. Warburton, *Spin-polarized electrons in monolayer MoS₂*, [Nature Nanotechnology](#) **14**, 432 (2019).
- [57] G. Aivazian, Z. Gong, A. M. Jones, R.-L. Chu, J. Yan, D. G. Mandrus, C. Zhang, D. Cobden, W. Yao, and X. Xu, *Magnetic control of valley pseudospin in monolayer WSe₂*, [Nature Physics](#) **11**, 148 (2015).
- [58] A. V. Stier, K. M. McCreary, B. T. Jonker, J. Kono, and S. A. Crooker, *Exciton diamagnetic shifts and valley Zeeman effects in monolayer WS₂ and MoS₂ to 65 Tesla*, [Nature Communications](#) **7**, 10643 (2016).
- [59] J. R. Schaibley, H. Yu, G. Clark, P. Rivera, J. S. Ross, K. L. Seyler, W. Yao, and X. Xu, *Valleytronics in 2D materials*, [Nature Reviews Materials](#) **1**, 16055 (2016).
- [60] A. K. Geim and I. V. Grigorieva, *Van der Waals heterostructures*, [Nature](#) **499**, 419 (2013).
- [61] K. S. Novoselov, A. Mishchenko, A. Carvalho, and A. H. C. Neto, *2D materials and van der Waals heterostructures*, [Science](#) **353**, aac9439 (2016).

- [62] Y. Y. Wang, R. X. Gao, Z. H. Ni, H. He, S. P. Guo, H. P. Yang, C. X. Cong, and T. Yu, *Thickness identification of two-dimensional materials by optical imaging*, [Nanotechnology](#) **23**, 495713 (2012).
- [63] R. V. Gorbachev, I. Riaz, R. R. Nair, R. Jalil, L. Britnell, B. D. Belle, E. W. Hill, K. S. Novoselov, K. Watanabe, T. Taniguchi, A. K. Geim, and P. Blake, *Hunting for monolayer boron nitride: optical and Raman signatures*, [Small](#) **7**, 465 (2011).
- [64] C. Lee, H. Yan, L. E. Brus, T. F. Heinz, J. Hone, and S. Ryu, *Anomalous lattice vibrations of single- and few-layer MoS₂*, [ACS Nano](#) **4**, 2695 (2010).
- [65] N. Leisgang, *Photonics of the transition metal dichalcogenides*, Master's thesis (2017).
- [66] P. J. Zomer, M. H. D. Guimarães, J. C. Brant, N. Tombros, and B. J. van Wees, *Fast pick up technique for high quality heterostructures of bilayer graphene and hexagonal boron nitride*, [Applied Physics Letters](#) **105**, 013101 (2014).
- [67] C. Handschin, *Quantum-transport in encapsulated graphene p-n junctions*, PhD thesis (2017).
- [68] D. G. Purdie, N. M. Pugno, T. Taniguchi, K. Watanabe, A. C. Ferrari, and A. Lombardo, *Cleaning interfaces in layered materials heterostructures*, [Nature Communications](#) **9**, 5387 (2018).
- [69] A. P. Rooney, A. Kozikov, A. N. Rudenko, E. Prestat, M. J. Hamer, F. Withers, Y. Cao, K. S. Novoselov, M. I. Katsnelson, R. Gorbachev, and S. J. Haigh, *Observing imperfection in atomic interfaces for van der Waals heterostructures*, [Nano Letters](#) **17**, 5222 (2017).
- [70] S. Shree, I. Paradisanos, X. Marie, C. Robert, and B. Urbaszek, *Guide to optical spectroscopy of layered semiconductors*, [Nature Reviews Physics](#) **3**, 39 (2021).
- [71] A. Raja, L. Waldecker, J. Zipfel, Y. Cho, S. Brem, J. D. Ziegler, M. Kulig, T. Taniguchi, K. Watanabe, E. Malic, T. F. Heinz, T. C. Berkelbach, and A. Chernikov, *Dielectric disorder in two-dimensional materials*, [Nature Nanotechnology](#) **14**, 832 (2019).
- [72] F. Cadiz, E. Courtade, C. Robert, G. Wang, Y. Shen, H. Cai, T. Taniguchi, K. Watanabe, H. Carrere, D. Lagarde, M. Manca, T. Amand, P. Renucci, S. Tongay, X. Marie, and B. Urbaszek, *Excitonic linewidth approaching the homogeneous*

- limit in MoS₂-based van der Waals heterostructures*, [Physical Review X](#) **7**, 021026 (2017).
- [73] J. Zipfel, M. Kulig, R. Perea-Causín, S. Brem, J. D. Ziegler, R. Rosati, T. Taniguchi, K. Watanabe, M. M. Glazov, E. Malic, and A. Chernikov, *Exciton diffusion in monolayer semiconductors with suppressed disorder*, [Physical Review B](#) **101**, 115430 (2020).
- [74] M. K. L. Man, S. Deckoff-Jones, A. Winchester, G. Shi, G. Gupta, A. D. Mohite, S. Kar, E. Kioupakis, S. Talapatra, and K. M. Dani, *Protecting the properties of monolayer MoS₂ on silicon based substrates with an atomically thin buffer*, [Scientific Reports](#) **6**, 20890 (2016).
- [75] C. R. Dean, A. F. Young, I. Meric, C. Lee, L. Wang, S. Sorgenfrei, K. Watanabe, T. Taniguchi, P. Kim, and K. Shepard, *Boron nitride substrates for high-quality graphene electronics*, [Nature Nanotechnology](#) **5**, 722 (2010).
- [76] Y. Hattori, T. Taniguchi, K. Watanabe, and K. Nagashio, *Layer-by-layer dielectric breakdown of hexagonal boron nitride*, [ACS Nano](#) **9**, 916 (2015).
- [77] R. Pisoni, T. Davatz, K. Watanabe, T. Taniguchi, T. Ihn, and K. Ensslin, *Absence of interlayer tunnel coupling of K-valley electrons in bilayer MoS₂*, [Physical Review Letters](#) **123**, 117702 (2019).
- [78] A. Laturia, M. L. Van de Put, and W. G. Vandenberghe, *Dielectric properties of hexagonal boron nitride and transition metal dichalcogenides: from monolayer to bulk*, [npj 2D Materials and Applications](#) **2**, 6 (2018).
- [79] U. Chandni, K. Watanabe, T. Taniguchi, and J. P. Eisenstein, *Evidence for defect-mediated tunneling in hexagonal boron nitride-based junctions*, [Nano Letters](#) **15**, 7329 (2015).
- [80] L. Ju, J. Velasco, E. Huang, S. Kahn, C. Nosisgia, H.-Z. Tsai, W. Yang, T. Taniguchi, K. Watanabe, Y. Zhang, G. Zhang, M. Crommie, A. Zettl, and F. Wang, *Photoinduced doping in heterostructures of graphene and boron nitride*, [Nature Nanotechnology](#) **9**, 348 (2014).
- [81] F. Vialla, M. Danovich, D. A. Ruiz-Tijerina, M. Massicotte, P. Schmidt, T. Taniguchi, K. Watanabe, R. J. Hunt, M. Szytniszewski, N. D. Drummond, T. G. Pedersen, V. I. Fal'ko, and F. H. L. Koppens, *Tuning of impurity-bound interlayer complexes in a van der Waals heterobilayer*, [2D Materials](#) **6**, 035032 (2019).

- [82] E. Hecht, *Optics* (Addison-Wesley), 4th edition (2001).
- [83] M. Fox, *Quantum optics: an introduction* (Oxford University Press) (2006).
- [84] R. W. Boyd, *Nonlinear optics* (Academic Press, Rochester, New York USA), 3rd edition (2008).
- [85] M. Fox, *Optical properties of solids* (Oxford University Press) (2010).
- [86] J. McIntyre and D. Aspnes, *Differential reflection spectroscopy of very thin surface films*, [Surface Science](#) **24**, 417 (1971).
- [87] A. Arora, A. Mandal, S. Chakrabarti, and S. Ghosh, *Magneto-optical Kerr effect spectroscopy based study of Landé g-factor for holes in GaAs/AlGaAs single quantum wells under low magnetic fields*, [Journal of Applied Physics](#) **113**, 213505 (2013).
- [88] P. Back, M. Sidler, O. Cotlet, A. Srivastava, N. Takemura, M. Kroner, and A. Imamoglu, *Giant paramagnetism-induced valley polarization of electrons in charge-tunable monolayer MoSe₂*, [Physical Review Letters](#) **118**, 237404 (2017).
- [89] Y. R. Shen, *The principles of nonlinear optics* (Wiley, New York) (2003).
- [90] G. Wang, X. Marie, I. Gerber, T. Amand, D. Lagarde, L. Bouet, M. Vidal, A. Balocchi, and B. Urbaszek, *Giant enhancement of the optical second-harmonic emission of WSe₂ monolayers by laser excitation at exciton resonances*, [Physical Review Letters](#) **114**, 097403 (2015).
- [91] S. Shree, D. Lagarde, L. Lombez, C. Robert, A. Balocchi, K. Watanabe, T. Taniguchi, X. Marie, I. C. Gerber, M. M. Glazov, L. E. Golub, B. Urbaszek, and I. Paradisanos, *Interlayer exciton mediated second harmonic generation in bilayer MoS₂*, [arXiv:2104.01225](#) (2021).
- [92] H. B. Ribeiro, M. A. Pimenta, C. J. S. d. Matos, R. L. Moreira, A. S. Rodin, J. D. Zapata, E. A. T. d. Souza, and A. H. C. Neto, *Unusual angular dependence of the Raman response in black phosphorus*, [ACS Nano](#) **9**, 4270 (2015).
- [93] P. N. Butcher, *Nonlinear optical phenomena* (Engineering Experiment Station, Ohio State University) (1965).
- [94] Y. Zhang, Y.-W. Tan, H. L. Stormer, and P. Kim, *Experimental observation of the quantum Hall effect and Berry's phase in graphene*, [Nature](#) **438**, 201 (2005).

- [95] F. Xia, H. Wang, D. Xiao, M. Dubey, and A. Ramasubramaniam, *Two-dimensional material nanophotonics*, [Nature Photonics](#) **8**, 899 (2014).
- [96] A. Kretinin, Y. Cao, J. Tu, G. Yu, R. Jalil, K. Novoselov, S. Haigh, A. Gholinia, A. Mishchenko, M. Lozada, T. Georgiou, C. R. Woods, F. Withers, P. Blake, G. Eda, A. Wirsig, C. Hucho, K. Watanabe, T. Taniguchi, A. K. Geim, and R. V. Gorbachev, *Electronic properties of graphene encapsulated with different two-dimensional atomic crystals*, [Nano Letters](#) **14**, 3270 (2014).
- [97] A. Mishchenko, J. S. Tu, Y. Cao, R. V. Gorbachev, J. R. Wallbank, M. T. Greenaway, V. E. Morozov, S. V. Morozov, M. J. Zhu, S. L. Wong, F. Withers, C. R. Woods, Y.-J. Kim, K. Watanabe, T. Taniguchi, E. E. Vdovin, O. Makarovskiy, T. M. Fromhold, V. I. Fal'ko, A. K. Geim, L. Eaves, and K. S. Novoselov, *Twist-controlled resonant tunnelling in graphene/boron nitride/graphene heterostructures*, [Nature Nanotechnology](#) **9**, 808 (2014).
- [98] J. Kunstmann, F. Mooshammer, P. Nagler, A. Chaves, F. Stein, N. Paradiso, G. Plechinger, C. Strunk, C. Schüller, G. Seifert, D. R. Reichman, and T. Korn, *Momentum-space indirect interlayer excitons in transition-metal dichalcogenide van der Waals heterostructures*, [Nature Physics](#) **14**, 801 (2018).
- [99] K. Liu, L. Zhang, T. Cao, C. Jin, D. Qiu, Q. Zhou, A. Zettl, P. Yang, S. G. Louie, and F. Wang, *Evolution of interlayer coupling in twisted molybdenum disulfide bilayers*, [Nature Communications](#) **5**, 4966 (2014).
- [100] A. M. van der Zande, J. Kunstmann, A. Chernikov, D. A. Chenet, Y. You, X. Zhang, P. Y. Huang, T. C. Berkelbach, L. Wang, F. Zhang, M. S. Hybertsen, D. A. Muller, D. R. Reichman, T. F. Heinz, and J. C. Hone, *Tailoring the electronic structure in bilayer molybdenum disulfide via interlayer twist*, [Nano Letters](#) **14**, 3869 (2014).
- [101] N. Kumar, S. Najmaei, Q. Cui, F. Ceballos, P. M. Ajayan, J. Lou, and H. Zhao, *Second harmonic microscopy of monolayer MoS₂*, [Physical Review B](#) **87**, 161403 (2013).
- [102] L. M. Malard, T. V. Alencar, A. P. M. Barboza, K. F. Mak, and A. M. de Paula, *Observation of intense second harmonic generation from MoS₂ atomic crystals*, [Physical Review B](#) **87**, 201401 (2013).

- [103] C. Janisch, Y. Wang, D. Ma, N. Mehta, A. L. Elías, N. Perea-López, M. Terrones, V. Crespi, and Z. Liu, *Extraordinary second harmonic generation in tungsten disulfide monolayers*, [Scientific Reports](#) **4**, 5530 (2015).
- [104] P. K. Nayak, Y. Horbatenko, S. Ahn, G. Kim, J.-U. Lee, K. Y. Ma, A.-R. Jang, H. Lim, D. Kim, S. Ryu, H. Cheong, N. Park, and H. S. Shin, *Probing evolution of twist-angle-dependent interlayer excitons in MoSe₂/WSe₂ van der Waals heterostructures*, [ACS Nano](#) **11**, 4041 (2017).
- [105] G. W. Mudd, M. R. Molas, X. Chen, V. Zólyomi, K. Nogajewski, Z. R. Kudrynskiy, Z. D. Kovalyuk, G. Yusa, O. Makarovskiy, L. Eaves, M. Potemski, V. I. Fal'ko, and A. Patané, *The direct-to-indirect band gap crossover in two-dimensional van der Waals Indium Selenide crystals*, [Scientific Reports](#) **6**, 39619 (2016).
- [106] D. A. Bandurin, A. V. Tyurnina, G. L. Yu, A. Mishchenko, V. Zólyomi, S. V. Morozov, R. K. Kumar, R. V. Gorbachev, Z. R. Kudrynskiy, S. Pezzini, Z. D. Kovalyuk, U. Zeitler, K. S. Novoselov, A. Patané, L. Eaves, I. V. Grigorieva, V. I. Fal'ko, A. K. Geim, and Y. Cao, *High electron mobility, quantum Hall effect and anomalous optical response in atomically thin InSe*, [Nature Nanotechnology](#) **12**, 223 (2017).
- [107] S. Deckoff-Jones, J. Zhang, C. E. Petoukhoff, M. K. Man, S. Lei, R. Vajtai, P. M. Ajayan, D. Talbayev, J. Madéo, and K. M. Dani, *Observing the interplay between surface and bulk optical nonlinearities in thin van der Waals crystals*, [Scientific Reports](#) **6**, 22620 (2016).
- [108] A. Yariv and P. Yeh, *Optical waves in crystals: propagation and control of laser radiation* (Wiley, New York) (1984).
- [109] Y. R. Shen, *Optical second harmonic generation at interfaces*, [Annual Review of Physical Chemistry](#) **40**, 327 (1989).
- [110] Y. Tang, K. C. Mandal, J. A. McGuire, and C. W. Lai, *Layer- and frequency-dependent second harmonic generation in reflection from GaSe atomic crystals*, [Physical Review B](#) **94**, 125302 (2016).
- [111] A. Sushko, K. De Greve, T. I. Andersen, G. Scuri, Y. Zhou, J. Sung, K. Watanabe, T. Taniguchi, P. Kim, H. Park, and M. D. Lukin, *High resolution imaging of reconstructed domains and moire patterns in functional van der Waals heterostructure devices*, [arXiv:1912.07446](#) (2019).

- [112] A. Weston, Y. Zou, V. Enaldiev, A. Summerfield, N. Clark, V. Zólyomi, A. Graham, C. Yelgel, S. Magorrian, M. Zhou, J. Zultak, D. Hopkinson, A. Barinov, T. H. Bointon, A. Kretinin, N. R. Wilson, P. H. Beton, V. I. Fal'ko, S. J. Haigh, and R. Gorbachev, *Atomic reconstruction in twisted bilayers of transition metal dichalcogenides*, [Nature Nanotechnology](#) **15**, 592 (2020).
- [113] I. Paradisanos, S. Shree, A. George, N. Leisgang, C. Robert, K. Watanabe, T. Taniguchi, R. J. Warburton, A. Turchanin, X. Marie, I. C. Gerber, and B. Urbaszek, *Controlling interlayer excitons in MoS₂ layers grown by chemical vapor deposition*, [Nature Communications](#) **11**, 2391 (2020).
- [114] D. A. B. Miller, D. S. Chemla, T. C. Damen, A. C. Gossard, W. Wiegmann, T. H. Wood, and C. A. Burrus, *Band-edge electroabsorption in quantum well structures: the quantum-confined Stark effect*, [Physical Review Letters](#) **53**, 2173 (1984).
- [115] A. A. High, E. E. Novitskaya, L. V. Butov, M. Hanson, and A. C. Gossard, *Control of exciton fluxes in an excitonic integrated circuit*, [Science](#) **321**, 229 (2008).
- [116] G. J. Schinner, J. Repp, E. Schubert, A. K. Rai, D. Reuter, A. D. Wieck, A. O. Govorov, A. W. Holleitner, and J. P. Kotthaus, *Confinement and interaction of single indirect excitons in a voltage-controlled trap formed inside double InGaAs quantum wells*, [Physical Review Letters](#) **110**, 127403 (2013).
- [117] J. A. Schuller, S. Karaveli, T. Schiros, K. He, S. Yang, I. Kyriassis, J. Shan, and R. Zia, *Orientation of luminescent excitons in layered nanomaterials*, [Nature Nanotechnology](#) **8**, 271 (2013).
- [118] J. Klein, J. Wierzbowski, A. Regler, J. Becker, F. Heimbach, K. Müller, M. Kaniber, and J. J. Finley, *Stark effect spectroscopy of mono- and few-layer MoS₂*, [Nano Letters](#) **16**, 1554 (2016).
- [119] Y. Guo, X. Wei, J. Shu, B. Liu, J. Yin, C. Guan, Y. Han, S. Gao, and Q. Chen, *Charge trapping at the MoS₂-SiO₂ interface and its effects on the characteristics of MoS₂ metal-oxide-semiconductor field effect transistors*, [Applied Physics Letters](#) **106**, 103109 (2015).
- [120] T. G. Pedersen, *Exciton Stark shift and electroabsorption in monolayer transition-metal dichalcogenides*, [Physical Review B](#) **94**, 125424 (2016).

- [121] A. Chernikov, A. M. van der Zande, H. M. Hill, A. F. Rigosi, A. Velauthapillai, J. Hone, and T. F. Heinz, *Electrical tuning of exciton binding energies in monolayer WS_2* , [Physical Review Letters](#) **115**, 126802 (2015).
- [122] M. Sidler, P. Back, O. Cotlet, A. Srivastava, T. Fink, M. Kroner, E. Demler, and A. İmamoğlu, *Fermi polaron-polaritons in charge-tunable atomically thin semiconductors*, [Nature Physics](#) **13**, 255 (2016).
- [123] D. K. Efimkin and A. H. MacDonald, *Many-body theory of trion absorption features in two-dimensional semiconductors*, [Physical Review B](#) **95**, 035417 (2017).
- [124] A. Manassen, E. Cohen, A. Ron, E. Linder, and L. N. Pfeiffer, *Exciton and trion spectral line shape in the presence of an electron gas in GaAs/AlAs quantum wells*, [Physical Review B](#) **54**, 10609 (1996).
- [125] A. Epping, L. Banszerus, J. Güttinger, L. Krückeberg, K. Watanabe, T. Taniguchi, F. Hassler, B. Beschoten, and C. Stampfer, *Quantum transport through MoS_2 constrictions defined by photodoping*, [Journal of Physics: Condensed Matter](#) **30**, 205001 (2018).
- [126] M. Sup Choi, G.-H. Lee, Y.-J. Yu, D.-Y. Lee, S. Hwan Lee, P. Kim, J. Hone, and W. Jong Yoo, *Controlled charge trapping by molybdenum disulphide and graphene in ultrathin heterostructured memory devices*, [Nature Communications](#) **4**, 1624 (2013).
- [127] H. Wang, Y. Wu, C. Cong, J. Shang, and T. Yu, *Hysteresis of electronic transport in graphene transistors*, [ACS Nano](#) **4**, 7221 (2010).
- [128] P. Hawrylak, *Optical properties of a two-dimensional electron gas: evolution of spectra from excitons to Fermi-edge singularities*, [Physical Review B](#) **44**, 3821 (1991).
- [129] O. A. Ajayi, J. V. Ardelean, G. D. Shepard, J. Wang, A. Antony, T. Taniguchi, K. Watanabe, T. F. Heinz, S. Strauf, X.-Y. Zhu, and J. C. Hone, *Approaching the intrinsic photoluminescence linewidth in transition metal dichalcogenide monolayers*, [2D Materials](#) **4**, 031011 (2017).
- [130] B. Scharf, T. Frank, M. Gmitra, J. Fabian, I. Žutić, and V. Perebeinos, *Excitonic Stark effect in MoS_2 monolayers*, [Physical Review B](#) **94**, 245434 (2016).

- [131] A. Shields, J. Osborne, M. Simmons, D. Whittaker, F. Bolton, D. Ritchie, and M. Pepper, *Stark effect of negatively and positively charged excitons in semiconductor quantum wells*, [Physica E](#) **2**, 87 (1998).
- [132] C. Jin, E. C. Regan, A. Yan, M. Iqbal Bakti Utama, D. Wang, S. Zhao, Y. Qin, S. Yang, Z. Zheng, S. Shi, K. Watanabe, T. Taniguchi, S. Tongay, A. Zettl, and F. Wang, *Observation of moiré excitons in WSe_2/WS_2 heterostructure superlattices*, [Nature](#) **567**, 76 (2019).
- [133] H. Chen, X. Wen, J. Zhang, T. Wu, Y. Gong, X. Zhang, J. Yuan, C. Yi, J. Lou, P. M. Ajayan, W. Zhuang, G. Zhang, and J. Zheng, *Ultrafast formation of interlayer hot excitons in atomically thin MoS_2/WS_2 heterostructures*, [Nature Communications](#) **7**, 12512 (2016).
- [134] C. Jiang, W. Xu, A. Rasmita, Z. Huang, K. Li, Q. Xiong, and W.-B. Gao, *Microsecond dark-exciton valley polarization memory in two-dimensional heterostructures*, [Nature Communications](#) **9**, 753 (2018).
- [135] D. Unuchek, A. Ciarrocchi, A. Avsar, Z. Sun, K. Watanabe, T. Taniguchi, and A. Kis, *Valley-polarized exciton currents in a van der Waals heterostructure*, [Nature Nanotechnology](#) **14**, 1104 (2019).
- [136] M. M. Fogler, L. V. Butov, and K. S. Novoselov, *High-temperature superfluidity with indirect excitons in van der Waals heterostructures*, [Nature Communications](#) **5**, 4555 (2014).
- [137] F.-C. Wu, F. Xue, and A. H. MacDonald, *Theory of two-dimensional spatially indirect equilibrium exciton condensates*, [Physical Review B](#) **92**, 165121 (2015).
- [138] D. Snoke, *Spontaneous Bose coherence of excitons and polaritons*, [Science](#) **298**, 1368 (2002).
- [139] A. A. High, J. R. Leonard, A. T. Hammack, M. M. Fogler, L. V. Butov, A. V. Kavokin, K. L. Campman, and A. C. Gossard, *Spontaneous coherence in a cold exciton gas*, [Nature](#) **483**, 584 (2012).
- [140] M. Combescot, R. Combescot, and F. Dubin, *Bose–Einstein condensation and indirect excitons: a review*, [Reports on Progress in Physics](#) **80**, 066501 (2017).
- [141] Z. Wang, D. A. Rhodes, K. Watanabe, T. Taniguchi, J. C. Hone, J. Shan, and K. F. Mak, *Evidence of high-temperature exciton condensation in two-dimensional atomic double layers*, [Nature](#) **574**, 76 (2019).

- [142] D. N. Shanks, F. Mahdikhanyarvejahany, C. Muccianti, A. Alfrey, M. R. Koehler, D. G. Mandrus, T. Taniguchi, K. Watanabe, H. Yu, B. J. LeRoy, and J. R. Schaibley, *Nanoscale trapping of interlayer excitons in a 2D semiconductor heterostructure*, [Nano Letters](#) **21**, 5641 (2021).
- [143] C. Chakraborty, N. Vamivakas, and D. Englund, *Advances in quantum light emission from 2D materials*, [Nanophotonics](#) **8**, 2017 (2019).
- [144] J. G. Roch, N. Leisgang, G. Froehlicher, P. Makk, K. Watanabe, T. Taniguchi, C. Schönenberger, and R. J. Warburton, *Quantum-confined Stark effect in a MoS₂ monolayer van der Waals heterostructure*, [Nano Letters](#) **18**, 1070 (2018).
- [145] I. Verzhbitskiy, D. Vella, K. Watanabe, T. Taniguchi, and G. Eda, *Suppressed out-of-plane polarizability of free excitons in monolayer WSe₂*, [ACS Nano](#) **13**, 3218 (2019).
- [146] G. Scuri, Y. Zhou, A. A. High, D. S. Wild, C. Shu, K. De Greve, L. A. Jauregui, T. Taniguchi, K. Watanabe, P. Kim, M. D. Lukin, and H. Park, *Large excitonic reflectivity of monolayer MoSe₂ encapsulated in hexagonal boron nitride*, [Physical Review Letters](#) **120**, 037402 (2018).
- [147] P. Back, S. Zeytinoglu, A. Ijaz, M. Kroner, and A. İmamoğlu, *Realization of an electrically tunable narrow-bandwidth atomically thin mirror using monolayer MoSe₂*, [Physical Review Letters](#) **120**, 037401 (2018).
- [148] A. Y. Joe, L. A. Jauregui, K. Pistunova, A. M. Mier Valdivia, Z. Lu, D. S. Wild, G. Scuri, K. De Greve, R. J. Gelly, Y. Zhou, J. Sung, A. Sushko, T. Taniguchi, K. Watanabe, D. Smirnov, M. D. Lukin, H. Park, and P. Kim, *Electrically controlled emission from singlet and triplet exciton species in atomically thin light-emitting diodes*, [Physical Review B](#) **103**, L161411 (2021).
- [149] P. Nagler, G. Plechinger, M. V. Ballottin, A. Mitioglu, S. Meier, N. Paradiso, C. Strunk, A. Chernikov, P. C. M. Christianen, C. Schüller, and T. Korn, *Interlayer exciton dynamics in a dichalcogenide monolayer heterostructure*, [2D Materials](#) **4**, 025112 (2017).
- [150] M. Förg, L. Colombier, R. K. Patel, J. Lindlau, A. D. Mohite, H. Yamaguchi, M. M. Glazov, D. Hunger, and A. Högele, *Cavity-control of interlayer excitons in van der Waals heterostructures*, [Nature Communications](#) **10**, 3697 (2019).

- [151] A. O. Slobodeniuk, . Bala, M. Koperski, M. R. Molas, P. Kossacki, K. Nogajewski, M. Bartos, K. Watanabe, T. Taniguchi, C. Faugeras, and M. Potemski, *Fine structure of K-excitons in multilayers of transition metal dichalcogenides*, [2D Materials](#) **6**, 025026 (2019).
- [152] E. Calman, M. Fogler, L. Butov, S. Hu, A. Mishchenko, and A. Geim, *Indirect excitons in van der Waals heterostructures at room temperature*, [Nature Communications](#) **9**, 1895 (2018).
- [153] I. Niehues, A. Blob, T. Stiehm, S. M. de Vasconcellos, and R. Bratschitsch, *Interlayer excitons in bilayer MoS₂ under uniaxial tensile strain*, [Nanoscale](#) **11**, 12788 (2019).
- [154] F. Carrascoso, D.-Y. Lin, R. Frisenda, and A. Castellanos-Gomez, *Biaxial strain tuning of interlayer excitons in bilayer MoS₂*, [Journal of Physics: Materials](#) **3**, 015003 (2019).
- [155] Z. Gong, G.-B. Liu, H. Yu, D. Xiao, X. Cui, X. Xu, and W. Yao, *Magnetoelectric effects and valley-controlled spin quantum gates in transition metal dichalcogenide bilayers*, [Nature Communications](#) **4**, 2053 (2013).
- [156] P. Nagler, F. Mooshammer, J. Kunstmann, M. V. Ballottin, A. Mitioglu, A. Chernikov, A. Chaves, F. Stein, N. Paradiso, S. Meier, G. Plechinger, C. Strunk, R. Huber, G. Seifert, D. R. Reichman, P. C. M. Christianen, C. Schüller, and T. Korn, *Interlayer excitons in transition-metal dichalcogenide heterobilayers*, [Physica Status Solidi \(b\)](#) **256**, 1900308 (2019).
- [157] S. Wu, J. S. Ross, G.-B. Liu, G. Aivazian, A. Jones, Z. Fei, W. Zhu, D. Xiao, W. Yao, D. Cobden, and X. Xu, *Electrical tuning of valley magnetic moment through symmetry control in bilayer MoS₂*, [Nature Physics](#) **9**, 149 (2013).
- [158] A. M. Jones, H. Yu, J. S. Ross, P. Klement, N. J. Ghimire, J. Yan, D. G. Mandrus, W. Yao, and X. Xu, *Spin-layer locking effects in optical orientation of exciton spin in bilayer WSe₂*, [Nature Physics](#) **10**, 130 (2014).
- [159] J. Lindlau, M. Selig, A. Neumann, L. Colombier, J. Forste, V. Funk, M. Forg, J. Kim, G. Berghäuser, T. Taniguchi, K. Watanabe, F. Wang, E. Malic, and A. Högele, *The role of momentum-dark excitons in the elementary optical response of bilayer WSe₂*, [Nature Communications](#) **9**, 2586 (2018).

- [160] Z. Wang, Y.-H. Chiu, K. Honz, K. F. Mak, and J. Shan, *Electrical tuning of interlayer exciton gases in WSe_2 bilayers*, [Nano Letters](#) **18**, 137 (2017).
- [161] A. Arora, T. Deilmann, P. Marauhn, M. Drüppel, R. Schneider, M. R. Molas, D. Vaclavkova, S. Michaelis de Vasconcellos, M. Rohlfing, M. Potemski, and R. Bratschitsch, *Valley-contrasting optics of interlayer excitons in Mo- and W-based bulk transition metal dichalcogenides*, [Nanoscale](#) **10**, 15571 (2018).
- [162] A. Arora, M. Drüppel, R. Schmidt, T. Deilmann, R. Schneider, M. R. Molas, P. Marauhn, S. Michaelis de Vasconcellos, M. Potemski, M. Rohlfing, and R. Bratschitsch, *Interlayer excitons in a bulk van der Waals semiconductor*, [Nature Communications](#) **8**, 639 (2017).
- [163] A. Arora, *Magneto-optics of layered two-dimensional semiconductors and heterostructures: progress and prospects*, [Journal of Applied Physics](#) **129**, 120902 (2021).
- [164] E. Lorchat, M. Selig, F. Katsch, K. Yumigeta, S. Tongay, A. Knorr, C. Schneider, and S. Höfling, *Excitons in bilayer MoS_2 displaying a colossal electric field splitting and tunable magnetic response*, [Physical Review Letters](#) **126**, 037401 (2021).
- [165] X. Fan, D. J. Singh, and W. Zheng, *Valence band splitting on multilayer MoS_2 : mixing of spin-orbit coupling and interlayer coupling*, [The Journal of Physical Chemistry Letters](#) **7**, 2175 (2016).
- [166] Q. Liu, L. Li, Y. Li, Z. Gao, Z. Chen, and J. Lu, *Tuning electronic structure of bilayer MoS_2 by vertical electric field: a first-principles investigation*, [The Journal of Physical Chemistry C](#) **116**, 21556 (2012).
- [167] N. Peimyoo, T. Deilmann, F. Withers, J. Escolar, D. Nutting, T. Taniguchi, K. Watanabe, A. Taghizadeh, M. F. Craciun, K. S. Thygesen, and S. Russo, *Electrical tuning of optically active interlayer excitons in bilayer MoS_2* , [Nature Nanotechnology](#) (2021).
- [168] P. Cristofolini, G. Christmann, S. I. Tsintzos, G. Deligeorgis, G. Konstantinidis, Z. Hatzopoulos, P. G. Savvidis, and J. J. Baumberg, *Coupling quantum tunneling with cavity photons*, [Science](#) **336**, 704 (2012).
- [169] C. Schneider, M. M. Glazov, T. Korn, S. Höfling, and B. Urbaszek, *Two-dimensional semiconductors in the regime of strong light-matter coupling*, [Nature Communications](#) **9**, 2695 (2018).

- [170] G. Muñoz-Matutano, A. Wood, M. Johnsson, X. Vidal, B. Q. Baragiola, A. Reinhard, A. Lemaître, J. Bloch, A. Amo, G. Nogues, B. Besga, M. Richard, and T. Volz, *Emergence of quantum correlations from interacting fibre-cavity polaritons*, [Nature Materials](#) **18**, 213 (2019).
- [171] A. Delteil, T. Fink, A. Schade, S. Höfling, C. Schneider, and A. İmamoğlu, *Towards polariton blockade of confined exciton-polaritons*, [Nature Materials](#) **18**, 219 (2019).
- [172] C. Attaccalite, S. Moroni, P. Gori-Giorgi, and G. B. Bachelet, *Correlation energy and spin polarization in the 2D electron gas*, [Physical Review Letters](#) **88**, 256601 (2002).
- [173] H. Dery, *Theory of intervalley Coulomb interactions in monolayer transition-metal dichalcogenides*, [Physical Review B](#) **94**, 075421 (2016).
- [174] K. Marinov, A. Avsar, K. Watanabe, T. Taniguchi, and A. Kis, *Resolving the spin splitting in the conduction band of monolayer MoS₂*, [Nature Communications](#) **8**, 1938 (2017).
- [175] R. Pisoni, A. Kormányos, M. Brooks, Z. Lei, P. Back, M. Eich, H. Overweg, Y. Lee, P. Rickhaus, K. Watanabe, T. Taniguchi, A. İmamoğlu, G. Burkard, T. Ihn, and K. Ensslin, *Interactions and magnetotransport through spin-valley coupled Landau levels in monolayer MoS₂*, [Physical Review Letters](#) **121**, 247701 (2018).
- [176] W. J. Ossau and R. A. Suris, *Optical properties of 2D systems with interacting electrons* (Kluwer Academic Publishers) (2003).
- [177] G. Plechinger, P. Nagler, A. Arora, R. Schmidt, A. Chernikov, A. G. Del Águila, P. C. Christianen, R. Bratschitsch, C. Schüller, and T. Korn, *Trion fine structure and coupled spin-valley dynamics in monolayer tungsten disulfide*, [Nature Communications](#) **7**, 12715 (2016).
- [178] E. Courtade, B. Han, S. Nakhaie, C. Robert, X. Marie, P. Renucci, T. Taniguchi, K. Watanabe, L. Geelhaar, J. M. J. Lopes, and B. Urbaszek, *Spectrally narrow exciton luminescence from monolayer MoS₂ and MoSe₂ exfoliated onto epitaxially grown hexagonal BN*, [Applied Physics Letters](#) **113**, 032106 (2018).
- [179] V. Huard, R. T. Cox, K. Saminadayar, A. Arnoult, and S. Tatarenko, *Bound states in optical absorption of semiconductor quantum wells containing a two-dimensional electron gas*, [Physical Review Letters](#) **84**, 187 (2000).

- [180] Z. Wang, K. F. Mak, and J. Shan, *Strongly interaction-enhanced valley magnetic response in monolayer WSe_2* , [Physical Review Letters](#) **120**, 066402 (2018).
- [181] J. G. Roch, D. Miserev, G. Froehlicher, N. Leisgang, L. Sponfeldner, K. Watanabe, T. Taniguchi, J. Klinovaja, D. Loss, and R. J. Warburton, *First-order magnetic phase transition of mobile electrons in monolayer MoS_2* , [Physical Review Letters](#) **124**, 187602 (2020).
- [182] D. Miserev, J. Klinovaja, and D. Loss, *Exchange intervalley scattering and magnetic phase diagram of transition metal dichalcogenide monolayers*, [Physical Review B](#) **100**, 014428 (2019).
- [183] D. K. Efimkin, E. K. Laird, J. Levinsen, M. M. Parish, and A. H. MacDonald, *Electron-exciton interactions in the exciton-polaron problem*, [Physical Review B](#) **103**, 075417 (2021).
- [184] M. A. Lampert, *Mobile and immobile effective-mass-particle complexes in non-metallic solids*, [Physical Review Letters](#) **1**, 450 (1958).
- [185] H. Bethe, *Berechnung der Elektronenaffinität des Wasserstoffs*, [Zeitschrift für Physik](#) **57**, 815 (1929).
- [186] R. N. Hill, *Proof that the H^- ion has only one bound state*, [Physical Review Letters](#) **38**, 643 (1977).
- [187] J. W. Christopher, B. B. Goldberg, and A. K. Swan, *Long tailed trions in monolayer MoS_2 : temperature dependent asymmetry and resulting red-shift of trion photoluminescence spectra*, [Scientific Reports](#) **7**, 14062 (2017).
- [188] F. Rana, O. Koksal, and C. Manolatou, *Many-body theory of the optical conductivity of excitons and trions in two-dimensional materials*, [Physical Review B](#) **102**, 085304 (2020).
- [189] T. C. Berkelbach, M. S. Hybertsen, and D. R. Reichman, *Theory of neutral and charged excitons in monolayer transition metal dichalcogenides*, [Physical Review B](#) **88**, 045318 (2013).
- [190] F. Cadiz, S. Tricard, M. Gay, D. Lagarde, G. Wang, C. Robert, P. Renucci, B. Urbaszek, and X. Marie, *Well separated trion and neutral excitons on superacid treated MoS_2 monolayers*, [Applied Physics Letters](#) **108**, 251106 (2016).

- [191] B. Peng, Q. Li, X. Liang, P. Song, J. Li, K. He, D. Fu, Y. Li, C. Shen, H. Wang, C. Wang, T. Liu, L. Zhang, H. Lu, X. Wang, J. Zhao, J. Xie, M. Wu, L. Bi, L. Deng, and K. P. Loh, *Valley polarization of trions and magnetoresistance in heterostructures of MoS₂ and yttrium iron garnet*, *ACS Nano* **11**, 12257 (2017).
- [192] I. Kylänpää and H.-P. Komsa, *Binding energies of exciton complexes in transition metal dichalcogenide monolayers and effect of dielectric environment*, *Physical Review B* **92**, 205418 (2015).
- [193] T. Goswami, R. Rani, K. S. Hazra, and H. N. Ghosh, *Ultrafast carrier dynamics of the exciton and trion in MoS₂ monolayers followed by dissociation dynamics in Au@MoS₂ 2D heterointerfaces*, *The Journal of Physical Chemistry Letters* **10**, 3057 (2019).
- [194] J. Jadczyk, J. Kutrowska-Girzycka, P. Kapuściński, Y. S. Huang, A. Wójs, and L. Bryja, *Probing of free and localized excitons and trions in atomically thin WSe₂, WS₂, MoSe₂ and MoS₂ in photoluminescence and reflectivity experiments*, *Nanotechnology* **28**, 395702 (2017).
- [195] G. D. Mahan, *Excitons in degenerate semiconductors*, *Physical Review* **153**, 882 (1967).
- [196] Y.-C. Chang, S.-Y. Shiao, and M. Combescot, *Crossover from trion-hole complex to exciton-polaron in n-doped two-dimensional semiconductor quantum wells*, *Physical Review B* **98**, 235203 (2018).
- [197] T. Korn, S. Heydrich, M. Hirmer, J. Schmutzler, and C. Schüller, *Low-temperature photocarrier dynamics in monolayer MoS₂*, *Applied Physics Letters* **99**, 102109 (2011).
- [198] C. Mai, A. Barrette, Y. Yu, Y. G. Semenov, K. W. Kim, L. Cao, and K. Gundogdu, *Many-body effects in valleytronics: direct measurement of valley lifetimes in single-layer MoS₂*, *Nano Letters* **14**, 202 (2014).
- [199] T. Yu and M. W. Wu, *Valley depolarization due to intervalley and intravalley electron-hole exchange interactions in monolayer MoS₂*, *Physical Review B* **89**, 205303 (2014).
- [200] M. M. Glazov, T. Amand, X. Marie, D. Lagarde, L. Bouet, and B. Urbaszek, *Exciton fine structure and spin decoherence in monolayers of transition metal dichalcogenides*, *Physical Review B* **89**, 201302 (2014).

- [201] H. Yu, X. Cui, X. Xu, and W. Yao, *Valley excitons in two-dimensional semiconductors*, [National Science Review](#) **2**, 57 (2015).
- [202] G. L. Bir, A. G. Aronov, and G. E. Pikus, *Spin relaxation of electrons scattered by holes*, *Zhurnal Eksperimental'noj i Teoreticheskoy Fiziki* **69**, 1382 (1975).
- [203] D. Sun, Y. Rao, G. A. Reider, G. Chen, Y. You, L. Brézin, A. R. Harutyunyan, and T. F. Heinz, *Observation of rapid exciton–exciton annihilation in monolayer molybdenum disulfide*, [Nano Letters](#) **14**, 5625 (2014).
- [204] S. Sim, J. Park, J.-G. Song, C. In, Y.-S. Lee, H. Kim, and H. Choi, *Exciton dynamics in atomically thin MoS_2 : interexcitonic interaction and broadening kinetics*, [Physical Review B](#) **88**, 075434 (2013).
- [205] C. Zhang, H. Wang, W. Chan, C. Manolatou, and F. Rana, *Absorption of light by excitons and trions in monolayers of metal dichalcogenide MoS_2 : experiments and theory*, [Physical Review B](#) **89**, 205436 (2014).
- [206] T. Scrace, Y. Tsai, B. Barman, L. Schweidenback, A. Petrou, G. Kioseoglou, I. Ozfidan, M. Korkusinski, and P. Hawrylak, *Magnetoluminescence and valley polarized state of a two-dimensional electron gas in WS_2 monolayers*, [Nature Nanotechnology](#) **10**, 603 (2015).
- [207] N. D. Mermin and H. Wagner, *Absence of ferromagnetism or antiferromagnetism in one- or two-dimensional isotropic Heisenberg models*, [Physical Review Letters](#) **17**, 1133 (1966).
- [208] Y. Liu, N. O. Weiss, X. Duan, H.-C. Cheng, Y. Huang, and X. Duan, *Van der Waals heterostructures and devices*, [Nature Reviews Materials](#) **1**, 16042 (2016).
- [209] E. Marchiori, L. Ceccarelli, N. Rossi, L. Lorenzelli, C. L. Degen, and M. Poggio, *Technical Review: Imaging weak magnetic field patterns on the nanometer-scale and its application to 2D materials*, [arXiv:2103.10382](#) (2021).
- [210] H. Mattiat, N. Rossi, B. Gross, J. Pablo-Navarro, C. Magén, R. Badea, J. Berzovsky, J. M. De Teresa, and M. Poggio, *Nanowire magnetic force sensors fabricated by focused-electron-beam-induced deposition*, [Physical Review Applied](#) **13**, 044043 (2020).
- [211] C. Zhao, T. Norden, P. Zhang, P. Zhao, Y. Cheng, F. Sun, J. P. Parry, P. Taheri, J. Wang, Y. Yang, T. Scrace, K. Kang, S. Yang, G.-X. Miao, R. Sabirianov,

- G. Kioseoglou, W. Huang, A. Petrou, and H. Zeng, *Enhanced valley splitting in monolayer WSe_2 due to magnetic exchange field*, [Nature Nanotechnology](#) **12**, 757 (2017).
- [212] T. Taniguchi and K. Watanabe, *Synthesis of high-purity boron nitride single crystals under high pressure by using $Ba-BN$ solvent*, [Journal of Crystal Growth](#) **303**, 525 (2007).
- [213] O. D. Pozo-Zamudio, S. Schwarz, J. Klein, R. C. Schofield, E. A. Chekhovich, O. Ceylan, E. Margapoti, A. I. Dmitriev, G. V. Lashkarev, D. N. Borisenko, N. N. Kolesnikov, J. J. Finley, and A. I. Tartakovskii, *Photoluminescence and Raman investigation of stability of $InSe$ and $GaSe$ thin films*, [arXiv:1506.05619](#) (2015).
- [214] Y. Cao, A. Mishchenko, G. L. Yu, E. Khestanova, A. P. Rooney, E. Prestat, A. V. Kretinin, P. Blake, M. B. Shalom, C. Woods, J. Chapman, G. Balakrishnan, I. V. Grigorieva, K. S. Novoselov, B. A. Piot, M. Potemski, K. Watanabe, T. Taniguchi, S. J. Haigh, A. K. Geim, and R. V. Gorbachev, *Quality heterostructures from two-dimensional crystals unstable in air by their assembly in inert atmosphere*, [Nano Letters](#) **15**, 4914 (2015).
- [215] S. Haigh, A. Gholinia, R. Jalil, S. Romani, L. Britnell, D. Elias, K. Novoselov, L. Ponomarenko, A. Geim, and R. Gorbachev, *Cross-sectional imaging of individual layers and buried interfaces of graphene-based heterostructures and superlattices*, [Nature Materials](#) **11**, 764 (2012).
- [216] M. Amani, D.-H. Lien, D. Kiriya, J. Xiao, A. Azcatl, J. Noh, S. R. Madhvapathy, R. Addou, K. Santosh, M. Dubey, K. Cho, R. M. Wallace, S.-C. Lee, J.-H. He, J. W. Ager, X. Zhang, E. Yablonovitch, and A. Javey, *Near-unity photoluminescence quantum yield in MoS_2* , [Science](#) **350**, 1065 (2015).
- [217] L. Yu, Y.-H. Lee, X. Ling, E. J. G. Santos, Y. C. Shin, Y. Lin, M. Dubey, E. Kaxiras, J. Kong, H. Wang, and T. Palacios, *Graphene/ MoS_2 hybrid technology for large-scale two-dimensional electronics*, [Nano Letters](#) **14**, 3055 (2014).
- [218] N. Piccioli, R. Le Toullec, F. Bertrand, and J. Chervin, *Constantes optiques de $InSe$ entre $10\ 500\ cm^{-1}$ ($1,30\ eV$) et $22\ 500\ cm^{-1}$ ($2,78\ eV$)*, [Journal de Physique](#) **42**, 1129 (1981).
- [219] I. H. Malitson, *Interspecimen comparison of the refractive index of fused silica*, [Journal of the Optical Society of America](#) **55**, 1205 (1965).

- [220] S. Adachi, *Optical constants of crystalline and amorphous semiconductors: numerical data and graphical information* (Kluwer Academic Publishers, Boston) (1999).
- [221] D. E. Aspnes and A. A. Studna, *Dielectric functions and optical parameters of Si, Ge, GaP, GaAs, GaSb, InP, InAs, and InSb from 1.5 to 6.0 eV*, [Physical Review B](#) **27**, 985 (1983).
- [222] C. Robert, M. A. Semina, F. Cadiz, M. Manca, E. Courtade, T. Taniguchi, K. Watanabe, H. Cai, S. Tongay, B. Lassagne, P. Renucci, T. Amand, X. Marie, M. M. Glazov, and B. Urbaszek, *Optical spectroscopy of excited exciton states in MoS₂ monolayers in van der Waals heterostructures*, [Physical Review Materials](#) **2**, 011001 (2018).
- [223] G. Kresse and J. Hafner, *Ab initio molecular dynamics for liquid metals*, [Physical Review B](#) **47**, 558 (1993).
- [224] G. Kresse and J. Furthmüller, *Efficient iterative schemes for ab initio total-energy calculations using a plane-wave basis set*, [Physical Review B](#) **54**, 11169 (1996).
- [225] P. E. Blöchl, *Projector augmented-wave method*, [Physical Review B](#) **50**, 17953 (1994).
- [226] G. Kresse and D. Joubert, *From ultrasoft pseudopotentials to the projector augmented-wave method*, [Physical Review B](#) **59**, 1758 (1999).
- [227] S. Grimme, J. Antony, S. Ehrlich, and H. Krieg, *A consistent and accurate ab initio parametrization of density functional dispersion correction (DFT-D) for the 94 elements H-Pu*, [The Journal of Chemical Physics](#) **132**, 154104 (2010).
- [228] J. Heyd and G. E. Scuseria, *Assessment and validation of a screened Coulomb hybrid density functional*, [The Journal of Chemical Physics](#) **120**, 7274 (2004).
- [229] J. Heyd, J. E. Peralta, G. E. Scuseria, and R. L. Martin, *Energy band gaps and lattice parameters evaluated with the Heyd-Scuseria-Ernzerhof screened hybrid functional*, [The Journal of Chemical Physics](#) **123**, 174101 (2005).
- [230] J. Paier, M. Marsman, K. Hummer, G. Kresse, I. C. Gerber, and J. G. Ángyán, *Screened hybrid density functionals applied to solids*, [The Journal of Chemical Physics](#) **124**, 154709 (2006).

- [231] M. Shishkin and G. Kresse, *Implementation and performance of the frequency-dependent GW method within the PAW framework*, [Physical Review B](#) **74**, 035101 (2006).
- [232] A. A. Mostofi, J. R. Yates, Y.-S. Lee, I. Souza, D. Vanderbilt, and N. Marzari, *wannier90: a tool for obtaining maximally-localised Wannier functions*, [Computer Physics Communications](#) **178**, 685 (2008).
- [233] W. Hanke and L. J. Sham, *Many-particle effects in the optical excitations of a semiconductor*, [Physical Review Letters](#) **43**, 387 (1979).
- [234] M. Rohlfing and S. G. Louie, *Electron-hole excitations in semiconductors and insulators*, [Physical Review Letters](#) **81**, 2312 (1998).
- [235] D. Y. Qiu, F. H. da Jornada, and S. G. Louie, *Optical spectrum of MoS₂: many-body effects and diversity of exciton states*, [Physical Review Letters](#) **115**, 119901 (2015).
- [236] A. Ramasubramaniam, D. Naveh, and E. Towe, *Tunable band gaps in bilayer transition-metal dichalcogenides*, [Physical Review B](#) **84**, 205325 (2011).
- [237] J. Xiao, M. Long, X. Li, Q. Zhang, H. Xu, and K. S. Chan, *Effects of van der Waals interaction and electric field on the electronic structure of bilayer MoS₂*, [Journal of Physics: Condensed Matter](#) **26**, 405302 (2014).
- [238] X. Lu and L. Yang, *Stark effect of doped two-dimensional transition metal dichalcogenides*, [Applied Physics Letters](#) **111**, 193104 (2017).
- [239] R. Akashi, M. Ochi, S. Bordács, R. Suzuki, Y. Tokura, Y. Iwasa, and R. Arita, *Two-dimensional valley electrons and excitons in noncentrosymmetric 3R-MoS₂*, [Physical Review Applied](#) **4**, 1467 (2015).
- [240] P. Massignan, M. Zaccanti, and G. M. Bruun, *Polarons, dressed molecules and itinerant ferromagnetism in ultracold Fermi gases*, [Reports on Progress in Physics](#) **77**, 034401 (2014).
- [241] H. Haug and S. W. Koch, *Quantum theory of the optical and electronic properties of semiconductors* (World Scientific), 4th edition (2004).
- [242] D. M. Whittaker and A. J. Shields, *Theory of X- at high magnetic fields*, [Physical Review B](#) **56**, 15185 (1997).

- [243] D. V. Rybkovskiy, I. C. Gerber, and M. V. Durnev, *Atomically inspired $k \cdot p$ approach and valley Zeeman effect in transition metal dichalcogenide monolayers*, [Physical Review B](#) **95**, 155406 (2017).

Nadine Martine Leisgang

Personal information

Mailing address: Spitalstrasse 37, 4226 Breitenbach, Switzerland
Email address: nadine.martine.leisgang@gmail.com
Date of birth: 28th July 1993
Place of birth: Basel, Switzerland
Citizenships: Swiss, German

Education

2017 – 2021 **PhD in Experimental Physics**, “PhD School Quantum Computing and Quantum Technology (QCQT)”, University of Basel, Switzerland

Thesis: “*Electrical control of excitons in a gated two-dimensional semiconductor*”

Advisor: Prof. Dr. Richard J. Warburton

QCQT Excellence Fellowship

2015 – 2017 **Master of Science in Physics**, University of Basel, Switzerland

Thesis: “*Photonics of the transition metal dichalcogenides*”

Advisor: Prof. Dr. Richard J. Warburton

Grade: 5.9 (out of 6.0)

QSIT INSPIRE Award

2012 – 2015 **Bachelor of Science in Physics**, University of Basel, Switzerland

Grade: 5.7 (out of 6.0)

2004 – 2012 **High School Diploma (Abitur)**, Gymnasium Scheinfeld, Germany

Grade: 1.6 (out of 1.0)

Awards

- June 2021 **Swiss Nanotechnology PhD Award**,
Swiss Micro- and Nanotechnology Network, Switzerland
- June 2021 **Nano Image Award**,
Swiss Micro- and Nanotechnology Network, Switzerland
- Mar.–Nov. 2021 **antelope 2021 Career Program** for excellent, advanced
doctoral students, Diversity, University of Basel, Switzerland
- Mar.–Nov. 2021 **ZOOM@Novartis Mentoring Program** for highly qualified
doctoral students, Diversity, University of Basel, Switzerland
- 2017 – 2021 **QCQT Excellence Fellowship**, “Quantum Computing and
Quantum Technology (QCQT)”, University of Basel, Switzerland
- Sept. 2019 **Best Poster Award**, Conference “Flatlands Beyond Graphene
2019”, Toulouse, France
- Sept. 2018 **Best Poster Award**, Conference “Flatlands Beyond Graphene
2018”, Leipzig, Germany
- Nov. 2016 **INSPIRE Potentials – QSIT Master Internship Award**,
–May 2017 NCCR “QSIT – Quantum Science and Technology”, Switzerland

List of publications

1. L. Sponfeldner, N. Leisgang, S. Shree, I. Paradisanos, K. Watanabe, T. Taniguchi, C. Robert, D. Lagarde, A. Balocchi, X. Marie, I. C. Gerber, B. Urbaszek, and R. J. Warburton, *Capacitively-coupled and inductively-coupled excitons in bilayer MoS_2* , [arXiv:2108.04248](#), [submitted](#) (2021).
2. N. Leisgang*, S. Shree*, I. Paradisanos*, L. Sponfeldner*, C. Robert, D. Lagarde, A. Balocchi, K. Watanabe, T. Taniguchi, X. Marie, R. J. Warburton, I. C. Gerber, and B. Urbaszek, *Giant Stark splitting of an exciton in bilayer MoS_2* , [Nature Nanotechnology](#) **15**, 901-907 (2020).
*These authors contributed equally.
3. I. Paradisanos, S. Shree, A. George, N. Leisgang, C. Robert, K. Watanabe, T. Taniguchi, R. J. Warburton, A. Turchanin, X. Marie, I. C. Gerber, and B. Urbaszek, *Controlling interlayer excitons in MoS_2 layers grown by chemical vapor deposition*, [Nature Communications](#) **11**, 2391 (2020).
4. J. G. Roch, D. Miserev, G. Froehlicher, N. Leisgang, L. Sponfeldner, K. Watanabe, T. Taniguchi, J. Klinovaja, D. Loss, and R. J. Warburton, *First-order magnetic phase transition of mobile electrons in monolayer MoS_2* , [Physical Review Letters](#) **124**, 187602 (2020).
5. J. G. Roch, G. Froehlicher, N. Leisgang, P. Makk, K. Watanabe, T. Taniguchi, and R. J. Warburton, *Spin-polarized electrons in monolayer MoS_2* , [Nature Nanotechnology](#) **14**, 432-436 (2019).
6. N. Leisgang, J. G. Roch, G. Froehlicher, M. Hamer, D. Terry, R. Gorbachev, and R. J. Warburton, *Optical second harmonic generation in encapsulated single-layer $InSe$* , [AIP Advances](#) **8**, 105120 (2018).
7. J. G. Roch, N. Leisgang, G. Froehlicher, P. Makk, K. Watanabe, T. Taniguchi, Ch. Schöenberger, and R. J. Warburton, *Quantum confined Stark effect in a MoS_2*

monolayer van der Waals heterostructure, [Nano Letters](#) **18**, 1070-1074 (2018).

*“Every exciting experiment, like every great work of art,
starts with an act of imagination.”*

— Jonah Lehrer

The art of fabrication



Optical micrograph image of a gated van der Waals heterostructure. The device consists of two monolayers of transition metal dichalcogenides encapsulated between insulating hexagonal boron nitride flakes. Direct gold contacts allow us to tune the carrier concentration in the optical active layers in the middle of the structure. Few-layer graphene sheets on the top and bottom of the stack serve as local gates to apply an electric field across the device.

This image reflects the complexity and – at the same time – the beauty of the fabrication of van der Waals heterostructures.